frontiers | Research Topics

Weather and climate extremes in the urban environment: Modeling and observations

Edited by
Chenghao Wang, Ashish Sharma, Quang-Van Doan, V. Vinoj and Zhaowu Yu

Published in
Frontiers in Environmental Science
Frontiers in Earth Science

ISSN 1664-8714
ISBN 978-2-83250-963-0
DOI 10.3389/978-2-83250-963-0

About Frontiers

Frontiers is more than just an open access publisher of scholarly articles: it is a pioneering approach to the world of academia, radically improving the way scholarly research is managed. The grand vision of Frontiers is a world where all people have an equal opportunity to seek, share and generate knowledge. Frontiers provides immediate and permanent online open access to all its publications, but this alone is not enough to realize our grand goals.

Frontiers journal series

The Frontiers journal series is a multi-tier and interdisciplinary set of open-access, online journals, promising a paradigm shift from the current review, selection and dissemination processes in academic publishing. All Frontiers journals are driven by researchers for researchers; therefore, they constitute a service to the scholarly community. At the same time, the *Frontiers journal series* operates on a revolutionary invention, the tiered publishing system, initially addressing specific communities of scholars, and gradually climbing up to broader public understanding, thus serving the interests of the lay society, too.

Dedication to quality

Each Frontiers article is a landmark of the highest quality, thanks to genuinely collaborative interactions between authors and review editors, who include some of the world's best academicians. Research must be certified by peers before entering a stream of knowledge that may eventually reach the public - and shape society; therefore, Frontiers only applies the most rigorous and unbiased reviews. Frontiers revolutionizes research publishing by freely delivering the most outstanding research, evaluated with no bias from both the academic and social point of view. By applying the most advanced information technologies, Frontiers is catapulting scholarly publishing into a new generation.

What are Frontiers Research Topics?

Frontiers Research Topics are very popular trademarks of the *Frontiers journals series*: they are collections of at least ten articles, all centered on a particular subject. With their unique mix of varied contributions from Original Research to Review Articles, Frontiers Research Topics unify the most influential researchers, the latest key findings and historical advances in a hot research area.

Find out more on how to host your own Frontiers Research Topic or contribute to one as an author by contacting the Frontiers editorial office: frontiersin.org/about/contact

Weather and climate extremes in the urban environment: Modeling and observations

Topic editors

Chenghao Wang — University of Oklahoma, United States
Ashish Sharma — University of Illinois at Urbana-Champaign, United States
Quang-Van Doan — University of Tsukuba, Japan
V. Vinoj — Indian Institute of Technology Bhubaneswar, India
Zhaowu Yu — Fudan University, China

Citation

Wang, C., Sharma, A., Doan, Q.-V., Vinoj, V., Yu, Z., eds. (2022). *Weather and climate extremes in the urban environment: Modeling and observations*.
Lausanne: Frontiers Media SA. doi: 10.3389/978-2-83250-963-0

Table of contents

frontiers in Environmental Science

ORIGINAL RESEARCH
published: 10 January 2022
doi: 10.3389/fenvs.2021.778254

Climate-Related Development Finance, Energy Structure Transformation and Carbon Emissions Reduction: An Analysis From the Perspective of Developing Countries

Nan Li[1], *Beibei Shi*[1,2]*, *Lei Wu*[1], *Rong Kang*[1,2] *and Qiang Gao*[3]

[1]School of Economics and Management, Northwest University, Xi'an, China, [2]Shaanxi Key Laboratory for Carbon Neutral Technology, Xi'an, China, [3]School of Economics and Finance, Xi'an Jiaotong University, Xi'an, China

With the frequent occurrence of extreme weather in cities, economic, ecological and social activities have been greatly impacted. The adverse effects of global extreme climate and effective governance have attracted more and more attention of scholars. Considering the differences between developed and developing countries in climate response capacity, a key issue is how to encourage developed countries to provide adequate assistance to developing countries and enhance their enthusiasm to participate in addressing climate change challenges. Given this background, we evaluated the carbon emission reduction effects of developing countries before and after a "quasi-natural experiment" which involved obtaining the assistance of climate-related funding from developed countries. Specifically, we analyzed the assistance behavior for recipient countries and found that climate assistance can effectively reduce the carbon emissions level of recipient countries, and this result has a better impact on non-island types and countries with higher levels of economic development. Furthermore, the achievement of this carbon emissions reduction target stems from the fact that climate assistance has promoted the optimization of the energy structure of recipient countries and promoted the substitution of renewable energy for coal consumption. In addition, climate-related development finance plays a significant role in promoting the scientific and technological level of recipient countries, especially the development impact of the adaptive climate-related development finance. Therefore, this paper suggests that the direction of climate assistance should focus more on island countries and countries with low economic development level, and pay more attention to the "coal withdrawal" of recipient countries and climate adaptation field.

Keywords: climate-related development finance, energy structure transformation, renewable energy development, developing countries, carbon emissions

OPEN ACCESS

Edited by:
Chenghao Wang,
Stanford University, United States

Reviewed by:
Yun Lin,
University of California, Los Angeles, United States
Jarko Fidrmuc,
Zeppelin University, Germany
Guangqin Li,
Anhui University of Finance and Economics, China

***Correspondence:**
Beibei Shi
shibeibei@nwu.edu.cn

Specialty section:
This article was submitted to Atmosphere and Climate, a section of the journal Frontiers in Environmental Science

Received: *16 September 2021*
Accepted: *20 December 2021*
Published: *10 January 2022*

Citation:
Li N, Shi B, Wu L, Kang R and Gao Q (2022) Climate-Related Development Finance, Energy Structure Transformation and Carbon Emissions Reduction: An Analysis From the Perspective of Developing Countries. Front. Environ. Sci. 9:778254. doi: 10.3389/fenvs.2021.778254

INTRODUCTION

With the continuous increase of greenhouse gas emissions, greenhouse gas emissions represented by carbon emissions have gradually attracted the attention of scholars. Since 1960, global total carbon emissions and carbon emissions per capita have shown an upward trend, especially the former, showing continuity and rapidity. As shown in **Figure 1**. It can be seen that the climate problem is

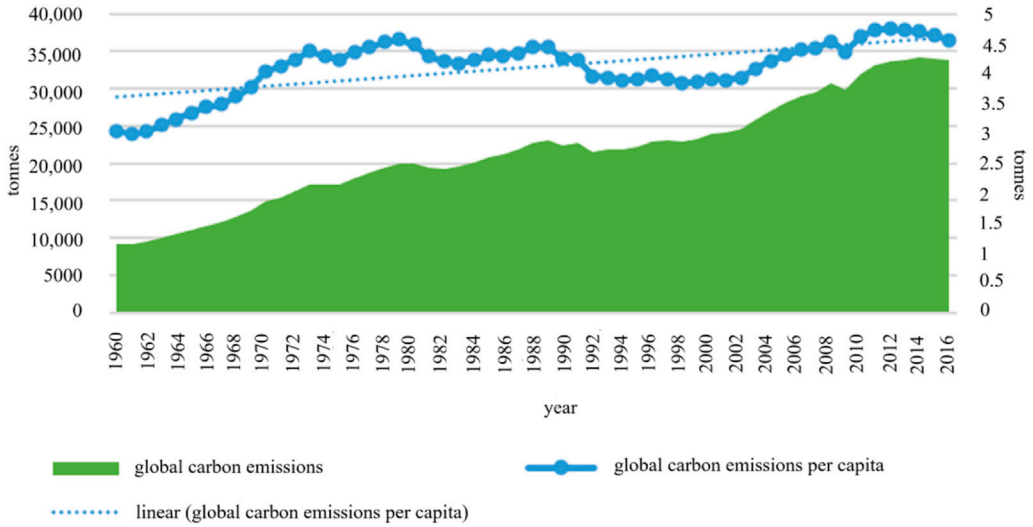

FIGURE 1 | Current status of global carbon emissions. Data source: Wind database (https://www.wind.com.cn/).

becoming more and more serious. Severe climate problems lead to frequent extreme weather and climate in the urban environment. Drought, flood and heat wave seriously threaten the economic development and ecological protection of the city. According to the report of the Food and Agriculture Organization of the United Nations (FAO) in 2021, food prices around the world have risen for 12 consecutive months, reaching the highest level in 10 years. And drought is one of the important reasons for this food crisis. In July 2021, Henan Province, China continued to experience extreme heavy rainfall. Zhengzhou, the provincial capital, suffered a severe rainstorm. The rainfall exceeded the historical extreme value. The rainstorm killed more than 300 people and the economic loss was difficult to measure. The fifth report issued by the Intergovernmental Panel on Climate Change (IPCC) concluded that since 1950, the number of land-based heavy rainfall events may have increased rather than decreased in more parts of the world (>66% probability). From a global perspective, with the increase of extreme rainfall, more noteworthy phenomena are the frequent occurrence of extreme weather such as drought and high temperature, which together pose a severe challenge to global climate governance.

Under the background of intensified climate change, Glasgow climate conference was held in November 2021, which is of great significance for promoting countries to increase the intensity and speed of emissions reduction and strengthening the cooperation between developed and developing countries so as to jointly advance the process of climate governance. The 2018 Nobel Prize in economics was awarded to William Nordhaus, a researcher in the field of climate change, which also reflects the urgency of raising global attention to climate governance. The disastrous impact of global climate change has introduced unprecedented challenges to human survival. Climate change increases the risk of extreme weather and natural disasters (Li et al., 2017; Pour et al., 2020; Sarkodie and Strezov, 2018), which is a great threat to the development of biodiversity and the maintenance of ecosystem balance. There is no doubt that human development needs to be based on the existence of natural sustainability. However, the abnormal climate phenomena caused by human economic activities directly threaten the operation of natural systems. When the global climate change exceeds a certain critical threshold, the natural basis for human survival may be completely destroyed. Without a stable ecosystem, there is no way for human economic development. Besides the impact on nature, abnormal climate change caused by human activities also affects human activities in turn. Some studies show that it has different degrees of impact on agriculture, tourism, and other industries in various countries (Vernon, 2006; Andric et al., 2019; Arsum et al., 2020).

In view of this situation, attracting more countries to actively participate in the process of climate governance is the key to promoting the solution of global climate problems. As an important part of the world, the role of developing countries could not be ignored. From an economic perspective, developing countries have become major participants in the global economy (Kovačević, 2004). With the economic growth of developing countries, their export and import capacity are expanding (Rondinelli and Kasarda, 1992). Due to the needs of economic development, greenhouse gas emissions in developing countries will show an upward trend in the future (Halsnæs, 1996). From the perspective of energy use, with the development of population and economy, the global demand for energy will continue to increase in the future, and most of this growth will occur in developing countries. The share of energy consumption in these countries will increase from 46 to 58% between 2004 and 2040 (Keho, 2016). It can be seen that the impact of economic development and energy use on global climate change is also increasing in developing countries. However, as an economy with a low degree of economic development, it is greatly restricted by capital and technology in promoting its own climate governance process.

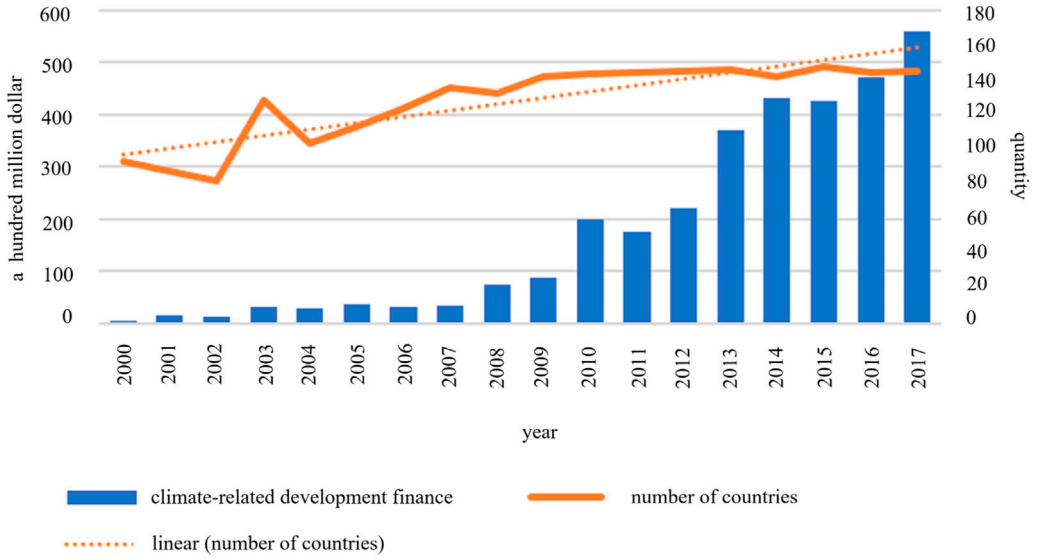

FIGURE 2 | Trends in the number and amount of developing countries supported by climate-related development finance. Data source: official website of Organization for Economic Co-operation and Development (OECD) (https://www.oecd.org/).

The excessive emission of greenhouse gases represented by carbon emissions is an important reason for the current serious climate problems, and the massive use of fossil energy is the key to excessive carbon emissions (Rehman et al., 2019; Shi et al., 2021; Li et al., 2021). For developing countries, energy subsidies are a common phenomenon (Kosmo, 1989), especially fossil fuel subsidies, which are huge and extensive (McCulloch et al., 2021). According to the International Energy Agency (IEA), fossil fuels receive more than four times as much cash support as renewable energy (Yau and Chen, 2021). Excessive subsidies to fossil energy may distort its price, resulting in inefficient energy use and wasteful consumption (Ouyang and Lin, 2014). Therefore, through the above analysis, it can be considered that the economic development of developing countries still relies heavily on fossil energy such as coal. Under this background, if developing countries want to smoothly promote their own climate governance process, they need to focus on the transformation of energy structure. In order to achieve this goal, it needs to reduce the dependence of economic development on coal, improve energy efficiency and actively develop renewable energy, and on this basis, improve the substitution degree of the latter to the former, which needs to be supported by a large amount of capital and a high level of technology. For developing countries, these two elements are precisely the most scarce.

Facing the severe challenge of climate change, all countries in the world have the responsibility and obligation to devote themselves to the process of climate governance. Due to historical reasons, developed countries should shoulder more responsibilities for world climate change. Facing the urgent situation of coping with climate change, the all-round support and guidance of developed countries is of positive significance to promote the process of global climate governance, especially to improve the enthusiasm of developing countries to participate in climate governance. The support of developed countries for climate-related development finance of developing countries is an important way to solve the financing gap of climate governance of the latter, which makes it possible for developing countries to explore diversified carbon emissions reduction paths.

Since 2000, the amount of climate-related development finance from developed countries has shown a rapid upward trend. By 2017, it has exceeded 56 billion US dollars, and the number of developing countries assisted has also shown an increasing trend. By 2017, more than 140 countries have benefited from the climate-related development finance, indicating that more and more countries have been actively guided into the process of climate governance. It can be seen that the positive climate assistance behavior of developed countries helps to mobilize the enthusiasm of more developing countries for climate governance. The specific results are shown in **Figure 2**.

Under this background, has climate-related development finance effectively played its role in reducing the carbon emissions level of recipient countries? Will this result be heterogeneous due to the different urgency of coping with climate change and countries with economic fragility, that is to say, does climate assistance focus on the countries that are in urgent need and priority need help? Furthermore, will the promotion of climate assistance optimize the energy structure of recipient countries, and thus have a certain radiative impact on changes in their carbon emissions? In addition, the impact of different types of climate-related development finance and the development status of different recipient sectors are the focus of this article.

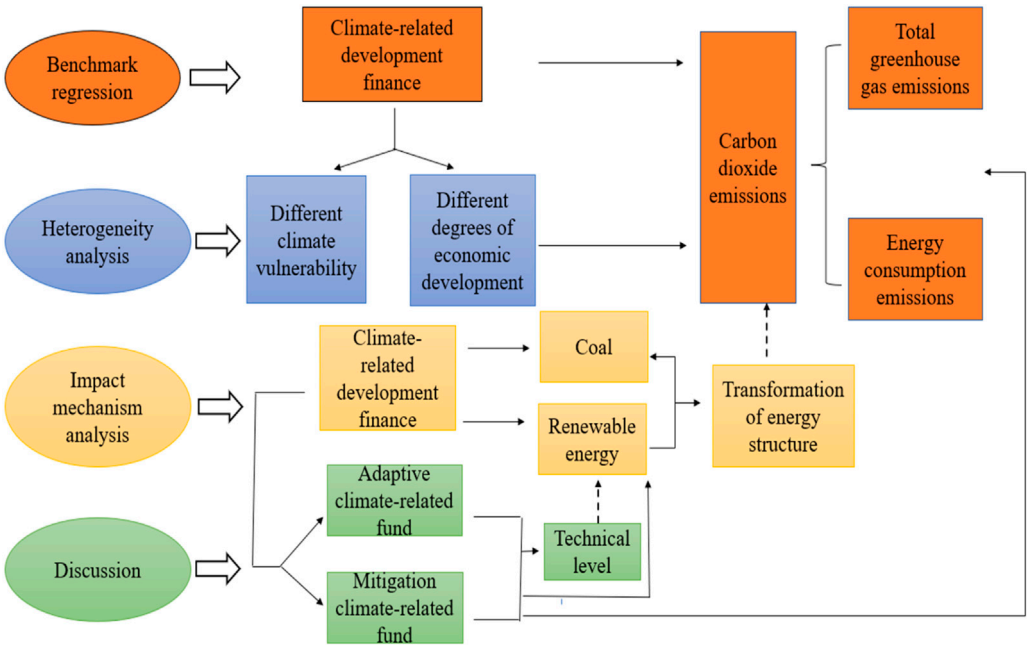

FIGURE 3 | Research procedure.

Through research in this article, it is found that climate assistance can effectively reduce the carbon emissions level of recipient countries, and this result has a better impact on non-island types and countries with higher levels of economic development. Furthermore, the achievement of this carbon emissions reduction target stems from the fact that climate assistance has promoted the optimization of the energy structure of recipient countries and promoted the substitution of renewable energy for coal consumption. In addition, climate-related development finance plays a significant role in promoting the scientific and technological level of recipient countries, especially the development impact of the adaptive climate-related development finance, which lays a foundation for the development of renewable energy. Furthermore, climate financing mainly focuses on environmental related fields such as transportation, energy and education, indicating that there is no deviation in the inflow of specific sectors.

At present, the research on climate assistance mainly focuses on acquisition, management, and distribution of climate-related funding, and there is little discussion on the impact of "South-North cooperation" climate governance model on carbon emissions reduction from the perspective of cooperation between developed and developing countries. Climate-related development finance in developed countries is an important force to promote global climate governance. Therefore, there is still a gap in the research focusing on climate assistance from developed countries to developing countries from the global level. Based on this, the marginal contributions of this study include the following: 1) from the global level, scientifically evaluate the carbon emissions reduction effect brought by climate assistance from developed countries to developing countries, and fill the research gap of "South-North cooperation" climate governance model on a global scale from a macro perspective. 2) This paper takes the total carbon emissions equivalent value of greenhouse gas emissions as the research object, expands the scope of the research object, corrects the previous research only taking carbon dioxide emissions as the unique index, and improves the accuracy of policy effect evaluation. Meanwhile, differences-in-differences method (DID) is used to study the subject of this paper, which could better eliminate the impact of other factors on the research object, and then accurately identify the "net effect" of the target policy to ensure the scientificity of the research. 3) Starting from the energy structure, especially the development of renewable energy, this paper deeply analyzes the internal transmission path of the impact of climate assistance on carbon emissions reduction in recipient countries, and supplements the analysis from the perspective of energy structure transformation. In addition, the impact analysis of different types of climate-related development finance also enriches the research content related to climate assistance.

The remainder of this paper is arranged as follows: **Section 2** introduces the literature review. **Section 3** includes the research methodology and data. **Section 4** presents the empirical results and discussion. **Section 5** presents the impact mechanism test. **Section 6** presents further discussions, and finally, conclusions are drawn in **Section 7**.

LITERATURE REVIEW

Whether climate-related development finance could effectively reduce the carbon emissions level of developing countries

receiving assistance is the focus of this paper. Based on this theme, this paper combs the research in related fields, mainly from the perspectives of research related to climate financing and ways of carbon emissions reduction. First, in terms of climate financing, funding to protect the environment and mitigate climate change had been relatively scarce for many years in developing countries (Ferraro and Pattanayak, 2006; Syed, 2019; Zhang, 2016), and certain industries greatly affected by climate change, such as fisheries, have lacked strong financial support (Guggisberg, 2019). Studies have indicated that the gap in climate adaptation financing is increasing, and whether climate adaptation financing has been appropriately managed and delivered is worth discussing (Khan et al., 2020). At the same time, the questions of how to make more effective use of existing adaptation funds and promote more adaptive investment have become key issues (Xu and Liu, 2018; Sam, 2014; Ornsaran et al., 2020). In recent years, the various financial programs supporting climate action and sustainable development have been expanding. Climate-related funds, such as the Global Environment Facility (GEF), the Green Climate Fund (GCF), and the World Bank BioCarbon Fund, differ in their size, funding type, and funding duration (Clark et al., 2018). To broaden the channels of climate financing, researchers proposed that more climate financing needs could be met by improving the climate financing within and among developing countries (south–south climate financing) (Ha et al., 2016; Ye, 2014; Dumisani, 2016). Private sector involvement can also expand the scale of climate financing (Stein et al., 2010) to supplement the lack of governmental environmental protection (Sudmant et al., 2017; Clark et al., 2018; Vandenbergh, 2018). In view of this, although the current scale and demand of climate financing cannot fully address the problem, the overall scale of climate financing is on the rise (Chen et al., 2019b).

As far as the management of climate financing is concerned, at present, global climate-related funding is still in a relatively developmental state (Pickering et al., 2017). Through research, some scholars proposed that international development and cooperation agencies should jointly manage climate-related funds, and should try to resolve any differences in the assistance objectives of the funds (Brunner and Enting, 2014; Pickering et al., 2015). For aid projects, a sound and mandatory data system should be established to track the climate-related funds of developed countries, to help developing countries cope with evolving climate change commitments, and to facilitate the verification of international climate assistance commitments (Simon et al., 2016).

Regarding the allocation of climate financing, the directional flow of climate-related funding is not only related to the economic and geographical distribution (Román et al., 2016) but also to political factors (Purdon, 2017; Geddes et al., 2020) and the strategic economic considerations of donor countries (Román et al., 2019). Developed countries from different regions have different methods of allocating climate-related funding to developing countries. In general, countries that are more vulnerable to climate change are eligible for more assistance (Betzold and Weiler, 2017; Scandurra et al., 2020); however, European countries are more concerned about the business partners they engage with and therefore prefer to allocate their climate-related funding to specific recipient countries, while the US and Japan allocate their climate aid funds through different projects Scandurra et al., 2017).

In addition, scholars have explored the specific factors influencing climate financing. The driving forces of international financing in developed countries has also been discussed, and the majority of countries are mainly influenced by their material interests (Urpelainen, 2012; Weikmans and Zaccai, 2017). Others argued that, if the promotion of green climate-related funding continues to play an active role in the global climate finance system, China should play the role of a bridge between the developed and developing countries. Guiding green climate-related fund voting reforms to eliminate political factors will help to lessen the negative impact of long-term development (Chen et al., 2019a).

Second, the discussion on the ways of carbon emissions reduction focuses more on the improvement of the carbon emissions trading market. Some scholars first analyzed the factors affecting carbon emission reduction, and believed that the efficiency of the emission reductions is closely related to the economic scale, economic structure, energy utilization efficiency, and energy structure of an economy (Xu and Song, 2010; Sun and Zhang, 2014; Hargrove et al., 2019). In regard to governance measures, emission trading systems (ETS) are a powerful tool to achieve carbon emission reductions (Zhang et al., 2020). An ETS regulates carbon emission activities through market means, improving the enthusiasm of enterprises to reduce emissions, and thus achieving the carbon emission reduction targets (Dong et al., 2019; Song and Xia, 2019). Due to the earlier emergence of a carbon emission trading market in the EU (European Union), Australia, and other regions or countries, scholars have authored a great deal of theoretical analyses and experience summaries on the mode of operations in existing markets (Qi and Wang, 2013; Liang and Cao, 2015). In addition, the market operation efficiency generated by a carbon quota allocation method was further compared and analyzed to provide theoretical support and an experience summary for the practical operation of the carbon market (Hu et al., 2018).

Through the review of literature, we can see that the current analysis of climate-related development finance mainly focuses on acquisition, management and distribution, while the research on the realization path of carbon emissions reduction mainly focuses on the improvement of market model. However, there is still a research gap on the impact of climate financing on carbon emissions reduction, especially on the impact of the model represented by climate assistance from developed countries on developing countries at the global level. On the one hand, the lack of this research will bias the scientific and comprehensive assessment of climate assistance, which may hinder the further promotion and improvement of climate assistance. On the other hand, the lack of this research will limit the discussion of the diversification of carbon emissions reduction approaches. Based on this, starting from the climate-related development finance behavior of developed countries, this paper attempts to evaluate the impact of climate-related development finance on carbon

emissions changes in developing countries to provide experience reference for improving the current climate assistance policies and promoting the exploration of diversified carbon emissions reduction methods in developing countries.

RESEARCH METHODOLOGY AND DATA

Methodology

In order to test the environmental impact of developed countries' climate assistance to developing countries, this paper selects total greenhouse gas emissions of carbon dioxide equivalent and energy consumption emissions of carbon dioxide equivalent of countries as a climate environmental indicator from 1990 to 2017. It also analyzes the climate-related development finance assistance behavior of developed countries to developing countries since 2000, which was published by the OECD as a quasi-natural experiment, and utilizes the DID (differences-in-differences) method to identify the causal effect. From the perspective of recipient countries, this paper regards developing countries (regions) receiving aid as intervention groups, and other developing countries (regions) not receiving aid as control groups. By comparing the samples in the intervention groups and control groups, we can evaluate the net effect of the "South-North cooperation" aid behavior. The specific model is set as follows:

$$Carbon_{it} = \alpha_0 + \alpha_1 CRF_{it} + \alpha_2 \sum Control_{it} + \mu_i + \delta_t + \varepsilon_{it} \quad (1)$$

In the formula above, $Carbon_{it}$ refers to total greenhouse gas emissions thousand tons of carbon dioxide equivalent (CO_2) and energy consumption emissions thousand tons of carbon dioxide equivalent ($energyCO_2$) in each country and region. CRF_{it} indicates whether country i is a recipient target in year t. This paper defines it by setting a dummy variable. If a country has received climate-related development finance, it is assigned a value of 1, which is regarded as an treatment group. Otherwise it is 0, and is regarded as a non-treatment group (control group). This definition could distinguish recipient countries from non-recipient countries, and lay a foundation for setting treatment group and non-treatment group, so as to meet the application conditions of DID method. The treatment group is the object affected by the policy, and the non-treatment group is the object not affected by the policy. Through the DID method, that is, after two differences between the treatment group and the non-treatment group, the "net effect" of policy implementation could be effectively identified, so that the policy could be evaluated more scientifically. Control refers to controlling other factors that may affect carbon emissions, while μ_i refers to the national fixed effect, δ_t refers to the time fixed effect , and ε_{it} refers to the random factors involved. α_1 is our major concern here.

In order to further analyze the internal reasons for the positive impact of climate assistance on carbon emissions reduction, this paper discusses the transmission mechanism by analyzing the relationship between climate assistance and energy structure change from the perspective of energy structure. The specific model is constructed as follows:

$$energy_{it} = \beta_0 + \beta_1 CRF_{it} + \beta_2 \sum Control_{it} + \mu_i + \delta_t + \varepsilon_{it} \quad (2)$$

$$coalpower_{it} = \gamma_0 + \gamma_1 renewables_{it} + \gamma_2 \sum Control_{it} + \mu_i + \delta_t + \varepsilon_{it} \quad (3)$$

$$coalpower_{it} = \theta_0 + \theta_1 renewables_{it} \times CRF_{it} + \theta_2 energy_{it} + \theta_3 \sum Control_{it} + \mu_i + \delta_t + \varepsilon_{it} \quad (4)$$

Among them, **formula (2)** represents the impact of climate assistance on energy changes in recipient countries. $energy_{it}$ represents proportion of coal power generation in total power generation ($coalpower_{it}$) and renewable energy power generation ($renewables_{it}$). **Formula (3)** shows the impact of renewable energy development on coal power consumption in developing countries, which can reflect the degree of substitution of the former for the latter. **Formula (4)** shows the impact of renewable energy development in developing countries on coal power consumption under the background of climate assistance.

In order to ensure the comprehensiveness of the regression results, the significance level of the results is also reported here. This paper uses *t* test for analysis. In addition, to make the research results more logical, this paper presents the subsequent research procedure in the form of a diagram. The specific results are shown in **Figure 3**.

Variable and Data Source Descriptions

Explained variable: the total greenhouse gas carbon emissions equivalent value (CO_2), energy consumption carbon emissions equivalent value ($energyCO_2$). The above two variables are measured by carbon emissions level, and the unit is thousand tons of carbon dioxide equivalent. The reason why the total greenhouse gas carbon emissions equivalent value is selected as the research object is that non carbon dioxide emissions may distort the results of climate change policies. Limiting carbon dioxide emissions in climate change policy analysis will greatly underestimate the actual impact of policies. Therefore, it is necessary to take non-carbon dioxide emissions as the research object (Nong et al., 2021). In addition, because the total carbon emissions can't fully reflect a country's contribution to carbon emissions reduction, this paper makes a supplementary analysis from carbon emissions per capita and carbon emissions per unit of GDP in benchmark regression.

Core explanatory variables: In this paper, we select the climate assistance behavior in 2000 as the core explanatory variable, and the value of the countries receiving assistance is 1[1], otherwise it is 0. In addition, the amount of climate-related development finance, the amount of a climate-related development finance with adaptation (*adapt*), and the amount of a climate-related development finance with mitigation (*mitigate*) are also regarded as the core explanatory variables in the subsequent test.

Control variable: Considering the great influence of economic factors on carbon emissions, this paper mainly identifies and controls carbon emissions from the perspectives of economic development, consumption, and investment and trade activities,

[1]Considering the integrity of the data, this paper eliminates the countries with serious data gaps. There are 145 recipient countries finally included in the analysis of this paper. A list of specific countries is presented in the appendix.

TABLE 1 | Descriptive statistical analysis of major variables.

Variable	Variable meaning	Computing method	Mean	Sd
CO_2	the total greenhouse gas carbon emissions equivalent value	logarithm of total greenhouse gas emissions thousand tons of carbon dioxide equivalent	2.2531	4.3945
energyCO_2	energy consumption carbon emissions equivalent value	logarithm of energy consumption emissions thousand tons of carbon dioxide equivalent	2.0998	4.1522
perCO_2	greenhouse gas emissions thousand tons of carbon dioxide equivalent per capita	logarithm of greenhouse gas emissions thousand tons of carbon dioxide equivalent per capita	0.7808	1.5896
perenergyCO_2	energy consumption emissions thousand tons of carbon dioxide equivalent per capita	logarithm of energy consumption emissions thousand tons of carbon dioxide equivalent per capita	0.6510	1.4072
gdpCO_2	greenhouse gas emissions thousand tons of carbon dioxide equivalent per unit of GDP	logarithm of greenhouse gas emissions thousand tons of carbon dioxide equivalent per unit of GDP	1.9152	3.7373
gdpenergyCO_2	energy consumption emissions thousand tons of carbon dioxide equivalent per unit of GDP	logarithm of energy consumption emissions thousand tons of carbon dioxide equivalent per unit of GDP	1.7626	3.4932
CRF	climate-related development finance	recipient country or not, dummy variable (0,1)	0.5386	0.4985
GDP	gross domestic product	logarithm of GDP amount	4.3805	2.228
GDP^2	GDP square	logarithm of the square of GDP	24.1526	20.7653
priconsum	private consumption	logarithm of household consumption	3.9283	2.1984
pubconsum	public consumption	logarithm of government consumption	2.5093	2.1146
grosscapital	total capital formation	logarithm of total capital formation	2.8833	2.2681
fixedcapit	fixed capital formation	logarithm of fixed capital formation	2.8296	2.2536
export	total exports	logarithm of total exports	3.1594	2.3769
import	total imports	logarithm of total imports	3.4605	2.0555
urban	urbanization level	(urban population/total population)*100	3.8404	0.5023
island	island country and region	island or not, dummy variable (0,1)	0.3121	0.4634
poordegree	poorest countries	poorest country or not, dummy variable (0,1)	0.2832	0.4506
coalpower	proportion of coal power generation in total	proportion of coal power generation in total	29.1878	31.8574
renewables	renewable energy power production capacity	renewable energy power production capacity	0.6825	7.2038
researcher	researcher	logarithm of researcher	5.8437	1.4452
adapt	climate adaptation related funds	sum of annual climate adaptation assistance	0.2156	0.9334
mitigate	climate mitigation related funds	sum of annual climate mitigation assistance	0.5043	2.4836

Source: by the author.

respectively, using GDP (*GDP*) (Wang, 2011) and its square (GDP^2) (Acaravci and Ozturk, 2010), household consumption expenditure (*priconsum*) (Nonhebel and Moll, 2008), government consumption expenditure (*pubconsum*), total capital (*grosscapital*), fixed capital (*grossfixedcapit*), as well as export (*export*) and import (*import*) (Ferdousi and Qamruzzaman, 2017) to express the correlation. In addition, this paper believes that the degree of urbanization has a direct impact on regional energy consumption (Liu, 2009). Therefore, this paper uses the proportion of urban population in the total population to measure the degree of urbanization (*urban*) and adds it into the control variables.

This paper addresses developing countries, and the original data of climate-related development finance comes from the open database of the OECD[2]. The data related to carbon emissions are mainly from Wind database. The data of proportion of coal power generation in total and renewable energy power production capacity are mainly from the World Bank (WB). The rest of the data comes from the public data collected by the United Nations Statistics Division (UNSD). In this study, all the variables involved were analyzed using descriptive statistics. The mean of a variable represents the average level of all countries under this variable, and standard deviation represents dispersion degree of data of all countries under this variable. Since many variables need to be placed in the same model for analysis, a large numerical gap between variables may impact the stability of regression results. The mean value in a reasonable range shows that the relationship between variables is stable, which is conducive to improving the scientificity of regression results. Standard deviation in a reasonable range indicates that there is no abnormal value and the data is reliable. It can be seen that the values of all the variables were in a reasonable range, which shows that the variables selected in this study were effective. The specific results are shown in **Table 1**.

EMPIRICAL RESULTS AND DISCUSSION

Impact of Climate-Related Development Finance Behavior on Carbon Emissions: DID Estimates

This paper estimated model (1) to evaluate the effect of the assistance behavior of climate-related funding on the carbon emissions of recipients. The results are shown in **Table 2**. As can be seen from columns (1)—(2), the assistance behavior of climate-related development finance had an inhibitory effect on the total greenhouse gas carbon emissions equivalent value and

[2]This paper only collates the information of the countries with clear assistance objectives and excludes the other countries without clear assistance objectives.

[2]This paper only collates the information of the countries with clear assistance objectives and excludes the other countries without clear assistance objectives.

TABLE 2 | The impact of the assistance behavior of climate-related development finance on carbon emissions of recipient countries.

	CO_2	$energyCO_2$	$perCO_2$	$perenergyCO_2$	$gdpCO_2$	$gdpenergyCO_2$
	(1)	(2)	(3)	(4)	(5)	(6)
CRF	−0.6800***	−0.6034***	−0.2110***	−0.1505**	−0.5364***	−0.4618***
	(0.2154)	(0.1957)	(0.0771)	(0.0636)	(0.1845)	(0.1645)
GDP	0.4738	0.2505	0.2334	0.1139	0.4967	0.2303
	(0.4460)	(0.4051)	(0.1596)	(0.1316)	(0.3820)	(0.3406)
GDP^2	−0.0123	−0.0130	−0.0023	−0.0039	−0.0122	−0.0132
	(0.0140)	(0.0128)	(0.0050)	(0.0041)	(0.0120)	(0.0107)
priconsum	−0.5427*	−0.5118*	−0.2880***	−0.2353**	−0.5197*	−0.4753**
	(0.3120)	(0.2834)	(0.1117)	(0.0921)	(0.2672)	(0.2383)
pubconsum	−0.0885	0.0410	0.0585	0.0895*	−0.0884	0.0440
	(0.1749)	(0.1588)	(0.0626)	(0.0516)	(0.1498)	(0.1336)
grosscapital	−0.1342	0.0184	−0.0047	0.0786	−0.1216	0.0248
	(0.2590)	(0.2352)	(0.0927)	(0.0764)	(0.2218)	(0.1978)
fixedcapit	−0.0888	−0.1895	−0.1044	−0.1383*	−0.0930	−0.1710
	(0.2662)	(0.2418)	(0.0953)	(0.0785)	(0.2280)	(0.2033)
export	−0.2317	−0.0649	−0.0820	0.0188	−0.2617*	−0.0645
	(0.1805)	(0.1640)	(0.0646)	(0.0533)	(0.1546)	(0.1379)
import	0.4209*	0.2874	0.1931**	0.1077	0.4321**	0.2737
	(0.2531)	(0.2299)	(0.0906)	(0.0747)	(0.2168)	(0.1933)
Year fixed effect	Yes	Yes	Yes	Yes	Yes	Yes
Region fixed effect	Yes	Yes	Yes	Yes	Yes	Yes
_cons	3.4511***	3.5917***	1.0540***	0.9785***	2.8670***	3.0838***
	(0.7412)	(0.6731)	(0.2652)	(0.2187)	(0.6348)	(0.5661)
N	4,746	4,746	4,746	4,746	4,746	4,746
F	21.7255	21.0733	17.3932	14.3128	22.0247	21.4325
r2_a	0.1081	0.1041	0.0812	0.0610	0.1099	0.1063

*Note: *, **, *** are significant at the level of 10, 5 and 1%, respectively; In parentheses is the value of standard error.*

energy consumption carbon emissions equivalent value of recipient countries, and above results passed the 1% significance level test (the *p*-values here are all 0.002), respectively. Specifically, there was a unit of assistance behavior of climate-related development finance, the total greenhouse gas carbon emissions equivalent value in recipient countries will be reduced by 68%, while energy consumption carbon emissions equivalent value will be reduced by 60%. This shows that assistance behavior of climate-related development finance can effectively reduce the carbon emissions level of recipient countries and improve their climate governance status. Because the total carbon emissions can't fully reflect a country's contribution to carbon emission reduction, this paper makes a supplementary analysis from carbon emissions per capita and carbon emissions per unit of GDP. The specific results are listed in column (3)—(6). It can be seen that climate assistance behavior also helps to reduce carbon emissions per capita and carbon emissions per unit of GDP in recipient countries, which demonstrates that the climate assistance behavior of developed countries to developing countries is effective in reducing local carbon emissions.

The reason for this result may be that the economic development level of developing countries is generally low and their financial strength is weak, particularly given the limited financial support for addressing the challenges of climate change. The financial support provided by developed countries eliminates, to some extent, the financing gap of climate finance in developing countries. This provides more opportunities for exploring feasible ways to reduce carbon dioxide and, thus, directly promotes the realization of carbon emission reduction in these countries. Additional data analysis revealed that the number of developing countries receiving assistance expanded from 93 in 2000 to 145 in 2017, and the support for climate-related development finance for developing countries increased from 398 million dollars in 2000 to 56 billion dollars in 2017. This demonstrates that it is the support of external capital inflow that promotes the realization of carbon emission reduction effects in developing countries.

It is necessary for developed countries to provide climate assistance to developing countries. Most developing countries mainly rely on the development of fossil energy such as coal to promote economic development (Akram et al., 2020). This model of sacrificing the environment for economic growth is an important reason that restricts them to achieving good results in climate governance. Therefore, promoting the process of climate assistance to developing countries can provide them with sufficient funds from the outside, so that the funds can flow into the fields of environmental governance, renewable energy development, education and scientific research, fundamentally change their economic development model, and then achieve sustainable development. In addition, climate governance is a problem that all countries in the world need to face. Therefore, climate assistance from developed countries to developing countries is a new attempt to jointly address the challenge of climate change, which is conducive to give full play to the financial and technological advantages of developed countries, and mobilize more developing countries to participate in the process of climate governance, so as to

TABLE 3 | The impact of assistance behavior of climate-related development finance on carbon emissions of recipient countries under different climate vulnerabilities.

	CO_2	CO_2	energyCO_2	energyCO_2
	(1)	(2)	(3)	(4)
CRF*island	−0.2942		−0.1530	
	(0.2703)		(0.2427)	
CRF*nonisland		−0.8755***		−0.8337***
		(0.3032)		(0.2762)
Control variable	Yes	Yes	Yes	Yes
Year fixed effect	Yes	Yes	Yes	Yes
Region fixed effect	Yes	Yes	Yes	Yes
_cons	1.2875	5.4659***	1.9266***	5.2343***
	(0.8153)	(1.1049)	(0.7322)	(1.0065)
N	1,480	3,266	1,480	3,266
F	7.3388	16.7354	6.7011	16.4168
r2_a	0.1059	0.1210	0.0933	0.1183

*Note: *, **, *** are significant at the level of 10, 5 and 1%, respectively; In parentheses is the value of standard error.*

promote the faster realization of the global carbon emission reduction target. Therefore, assistance of climate-related fund is necessary and effective at present.

Heterogeneity Analysis of the Impact of the Assistance Behavior of Climate-Related Development Finance on Carbon Emissions

Heterogeneity analysis of island countries and non-island countries. The essence of developed countries' assistance behavior in regard to climate-related development finance to developing countries is that they help developing countries jointly cope with the challenges brought about by climate change. Thoughtful analysis shows that the assistance behavior of climate-related development finance effectively reduced carbon emissions in developing countries, but whether this effectiveness fully meets the needs of developing countries requires further discussion. Based on this, this paper divides developing countries into island countries and non-island countries for analysis. The reason why developing countries are divided into island countries and non-island countries here is that this paper attempts to discuss whether climate assistance focuses on such countries threatened by sea-level rise, that is, island countries. Under the influence of climate change, island countries are more vulnerable to the threat of sea level rise and food crisis (Organization, 2008; Bijay et al., 2013). Therefore, from the theoretical perspective, climate assistance should focus more on such countries to help them improve their ability to deal with climate change. The island countries here are mainly composed of Small Island Developing States (SIDS) and other island countries.[3]

Through the comparison, the results (see **Table 3**) show that compared with island countries, assistance behavior of climate-related development finance had a positive impact on carbon emissions reduction of non-island countries. There was one unit of assistance behavior of climate-related development finance, and the total carbon dioxide equivalent of greenhouse gas emissions in non-island countries will be reduced by 87%, while energy consumption carbon emissions equivalent value will be reduced by 83%. And the above results passed the 1% significance level test (the p-values here are 0.004 and 0.003, respectively). Assistance behavior of climate-related development finance also had an inhibitory effect on the carbon emissions reduction of island countries, but the effect is not significant, indicating that the climate governance effect of island countries that are more urgent to deal with the challenge of climate change is not ideal under the background of climate assistance. This result also reflects that climate assistance should focus on island countries more affected by climate change in the future, that is, there is a deviation in the current direction of climate assistance behavior. The foresight report on small island developing States issued by the United Nations Environment Programme (UNEP) in 2014 pointed out that with global warming and the increase in the scale and frequency of natural disasters, 52 small island countries around the world face trillions of dollars of economic losses every year. Extreme climate promotes the rise of sea level, which directly increases the threat of flood and coastal erosion to urban tourism and the damage to infrastructure. The deviation of climate-related development finance direction to island countries makes such countries more passive in climate governance.

This paper combs the island countries and non-island countries involved, and finds that in terms of quantity, the number of island countries is 54, while the number of non-island countries is 119. This makes it easier for climate finance to focus on non-island countries. In addition, developed countries may have assistance preferences in the process of climate assistance, which is closely related to factors such as history, geopolitics, economic and trade relations. Due to relevant factors, island countries are generally not as concerned as other countries. Therefore, island countries may receive less attention in the climate-related development finance. This paper also combs the assistance financing and finds that the total amount of climate financing received by island countries was 38.96 billion dollars from 2000 to 2017. And the total amount of climate financing received by non-island countries was 308.75 billion dollars from 2000 to 2017. This also confirms the speculation that a larger number of non-island countries receive higher attention.

The positive impact of climate assistance on carbon emissions reduction of island countries is not significant. In order to make a more detailed analysis of the situation in the group of island countries and discuss the importance of climate-related development finance inflow, this paper takes island countries as the research object, and divides them into strong climate assistance island countries and weak climate assistance island countries according to the degree of assistance amount to analyze the carbon emissions reduction effect of climate assistance. Through the analysis, it is found that climate assistance has a

[3]Here, SIDS includes 43 small island developing States (some small island developing States have been eliminated due to the serious lack of data) and 11 other island developing States. The specific list is presented in detail in the appendix.

more significant impact on the carbon emissions reduction effect of island countries receiving more assistance. The results of total carbon emission and energy carbon emissions passed the significance level test of 5 and 10% respectively (*p*-values are 0.040 and 0.053, respectively). However, climate assistance has no positive effect on carbon emissions reduction in island countries with less assistance. Therefore, it can be considered that within the group of island countries, the inflow of assistance funds is indeed an important factor affecting the realization of the carbon emissions reduction targets of island countries, so it is necessary to increase the support for climate assistance to island countries. The specific results are shown in **Supplementary Appendix Table A1** of the appendix.

The purpose of climate assistance is to help developing countries in need of better climate governance. Facing the threat of climate change, island countries are more affected by the impact of sea level rise, food crisis and extreme weather on domestic economic development. Therefore, the flow direction and assistance effect of climate assistance fund should focus more on such countries. At present, the effect of climate assistance to island countries is not ideal. On the one hand, it shows that the flow of assistance funds is not inclined to the focus of such countries. On the other hand, it also shows that island countries need more investment in climate governance to produce the target effect. Study has shown that climate-related development finance flowing to developing countries accounts for only 4% of the reported total (Donner et al., 2016), which could be inferred that less funds flow to island countries. Therefore, it is worth discussing whether the direction of climate assistance needs to be adjusted in the future.

Heterogeneity analysis under different economic development levels. The differences in the economic development levels among countries indicate the different needs for aid recipients. Countries with low economic development levels may require more attention and assistance coping with the series of challenges related to climate change. Assistance is an important component of financing for such countries (Bourguignon and Platteau, 2021). Based on this, and in accordance with the list of the least developed countries released by the United Nations in 2014, this paper categorized developing countries into countries with a high degree of economic development and countries with a low degree of economic development,[4] and then evaluated the assistance effect of recipient countries with different levels of economic development. The specific results are in **Table 4**.

It can be seen that compared with countries with low economic development level, climate assistance behavior had a significant inhibitory effect on carbon emissions of countries with high economic development level. Specifically, there was one unit of assistance behavior of climate-related development finance, and the total carbon dioxide equivalent of greenhouse gas emissions in countries with high economic development level will be reduced by 81%, while the carbon dioxide equivalent of energy consumption will be reduced by 70%. And the above results passed the 1% significance level test (the *p*-values here are all 0.001). However, the effect of climate assistance behavior on carbon emissions reduction in low economic development countries is not ideal. This result shows that climate-related development finance mainly flow to countries with high levels of economic development and insufficient investment in countries with low levels of economic development, indicating that the current direction of climate assistance has deviated. For countries with low economic development level, their coping ability is weak in the face of extreme weather and climate. In 2016, the World bank issued a relevant report pointing out that poverty makes relevant regions unable to resist natural disasters, and at the same time, the emergence of extreme climate will in turn exacerbate the problem of global poverty. It can be seen that it is necessary to pay attention to climate assistance to countries with low economic development level.

As the number of low-economy developing countries in this paper is only 48, the rest are high-economy developing countries. It can be considered that in terms of quantity, developing countries with high economy are more likely to get attention. To confirm this prediction, this paper further analyzed the amount of assistance funds received by these two types of countries, and found that low-economic developing countries received a total of 72.20 billion dollars in climate assistance funds from 2000 to 2017, while high-economic developing countries received 273.41 billion dollars. It is the high economic developing countries that have received more climate funding and attention, so their carbon emissions reduction effect is more significant than that of low economic developing countries.

For countries with low economic development, it is easier to drive economic development by sacrificing the environment and using cheaper fuels such as coal. At the same time, due to the low level of economic development, the funds invested in the field of

TABLE 4 | The influence of assistance behavior of climate-related development finance on carbon emissions of recipient countries under different levels of economic development.

	CO_2	CO_2	$energyCO_2$	$energyCO_2$
	(1)	(2)	(3)	(4)
CRF*low	0.4892		0.3889	
	(0.9123)		(0.7368)	
CRF*high		-0.8168***		-0.7072***
		(0.2359)		(0.2203)
Control variable	Yes	Yes	Yes	Yes
Year fixed effect	Yes	Yes	Yes	Yes
Region fixed effect	Yes	Yes	Yes	Yes
_cons	1.6645*	3.7552***	1.6552**	4.0854***
	(0.9111)	(1.0987)	(0.7358)	(1.0263)
N	1,336	3,410	1,336	3,410
F	8.0097	16.1591	8.4239	15.5222
r2_a	0.1328	0.1106	0.1411	0.1052

*Note: *, **, *** are significant at the level of 10, 5 and 1%, respectively; In parentheses is the value of standard error.*

[4]Here, the least developed countries released by the United Nations in 2014 are regarded as countries with low economic development level, while the rest are regarded as countries with high economic development level. This paper takes this as the division standard of national economic level. Among them, there are 48 countries with low economic development level, and the specific list of countries is shown in the appendix.

climate governance are also very limited. Therefore, the support of the climate-related development finance for the sustainable development of such countries needs to be greater. At present, the impact of climate assistance on carbon emissions reduction in countries with low economic development has not achieved positive results. It can be considered that the attention of climate-related development finance to such countries needs to be further improved, the existing direction of climate assistance should be adjusted, and the number of climate-related development finance for countries with low economic development should be increased, so as to improve the climate governance capacity of such economically vulnerable countries.

ANALYSIS ON THE RELATIONSHIP BETWEEN CLIMATE ASSISTANCE AND ENERGY STRUCTURE CHANGE

It can be seen from the above description that, the climate support behavior of developed countries significantly reduces the carbon dioxide emissions of developing countries. However, for developing countries, the way in which the climate-related development finance supports to achieve the carbon emission target needs further discussion. In other words, clarifying the intermediary transmission mechanism can contribute better grasping the focus and effects of climate-related fund in developing countries. This paper summarizes the specific sectors that have received the climate-related development finance, and found that the field of renewable energy power generation and non-renewable energy power generation is one of the key areas concerned by the climate-related development finance (renewable energy power generation and non-renewable energy power generation belong to transportation, energy and business services sectors), and the change of energy consumption has a great impact on carbon emissions. The success of a country's energy structure transformation is directly related to the realization of carbon emission reduction targets. Therefore, this paper attempts to explore whether climate assistance helps to optimize the energy structure of developing countries from the perspective of the change of energy structure.

Here, the proportion of coal power generation in the total power generation represents the fossil energy consumption in developing countries, and the renewable energy power generation (excluding hydropower) represents the development of renewable energy in developing countries. As the level of urbanization has a direct impact on energy demand, this paper analyzes the impact of climate assistance on energy development by adding the level of urbanization into the control variables. It can be seen in **Table 5** that columns (1)—(2) show the impact of climate assistance on the proportion of coal power generation in total power generation and renewable energy power generation in recipient countries. It can be seen that climate assistance behavior had not played an ideal effect in reducing fossil energy consumption of developing countries, but it promoted the development of renewable energy in developing countries and this result passed the 5% significance level test (the *p*-values here is 0.019).

TABLE 5 | Analysis on the relationship between climate assistance and energy structure change.

	Coalpower	Renewables	Coalpower	Coalpower
	(1)	(2)	(3)	(4)
CRF	1.0599	2.9393**		1.2913
	(1.3119)	(1.2552)		(1.3170)
renewables			−0.0383*	
			(0.0212)	
CRF *renewables				−0.0368*
				(0.0212)
Control variable	Yes	Yes	Yes	Yes
Year fixed effect	Yes	Yes	Yes	Yes
Region fixed effect	Yes	Yes	Yes	Yes
_cons	−40.0572***	−28.8609***	−43.6053***	−40.3344***
	(14.5995)	(9.9976)	(14.2077)	(14.5817)
N	871	2045	871	871
F	3.4923	14.9649	3.5784	3.4877
r2_a	0.0442	0.1546	0.0474	0.0466

*Note: *, **, *** are significant at the level of 10, 5 and 1%, respectively; In parentheses is the value of standard error.*

The reason for this result may be the price advantage of fossil energy and the impact of the development of technology to a certain extent. At present, developing countries mainly use fossil energy to promote economic development (Zhang et al., 2021), which has a large price advantage and market share. Therefore, coal consumption accounts for a large proportion in the development process (Zhang et al., 2018). Under this background, it will take a long time to achieve the "coal withdrawal" process and more external attention and investment are needed to promote the decline of coal consumption in developing countries. Further, with the economic development and the support of climate-related development finance for the development of many sectors, the scientific and technological level of developing countries has been further improved. For renewable energy, its development needs to be supported by capital (Wen et al., 2022) and technology. In this situation, renewable energy in recipient countries is bound to develop rapidly. The high dependence of recipient countries' economic development on fossil energy has brought great challenges to their climate and environmental governance. The consumption of fossil energy dominated by coal is the source of urban air pollution and temperature rise. The frequent occurrence of extreme weather such as high temperature, heat wave and extreme precipitation in cities shows that climate governance is urgent. To fundamentally reverse this phenomenon, it is necessary to accelerate the reduction of developing countries' dependence on fossil energy and vigorously promote the development of renewable energy.

Climate assistance has not achieved the desired effect on the decline of coal consumption in recipient countries, but has played a positive role in the development of renewable energy. Then, could the development of renewable energy help to reduce the proportion of coal consumption? In other words, it is worth discussing whether the development of renewable energy will play a catalytic role in the "coal withdrawal" process of recipient countries. Based on this, this paper further analyzes the

impact of the development of renewable energy on the change of coal consumption in developing countries.

We can see from column (3) that the development of renewable energy helps to reduce the proportion of coal consumption. Specifically, the development of renewable energy will increase by 1 unit, and the proportion of coal power generation will decrease by 0.0383 units, and this results have passed the 10% significance level test (the *p*-value here is 0.071). In other words, the development of renewable energy has a significant substitution effect on coal. In this paper, the above relationship is tested again under the background of climate assistance. It is found that the development of renewable energy in recipient countries also has a positive substitution for coal under the background of climate assistance. In conclusion, it can be seen that climate assistance reduced carbon emissions by promoting the development of renewable energy in recipient countries and promoting the positive transformation of their energy structure on this basis. The specific results are shown in column (4).

From the above results, it can be seen that under the background of climate assistance, renewable energy in recipient countries has developed rapidly, which has a positive impact on promoting the transformation of energy structure. But it can't be ignored that the process of "coal withdrawal" in recipient countries is still facing great challenges and pressure. In order to more clearly reflect the current situation of fossil energy consumption in developing countries, this paper sorts out the proportion of fossil energy consumption in the total energy consumption and the total consumption of hard coal in developing countries.

From the summary of this article, the average consumption proportion of fossil energy in developing countries shows a slow fluctuating upward trend, but the consumption proportion has declined in some years. From the numerical point of view, the proportion of fossil energy consumption exceeds 50%. From the total consumption of hard coal in developing countries, it can be seen that the consumption of hard coal has shown an upward trend since 2000, peaked in 2015, and then began to decline in 2016. To sum up, developing countries are still heavily dependent on fossil energy, but there is a trend and possibility to reduce fossil energy consumption. Therefore, under the climate assistance background, how to better promote the overall "coal withdrawal" process in developing countries and realize the greater substitution of renewable energy for fossil energy become the key to solve the problem of climate governance in developing countries. The specific results are shown in **Supplementary Appendix Figure A1** and **Supplementary Appendix Figure A2** of the appendix.

DISCUSSION

Impact of Climate-Related Development Finance on Science and Technology Development in Developing Countries

Climate assistance has a positive impact on the development of renewable energy in developing countries, so the way to achieve this result is worthy of in-depth discussion. As the development of renewable energy requires high technology, the level of science and technology could be regarded as the key to the development of renewable energy (Geng and Ji, 2016). And after sorting out the key areas of climate assistance, this paper found that climate-related development finance of developed countries pay special attention to the education field of developing countries (this field is included in department of education, health and infrastructure). Education is the basic support for a country's scientific research and development, which helps to improve the quality of human capital and promote the realization of scientific and technological innovation (Dakhli and De, 2004; Wu, 2006; Xu et al., 2006). The inflow of climate-related development finance into the field of education can be regarded as support for the scientific and technological development of the recipient country. Therefore, the research on the current situation of science and technology development in recipient countries under climate assistance will help this paper further understand the reasons for the rapid development of renewable energy.

Based on this background, from the perspective of science and technology, this paper attempts to deeply explore the impact of climate-related development finance on the scientific and technological level of developing countries, so as to better identify the key factors promoting the positive transformation of energy structure. This paper selects the number of scientific researchers in developing countries as the proxy variable of scientific and technological level. In addition, because the impact of different types of climate-related development finance may be different, this paper analyzes the impact of the development of total climate-related development finance (*totalfund*), adaptive climate-related development finance (*adapt*) and mitigation climate-related development finance (*mitigate*) on technology development respectively. As shown in **Table 6**.

From columns (1)—(2), it can be seen that climate-related development finance helps to promote the increase of the number of scientific researchers in recipient countries, indicating that climate-related development finance has a positive impact on promoting the improvement of scientific and technological level of recipient countries (the *p*-values here are 0.013 and 0.065, respectively). Columns (3)—(6) show impact of the adaptation and mitigation climate-related development finance on the number of scientific researchers in the recipient country. Whether from the regression coefficient or significant results, the development of the adaptation climate-related development finance has a more positive impact on the increase of the number of scientific researchers in the recipient country (the *p*-values here are 0.034 and 0.095, respectively). In other words, compared with the mitigation climate-related development finance, the development of adaptive climate-related development finance plays a greater role in promoting the technological progress of recipient countries. In conclusion, the increase of climate-related development finance can indeed have a positive impact on the improvement of scientific and technological level in developing countries, and technological progress plays an important supporting role in the development of renewable energy.

TABLE 6 | Impact of climate-related development finance on science and technology development in developing countries.

	Researcher	Researcher	Researcher	Researcher	Researcher	Researcher
	(1)	(2)	(3)	(4)	(5)	(6)
totalfund	0.0093**	0.0082*				
	(0.0037)	(0.0044)				
adapt			0.0271**	0.0239*		
			(0.0128)	(0.0143)		
mitigate					0.0099**	0.0076
					(0.0044)	(0.0050)
Control variable	No	Yes	No	Yes	No	Yes
Year fixed effect	Yes	Yes	Yes	Yes	Yes	Yes
Region fixed effect	Yes	Yes	Yes	Yes	Yes	Yes
_cons	5.4651***	6.7689***	5.4607***	6.6317***	5.4646***	6.5871***
	(0.0687)	(1.3894)	(0.0688)	(1.3805)	(0.0688)	(1.3811)
N	702	457	702	457	702	457
F	12.5080	11.5704	12.3777	11.5271	12.4081	11.4918
r2_a	0.1411	0.3258	0.1386	0.3247	0.1392	0.3237

*Note: *, **, *** are significant at the level of 10, 5 and 1%, respectively; In parentheses is the value of standard error.*

Therefore, it can be considered that the impact of climate assistance on renewable energy in developing countries is mainly achieved by promoting the improvement of local technological level.

It is necessary to promote inflow of climate-related development finance into field of education in developing countries, and the development of adaptive climate-related development finance is indispensable. To fundamentally promote the transformation of the economic development model of developing countries and gradually reduce their dependence on fossil energy dominated by coal, it needs to vigorously improve the utilization efficiency of energy (Sarkar and Singh, 2010) and the substitution of renewable energy, which all need to be based on the improvement of technical level. The sustainable development of cities needs to balance the relationship between economy and environment, and technological innovation is the key to achieve the balance between the two. On the premise of ensuring the level of economic development, the improvement of technical level can improve energy utilization efficiency, promote the reduction of fossil energy consumption, lay a technical foundation for the development of renewable energy, and finally achieve the goal of environmental protection. Therefore, to promote the improvement of urban climate and environment in developing countries and reduce the frequency of extreme weather, so as to maintain the sustainable development model, we need to fundamentally improve the technical level. The development of education can provide a strong foundation for the training of scientific researchers and the improvement of technical level in a country. Therefore, paying attention to the investment in education in developing countries and guiding the climate-related development finance to flow more into the field of education is the fundamental policy to promote the sustainable transformation and development of developing countries in the long term.

Through the above analysis, it can be seen that different types of climate-related development finance have different results in supporting local technology development. Compared with the mitigation climate-related development finance, the effect of the adaptive climate-related development finance is more significant. In view of this result, this paper makes a comparative analysis on the development trend of these two types of climate-related development finance, trying to clarify the relationship between this result and the development of assistance amount, that is, does the positive effect of adaptive climate assistance also mean that this type of assistance amount is higher? So as to clarify whether there is a deviation from the current assistance direction. The specific results are shown in **Figure 4**.

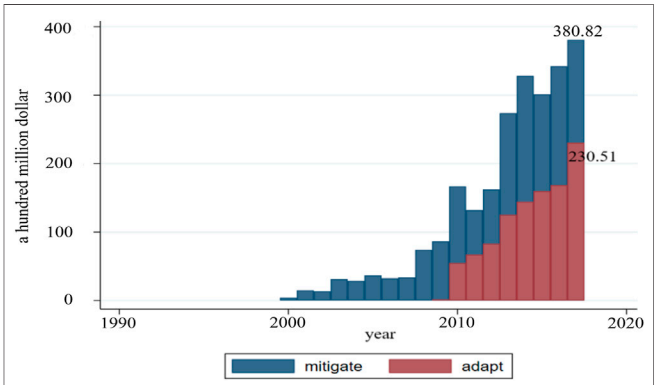

FIGURE 4 | Development comparison of mitigation and adaptation climate-related development finance. Data source: official website of Organization for Economic Co-operation and Development (OECD) (https://www.oecd.org/).

It can be seen that the mitigation climate-related development finance has been paid attention to since 2000, and has shown a rapid upward trend. By 2017, the amount of assistance in this field has exceeded 38 billion US dollars. The development of adaptive climate assistance started late and the development speed is relatively slow. In 2017, the amount of assistance received in this field was about 23 billion dollars. Combined with the results in **Table 6**, it is not difficult to find that the field of adaptive climate has received less attention, but it has a better positive

TABLE 7 | Impact of different types of climate-related development finance on changes in carbon emissions and renewable energy in recipient countries.

	CO_2	CO_2	$energyCO_2$	$energyCO_2$	Renewables	Renewables
	(1)	(2)	(3)	(4)	(5)	(6)
adapt	−0.0905*		−0.0845*		0.4988***	
	(0.0505)		(0.0458)		(0.1191)	
mitigate		−0.0268		−0.0291		0.3945***
		(0.0200)		(0.0181)		(0.0466)
Control variable	Yes	Yes	Yes	Yes	Yes	Yes
Year fixed effect	Yes	Yes	Yes	Yes	Yes	Yes
Region fixed effect	Yes	Yes	Yes	Yes	Yes	Yes
_cons	3.3555***	3.3627***	3.5219***	3.5242***	3.2775*	2.6191
	(0.7463)	(0.7416)	(0.6769)	(0.6734)	(1.7586)	(1.7332)
N	4,698	4,746	4,698	4,746	4,698	4,746
F	21.1712	21.4604	20.5012	20.8488	16.2511	18.0664
r2_a	0.1059	0.1065	0.1017	0.1028	0.0747	0.0855

*Note: *, **, *** are significant at the level of 10, 5 and 1%, respectively; In parentheses is the value of standard error.*

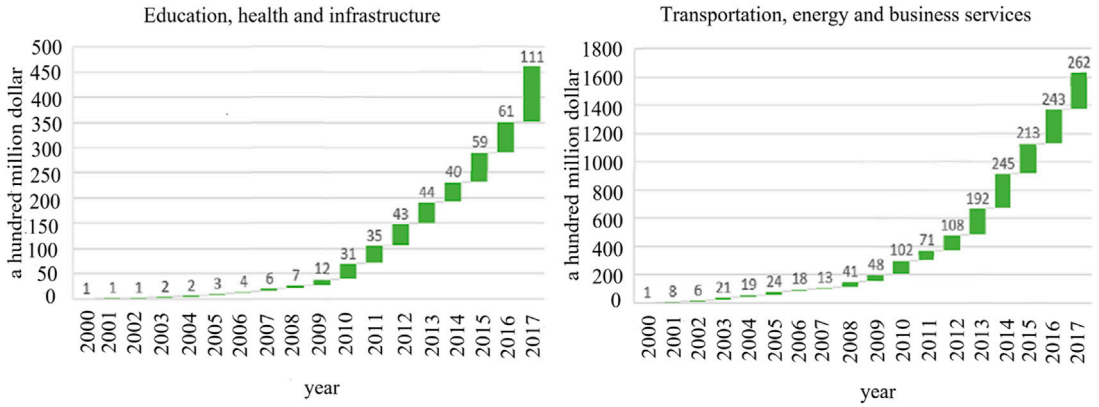

FIGURE 5 | Support of climate-related development finance for sectors I and II. Data source: official website of Organization for Economic Co-operation and Development (OECD) (https://www.oecd.org/).

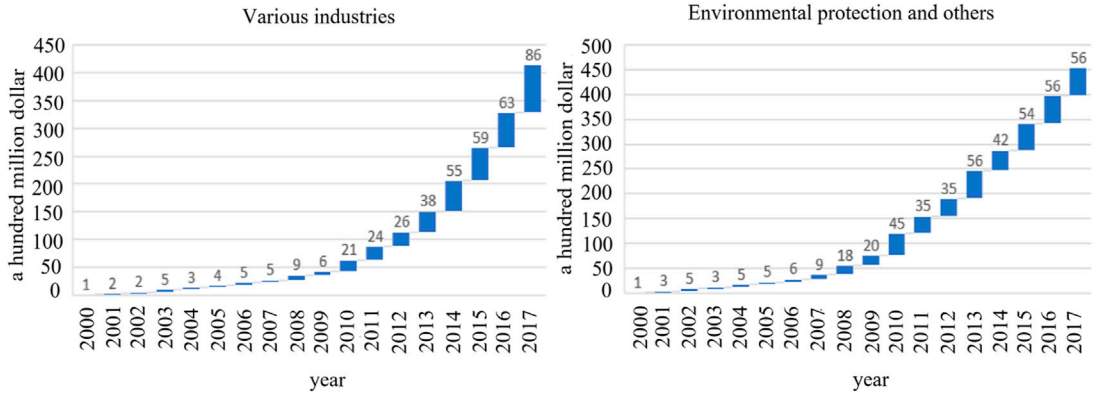

FIGURE 6 | Support of climate-related development finance for sectors III and IV. Data source: official website of Organization for Economic Co-operation and Development (OECD) (https://www.oecd.org/).

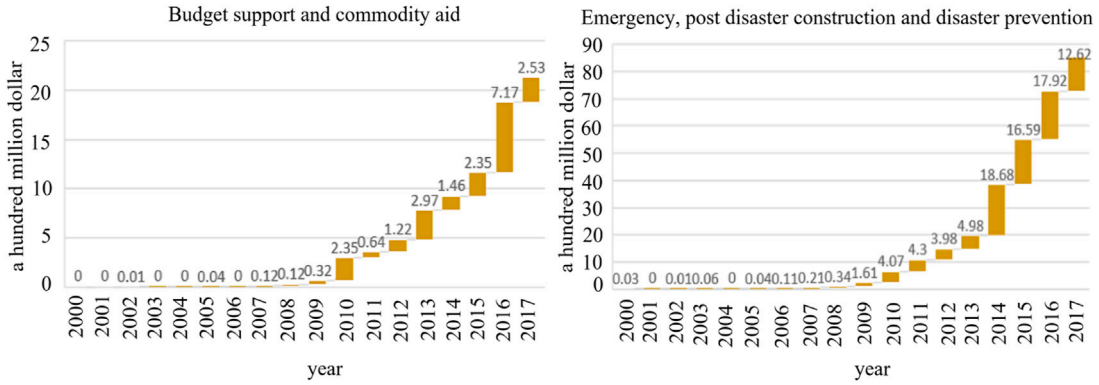

FIGURE 7 | Support of climate-related development finance for sectors VI and VIII. Data source: official website of Organization for Economic Co-operation and Development (OECD) (https://www.oecd.org/).

impact on the technological development of developing countries. Therefore, whether more attention needs to be paid to adaptive climate is worth discussing.

Analysis on the Impact of Different Types of Climate-Related Development Finance and Assistance Received by Different Sectors

In view of the large differences in the scale of climate-related development finance flowing into the two fields of climate adaptation and climate mitigation, this paper analyzes the carbon emission reduction results and the development impact of renewable energy brought by the two types of climate-related development finance, and tries to compare the effectiveness of the results brought by the current focus on the fields of climate adaptation and climate mitigation to better evaluate the development status of the two types of climate assistance. The specific results are shown in **Table 7**.

Columns (1)—(4) show the impact of these two types of climate-related development finance on carbon emissions of recipient countries. It can be seen that the development of these two types of climate-related development finance helps to reduce carbon emissions of recipient countries, but the emissions reduction effect brought by adaptive climate assistance is more significant, and the result passed the 10% significance level test (the *p*-values here are 0.073 and 0.065, respectively). From columns (5)—(6), it can be seen that these two types of climate-related development finance have a positive role in promoting the development of renewable energy in recipient countries (the *p*-values here are 0.000), but by comparing the regression coefficient, it is found that the promotion effect of adaptive climate assistance is better. Combined with **Figure 4**, this paper believes that under the background of more mitigation climate-related development finance, its impact on carbon emissions reduction and renewable energy development is not as good as that brought by the adaptation climate-related development finance. In the face of extreme weather in cities, it is particularly important to adapt to the climate. In order to cope with possible floods, the construction of urban coastline and the improvement of urban infrastructure are an important part of adapting to the climate. At the same time, in order to reduce the adverse effects of extreme drought, rational allocation of urban water and agricultural irrigation water is also a typical way to adapt to climate change. Better adaptation to the climate is conducive to the sustainable development of all cities. So the current attention to adaptive climate assistance should be further improved (Pauw, 2021).

The support of climate-related development finance is the basis for promoting climate governance and the development of specific recipient sectors in recipient countries. Therefore, it is very necessary to study the preference and direction of fund inflow. From the perspective of different types of climate assistance, we have carried out a detailed analysis of the trend of fund inflow and its impact on carbon emissions reduction. And does the fund have a certain preference and focus on the inflow of different sectors? Based on this, this paper analyzes the current focus of climate-related development finance on key sectors. Due to the large difference in the amount of climate assistance received by recipient departments, this paper presents it through two figures. The specific results are shown in **Figure 5**, **Figure 6** and **Figure 7**.

Through comparison, it can be seen that the four sectors "Education, health and infrastructure," "Transportation, energy and business services," "Various industries" and "Environmental protection and others" receive more climate-related development finance, and the development of climate-related development finance is faster, especially the two sectors "Education, health and infrastructure" and "Transportation, energy and business services" receive more attention. The two sectors "Budget support and commodity aid" and "Emergency, post disaster construction and disaster prevention" received less attention. It can be seen that climate assistance is more focused on environmental related sectors at present, such as transportation and energy. Therefore, there is no deviation in the current direction of climate assistance in support of specific sectors.

CONCLUSION

Taking developing countries as the research object, this paper uses the differences-in- differences method (DID) to identify the

causality of the impact of climate assistance behavior in developed countries on carbon emissions in developing countries. Through the research, it is found that climate assistance could significantly reduce the carbon emissions level of recipient countries, indicating that the promotion of climate assistance is necessary. First, this paper proves the conclusion that climate assistance behavior helps to reduce the carbon emissions level of recipient countries through DID method, that is to say, climate assistance behavior has been affirmed. Second, from the perspective of the quantity of climate financing, this paper further analyzes the carbon emissions reduction effects of the two types of climate financing to illustrate the significance of climate finance flows to recipient countries. Finally, it can be seen from **Figure 2** that the scale of climate financing shows an expanding trend. Combined with the previous analysis, this paper believes that the existence and scale expansion of climate financing have a positive impact on the realization of carbon emissions reduction targets of recipient countries. However, the impact of this result on island types and recipient countries with low level of economic development has not achieved the desired effect. The positive impact of climate assistance on carbon emissions reduction in recipient countries is mainly realized by promoting the transformation of energy structure in target countries. Furthermore, climate-related development finance plays a positive role in promoting the technical level of recipient countries, especially the development of the adaptive climate-related development finance, Meanwhile, compared with the mitigation climate-related development finance, adaptation climate-related development finance has a more positive effect on carbon emissions reduction and renewable energy development. In addition, the climate-related development finance is mostly directed to the fields of transportation, energy and education at present.

This paper systematically analyzes the current situation, impact effects and existing problems of the "South-North cooperation" climate governance model, in order to provide reference for the rational adjustment and improvement of the direction of climate assistance in the future, and provide empirical support for further improving the enthusiasm of climate assistance in developed countries and guiding more developing countries to participate in the process of global climate governance. The frequent occurrence of extreme weather caused by climate change poses a great threat to the economic development and ecological protection of countries all over the world. In the face of extreme weather and climate, countries need to strengthen financial and technical cooperation and jointly contribute wisdom in exploring diversified and effective climate governance models. The specific conclusions are as follows:

First, climate assistance can significantly reduce the total carbon emissions equivalent of greenhouse gases and carbon emissions equivalent of energy consumption in recipient countries, and this result does not change in the analysis of carbon emissions per capita and carbon emissions per unit GDP. For the achievement of carbon emissions reduction target, it has a better effect on non-island countries and countries with high degree of economic development. The existence of climate assistance is meaningful, and the assistance of developed countries to climate governance in developing countries should be further promoted, including the amount of investment in the climate-related development finance and the scope of developing countries assisted. Further increasing the amount of developed countries' investment in climate assistance and expanding the scope of benefits can better supplement the funding gap for climate governance in developing countries, and lay a foundation and provide a bridge for mobilizing more countries to participate in climate governance. At the same time, the direction of climate assistance should be adjusted, focusing on island countries and countries with low economic development that are more urgent to deal with the challenge of climate change, and giving more attention and financial support to these two types of countries to help regions with more dangerous situations better deal with climate change.

Second, climate assistance helps to promote the transformation of energy structure in recipient countries. Specifically, it promotes the development of renewable energy in recipient countries and significantly promotes the substitution of renewable energy for coal consumption, which provides important support for developing countries to achieve carbon emission reduction targets. But it could not be ignored that direct impact of climate assistance in promoting the process of "coal withdrawal" in recipient countries is still very limited. At present, the consumption of fossil energy in developing countries is still large, but it shows a downward trend. Under this background, climate assistance should increase investment and subsidies in renewable energy and other clean energy in developing countries and improve their market competitiveness and price advantage to accelerate their substitution for fossil energy. And helping developing countries improve the utilization efficiency of fossil energy represented by coal, reduce their dependence on coal, and then promote the process of "coal withdrawal."

Third, climate-related development finance helps to improve the scientific and technological level of developing countries, especially the development of the adaptive climate-related development finance, which makes it possible to promote the development of renewable energy and the transformation of energy structure in developing countries. The amount and development speed of mitigation climate-related development finance are higher than that of the adaptation climate-related development finance, but the latter has a better impact on carbon emission reduction and renewable energy development. In addition, the inflow sectors of climate-related development finance are mainly concentrated in transportation, energy, education and other sectors, indicating that there is no deviation in the assistance direction focusing on specific sectors. At present, the amount of the two types of climate-related development finance should be appropriately adjusted, and more attention should be paid to climate adaptation assistance. For developing countries, especially those that are particularly urgent to deal with the climate crisis, better adaptation to climate change in a certain period of time is more meaningful to ensure their lives and promote economic development. At the same time, increase the inflow of climate assistance funds to developing countries in the fields of transportation, energy and education, promote the

development of sectors related to the environment, and vigorously supporting the development of education will help lay the foundation for the progress of science and technology in developing countries.

DATA AVAILABILITY STATEMENT

The original contributions presented in the study are included in the article/**Supplementary Material**, further inquiries can be directed to the corresponding author.

AUTHOR CONTRIBUTIONS

NL: Conceptualization, Methodology, Formal analysis, and Writing—original draft. BS: Conceptualization, Methodology, Formal analysis, and Writing—original draft. LW: Data curation, Visualization, and Writing—original draft. RK: Formal analysis, Data curation, and Visualization. QG: Data curation, and Writing—original draft.

FUNDING

This research is funded by the Youth Project of National Natural Science Foundation of China (No. 72103163), Shaanxi Provincial Natural Science Basic Research Program (No. 2021JQ-457), China-Central Eastern European Countries Higher Joint Education Project (No. 202028). This research is also supported by Shaanxi Key Laboratory for Carbon Neutral Technology.

SUPPLEMENTARY MATERIAL

The Supplementary Material for this article can be found online at: https://www.frontiersin.org/articles/10.3389/fenvs.2021.778254/full#supplementary-material

REFERENCES

Acaravci, A., and Ozturk, I. (2010). On the Relationship between Energy Consumption, CO2 Emissions and Economic Growth in Europe. *Energy* 35, 5412–5420. doi:10.1016/j.energy.2010.07.009

Akram, R., Chen, F., Khalid, F., Ye, Z., and Majeed, M. T. (2020). Heterogeneous Effects of Energy Efficiency and Renewable Energy on Carbon Emissions: Evidence from Developing Countries. *J. Clean. Prod.* 247, 119122. doi:10.1016/j.jclepro.2019.119122

Andric, I., Muammer, K., and Sami, G. A. (2019). A Review of Climate Change Implications for Built Environment: Impacts, Mitigation Measures and Associated Challenges in Developed and Developing Countries. *J. Clean. Prod.* 20, 83–102. doi:10.1016/j.jclepro.2018.11.128

Arsum, P. A., Philip, E. A., Van, B., Fenda, A. A., Akiwumi, B., and Kenyon, C. L. (2020). Impacts of Climate Change on the Tourism Sector of a Small Island Developing State: A Case Study for the Bahamas. *Environ. Dev.* 37 (5964), 100556. doi:10.1016/j.envdev.2020.100556

Betzold, C., and Weiler, F. (2017). Allocation of Aid for Adaptation to Climate Change: Do Vulnerable Countries Receive More Support? *Int. Environ. Agreements* 17, 17–36. doi:10.1007/s10784-016-9343-8

Bijay, P., Filho, W. L., and Schulte, V. (2013). "Understanding the Links between Climate Change and Disaster Management in Pacific Island Countries," in *Climate Change Management* (Berlin, Heidelberg: Springer), 55–69. doi:10.1007/978-3-642-31110-9_4

Bourguignon, F., and Platteau, J. P. (2021). Aid Allocation: The Role of External Discipline. *Int. Econ.* doi:10.1016/j.inteco.2021.06.008

Brunner, S., and Enting, K. (2014). Climate Finance: a Transaction Cost Perspective on the Structure of State-To-State Transfers. *Glob. Environ. Change* 27, 138–143. doi:10.1016/j.gloenvcha.2014.05.005

Chen, L., Wang, W. T., Zhu, L. C., and Zhang, D. W. (2019a). The Role and Development of Green Climate Fund in the Global Climate Governance System. *Progressus Inquisitiones de Mutatione Clim.* 15, 326–334. doi:10.12006/j.issn.1673-1719.2018.138

Chen, L., Zhang, D. W., and Zhu, L. C. (2019b). Global Climate Financing Situation and Prospect. *Environ. Prot.* 1, 33–38.

Clark, R., Reed, J., and Sunderland, T. (2018). Bridging Funding Gaps for Climate and Sustainable Development: Pitfalls, Progress and Potential of Private Finance. *Land Use Policy* 71, 335–346. doi:10.1016/j.landusepol.2017.12.013

Dakhli, M., and De Clercq, D. (2004). Human Capital, Social Capital, and Innovation: a Multi-Country Study. *Entrepreneurship Reg. Dev.* 16, 107–128. doi:10.1080/0898562041000167783

Dong, F., Dai, Y., Zhang, S., Zhang, X., and Long, R. (2019). Can a Carbon Emission Trading Scheme Generate the Porter Effect? Evidence from Pilot Areas in China. *Sci. Total Environ.* 653, 565–577. doi:10.1016/j.scitotenv.2018.10.395

Donner, S. D., Kandlikar, M., and Webber, S. (2016). Measuring and Tracking the Flow of Climate Change Adaptation Aid to the Developing World. *Environ. Res. Lett.* 11, 054006. doi:10.1088/1748-9326/11/5/054006

Dumisani, C. (2016). Moving Past the Rhetoric: Policy Considerations that Can Make Sino-African Relations to Improve Africa's Climate Change Resilience and the Attainment of the Sustainable Development Goals. *Adv. Clim. Change Res.* 7, 253–263. doi:10.1016/j.accre.2016.11.002

Ferdousi, F., and Qamruzzaman, M. (2017). Export, Import, Economic Growth, and Carbon Emissions in Bangladesh: a Granger Causality Test under VAR (Restricted) Environment. *Manage. Cities Reg.* Chapters. doi:10.5772/intechopen.70782

Ferraro, P. J., and Pattanayak, S. K. (2006). Money for Nothing? A Call for Empirical Evaluation of Biodiversity Conservation Investments. *Plos Biol.* 4, e105. doi:10.1371/journal.pbio.0040105

Geddes, A., Schmid, N., Schmidt, S. T., and Steffen, B. (2020). The Politics of Climate Finance: Consensus and Partisanship in Designing green State Investment banks in the United Kingdom and Australia. *Energ. Res. Soc. Sci.* 69, 101583. doi:10.1016/j.erss.2020.101583

Geng, J. B., and Ji, Q. (2016). Technological Innovation and Renewable Energy Development: Evidence Based on Patent Counts. *Ijgenvi* 15, 217. doi:10.1504/ijgenvi.2016.076945

Guggisberg, S. (2019). Funding Coastal and marine Fisheries Projects under the Climate Change Regime. *Mar. Pol.* 107, 103352.1–103352.10. doi:10.1016/j.marpol.2018.11.015

Ha, S., Hale, T., and Ogden, P. (2016). Climate Finance in and between Developing Countries: an Emerging Opportunity to Build on. *Glob. Pol.* 7, 1. doi:10.1111/1758-5899.12293

Halsnæs, K. (1996). The Economics of Climate Change Mitigation in Developing Countries. *Energy Policy* 24, 917–926. doi:10.1016/s0301-4215(96)80357-0

Hargrove, A., Qandeel, M., and Sommer, J. M. (2019). Global Governance for Climate justice: A Cross-National Analysis of CO2 Emissions. *Glob. Transitions* 1, 190–199. doi:10.1016/j.glt.2019.11.001

Hu, Y.-c., Zhou, W., and Yuan, T. (2018). Environmental Impact Assessment of Ecological Migration in China: a Survey of Immigrant Resettlement Regions. *J. Zhejiang Univ. Sci. A.* 19, 240–254. doi:10.1631/jzus.a1600669

Keho, Y. (2016). What Drives Energy Consumption in Developing Countries? the Experience of Selected African Countries. *Energy Policy* 91, 233–246. doi:10.1016/j.enpol.2016.01.010

Khan, M., Robinson, S.-a., Weikmans, R., Ciplet, D., and Roberts, J. T. (2020). Twenty-Five Years of Adaptation Finance through a Climate justice Lens. *Clim. Change* 161, 251–269. doi:10.1007/s10584-019-02563-x

Kosmo, M. (1989). Commercial Energy Subsidies in Developing Countries Opportunity for Reform. *Energy Policy* 17, 244–253. doi:10.1016/0301-4215(89)90049-9

Kovacevic, R. (2004). The Position of Developing Countries in International Trade. *Ekon Anal.* 49, 65–97. doi:10.2298/eka0462065k

Li, X., Zhou, Y., Asrar, G. R., Imhoff, M., and Li, X. (2017). The Surface Urban Heat Island Response to Urban Expansion: A Panel Analysis for the Conterminous United States. *Sci. Total Environ.* 605-606, 426–435. doi:10.1016/j.scitotenv.2017.06.229

Li, N., Shi, B., and Kang, R. (2021). Information Disclosure, Coal Withdrawal and Carbon Emissions Reductions: A Policy Test Based on China's Environmental Information Disclosure. *Sustainability* 13, 9758. doi:10.3390/su13179758

Liang, Y. C., and Cao, Y. K. (2015). Analysis on the Market Framework of Carbon Emission Trading System in Australia. *World For. Res.* 2, 86–90. doi:10.13348/j.cnki.sjlyyj.2015.02.012

Liu, Y. (2009). Exploring the Relationship between Urbanization and Energy Consumption in China Using ARDL (Autoregressive Distributed Lag) and FDM (Factor Decomposition Model). *Energy* 34, 1846–1854. doi:10.1016/j.energy.2009.07.029

McCulloch, N., Moerenhout, T., and Yang, J. (2021). Fuel Subsidy Reform and the Social Contract in Nigeria: A Micro-economic Analysis. *Energy Policy* 156, 112336. doi:10.1016/j.enpol.2021.112336

Nong, D., Simshauser, P., and Nguyen, D. B. (2021). Greenhouse Gas Emissions vs CO2 Emissions: Comparative Analysis of a Global Carbon Tax. *Appl. Energ.* 298, 117223. doi:10.1016/j.apenergy.2021.117223

Nonhebel, S., and Moll, H. C. (2008). The Relationship between Household Expenditures and Environmental Impact. *Energ. Environ. Stud.*, 1–8.

Organization, A. (2008). Climate Change and Food Security in Pacific Island Countries. *Clim. Change Food Security Pac. Isl. Countries* 40, 301–313. doi:10.1002/9783527665334.ch1

Ornsaran, P. M., Robbert, B., and Victor, C. (2020). What Makes Internationally-Financed Climate Change Adaptation Projects Focus on Local Communities? A Configurational Analysis of 30 Adaptation Fund Projects. *Glob. Environ. Change* 61, 102035. doi:10.1016/j.gloenvcha.2020.102035

Ouyang, X., and Lin, B. (2014). Impacts of Increasing Renewable Energy Subsidies and Phasing Out Fossil Fuel Subsidies in China. *Renew. Sustain. Energ. Rev.* 37, 933–942. doi:10.1016/j.rser.2014.05.013

Pauw, W. P. (2021). The Adaptation Finance gap Can Only Be Closed by Limiting the Adaptation Costs. *One Earth* 4, 1352–1355. doi:10.1016/j.oneear.2021.09.002

Pickering, J., Skovgaard, J., Kim, S., Roberts, J. T., Rossati, D., Stadelmann, M., et al. (2015). Acting on Climate Finance Pledges: Inter-agency Dynamics and Relationships with Aid in Contributor States. *World Dev.* 68, 149–162. doi:10.1016/j.worlddev.2014.10.033

Pickering, J., Betzold, C., and Skovgaard, J. (2017). Special Issue: Managing Fragmentation and Complexity in the Emerging System of International Climate Finance. *Int. Environ. Agreements* 17, 1–16. doi:10.1007/s10784-016-9349-2

Pour, S. H., Wahab, A. K. A., Shahid, S., Asaduzzaman, M. d., and Dewan, A. (2020). Low Impact Development Techniques to Mitigate the Impacts of Climate-Change-Induced Urban Floods: Current Trends, Issues and Challenges. *Sustain. Cities Soc.* 62, 102373. doi:10.1016/j.scs.2020.102373

Purdon, M. (2017). Neoclassical Realism and International Climate Change Politics: Moral Imperative and Political Constraint in International Climate Finance. *J. Int. Relat. Dev.* 20, 263–300. doi:10.1057/jird.2013.5

Qi, S. Z., and Wang, B. B. (2013). Initial Quota Allocation of Carbon Trading: a Comparative Analysis of Models and Methods. *Wuhan Univ. J.(Philos. Soc. Sci.)* 5, 19–28.

Rehman, A., Rauf, A., Ahmad, M., Chandio, A. A., and Zhang, D. Y. (2019). The Effect of Carbon Dioxide Emission and the Consumption of Electrical Energy, Fossil Fuel Energy, and Renewable Energy, on Economic Performance: Evidence from Pakistan. *Environ. Sci. Pollut. Res.* 26, 21760–21773. doi:10.1007/s11356-019-05550-y

Román, V. M., Arto, I., Ansuategi, A., and Galarraga, I. (2019). The Economic Implications of Tied Aid and Local Content Requirements for Climate Finance. *Clim. Change Econ.* 11, 2050002. doi:10.1142/s2010007820500025

Román, V. M., Arto, I., and Ansuategi, A. (2016). The Geographic Distribution of the Economic Impact of Climate Finance. Working Papers. 5, BC3.

Rondinelli, D. A., and Kasarda, J. D. (1992). Foreign Trade Potential, Small enterprise Development and Job Creation in Developing Countries. *Small Business Econ.* 4, 253–265. doi:10.1007/bf00388621

Sam, B. (2014). Subnational Climate justice? Adaptation Finance Distribution and Climate Vulnerability. *World Dev.* 58, 130–142. doi:10.1016/j.worlddev.2014.01.014

Sarkar, A., and Singh, J. (2010). Financing Energy Efficiency in Developing Countries—Lessons Learned and Remaining Challenges. *Energy Policy* 38, 5560–5571. doi:10.1016/j.enpol.2010.05.001

Sarkodie, S. A., and Strezov, V. (2018). Economic, Social and Governance Adaptation Readiness for Mitigation of Climate Change Vulnerability: Evidence from 192 Countries. *Sci. Total Environ.* 15, 150–164. doi:10.1016/j.scitotenv.2018.11.349

Scandurra, G., Romano, A., Carfora, A., and Ronghi, M. (2017). *Climate Finance as an Instrument to Promote the green Growth in Developing Countries*. Berlin: Springer-Verlag.

Scandurra, G., Thomas, A., Passaro, R., Bencini, J., and Carfora, A. (2020). Does Climate Finance Reduce Vulnerability in Small Island Developing States? an Empirical Investigation. *J. Clean. Prod.* 256, 120–330. doi:10.1016/j.jclepro.2020.120330

Shi, B. B., Wu, L., and Kang, R. (2021). Clean Development, Energy Substitution, and Carbon Emissions: Evidence from Clean Development Mechanism (CDM) Project Implementation in China. *Sustainability* 13, 860. doi:10.3390/su13020860

Simon, D. D., Milind, K., and Sophie, W. (2016). Measuring and Tracking the Flow of Climate Change Adaptation Aid to the Developing World. *Environ. Res. Lett.* 11, 054006. doi:10.1088/1748-9326/11/5/054006

Song, D. Y., and Xia, T. X. (2019). Performance Evaluation of Carbon Trading Pilot Policy in China. *Stat. Decis.* 11, 157–160. doi:10.13546/j.cnki.tjyjc.2019.11.037

Stein, P., Goland, T., and Schiff, R. (2010). *Two Trillion and Counting: Assessing the Credit gap for Micro, Small, and Medium-Size Enterprises in the Developing World*. Washington DC: World Bank.

Sudmant, A., Colenbrander, S., Gouldson, A., and Chilundika, N. (2017). Private Opportunities, Public Benefits? the Scope for Private Finance to Deliver Low-Carbon Transport Systems in Kiga. *Rwanda. Urban Clim.* 20, 59–74. doi:10.1016/j.uclim.2017.02.011

Sun, X., and Zhang, K. M. (2014). Empirical Analysis on the Influencing Factors of Carbon Emission Intensity in China. *Stat. Res.* 31, 61–67. doi:10.3969/j.issn.1002-4565.2014.02.009

Syed, M. R. (2019). Structural Analogy in Development and Climate Aid: The Case of bangladesh. *J. Dev. Pol. Pract.* 4, 89–116. doi:10.1177/2455133318812983

Urpelainen, J. (2012). Strategic Problems in North–South Climate Finance: Creating Joint Gains for Donors and Recipients. *Environ. Sci. Pol.* 21, 14–23. doi:10.1016/j.envsci.2012.03.001

Vandenbergh, P. M. (2018). Keynote: Motivating Private Climate Governance: the Role of the Efficiency gap. *Ark. L. Rev.* 71 (2), 1.

Vernon, L. (2006). Potential Impacts of Climate Change on Agricultural Land Use Suitability : Lupins. *Department Agric.*

Wang, K. M. (2011). The Relationship between Carbon Dioxide Emissions and Economic Growth: Quantile Panel-type Analysis. *Qual. Quant.* 47, 1337–1366. doi:10.1007/s11135-011-9594-y

Weikmans, R., and Zaccai, E. (2017). An Analysis of justice Conceptions in Climate Change Adaptation Aid. *Dev. Durable Territ.* 8 (1). doi:10.4000/developpementdurable.11668

Wen, J., Okolo, C. V., Ugwuoke, I. C., and Kolani, K. (2022). Research on Influencing Factors of Renewable Energy, Energy Efficiency, on Technological Innovation. Does Trade, Investment and Human Capital Development Matter? *Energy Policy* 160, 112718. doi:10.1016/j.enpol.2021.112718

Wu, Y. M. (2006). Application of Spatial Econometric Model in Provincial R & D and Innovation. *J. Quant. Tech. Econ.* 23 (5), 74–85+130. doi:10.3969/j.issn.1000-3894.2006.05.009

Xu, Y. S., and Liu, Q. (2018). Status Quo and prospect of the Global Climate Adaptation Finance. *J. Cent. Univ. Finance Econ.* 8, 25–36.

Xu, G. Y., and Song, D. Y. (2010). Empirical Study on Environmental Kuznets Curve of Carbon Emission in China - Based on Provincial Panel Data. *China Ind. Econ.* 5, 37–47.

Xu, H. L., Qi, P., and Zhu, S. J. (2006). Trade Openness, Human Capital and Total Factor Productivity: An Empirical Analysis Based on China's Inter Provincial Panel Data. *The J. World Econ.* 29 (12), 3–1096.

Yau, R., and Chen, G. H. (2021). Assessing Energy Subsidy Policies in a Structural Macroeconomic Model. *Energ. Econ.* 103, 105509. doi:10.1016/j.eneco.2021.105509

Ye, Y. (2014). Climate Finance, Africa and China's Role. *Afr. East-asian Aff.* 1, 36–57. doi:10.7552/0-1-120

Zhang, Y. Q., Liu, C. J., Li, K., and Zhou, Y. (2018). Strategy on China's Regional Coal Consumption Control: A Case Study of Shandong Province. *Energy Policy* 112, 316–327. doi:10.1016/j.enpol.2017.10.035

Zhang, H. R., Zhang, R. X., Li, G. M., Li, W., and Choi, Y. (2020). Has China's Emission Trading System Achieved the Development of a Low-Carbon Economy in High-Emission Industrial Subsectors? *Sustainability* 12, 1–20. doi:10.3390/su12135370

Zhang, G. X., Nuruzzaman, M., and Su, B. (2021). Nexus between Household Energy Consumption and Economic Growth in Bangladesh (1975–2018). *Energy Policy* 156, 112420. doi:10.1016/j.enpol.2021.112420

Zhang, P. (2016). Study on the Demand of Climate Finance for Developing Countries Based on Submitted INDC. *Adv. Clim. Change Res.* 7, 99–104. doi:10.1016/j.accre.2016.05.002

Conflict of Interest: The authors declare that the research was conducted in the absence of any commercial or financial relationships that could be construed as a potential conflict of interest.

Publisher's Note: All claims expressed in this article are solely those of the authors and do not necessarily represent those of their affiliated organizations, or those of the publisher, the editors and the reviewers. Any product that may be evaluated in this article, or claim that may be made by its manufacturer, is not guaranteed or endorsed by the publisher.

frontiers in Environmental Science

ORIGINAL RESEARCH
published: 21 January 2022
doi: 10.3389/fenvs.2021.795474

Formulating Operational Mitigation Options and Examining Intra-Urban Social Inequality Using Evidence-Based Urban Warming Effects

Yuanhui Zhu[1], *Soe W. Myint*[1]*, *Danica Schaffer-Smith*[2,3], *Rebecca L. Muenich*[4], *Daoqin Tong*[1] *and Yubin Li*[1]

[1]School of Geographical Sciences and Urban Planning, Arizona State University, Tempe, AZ, United States, [2]School of Life Sciences, Arizona State University, Tempe, AZ, United States, [3]The Nature Conservancy, Durham, NC, United States, [4]School of Sustainable Engineering, Arizona State University, Tempe, AZ, United States

Human-induced climate change is bringing warmer conditions to the Southwestern United States. More extreme urban heat island (UHI) effects are not distributed equally, and often impact socioeconomically vulnerable populations the most. This study aims to quantify how land surface temperature (LST) changes with increasing green vegetation landscapes, identify disparities in urban warming exposure, and provide a method for developing evidence-based mitigation options. ECOSTRESS LST products, detailed land use and land cover (LULC) classes, and socioeconomic variables were used to facilitate the analysis. We examined the relationship between LST and the fractions of LULC and socioeconomic factors in the city of Phoenix, Arizona. A machine learning approach (Random Forest) was used to model LST changes by taking the LULC fractions (scenario-based approaches) as the explanatory variables. We found that vegetation features—trees, grass, and shrubs—were the most important factors mitigating UHI effects during the summer daytime. Trees tended to lower surface temperature more effectively, whereas we observed elevated daytime LST most often near roads. Meanwhile, higher summer daytime temperatures were observed on land with unmanaged soil compared to the built environment. We found that affluent neighborhoods experienced lower temperatures, while low-income communities experienced higher temperatures. Scenario analyses suggest that replacing 50% of unmanaged soil with trees could reduce average summer daytime temperatures by 1.97°C if the intervention was implemented across all of Phoenix and by 1.43°C if implemented within the urban core only. We suggest that native trees requiring little to no additional water other than rainfall should be considered. We quantify mitigation options for urban warming effect under vegetation management interventions, and our results provide some vital insight into existing disparities in UHI impacts. Future UHI mitigation strategies seriously need to consider low-income communities to improve environmental justice. These can be used to guide the development of sustainable and equitable policies for vegetation management to mitigate heat exposure impacts on communities.

OPEN ACCESS

Edited by:
Chenghao Wang,
Stanford University, United States

Reviewed by:
Weiqi Zhou,
Research Center for Eco-environmental Sciences (CAS), China
Tao Zhang,
Iowa State University, United States

***Correspondence:**
Soe W. Myint
Soe.Myint@asu.edu

Specialty section:
This article was submitted to Environmental Informatics and Remote Sensing, a section of the journal Frontiers in Environmental Science

Received: *15 October 2021*
Accepted: *09 December 2021*
Published: *21 January 2022*

Citation:
Zhu Y, Myint SW, Schaffer-Smith D, Muenich RL, Tong D and Li Y (2022) Formulating Operational Mitigation Options and Examining Intra-Urban Social Inequality Using Evidence-Based Urban Warming Effects. Front. Environ. Sci. 9:795474. doi: 10.3389/fenvs.2021.795474

Keywords: ECOSTRESS, land surface temperature, land use and land cover, socioeconomic status, scenario analysis, Phoenix

1 INTRODUCTION

Urbanization, or the conversion of natural landscapes to the human-built environment, is driven by population growth and socioeconomic development (Bettencourt et al., 2007; Grimm et al., 2008; Peng et al., 2012; Seto et al., 2012). These changes in land use and land cover (LULC) can cause land surface temperature (LST) changes through alteration of the albedo, roughness, and heat flux exchange of the land surface in urban and sub-urban environments (Estoque et al., 2017; Singh et al., 2017). The LULC changes are accompanied by well-known urban heat island (UHI) issues. The UHI is a particularly important issue because it is leading to substantial challenges to urban ecosystem functionality (e.g., the loss of vegetation), the increase of energy and water consumption, and heightened risks of heat-related mortality and morbidity among vulnerable groups (Chen et al., 2006; Tran et al., 2006; Buyantuyev and Wu, 2010; Zhou et al., 2011; Jesdale et al., 2013; Wang et al., 2018). To counterbalance these negative impacts, formulating operational UHI mitigation options and examining intra-urban social inequality are needed.

Most studies focus on the effect of LULC changes, impervious surface expansion, and landscape configuration on UHI (Dousset and Gourmelon, 2003; Voogt and Oke, 2003; Weng et al., 2004; Chen et al., 2006; Tran et al., 2006; Weng, 2009). There is substantial evidence that urbanization drives LULC changes (e.g., vegetated features converted to built-up areas), which also impacts LST (Pan et al., 2019). Moreover, socioeconomic disparities are well recognized factors in connection to UHI, and these factors merit attention in identifying UHI problem areas and developing solutions (Harlan et al., 2006). It is essential to identify the inequalities in LST exposure associated with different socioeconomic groups. Hence, the available socioeconomic data need to be assessed to explain observed LST distributions. LST has disproportionately influenced the neighborhoods with family types and dwellings, where areas with low-income, higher Black and Hispanic populations may experience higher levels of UHI (Oreszczyn et al., 2006; Mashhoodi, 2021). Previous studies on LST and social inequality have focused on the cities of Phoenix, New York, Los Angeles and Chicago (Jenerette et al., 2011; Chow et al., 2012; Mitchell and Chakraborty, 2015). For example, urban residents in metropolitan Phoenix with lower income usually face greater risk of heat stress than wealthier neighborhoods because the latter can afford air conditioning and water to supply green vegetation (Harlan et al., 2006; Chow et al., 2012). The more limited resources available to socially vulnerable populations raise inequality concerns (Li et al., 2016; Tang et al., 2017; Li et al., 2020). Therefore, more attention should be paid to socioeconomic disparities in connection to LST.

UHI is a particularly important issue for the desert cities of southwestern United States, as climate change is bringing even hotter and drier conditions to the region, which is experiencing substantial population growth (Christensen and Lettenmaier, 2007; Seager et al., 2007; Barnett and Pierce, 2008). For example, Phoenix, Arizona's mean daily temperature has increased by 3.1°C during the last 50 years due to climate change and rapid urbanization, while summer nighttime temperatures have increased by as much as 6°C (Brazel et al., 2000). The conversion to built-up areas from all other LULC types has been determined as the dominant cause of the UHI effect in Phoenix (Wang C. et al., 2016). However, desert cities do not fit the conventional UHI trend but show unique patterns of LST variation. For arid desert regions specifically, tree cover typically reduces summer daytime temperature more effectively than grass, while unmanaged soil and dark impervious surfaces (e.g., asphalt surfaces) elevate temperature more than buildings (Myint et al., 2013; Zhang et al., 2019). Urban areas in desert cities can be cooler in summer than suburban regions where vegetation is sparse, and unmanaged soil is the primary reflecting surface (Xian and Crane, 2006; Lazzarini et al., 2013; Myint et al., 2013). Unlike other cities, higher densities of built infrastructure are not necessarily responsible for extreme heat in desert communities (Hartz et al., 2006; Cui and De Foy, 2012; Lazzarini et al., 2013). However, there is an emerging need to explore the UHI in harsh environments to develop effective and practical solutions that can be implemented immediately to mitigate urban warming effects.

Maintaining and enhancing urban vegetation is a well-tested mitigation and adaptation strategy for UHI in arid desert areas (Bowler et al., 2010; Myint et al., 2010; Huang and Cadenasso, 2016). Green vegetation surfaces store less heat than unmanaged soil, buildings, parking lots, streets, and other impervious surfaces, although the impact of trees, shrubs, and grass on the UHI may vary (Guhathakurta and Gober, 2010; Myint et al., 2010; Myint et al., 2013). It has been widely accepted that increasing green vegetation surfaces can effectively mitigate UHI (Weng et al., 2004; Zhou et al., 2011; Li et al., 2013). Studies in the Sonoran and Mojave Deserts, and the Phoenix Metropolitan Area specifically, have demonstrated that areas dominated by drought tolerant shrubs and woody plants show strong daytime transpirative cooling effects (Smith, 1978; Hamerlynck et al., 2000; Wang et al., 2019). Consequently, there is an increased interest in the effect of both the type and extent of greenspace on the level of UHI and formulating operational action plans to mitigate urban warming effects. In addition, the intensity of cooling effects on LST by increasing green space need to be quantified to provide insights for green infrastructure planning and management. However, most impervious surfaces in urban centers cannot realistically be changed or replaced by other LULC features with less heat storage to mitigate the UHI effect. Opportunities may exist to convert areas of unmanaged soil in desert cities to green vegetation to lower LST. This is an operational UHI mitigation option in desert cities. However, there is a lack of research on determining the

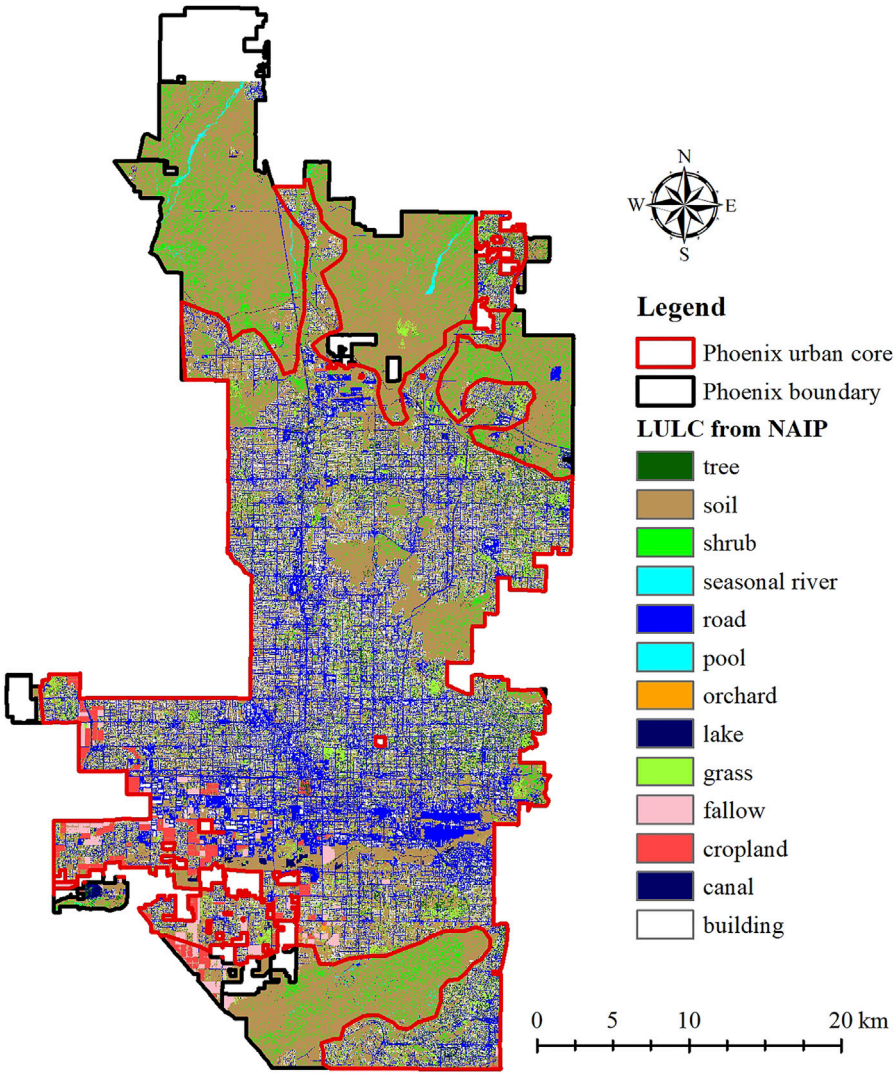

FIGURE 1 | Land use and land cover map derived from 1-m resolution data acquired by the National Agricultural Imagery Program (NAIP) within the city limits of Phoenix, Arizona.

intensity of heat reduction possible in response to the level of conversion from unmanaged soil to green vegetation biomass.

Remotely sensed data is well-suited for examining the relationships between urban LULC and LST (Voogt and Oke, 2003; Lu and Weng, 2006; Connors et al., 2013; Myint et al., 2013; Maimaitiyiming et al., 2014; Fan et al., 2015; Myint et al., 2015; Wang C. et al., 2016). To define urban heat islands, LST derived from remote sensing data is widely used as an indicator. Satellite-based LST is considered superior to other types of sensors (e.g., urban weather station, flux tower) for tracking spatial distributions of temperature (Nichol and To, 2012). Thermal remote sensing sources can retrieve LST across a wide range of the earth surface at various temporal and spatial scales (Chen et al., 2006). LST has been studied with different space-borne sensors at different spatial resolutions, including the Moderate Resolution Imaging Spectroradiometer (MODIS; 1-km) (Tran et al., 2006), Advanced Very High Resolution Radiometer (AVHRR; 1-km) (Streutker, 2003), LANDSAT (60–90-m) (Chen et al., 2006), and the Advanced Spaceborne Thermal Emission and Reflection Radiometer (ASTER; 90-m) (Stathopoulou et al., 2009). NASA's ECOsystem Spaceborne Thermal Radiometer Experiment on Space Station (ECOSTRESS), launched in June 2018, covers several key biomes of the terrestrial biosphere using surface temperature information measured from the thermal infrared (TIR) bands (Hulley et al., 2017; Hook and Hulley, 2019). It can be used to study the heat stress of urban green spaces and provide surface temperature and emissivity (Level 2 product, 70-m) with high spatiotemporal resolution.

This study aims to fill the gap in managing vegetation to reduce urban heat island impacts and examine intra-urban social inequality. We applied an evidence-based approach, a problem-solving tactic using features, objects, phenomena, and changes

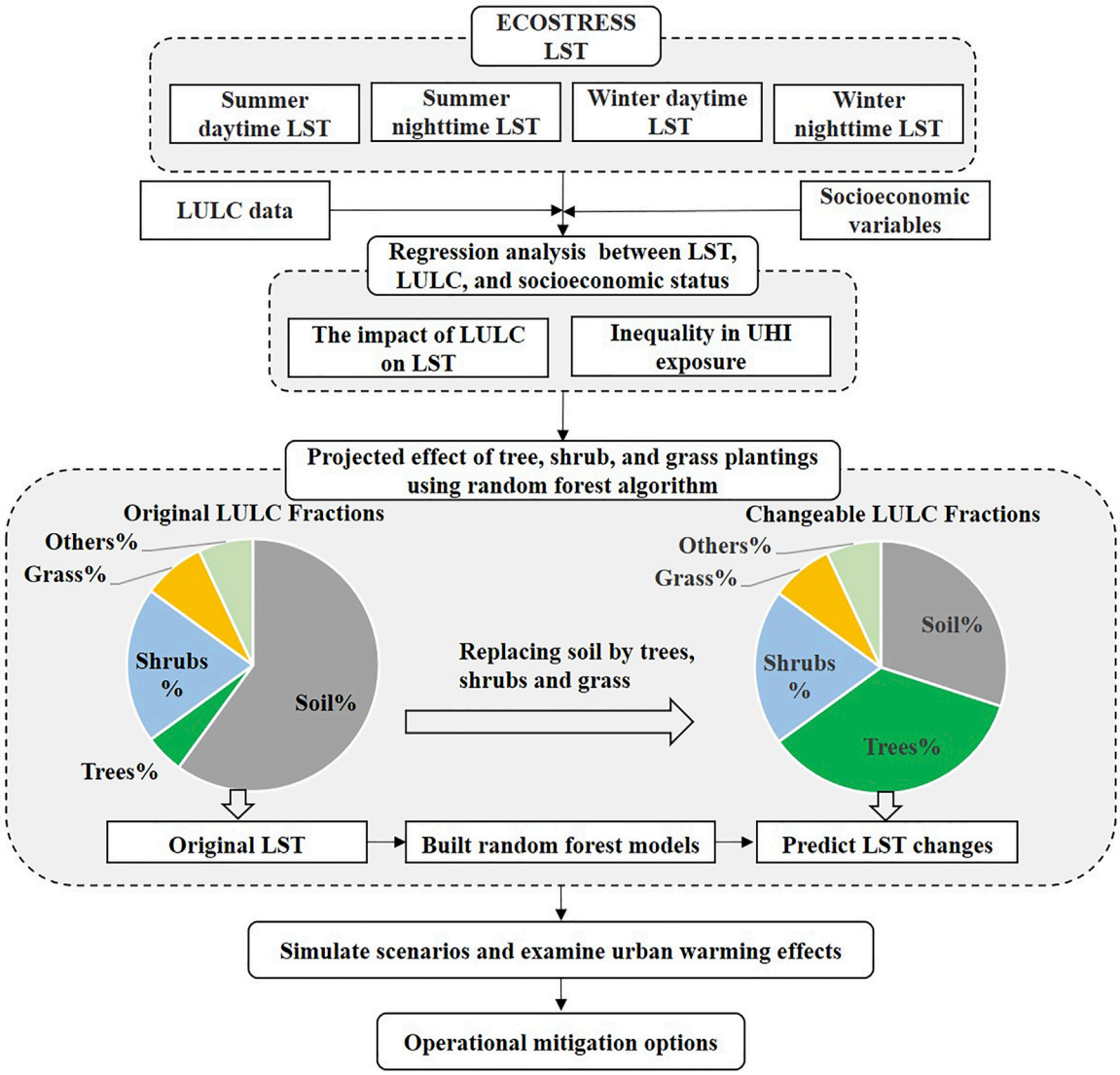

FIGURE 2 | Data processing and analytical procedure.

apparent in remotely sensed data, to mitigate urban warming effects by intervening the key contributing factors of LST. We investigate satellite-based LST across the city of Phoenix, Arizona and examine the relationship between LST measurements, detailed LULC, as well as socioeconomic factors to understand LST patterns and the distribution of heat exposure. We employ scenario analyses to predict the LST changes that could result from urban vegetation management interventions aimed at improving urban sustainability and the quality of life.

2 MATERIALS AND METHODS

2.1 Study Area

Phoenix is the sixth most populous city in the United States with an estimated population of approximately 1.68 million (2019) within a 1,941 km^2 area (United States Census Bureau, 2019; Zhang et al., 2019) (**Figure 1**). Phoenix has a subtropical desert climate with mild winters and scorching summers; daily maximum temperatures exceed 38°C throughout summer, making Phoenix the hottest city in the United States. Average annual precipitation is 195 mm (Fan et al., 2015), with most rainfall attributed to winter storms from December to March, or the monsoon season from July to September. The study area is characterized by a diversity of urban land use and land cover classes, including impervious surfaces (road and building), agriculture (active cropland, orchard, and fallow), shrub, tree, grass, unmanaged soil, and water (permanent river and canal, seasonal river, swimming pool). Phoenix is continuing to experience rapid urbanization, tracking with global trends toward development of desert environments (Wang et al., 2019), and represents a key case study for understanding urban-induced climate change.

TABLE 1 | List of the selected ECOSTRESS LST products in different periods.

Sensor	Date	Time
ECOSTRESS LST (ECO2LSTE v001)	2019-08-02, 2019-08-05, 2019-08-25	Summer daytime
	2019-06-30, 2019-07-11, 2019-08-28	Summer nighttime
	2019-02-24, 2019-02-28, 2019-12-27	Winter daytime
	2019-01-29, 2019-01-04, 2019-01-08	Winter nighttime

2.2 Data and Methods

We employed high-resolution LULC and socioeconomic variables collected at the U.S. Census block group level, and satellite-derived 70 m LST measurements. To understand the distribution of UHI across Phoenix, we explored the spatial correlation of the LST, LULC fractions, socioeconomic and demographic variables. To identify options for UHI mitigation within the city boundaries, we then developed random forest (RF) algorithms to model LST changes with LULC composition changes. We examined UHI within the entire extent of Phoenix, and also within the urban core areas of the city alone (**Figure 1**). We manually delineated regions with a high density of anthropogenic features and settlements (i.e., residential, commercial, industrial land uses) as the "urban core" and excluded open spaces in outlying areas within the city boundary. The majority of Phoenix's population resides in the urban core, which is subject to more serious water uses and heat-related health problems linked to the UHI effect (Gober et al., 2009). A flow chart that demonstrates the data processing and analytical procedure used in this study is presented in **Figure 2**.

2.2.1 ECOSTRESS Data and LST Products

To explore the UHI phenomenon in Phoenix, we used ECOSTRESS data. ECOSTRESS consists of five thermal infrared (TIR) bands (Hulley et al., 2017). ECOSTRESS data have been available since June 29, 2018 with global coverage. We used the 70 m surface temperature and emissivity (Level 2) product which is available on a 3–5 days interval. The LST product (ECO2LSTE v001) is derived from five TIR bands based on a physics-based Temperature/Emissivity Separation (TES) algorithm (Hook and Hulley, 2019). We chose three scenes per season to reflect seasonal daytime and nighttime differences (**Table 1**). A total of 622,179 observations derived from ECOSTRESS LST within Phoenix City area were obtained for each selected time period.

2.2.2 Land Use and Land Cover Data

To explore the relationship between LST and LULC, we obtained a high-resolution land cover map derived from NAIP. NAIP 1-m images have four bands, including red, green, blue, and infrared wavelengths. The images of the study area were acquired on June 10, 2010 during the growing season (Li et al., 2014). As part of the Central Arizona-Phoenix Long Term Ecological Research Program, the Aerial Photography Field Office (APFO) generated the LULC map using an object-based image analysis (OBIA) method leveraging multiple image segmentation algorithms to achieve an overall accuracy of 91.9% (Li et al., 2014). The final land cover classification included thirteen detailed LULC classes, including buildings, roads, unmanaged soil, trees, shrubs, grass, fallow, swimming pools, seasonal rivers, lakes, canals, cropland, and orchards (**Figure 1**).

2.2.3 Socioeconomic Variables

When evaluating UHI relationship with communities, social and economic factors are important considerations. The increased UHI is not caused by socioeconomic variables, rather UHI spatial disparities are related to the characteristics of these variables. To explore the relationship between the spatial distribution of LST and socioeconomic characteristics, we used data from the U.S. Census (https://www.census.gov/en.html). The most recent census (2019) provided a variety of socioeconomic variables, including household property values, median household income, per capita income, and poverty status of household at the block group level based on 5-year American Community Survey (ACS) estimates. We selected the percentage of household below poverty level reported at the block group level, which was calculated based on the number of households with the income below poverty level divided by the total number of households in each block.

2.2.4 Assessing the Relationship Between LST, LULC, and Socioeconomic Status

We obtained ECOSTRESS-based LST, high resolution LULC, and socioeconomic and demographic variables collected at the U.S. Census block group level to explore the contributing factors or effects of LST. Univariate regression models were used to quantify the relationship between LST and other variables. Some preprocessing was required to examine these datasets together, which were in different formats, derived from different sources.

To minimize errors that might occur due to misregistration of ECOSTRESS or random error, and temperature variation, we calculated the mean LST from the set of three distinct scenes representing each season and time of day combination (summer daytime, summer nighttime, winter daytime, and winter nighttime) (**Figure 3**). For each 70-m LST pixel, we computed the fraction of each LULC class and the proximity to buildings and roads within 100 m.

Anthropogenic features (buildings and roads) representing urban development intensity have been demonstrated to significantly increase LST (Pan et al., 2019). Decreasing the extent of anthropogenic features can be one of the most effective approaches to mitigate UHI. We explored the combined effects of vegetation cover and development intensity to better understand the potential for vegetation planting to lower LST. To better understand the effect of landscape factors on UHI, we considered the combined effects

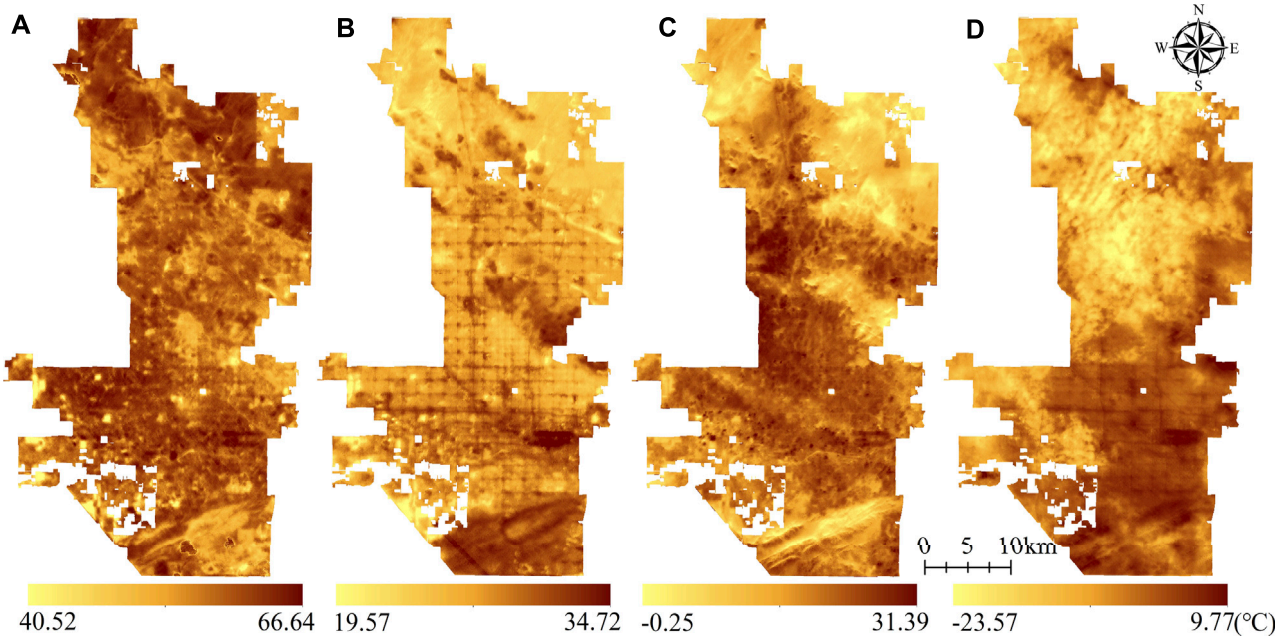

FIGURE 3 | Land surface temperature derived from ECOSTRESS data over Phoenix during **(A)** summer daytime, **(B)** summer nighttime, **(C)** winter daytime, and **(D)** winter nighttime.

of vegetation cover and development intensity by multiplying the tree cover fraction by proximity to buildings and roads for each 70-m pixel. We selected proximity to buildings and roads within 0–100 m because we assumed a negligible effect of building and roads on LST beyond 100 m.

In order to explore LST disparities in socioeconomic variables, average LST was calculated for each census block group within Phoenix's urban core areas, because most of the population resides in the urban core. Block groups (BGs) are statistical divisions of census tracts used by the United States Census Bureau which are the smallest unit for sample data published by the Bureau. They generally contain clusters of blocks within the same census tract and have between 600 and 3,000 people. Please note that our study area contained 974 block groups in 2019. Each block group included the mean LST and associated socioeconomic variables. Regression analyses were conducted to examine the relationship between household property values, median household income, per capita income, poverty status of household and LST at the block group level.

2.2.5 Simulating Scenarios of LST Changes

We expected that increasing the extent of green vegetation in areas that are currently dominated by unmanaged soil would help to mitigate the UHI effect. To explore the relative effectiveness of trees, shrubs, and grass vegetation for mitigating UHI, we developed models to simulate LST changes associated with planting each type of vegetation in unmanaged soil regions of Phoenix. LULC fractions (proportion of LULC with 1 m resolution at 70 m × 70 m grid) were used to model LST changes because spatial disparities of LST are mainly caused by landscape heterogeneity in a specific area.

We used RF approaches to model LST changes that would result from replacing 10, 20, 30, 40, and 50% of unmanaged soil with trees, shrubs, or grass, respectively. We select replacing 10–50% of unmanaged soil as simulating scenarios considering the feasibility of the options and applicability of the level of operations depending on budget constraints. We randomly selected 70% of pixels to train the RF models, and the remaining pixels to validate the accuracies of our models. To account for spatial variation in LST due to landscape heterogeneity, we incorporated observed LST for pixels with a range of landscape composition—specifically with a range of proportional cover of each type of vegetation (trees, grass, and shrubs). We incorporated additional static variables, including the fraction of river, road, pool, orchard, lake, fallow, cropland, canals, and buildings for the lands converted from unmanaged soil to vegetation. For all of Phoenix and the Phoenix urban core only (**Figure 1**), we calculated the mean LST change under each intervention scenario.

Meanwhile, we also quantified the most influential factors affecting UHI mitigation effectiveness using the RF variable importance. The RF algorithm combines bootstrap aggregating and random feature selection to build decision trees. In this process, it randomly uses 2/3 of the samples as "in-bag data" and the remaining samples as "out-of-bag data" (OOB) to measure the model's error. The importance of each input variable (LULC fractions) was quantified using the mean decrease in accuracy (MDA)—the OOB model's error

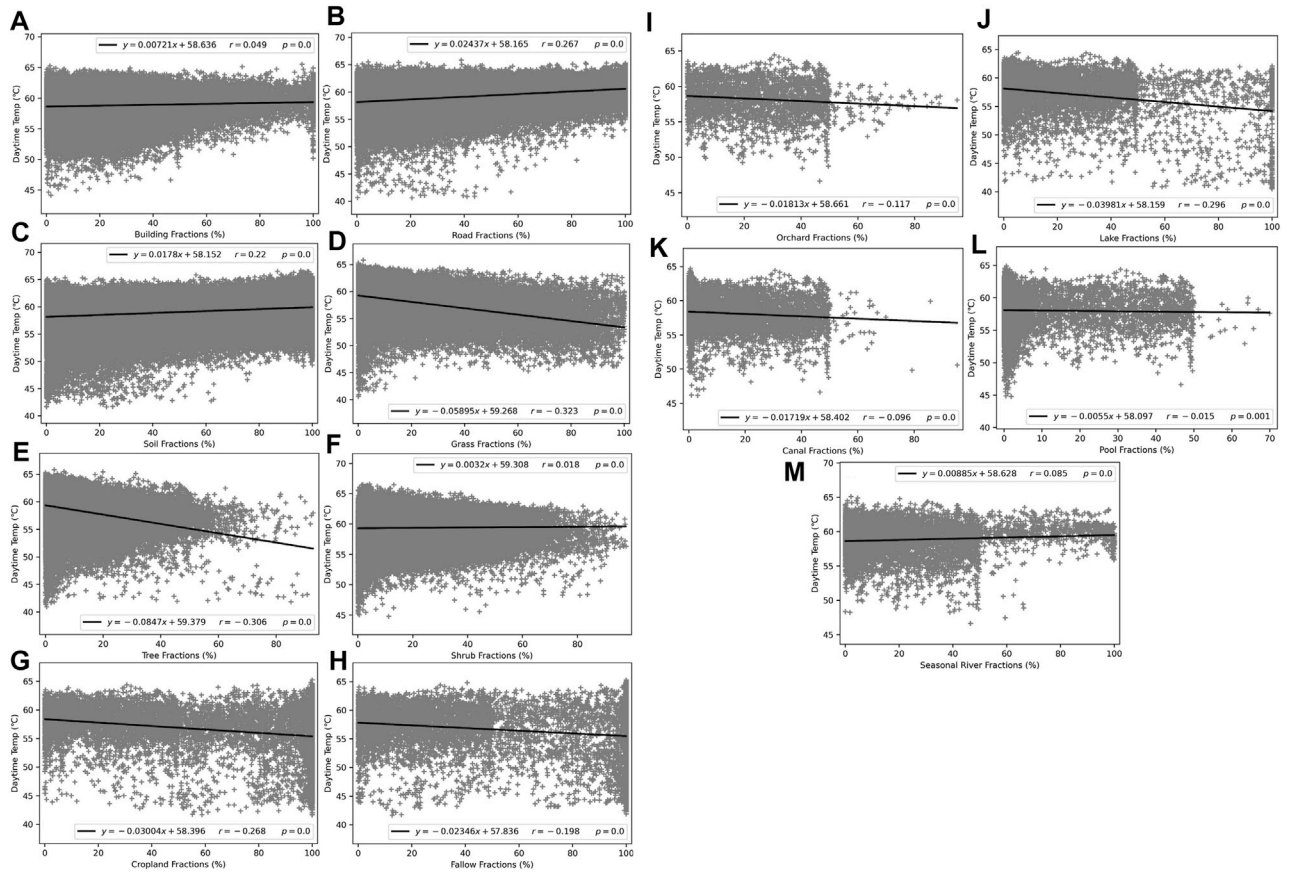

FIGURE 4 | Relationships between summer daytime LST and LULC fractions in Phoenix including the percent cover of **(A)** road, **(B)** building, **(C)** active cropland, **(D)** orchard, **(E)** fallow, **(F)** shrub, **(G)** tree, **(H)** grass, **(I)** unmanaged soil, **(J)** permanent river, **(K)** canal, **(L)** seasonal river, and **(M)** swimming pool, determined by linear regression.

difference between the original dataset and a dataset with the randomly permutated input variable.

3 RESULTS

3.1 Regression Analysis Between LULC Fractions and LST

For summer daytime, all LULC fractions had a significant correlation with surface LST (**Figure 4**). Road fraction had the most significant association (slope = 0.0244) with daytime summer surface temperature, followed by unmanaged soil fraction (slope = 0.0178). Building and seasonal river fractions had comparatively smaller effects on LST. Shrub fractions had a weak positive association (slope = 0.0032) with LST. Shrub vegetation most commonly occurs in suburban areas where unmanaged soil is the dominant LULC class. Therefore, we expect that these areas' temperatures are primarily influenced by unmanaged soil and show a higher trend than the urban core. The other nine LULC classes had a consistently negative relationship with LST; tree (slope = −0.0847) and grass (slope = −0.0590) fractions showed the strongest UHI mitigating effect. Lake, cropland, fallow, orchard, canal, and pool fractions also had negative associations with summer daytime LST. These LULC classes involve either vegetation or water, thus lowering daytime surface temperatures in the summer. Pool fractions showed the weakest UHI mitigating effect (slope = −0.0055) on summer daytime temperature.

For summer nighttime, we selected key variables (building, road, tree, grass, shrub, and soils) to explore the relationship between LULC classes and LST. These classes are the most critical factors for urban surface temperatures (Myint et al., 2010; Myint et al., 2013; Li et al., 2016). We found that summer nighttime temperatures were related with a selected set of LULC classes (**Figure 5**). Anthropogenic features did not all have the same relationship with LST. Road fractions were weakly positively correlated with summer nighttime temperatures (slope = 0.0185). In contrast, building fractions have a weak cooling effect (slope = −0.0013). Vegetation cover (trees, shrubs, and

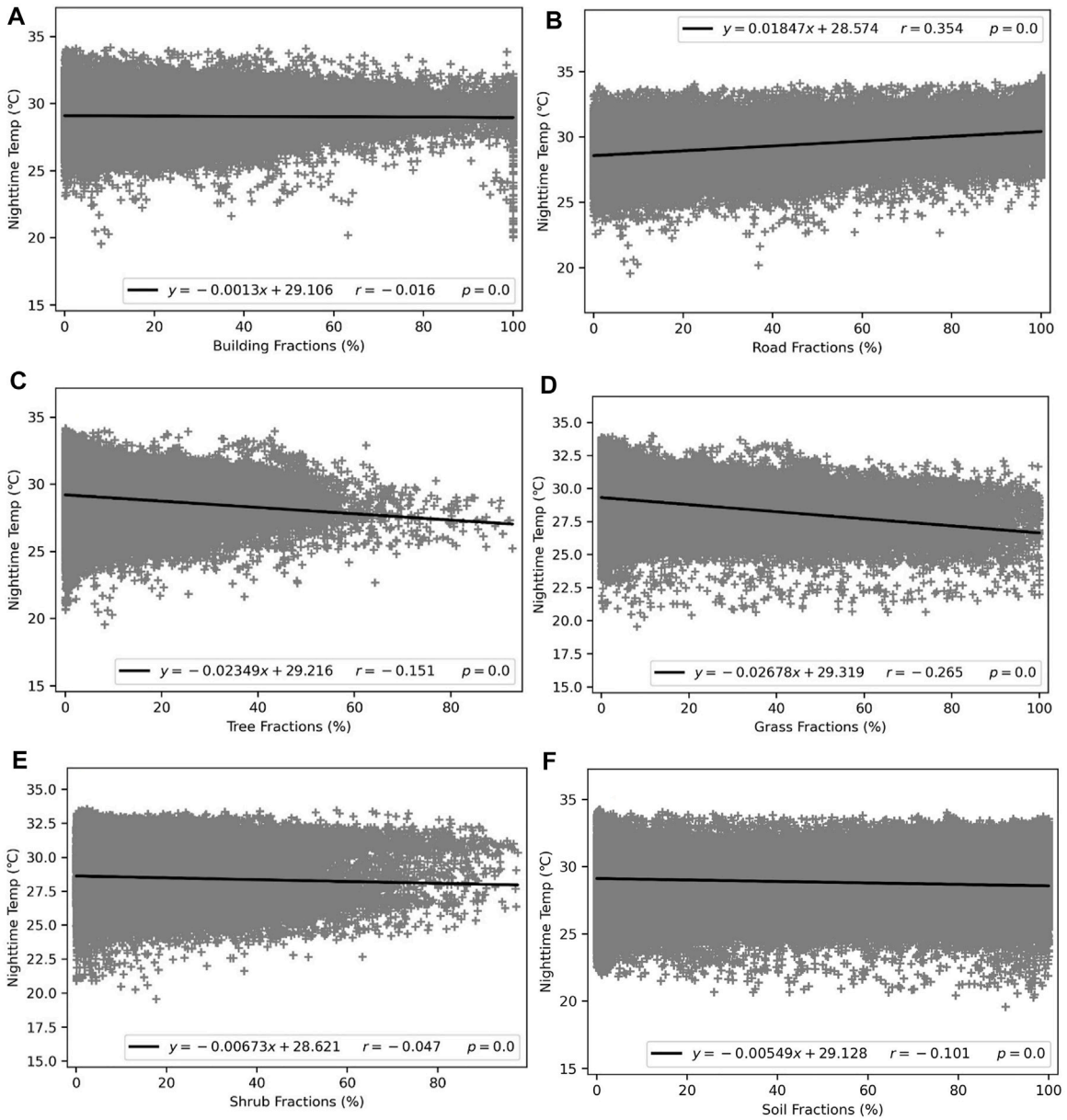

FIGURE 5 | Relationship between summer nighttime LST and selected LULC fractions in Phoenix including **(A)** building, **(B)** road, **(C)** tree, **(D)** grass, **(E)** shrub, and **(F)** soils, determined by linear regression.

grass) presents significant negative correlations with LST, with slopes of −0.02349 for trees, −0.00672 for shrubs, and −0.02678 for grass. While trees and grass seem to effectively lower summer nighttime temperature, shrub fractions have a weaker mitigating influence. We also found that soils can lower summer nighttime surface temperature slightly (slope = −0.00549). The relationship between LULC classes and LST in winter daytime and winter nighttime is detailed in the **Supplementary Material**.

Although buildings and roads have strong relationships with LST for summer days and nights, we found that vegetation cover and distance moderated these effects (**Figure 6**). For summer daytime LST, the impacts of elevated LST were strongly close to these figures, dissipating with distance up to 100-m away (**Figures 6A,B**). The effect of roads was persistent at greater distances (slope = −0.0185) compared to buildings (slope = −0.00185). Additional linear regressions revealed significant negative relationships between LST and the combined effects of tree fractions and distances from 0 to 100 m to anthropogenic features (**Figures 6C,D**). Their regression slopes were steeper than any other variables (LULC types). For summer daytime, the combined effects were stronger predictors of LST than any LULC fractions alone. The combined effects between tree fraction and distance to road

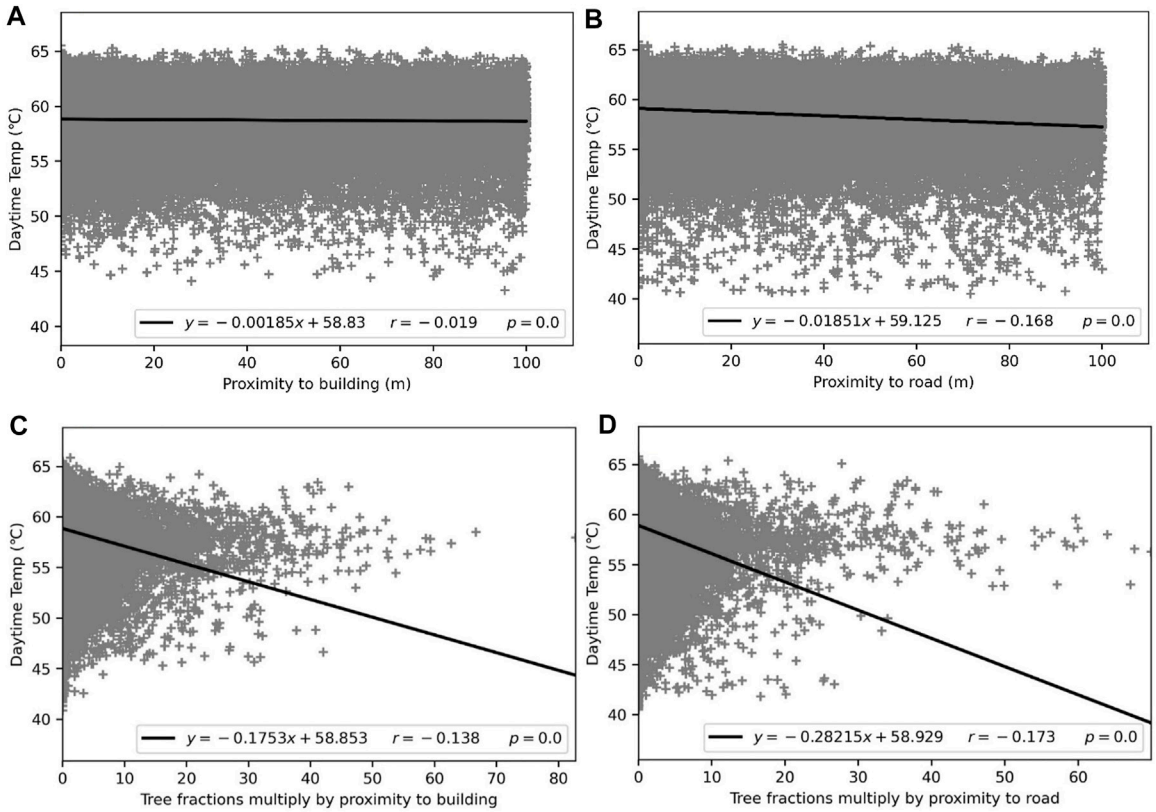

FIGURE 6 | Relationship between summer daytime LST and **(A)** proximity to building, **(B)** proximity to road, **(C)** interaction of tree fraction and proximity to building, and **(D)** interaction of tree fraction and proximity to road, determined by linear regression.

TABLE 2 | Statistics of the percentage of unmanaged soil according to their slope categories across the City of Phoenix.

Slope (°)	0–1.14	1.15–5.73	5.74–10.32	10.33–14.92	>14.92
Unmanaged soil (%)	19.74	61.70	7.18	4.33	7.05

(slope = −0.282) was more strongly related to summer daytime surface temperature than the interaction between tree fraction and distance from buildings.

In addition, the percentages of unmanaged soil according to the terrain conditions were explored because the terrain slope can be a useful parameter for the selection of suitable vegetation species. That would be further helpful for implementing urban forestry programs. Hence, we downloaded the terrain dataset derived from NASA's Shuttle Radar Topography Mission (SRTM) from the USGS website (https://earthexplorer.usgs.gov/). Then the slope layer was generated using the SRTM data. Slope intensity values were later split into five categories with regard to their standard deviation. For each slope category area, we calculated the percentage of unmanaged soil (**Table 2**). The results showed that the slope lower than 5.73° occupied more than 80% of the unmanaged soil category, whereas the areas of unmanaged soil with slope greater than 14.92° have 7.05%. This demonstrates that unmanaged soil in our study area mainly occurs on flat terrain, and hence slope does not play an important role in mitigating urban warming effect.

3.2 Distribution of UHI Impacts by Socioeconomic Status

We identified strong correlations between the spatial distribution of summer daytime and nighttime LST and the spatial distribution of socioeconomic disparities (**Figure 7**). The relationship between the socio-economic indicators including house property values, median household income, per capita income and percentage of household below poverty level, and surface temperatures were explored in summer days and nights in the urban core. We found that household property values were significantly negatively correlated with summer day and night temperatures. The regression slopes for summer daytime were steeper, implying that communities with lower property values tend to have disproportionate exposure to UHI, while

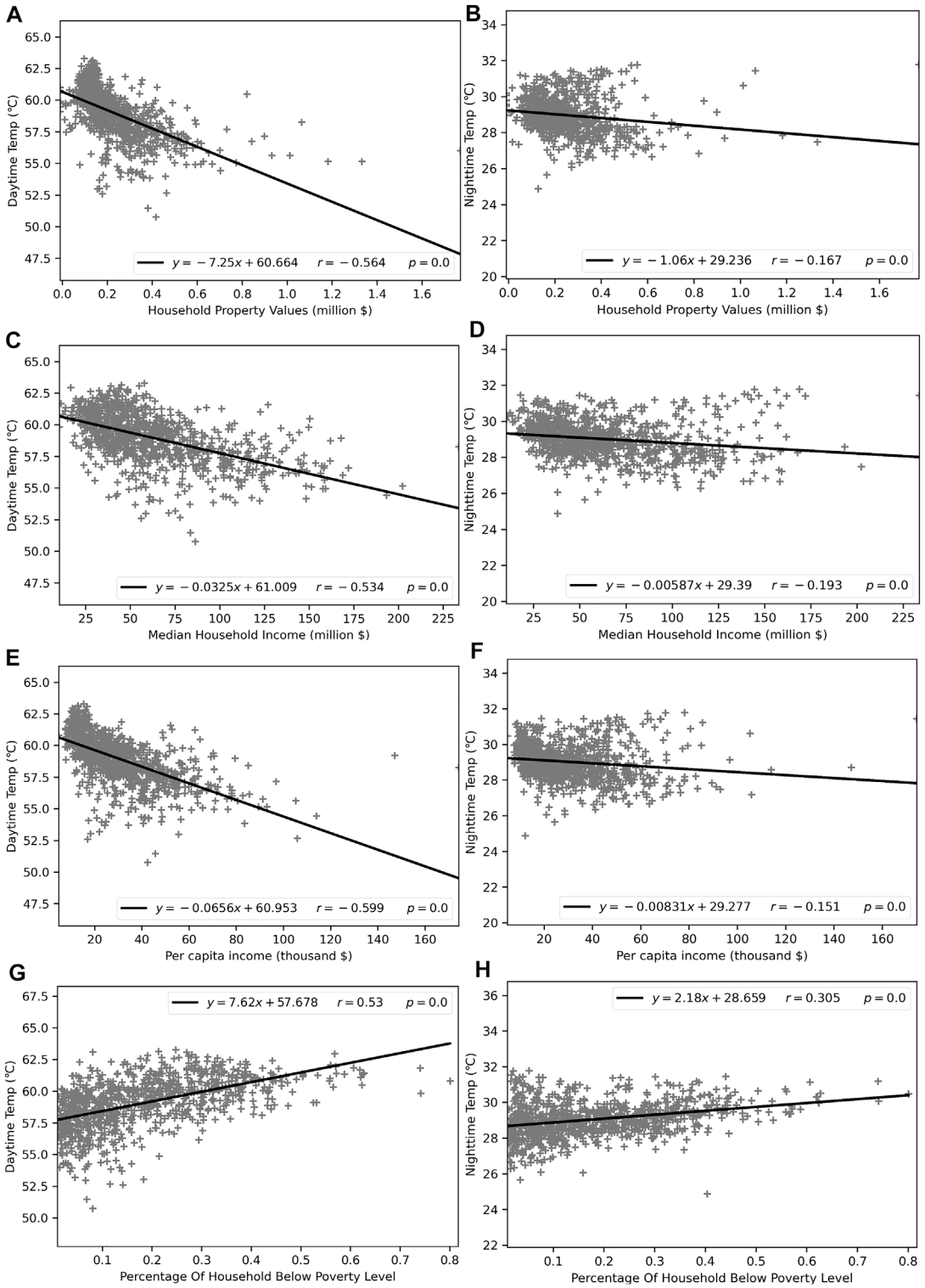

FIGURE 7 | Disproportionate impacts of UHI on socioeconomically disadvantaged communities in Phoenix's urban core were identified by linear regression between **(A)** summer daytime LST and house property values, **(B)** summer nighttime LST and house property values, **(C)** summer daytime LST and median household income, **(D)** summer nighttime LST and median household income, **(E)** summer daytime LST and per capita income, **(F)** summer nighttime LST and per capita income, **(G)** summer daytime LST and percentage of households below the poverty line, and **(H)** summer nighttime LST and percentage of household below the poverty line.

TABLE 3 | Importance of LULC composition for explaining LST patterns across Phoenix according to RF models for Phoenix total extent and the urban core only.

Variable importance ranking (Phoenix total extent)				Variable importance ranking (Phoenix urban core)			
LULC	**SD**	**SN**	**Total**	**Rank**	**SD**	**SN**	**Total**
Soil	0.22	0.3	0.52	Soil	0.21	0.24	0.45
Shrub	0.15	0.25	0.4	Road	0.15	0.23	0.38
Tree	0.17	0.08	0.25	Tree	0.21	0.13	0.34
Grass	0.14	0.1	0.24	Grass	0.16	0.15	0.31
Road	0.08	0.14	0.22	Building	0.09	0.09	0.18
Pool	0.03	0.02	0.05	Shrub	0.07	0.1	0.17
Cropland	0.05	0.02	0.07	Pool	0.04	0.03	0.07
Building	0.06	0.05	0.11	Cropland	0.03	0.01	0.04
Fallow	0.04	0.02	0.06	Fallow	0.02	0.01	0.03
Lake	0.03	0	0.03	Lake	0.01	0.01	0.02
Seasonal river	0.01	0.01	0.02	Canal	0.01	0.01	0.02
Canal	0.01	0	0.01	Seasonal river	0	0	0
Orchard	0	0	0	Orchard	0	0	0

Note: LULC, LST, and RF, represent land use and land cover, land surface temperature and random forest, respectively. SD, and SN, represent summer daytime and summer nighttime. Total represents the sum of SD, and SN.

TABLE 4 | Projected mean summer daytime temperatures across Phoenix total extent and the urban core alone that would result from replacement of 10, 20, 30, 40, or 50% of unmanaged soil by trees, shrubs, or grass, based on random forest (RF) scenario models.

Study area	UHI mitigation	Soil % replacement scenario				
		10%	**20%**	**30%**	**40%**	**50%**
Phoenix total extent (Mean LST = 59.04°C)	Replaced by tree	58.63	58.13	57.89	57.41	57.07 (–1.97)
	Replaced by grass	58.41	58.02	58.10	57.59	57.12 (–1.92)
	Replaced by shrub	58.18	58.05	57.95	57.84	57.71 (–1.33)
Phoenix urban core (Mean LST = 58.75°C)	Replaced by tree	58.37	57.98	57.70	57.44	57.32 (–1.43)
	Replaced by grass	58.56	58.31	58.07	57.81	57.63 (–1.11)
	Replaced by shrub	57.55	57.48	57.42	57.39	57.32 (–1.42)

communities with higher property values have lower exposure. We found similar patterns for median household income and per capita income. We observed a positive correlation between the percentage of households below the poverty level in a census block group and LST in both summer day and night, with a stronger relationship. For further details about the correlations between the LST and socioeconomic variables for winter day and night please see the **Supplementary Material**.

3.3 Projected Effect of Tree, Shrub, and Grass Plantings for UHI Mitigation

To understand how LULC contributes to LST distributions across Phoenix total extent and within the urban core only for different times of day in summer, we evaluated the relative importance of LULC fractions using the RF variable importance (**Table 3**). We observed that the fraction of unmanaged soil was the most important LULC composition explaining LST patterns across the whole city and the urban core roads, grass, and trees were among the top five variables in both regions. However, the fractional cover of shrubs was the second most important LULC for the whole city, different from urban core. Shrubs mainly grow in suburban areas and present a more significant effect on LST than in Urban Core. Other than the whole city, buildings have a more significant impact on urban core. Other factors, such as orchard, canal, seasonal river, lake, and fallow, present a consistently ineffective influence on LST in both areas.

Our scenario-based analysis based on RF demonstrated that LST could be effectively reduced by converting currently unmanaged soil to trees, shrubs, and grass (**Table 4**). We found that the mean summer daytime LST across Phoenix total extent (59.04°C) was higher than mean LST within the urban core (58.75°C). Phoenix total area extent and urban core cover unmanaged soil areas of 656 km^2 (occupying the total area of 33.80%) and 361 km^2 (occupying the total area of 26.78%), respectively. When trees, shrubs, or grass replace 10, 20, 30, 40, and 50% of unmanaged soil, the mean LST decreased accordingly.

For Phoenix total extent, replacing unmanaged soil with trees produced the greatest cooling effect, followed by grass and shrubs in summer daytime. The RF scenario replacing 50% of unmanaged soil with trees and grass across Phoenix total extent reduced LST by 1.97°C and 1.92°C, respectively. The effect of trees and grass planting on LST were similar. For Phoenix urban core, the results of the RF scenario showed replacing unmanaged soil with trees produced the greatest cooling effect, followed by shrubs and grass with lowering

TABLE 5 | Changes in mean temperatures in Phoenix total extent and urban core when replacing 10, 20, 30, 40, and 50% of unmanaged soil by trees, shrubs, or grass based on RF during summer nighttime.

Study area	UHI mitigation	Soil % replacement scenario				
		10%	20%	30%	40%	50%
Phoenix total extent (Mean LST = 28.85°C)	Replaced by tree	28.61	28.49	28.53	28.41	28.40 (–0.46)
	Replaced by grass	28.71	28.54	28.62	28.49	28.29 (–0.57)
	Replaced by shrub	28.64	28.60	28.59	28.59	28.65 (–0.21)
Phoenix urban core (Mean LST = 29.14°C)	Replaced by tree	29.04	28.96	28.93	28.90	28.87 (–0.27)
	Replaced by grass	28.96	28.87	28.80	28.72	28.64 (–0.50)
	Replaced by shrub	28.92	28.88	28.82	28.77	28.74 (–0.41)

1.43°C, 1.42°C, and 1.11°C, respectively. Planting these three types of vegetation achieve the similar effects for cooling in the urban core alone. We found that tree plantings had the greatest effect on lowering LST across vegetation intervention scenarios for Phoenix total extent and for the urban core alone.

We found that the mean summer nighttime LST across Phoenix (28.86°C) was lower than the urban core (29.14°C). Through scenario analysis with RF models, we found that mean summer nighttime LST dropped gradually across Phoenix total extent and within the urban core when progressively more unmanaged soil was replaced by trees, shrubs, or grass (**Table 5**). Replacing unmanaged soil across Phoenix total extent with grass delivered the best cooling effect, followed by trees and shrubs from the RF approach. The RF scenario replacing 50% of unmanaged soil with grass, trees and shrubs across Phoenix total extent reduced LST by 0.57°C and 0.46°C, and 0.21°C, respectively. For Phoenix urban core, the models indicated that grass had the best cooling effect, followed by shrubs and trees with the LST reduction of 0.50°C, 0.41°C, and 0.27°C, respectively. We found that grass plantings were the greatest effective than other two vegetation types for cooling across vegetation intervention scenarios neither in Phoenix total extent nor the urban core alone. Changes in mean temperatures in Phoenix total extent and urban core detailed in **Supplementary Material** during winter daytime.

4 DISCUSSION

4.1 The Impact of LULC on LST

Urbanization creates a concentration of anthropogenic features (e.g., impervious surfaces) leading to the UHI with implications for water and energy consumption, ecosystem services and human health in Phoenix and other cities. We discovered significant positive relationships between road fractions and surface temperatures in all time periods considered in this study. Consistent with previous studies (Myint et al., 2013; Wang C. et al., 2016; Mohajerani et al., 2017), we found that the extent of roads impacts surface temperatures more than other factor during summer days and nights. Contrary to previous studies which identify buildings as a driver of increasing surface temperatures in summer (Zhou et al., 2011; Bokaie et al., 2016), we found that buildings are not associated with high daytime surface temperatures, yet are associated with lower nighttime temperatures in our study area.

The distinct impacts of buildings and roads are likely caused by differences in their composition materials. Roads, parking lots, driveways, and sidewalks are primarily made of asphalt—a dark surface—while buildings are composed of bright materials. Darker surfaces usually absorb and retain heat longer than white or bright-colored surfaces (Mohajerani et al., 2017). Conversely, most rooftops and walls of buildings in Phoenix are composed of bright materials resulting in lower heat retention and high surface reflectance (Myint et al., 2013). Furthermore, the perimeters of buildings are usually associated with vegetation covers, such as grass or trees providing a cooling effect. Some building rooftops in Phoenix are "cool roofs" with solar panels that produce emissions-free electricity to cool the buildings. Finally, buildings can provide shade during the day, thereby acting somewhat similar to the effect of vegetation and reinforcing a cooling effect. These features can explain why roads cause more significant temperature increases than buildings in Phoenix.

It is not surprising that the urban core areas had higher summer nighttime LST compared to Phoenix total extent; anthropogenic features (buildings and roads) in the urban core absorbed and retained more heat than unmanaged soil in suburban areas. Surprisingly, we found that unmanaged soil was associated with higher summer daytime LST than buildings in Phoenix. Unmanaged soil mainly exists outside the urban core, while buildings, trees, and grass are concentrated within the urban core—this may explain why summer daytime temperatures in suburban areas are generally hotter than in the urban core. Unmanaged soil is the primary reflecting surface in Phoenix; which is also true of other desert cities and is an important consideration for managers interested in mitigating UHI.

In addition, the relationship between swimming pool fractions and summer daytime temperature was the lowest (**Figure 4L**) since swimming pool fraction values could be very low at 70 × 70 spatial resolution in some cases. Therefore, we conclude that swimming pools do not significantly impact daytime surface temperature, nor do they effectively lower the

thermal energy in a desert area. This finding is the same as what was reported in Myint et al. (2013).

Our study gives particular attention to trees, grass, and shrubs because these vegetation features generally have cooler surface temperatures than other LULC (Zhang et al., 1998; Tran et al., 2006), and they also provide important ecosystem services within the urban landscape. We found that vegetation features have a cooling effect on summer day and summer night surface temperatures. Trees are the most effective for cooling summer daytime temperature, while grass is more effective for cooling summer nighttime temperatures. Shrubs were generally less effective for cooling UHI, likely because shrubs mainly grow in suburban areas where unmanaged soil dominates.

4.2 Inequality in UHI Exposure

We documented disparities in the distribution of UHI within Phoenix's urban core, based on property values, median household income, and the percentage of household below poverty level. Lower socioeconomic status census block groups are more likely to be exposed to high temperatures in the summer, while affluent neighborhoods may experience relatively cooler temperatures. Land cover features may contribute to these disparities (Uejio et al., 2011). Political and socioeconomic factors may cause LULC and management (e.g., xeric residential versus mesic residential) differences among communities, thus leading to LST spatial disparities (Harlan et al., 2006; Chow et al., 2012). These findings are consistent with the luxury effect, which suggests that ecosystem variation conforms to socioeconomic status (Hope et al., 2003). Residential landscape composition is typically associated with the period of development and income levels. In Phoenix, affluent neighborhoods have more vegetation (trees and grass lawns), and their cooling influence is more accessible for these residents, whereas low income neighborhoods tend to have little vegetation or access to greenspace (Harlan et al., 2006; Jenerette et al., 2007; Jenerette et al., 2011; Li et al., 2016). Mean temperatures higher than 100°F (37.78°C) can persist for at least 3 months in our study area, imposing an extended burden on vulnerable residents in Phoenix, which could be alleviated with strategic vegetation-based UHI mitigation. Such analyses provide the implications that future urban heat mitigation options should focus on communities with lower socioeconomic status to achieve environmental justice instead of simply concentrating on cooling effect.

4.3 Operational Urban Warming Mitigation Through Sustainable Planning

One strategy to mitigate the UHI effects, which are more intense for desert cities than other urban centers, is to increase green vegetation landscapes. Previous studies have suggested that increasing green space can achieve significant cooling potentials (Zhang et al., 2017). The city of Phoenix has launched an urban planning effort to mitigate UHI by increasing the amount of green space (Phoenix, C.O., 2010), however, the potential cooling effect across the region has not been quantitatively assessed. In Phoenix, there exists a large extent of unmanaged soil which is unconsolidated material that supports plant growth. From our analysis, unmanaged soil caused higher summer daytime LST than buildings. It was the most important composition explaining LST patterns as well. Vegetation (trees, grass, and shrubs) are the top five variables explaining LST patterns and has been well-documented to alleviate UHI (Bowler et al., 2010; Myint et al., 2010; Huang and Cadenasso, 2016). Therefore, we determined that replacing unmanaged soil—a primary contributor to UHI—with vegetation is an operational option to mitigate UHI.

We have two study areas—the total extent of Phoenix and the city's urban core—to explore LST changes based on scenario models. Phoenix urban core is necessary to be explored due to owning the majority of Phoenix's population and facing more severe heat-related issues. Scenario models demonstrate that these two areas have the similar ranking in the importance of LULC composition for explaining LST patterns. We observed that unmanaged soil was the most important variable across these two areas because open land areas are the primary reflecting surface in desert cities. Vegetation features (trees, grass, and shrubs) were also one of the most important variables. Other than the whole city, buildings and roads have more significant impacts on urban core. This is because building and road categories are one of the main land cover types and has more impact on UHI than the whole city. The results of UHI mitigation derived from scenario-based models present the analogous change trends in Phoenix total extent and urban core when replacing 10, 20, 30, 40, and 50% of unmanaged soil by trees, shrubs, or grass.

Our scenario models demonstrate that tree plantings represent the best strategy to lower summer daytime LST, while grass is more effective summer nighttime in Phoenix total extent and urban core. The results are consistent with our regression analysis between LULC fractions and LST where the strongest UHI mitigating effect was shown by trees in summer daytime and by grass in summer nighttime, respectively. Scenario-based models present that the benefit of increased vegetation cover on heat mitigation was more pronounced on summer daytime than on summer nighttime. Previous studies demonstrated that interactions between vegetation cover and land surface on higher LST are stronger, thus producing higher cooling effect by planting vegetation in the areas with higher LST (Ziter et al., 2019). The benefit of planting vegetation in an urban area may be amplified on days with extreme heat. In our study, most unmanaged soil occurs mainly outside the urban core where the minority of the population resides. We explored the LST changes based on scenario models in Phoenix total extent and urban core. The latter has the majority of population and faces more severe heat exposure. Hence, planting vegetation in unmanaged soil needs to focus on urban core area to achieve the optimal intervention to mitigate UHI.

We assume that landscape compositions will determine spatial disparities of surface temperatures under the same solar radiation in a specific area. Therefore, LULC fractions can be used as explanatory variables to model LST. In this study, we demonstrated that tree or grass plantings provide the best strategy to cool the environment. We focused solely on

vegetation interventions for urban UHI mitigation without considering the tradeoffs of the cost and other environmental factors, such as outdoor water use, energy consumption, biodiversity, air pollution, and landscape configuration. It is reported that shade trees in xeric landscapes requires less irrigation than grass because of different cooling mechanisms of grass and trees—grass primarily lowers LST by latent heat of vaporization through ET, while trees are mainly induced by radiative shading (Wang Z.-H. et al., 2016). Different irrigation requirement imposes the constraints on water resource management and planning especially for cities in arid areas. Therefore, shade provided by trees should be taken into account more seriously than grass in addition to the point of saving of irrigation water use by trees. Since water conservation is crucial in a desert city, we suggest native tree species (e.g., Palo Verde, Desert Ironwood, Mesquite, Acacia, Desert Willow) requiring little to no irrigated water other than rainfall would be the best option to minimize urban heat island effect in the city of Phoenix. Drought tolerant species and less water use species are also an option for mitigating surface temperatures. We believe that the actionable options provided above are manageable and can be implemented immediately to mitigate urban warming effect in arid, semi-arid, and dry climate regions.

5 CONCLUSION AND PERSPECTIVES

We explored the relationship between urban LULC fractions, socioeconomic factors, and LST measured from ECOSTRESS satellite images in Phoenix. Socioeconomically vulnerable communities are disproportionately exposed to UHI, particularly high summer daytime temperatures; disparities in exposure to UHI may cause a higher incidence of heat-related health problems (e.g., asthma, bronchitis, lung diseases, heart diseases, heat stroke) in underprivileged communities. UHI disparities are linked to LULC composition differences, which also vary with socioeconomic factors across the city. We found that unmanaged soil significantly increases temperatures in the city, followed by roads and buildings. Vegetation features help to moderate high daytime temperatures. Trees lower daytime surface temperature more effectively than grass and shrub cover, making them the optimal intervention to mitigate UHI and potentially reduce energy demand in desert cities. Through scenario analysis, we found that replacing 50% of unmanaged soil with trees could reduce average summer daytime temperatures by as much as 1.97°C if the intervention was implemented across all of Phoenix and by 1.43°C if implemented within the urban core only. Since Phoenix city is located in a desert environment, native trees requiring little to no additional water other than rainfall would be ideal to mitigate urban warming effects. It is recommended that policymakers and planners incorporate and optimize the spatial configuration of urban landscapes by increasing green infrastructure in unmanaged soil and pay more attention to environmental social justice or equity in urban planning and urban forestry programs.

DATA AVAILABILITY STATEMENT

The original contributions presented in the study are included in the article/**Supplementary Material**, further inquiries can be directed to the corresponding author.

AUTHOR CONTRIBUTIONS

SM and YZ conceived the study and developed the methodology, carried out the data analysis. YZ, SM, and DS-S interpreted results and co-wrote the manuscript. RM, DT, and YL provided critical feedback and helped shape the analysis and manuscript.

FUNDING

This work is funded by NASA (NASA grant number: 80NSSC20K0168).

SUPPLEMENTARY MATERIAL

The Supplementary Material for this article can be found online at: https://www.frontiersin.org/articles/10.3389/fenvs.2021.795474/full#supplementary-material

REFERENCES

Barnett, T. P., and Pierce, D. W. (2008). When Will Lake Mead Go Dry? *Water Resour. Res.* 44, W03201. doi:10.1029/2007wr006704

Bettencourt, L. M. A., Lobo, J., Helbing, D., Kuhnert, C., and West, G. B. (2007). Growth, Innovation, Scaling, and the Pace of Life in Cities. *Proc. Natl. Acad. Sci.* 104, 7301–7306. doi:10.1073/pnas.0610172104

Bokaie, M., Zarkesh, M. K., Arasteh, P. D., and Hosseini, A. (2016). Assessment of Urban Heat Island Based on the Relationship between Land Surface Temperature and Land Use/Land Cover in Tehran. *Sustainable Cities Soc.* 23, 94–104. doi:10.1016/j.scs.2016.03.009

Bowler, D., Buyung-Ali, L., Knight, T., and Pullin, A. (2010). How Effective Is 'greening'of Urban Areas in Reducing Human Exposure to Ground Level Ozone Concentrations, UV Exposure and the 'urban Heat Island Effect'? CEE Review 08-004 (SR41). *Environ. Evid.* 5, 1–6. doi:10.1186/s13750-016-0054-y

Brazel, A., Selover, N., Vose, R., and Heisler, G. (2000). The Tale of Two Climates-Baltimore and Phoenix Urban LTER Sites. *Clim. Res.* 15, 123–135. doi:10.3354/cr015123

Buyantuyev, A., and Wu, J. (2010). Urban Heat Islands and Landscape Heterogeneity: Linking Spatiotemporal Variations in Surface Temperatures to Land-Cover and Socioeconomic Patterns. *Landscape Ecol.* 25, 17–33. doi:10.1007/s10980-009-9402-4

Chen, X.-L., Zhao, H.-M., Li, P.-X., and Yin, Z.-Y. (2006). Remote Sensing Image-Based Analysis of the Relationship between Urban Heat Island and Land Use/cover Changes. *Remote Sensing Environ.* 104, 133–146. doi:10.1016/j.rse.2005.11.016

Chow, W. T. L., Chuang, W.-C., and Gober, P. (2012). Vulnerability to Extreme Heat in Metropolitan Phoenix: Spatial, Temporal, and Demographic

Dimensions. *The Prof. Geographer* 64, 286–302. doi:10.1080/00330124.2011.600225

Christensen, N. S., and Lettenmaier, D. P. (2007). A Multimodel Ensemble Approach to Assessment of Climate Change Impacts on the Hydrology and Water Resources of the Colorado River Basin. *Hydrol. Earth Syst. Sci.* 11, 1417–1434. doi:10.5194/hess-11-1417-2007

Connors, J. P., Galletti, C. S., and Chow, W. T. L. (2013). Landscape Configuration and Urban Heat Island Effects: Assessing the Relationship between Landscape Characteristics and Land Surface Temperature in Phoenix, Arizona. *Landscape Ecol.* 28, 271–283. doi:10.1007/s10980-012-9833-1

Cui, Y. Y., and De Foy, B. (2012). Seasonal Variations of the Urban Heat Island at the Surface and the Near-Surface and Reductions Due to Urban Vegetation in Mexico City. *J. Appl. Meteorology Climatology* 51, 855–868. doi:10.1175/jamc-d-11-0104.1

Dousset, B., and Gourmelon, F. (2003). Satellite Multi-Sensor Data Analysis of Urban Surface Temperatures and Landcover. *ISPRS J. Photogrammetry Remote Sensing* 58, 43–54. doi:10.1016/s0924-2716(03)00016-9

Estoque, R. C., Murayama, Y., and Myint, S. W. (2017). Effects of Landscape Composition and Pattern on Land Surface Temperature: An Urban Heat Island Study in the Megacities of Southeast Asia. *Sci. Total Environ.* 577, 349–359. doi:10.1016/j.scitotenv.2016.10.195

Fan, C., Myint, S. W., and Zheng, B. (2015). Measuring the Spatial Arrangement of Urban Vegetation and its Impacts on Seasonal Surface Temperatures. *Prog. Phys. Geogr. Earth Environ.* 39, 199–219. doi:10.1177/0309133314567583

Gober, P., Brazel, A., Quay, R., Myint, S., Grossman-Clarke, S., Miller, A., et al. (2009). Using Watered Landscapes to Manipulate Urban Heat Island Effects: How Much Water Will it Take to Cool Phoenix? *J. Am. Plann. Assoc.* 76, 109–121. doi:10.1080/01944360903433113

Grimm, N. B., Faeth, S. H., Golubiewski, N. E., Redman, C. L., Wu, J., Bai, X., et al. (2008). Global Change and the Ecology of Cities. *science* 319, 756–760. doi:10.1126/science.1150195

Guhathakurta, S., and Gober, P. (2010). Residential Land Use, the Urban Heat Island, and Water Use in Phoenix: A Path Analysis. *J. Plann. Education Res.* 30, 40–51. doi:10.1177/0739456x10374187

Hamerlynck, E. P., Huxman, T. E., Loik, M. E., and Smith, S. D. (2000). Effects of Extreme High Temperature, Drought and Elevated CO2 on Photosynthesis of the Mojave Desert evergreen Shrub, Larrea Tridentata. *Plant Ecol.* 148, 183–193. doi:10.1023/a:1009896111405

Harlan, S. L., Brazel, A. J., Prashad, L., Stefanov, W. L., and Larsen, L. (2006). Neighborhood Microclimates and Vulnerability to Heat Stress. *Soc. Sci. Med.* 63, 2847–2863. doi:10.1016/j.socscimed.2006.07.030

Hartz, D. A., Prashad, L., Hedquist, B. C., Golden, J., and Brazel, A. J. (2006). Linking Satellite Images and Hand-Held Infrared Thermography to Observed Neighborhood Climate Conditions. *Remote sensing Environ.* 104, 190–200. doi:10.1016/j.rse.2005.12.019

Hook, S., and Hulley, G. (2019). Producer: NASA EOSDIS Land Processes DAAC, USGS Earth Resources Observation and Science (EROS) Center: Souix Falls, SD, USA. Available at: https://lpdaac.usgs.gov/products/eco2cldv001/. doi:10.5067/ECOSTRESS/ECO2LSTE.001

Hope, D., Gries, C., Zhu, W., Fagan, W. F., Redman, C. L., Grimm, N. B., et al. (2003). "Socioeconomics Drive Urban Plant Diversity. *Proceedings of the National Academy of Sciences* 100(15), 8788–8792.

Huang, G., and Cadenasso, M. L. (2016). People, Landscape, and Urban Heat Island: Dynamics Among Neighborhood Social Conditions, Land Cover and Surface Temperatures. *Landscape Ecol.* 31, 2507–2515. doi:10.1007/s10980-016-0437-z

Hulley, G., Hook, S., Fisher, J., and Lee, C. (2017). "ECOSTRESS, A NASA Earth-Ventures Instrument for Studying Links between the Water Cycle and Plant Health over the Diurnal Cycle," in Prceeding of the 2017 IEEE International Geoscience and Remote Sensing Symposium (IGARSS), Fort Worth, TX, USA, 23-28 July 2017 (IEEE), 5494–5496. doi:10.1109/igarss.2017.8128248

Jenerette, G. D., Harlan, S. L., Brazel, A., Jones, N., Larsen, L., and Stefanov, W. L. (2007). Regional Relationships between Surface Temperature, Vegetation, and Human Settlement in a Rapidly Urbanizing Ecosystem. *Landscape Ecol.* 22, 353–365. doi:10.1007/s10980-006-9032-z

Jenerette, G. D., Harlan, S. L., Stefanov, W. L., and Martin, C. A. (2011). Ecosystem Services and Urban Heat Riskscape Moderation: Water, green Spaces, and Social Inequality in Phoenix, USA. *Ecol. Appl.* 21, 2637–2651. doi:10.1890/10-1493.1

Jesdale, B. M., Morello-Frosch, R., and Cushing, L. (2013). The Racial/Ethnic Distribution of Heat Risk-Related Land Cover in Relation to Residential Segregation. *Environ. Health Perspect.* 121, 811–817. doi:10.1289/ehp.1205919

Lazzarini, M., Marpu, P. R., and Ghedira, H. (2013). Temperature-land Cover Interactions: The Inversion of Urban Heat Island Phenomenon in Desert City Areas. *Remote Sensing Environ.* 130, 136–152. doi:10.1016/j.rse.2012.11.007

Li, X., Li, W., Middel, A., Harlan, S. L., Brazel, A. J., and Turner, B. L. (2016). Remote Sensing of the Surface Urban Heat Island and Land Architecture in Phoenix, Arizona: Combined Effects of Land Composition and Configuration and Cadastral-Demographic-Economic Factors. *Remote Sensing Environ.* 174, 233–243. doi:10.1016/j.rse.2015.12.022

Li, X., Myint, S. W., Zhang, Y., Galletti, C., Zhang, X., and Turner, B. L. (2014). Object-based Land-Cover Classification for Metropolitan Phoenix, Arizona, Using Aerial Photography. *Int. J. Appl. Earth Observation Geoinformation* 33, 321–330. doi:10.1016/j.jag.2014.04.018

Li, X., Zhou, W., and Ouyang, Z. (2013). Relationship between Land Surface Temperature and Spatial Pattern of Greenspace: What Are the Effects of Spatial Resolution? *Landscape Urban Plann.* 114, 1–8. doi:10.1016/j.landurbplan.2013.02.005

Li, Y., Sun, Y., Li, J., and Gao, C. (2020). Socioeconomic Drivers of Urban Heat Island Effect: Empirical Evidence from Major Chinese Cities. *Sustainable Cities Soc.* 63, 102425. doi:10.1016/j.scs.2020.102425

Lu, D., and Weng, Q. (2006). Use of Impervious Surface in Urban Land-Use Classification. *Remote Sensing Environ.* 102, 146–160. doi:10.1016/j.rse.2006.02.010

Maimaitiyiming, M., Ghulam, A., Tiyip, T., Pla, F., Latorre-Carmona, P., Halik, Ü., et al. (2014). Effects of green Space Spatial Pattern on Land Surface Temperature: Implications for Sustainable Urban Planning and Climate Change Adaptation. *ISPRS J. Photogrammetry Remote Sensing* 89, 59–66. doi:10.1016/j.isprsjprs.2013.12.010

Mashhoodi, B. (2021). Environmental justice and Surface Temperature: Income, Ethnic, Gender, and Age Inequalities. *Sustainable Cities Soc.* 68, 102810. doi:10.1016/j.scs.2021.102810

Mitchell, B. C., and Chakraborty, J. (2015). Landscapes of thermal Inequity: Disproportionate Exposure to Urban Heat in the Three Largest US Cities. *Environ. Res. Lett.* 10, 115005. doi:10.1088/1748-9326/10/11/115005

Mohajerani, A., Bakaric, J., and Jeffrey-Bailey, T. (2017). The Urban Heat Island Effect, its Causes, and Mitigation, with Reference to the thermal Properties of Asphalt concrete. *J. Environ. Manage.* 197, 522–538. doi:10.1016/j.jenvman.2017.03.095

Myint, S. W., Brazel, A., Okin, G., and Buyantuyev, A. (2010). Combined Effects of Impervious Surface and Vegetation Cover on Air Temperature Variations in a Rapidly Expanding Desert City. *GIScience & Remote Sensing* 47, 301–320. doi:10.2747/1548-1603.47.3.301

Myint, S. W., Wentz, E. A., Brazel, A. J., and Quattrochi, D. A. (2013). The Impact of Distinct Anthropogenic and Vegetation Features on Urban Warming. *Landscape Ecol.* 28, 959–978. doi:10.1007/s10980-013-9868-y

Myint, S. W., Zheng, B., Talen, E., Fan, C., Kaplan, S., Middel, A., et al. (2015). Does the Spatial Arrangement of Urban Landscape Matter? Examples of Urban Warming and Cooling in Phoenix and Las Vegas. *Ecosystem Health and Sustainability* 1, 1–15. doi:10.1890/ehs14-0028.1

Nichol, J. E., and To, P. H. (2012). Temporal Characteristics of thermal Satellite Images for Urban Heat Stress and Heat Island Mapping. *ISPRS J. photogrammetry remote sensing* 74, 153–162. doi:10.1016/j.isprsjprs.2012.09.007

Oreszczyn, T., Hong, S. H., Ridley, I., Wilkinson, P., and Group, W. F. S. (2006). Determinants of winter Indoor Temperatures in Low Income Households in England. *Energy and Buildings* 38, 245–252. doi:10.1016/j.enbuild.2005.06.006

Pan, Z., Wang, G., Hu, Y., and Cao, B. (2019). Characterizing Urban Redevelopment Process by Quantifying thermal Dynamic and Landscape Analysis. *Habitat Int.* 86, 61–70. doi:10.1016/j.habitatint.2019.03.004

Peng, S., Piao, S., Ciais, P., Friedlingstein, P., Ottle, C., Bréon, F.-M., et al. (2012). Surface Urban Heat Island across 419 Global Big Cities. *Environ. Sci. Technol.* 46, 696–703. doi:10.1021/es2030438

City of Phoenix (2010). Tree and Shade Master Plan. Available at: https://www.phoenix.gov/parkssite/Documents/PKS_Forestry/PKS_Forestry_Tree_and_Shade_Master_Plan.pdf (Accessed May 05, 2022).

Seager, R., Ting, M., Held, I., Kushnir, Y., Lu, J., Vecchi, G., et al. (2007). Model Projections of an Imminent Transition to a More Arid Climate in Southwestern North America. *Science* 316, 1181–1184. doi:10.1126/science.1139601

Seto, K. C., Guneralp, B., and Hutyra, L. R. (2012). Global Forecasts of Urban Expansion to 2030 and Direct Impacts on Biodiversity and Carbon Pools. *Proc. Natl. Acad. Sci.* 109, 16083–16088. doi:10.1073/pnas.1211658109

Singh, P., Kikon, N., and Verma, P. (2017). Impact of Land Use Change and Urbanization on Urban Heat Island in Lucknow City, Central India. A Remote Sensing Based Estimate. *Sustainable Cities Soc.* 32, 100–114. doi:10.1016/j.scs.2017.02.018

Smith, W. K. (1978). Temperatures of Desert Plants: Another Perspective on the Adaptability of Leaf Size. *Science* 201, 614–616. doi:10.1126/science.201.4356.614

Stathopoulou, M., Synnefa, A., Cartalis, C., Santamouris, M., Karlessi, T., and Akbari, H. (2009). A Surface Heat Island Study of Athens Using High-Resolution Satellite Imagery and Measurements of the Optical and thermal Properties of Commonly Used Building and Paving Materials. *Int. J. Sustainable Energ.* 28, 59–76. doi:10.1080/14786450802452753

Streutker, D. (2003). Satellite-measured Growth of the Urban Heat Island of Houston, Texas. *Remote Sensing Environ.* 85, 282–289. doi:10.1016/s0034-4257(03)00007-5

Tang, J., Di, L., Xiao, J., Lu, D., and Zhou, Y. (2017). Impacts of Land Use and Socioeconomic Patterns on Urban Heat Island. *Int. J. Remote Sensing* 38, 3445–3465. doi:10.1080/01431161.2017.1295485

Tran, H., Uchihama, D., Ochi, S., and Yasuoka, Y. (2006). Assessment with Satellite Data of the Urban Heat Island Effects in Asian Mega Cities. *Int. J. Appl. Earth Observation Geoinformation* 8, 34–48. doi:10.1016/j.jag.2005.05.003

Uejio, C. K., Wilhelmi, O. V., Golden, J. S., Mills, D. M., Gulino, S. P., and Samenow, J. P. (2011). Intra-urban Societal Vulnerability to Extreme Heat: the Role of Heat Exposure and the Built Environment, Socioeconomics, and Neighborhood Stability. *Health & Place* 17, 498–507. doi:10.1016/j.healthplace.2010.12.005

United States Census Bureau (2019). QuickFacts. Phoenix City: Arizona.

Voogt, J. A., and Oke, T. R. (2003). Thermal Remote Sensing of Urban Climates. *Remote sensing Environ.* 86, 370–384. doi:10.1016/s0034-4257(03)00079-8

Wang, C., Middel, A., Myint, S. W., Kaplan, S., Brazel, A. J., and Lukasczyk, J. (2018). Assessing Local Climate Zones in Arid Cities: The Case of Phoenix, Arizona and Las Vegas, Nevada. *ISPRS J. Photogrammetry Remote Sensing* 141, 59–71. doi:10.1016/j.isprsjprs.2018.04.009

Wang, C., Myint, S., Wang, Z., and Song, J. (2016a). Spatio-temporal Modeling of the Urban Heat Island in the Phoenix Metropolitan Area: Land Use Change Implications. *Remote Sensing* 8, 185. doi:10.3390/rs8030185

Wang, C., Wang, Z.-H., Wang, C., and Myint, S. W. (2019). Environmental Cooling provided by Urban Trees under Extreme Heat and Cold Waves in U.S. Cities. *Remote Sensing Environ.* 227, 28–43. doi:10.1016/j.rse.2019.03.024

Wang, Z.-H., Zhao, X., Yang, J., and Song, J. (2016b). Cooling and Energy Saving Potentials of Shade Trees and Urban Lawns in a Desert City. *Appl. Energ.* 161, 437–444. doi:10.1016/j.apenergy.2015.10.047

Weng, Q., Lu, D., and Schubring, J. (2004). Estimation of Land Surface Temperature-Vegetation Abundance Relationship for Urban Heat Island Studies. *Remote sensing Environ.* 89, 467–483. doi:10.1016/j.rse.2003.11.005

Weng, Q. (2009). Thermal Infrared Remote Sensing for Urban Climate and Environmental Studies: Methods, Applications, and Trends. *ISPRS J. Photogrammetry Remote Sensing* 64, 335–344. doi:10.1016/j.isprsjprs.2009.03.007

Xian, G., and Crane, M. (2006). An Analysis of Urban thermal Characteristics and Associated Land Cover in Tampa Bay and Las Vegas Using Landsat Satellite Data. *Remote Sensing Environ.* 104, 147–156. doi:10.1016/j.rse.2005.09.023

Zhang, X., Aono, Y., and Monji, N. (1998). Spatial Variability of Urban Surface Heat Fluxes Estimated from Landsat TM Data under Summer and winter Conditions. *J. Agric. Meteorol.* 54, 1–11. doi:10.2480/agrmet.54.1

Zhang, Y., Middel, A., and Turner, B. L. (2019). Evaluating the Effect of 3D Urban Form on Neighborhood Land Surface Temperature Using Google Street View and Geographically Weighted Regression. *Landscape Ecol.* 34, 681–697. doi:10.1007/s10980-019-00794-y

Zhang, Y., Murray, A. T., and Turner, B. L. (2017). Optimizing green Space Locations to Reduce Daytime and Nighttime Urban Heat Island Effects in Phoenix, Arizona. *Landscape Urban Plann.* 165, 162–171. doi:10.1016/j.landurbplan.2017.04.009

Zhou, W., Huang, G., and Cadenasso, M. L. (2011). Does Spatial Configuration Matter? Understanding the Effects of Land Cover Pattern on Land Surface Temperature in Urban Landscapes. *Landscape Urban Plann.* 102, 54–63. doi:10.1016/j.landurbplan.2011.03.009

Ziter, C. D., Pedersen, E. J., Kucharik, C. J., and Turner, M. G. (2019). Scale-dependent Interactions between Tree Canopy Cover and Impervious Surfaces Reduce Daytime Urban Heat during Summer. *Proc. Natl. Acad. Sci. USA* 116, 7575–7580. doi:10.1073/pnas.1817561116

Conflict of Interest: The authors declare that the research was conducted in the absence of any commercial or financial relationships that could be construed as a potential conflict of interest.

Publisher's Note: All claims expressed in this article are solely those of the authors and do not necessarily represent those of their affiliated organizations, or those of the publisher, the editors and the reviewers. Any product that may be evaluated in this article, or claim that may be made by its manufacturer, is not guaranteed or endorsed by the publisher.

frontiers in Earth Science

ORIGINAL RESEARCH
published: 18 February 2022
doi: 10.3389/feart.2022.823286

Future Changes of Summer Heat Waves Over Urban Agglomerations in Eastern China Under 1.5°C and 2.0°C Global Warming

Hongyun Ma[1]*, *Ying Wang*[1] and *Zhaohui Lin*[2]

[1]Collaborative Innovation Center on Forecast and Evaluation of Meteorological Disasters (CIC-FEMD)/Key Laboratory of Meteorological Disaster, Ministry of Education (KLME), Nanjing University of Information Science and Technology, Nanjing, China, [2]International Center for Climate and Environment Sciences, Institute of Atmospheric Physics, Chinese Academy of Sciences, Beijing, China

OPEN ACCESS

Edited by:
Zhaowu Yu,
Fudan University, China

Reviewed by:
Huopo Chen,
Institute of Atmospheric Physics (CAS), China
Zhichao He,
Snow and Landscape Research (WSL), Switzerland

***Correspondence:**
Hongyun Ma
hyma@nuist.edu.cn

Specialty section:
This article was submitted to Interdisciplinary Climate Studies, a section of the journal Frontiers in Earth Science

Received: 27 November 2021
Accepted: 18 January 2022
Published: 18 February 2022

Citation:
Ma H, Wang Y and Lin Z (2022) Future Changes of Summer Heat Waves Over Urban Agglomerations in Eastern China Under 1.5°C and 2.0°C Global Warming. Front. Earth Sci. 10:823286. doi: 10.3389/feart.2022.823286

Extreme hot events have increased evidently under global warming, particularly in the urban areas. This study aims to explore the detailed features of future changes in summer heat waves (HWs) over three major urban agglomerations (Beijing Tianjin Hebei, BTH; Yangtze River Delta, YRD; Pearl River Delta, PRD) in eastern China under 1.5 and 2.0°C warming scenario by using the Weather Research and Forecasting model (WRF) with the updated land cover data for China (ChinaLC), which is also coupled with urban canopy model. Based on the future projection results from Community Earth System Model (CESM) under the Representative Concentration Pathway (RCP) 4.5, dynamic downscaling with high-resolution WRF has been performed to project the future changes in frequency, duration and intensity of summer HWs in urban agglomerations under 1.5 and 2.0°C warming scenarios respectively. Compared with the historical period, it is found that both the summer HWs indices and the HWs affected areas all increase significantly under 1.5 and 2.0°C warming scenarios. The increasing rates of the three HWs indices are above 50% under 1.5°C warming situation, and 70% for 2.0°C warming scenario, with the increasing rate of HWs intensity even exceeding 200%. It is noted that an additional 0.5°C warming from 1.5 to 2.0°C can produce much larger impact on the future HWs changes in YRD, with the HWs intensity increased by 75.5% from 1.5 to 2.0°C warming scenarios. It is further found that the changes of HWs indices in urban area is much higher than that of non-urban areas under 1.5 and 2.0°C warming, indicating that the urban areas will face higher risk of heat-related illness or environments than suburban or rural areas in the future. Our results can provide further scientific support for the mitigation and adaption strategy for the future HWs risk in mega-cities.

Keywords: heat waves, dynamic downscaling, urban agglomerations, 1.5°C and 2.0°C global warming, future projection

INTRODUCTION

Heat waves are extreme events associated with particularly sustained high temperatures (Frich et al., 2002; Perkins 2015; Hua et al., 2021; Yu et al., 2021; Yang et al., 2021a), which can produce adverse impacts on human mortality, regional economies, and natural ecosystems (Kovats and Hajat 2008; McMichael and Lindgren 2011; Lesk et al., 2016). For instance, the long-lasting and widespread HWs in 2013 over eastern China brought 59 billion RMB direct economic losses (Sun et al., 2014). Observational data over the past few decades indicate that the frequency of HWs has increased all over the world (Seneviratne et al., 2014; Perkins 2015; Yang et al., 2021b). Under global warming, HWs are projected to become more intense, frequent and longer lasting over most land areas in the late 21st century (Meehl and Tebaldi 2004; Coumou and Robinson 2013; Su and Dong 2019a).

In urban areas, surface air temperatures are generally higher than those in rural areas due to the urban heat island (UHI) effect (Oke 1982). This indicates that the urban areas are more exposed to the risk from HWs (Stone et al., 2010; Ren and Zhou 2014). More than 55% of the world's total population is currently living in urban areas, which is expected to increase in the future with the expansion of urbanization and the growth of population (http://world-statistics.org). These urban residents are directly affected by the combined influence of global warming caused by greenhouse gases and the UHI effect caused by urbanization, which makes them more vulnerable to the effect of heat extremes (IPCC, 2014; Sun et al., 2014; Yu et al., 2018).

Since the 1980s, urbanization has rapidly accelerated in China, especially in eastern China, where the economy develops apace with high population density (Wang et al., 2012; Gong et al., 2019). An evident increased trend in summer HWs over eastern China is found during the last decade (Chen and Li 2017; Su and Dong 2019b). Recent studies suggest that the increasing frequency of extreme summer heat wave in eastern China is attributable to the anthropogenic emission of greenhouse gases and the expansion of UHI due to rapid urbanization (e.g., Dian-Xiu et al., 2014; Sun et al., 2016). It is also found that most of the densely populated regions, such as eastern China, will expect to witness larger increases of extreme heat events than the other regions of East Asia under 1.5 and 2.0°C warming scenarios (Li et al., 2018). Yu et al. (2018) further suggested that the additional 0.5°C temperature rise from 1.5 to 2.0°C warming will lead to significantly increased extreme HWs in China's urban agglomerations.

It is noted that most of the previous studies used datasets from Coupled Model Intercomparison Project Phase 5 (CMIP5) models under different RCP scenarios to investigate the changes of weather and climate extremes in response to global warming. However, due to the coarse resolution and imperfect parameterization scheme of urban land surface physical processes, most of the existing climate system models can not reasonably depict the differences between cities and their surrounding areas, which might lead to larger uncertainties in the simulation and projection of extreme weather and climate events in urban areas (Pachauri et al., 2014). To reduce regional-scale biases, dynamical downscaling with regional model driven by global climate system models' output is widely adopted because of the higher spatial resolution and better representation of physical processes for regional climate models (Grossman-Clarke et al., 2017; Chen et al., 2018; Wu et al., 2020; Ge et al., 2021).

Therefore, this study aims to reasonably project the future changes of HWs in typical urban agglomerations in eastern China by dynamical downscaling using the high-resolution WRF model. To improve the representation of physical processes in urban areas, the WRF model coupled with urban canopy model (UCM) was employed. The global future climate projections were derived from the National Center for Atmospheric Research (NCAR) Community Earth System Model under the RCP4.5 scenario. Three major urban agglomerations in eastern China (Beijing-Tianjin-Hebei, BTH; Yangtze River Delta, YRD; Pearl River Delta, PRD) were selected as the research regions in this study. The structure of this paper is organized as follows, the details of the data and methodology are described in *Section Data and Methods*. the performance of the downscaled simulation of HWs over three urban agglomerations is systematically evaluated and the future changes in temperature and HWs are presented in *Section Results*. The discussion and conclusion are in *Section Conclusion and Discussion*.

DATA AND METHODS

Study Areas

In this study, the three urban agglomerations located in coastal Eastern China, i.e., Beijing-Tianjin-Hebei region (BTH), the Yangtze River Delta (YRD), and the Pearl River Delta (PRD), are selected as research areas. These three regions are the most mature and competitive urban agglomerations in China, with the largest population density and the highest level of national economic development, which is the inevitable outcome of China's new industrialization processes (Fang 2015). More specifically, the three urban agglomerations have an area of 370×10^3 km^2, with a population of 102.19 million and a GDP of CNY 30.82 trillion (Chou et al., 2021), and these suggest that the degree of exposure and vulnerability to climate disasters and potential economic losses in three urban agglomerations are much larger than that in other regions.

Model, Experiments Design, and Meteorological Data

The regional model used for dynamic downscaling in this study is the WRF model version 3.9.1 (Skamarock and Klemp 2008), which is coupled with the Urban Canopy Model (UCM) (WRF/UCM; Kusaka et al., 2001; Kusaka and Kimura 2004). Two one-way nesting strategy has been configured for WRF, with 15 km spatial resolution for outer domain and 5 km resolution for inner domain. As shown in **Figure 1**, three urban agglomerations are all located in the innermost domain, with 78 × 90 grid cells for BTH region, 90 × 110 for YRD and 45 × 57 grid points for PRD respectively. The Lambert conformal map projection was adopted for the model's horizontal coordinates. The vertical grid

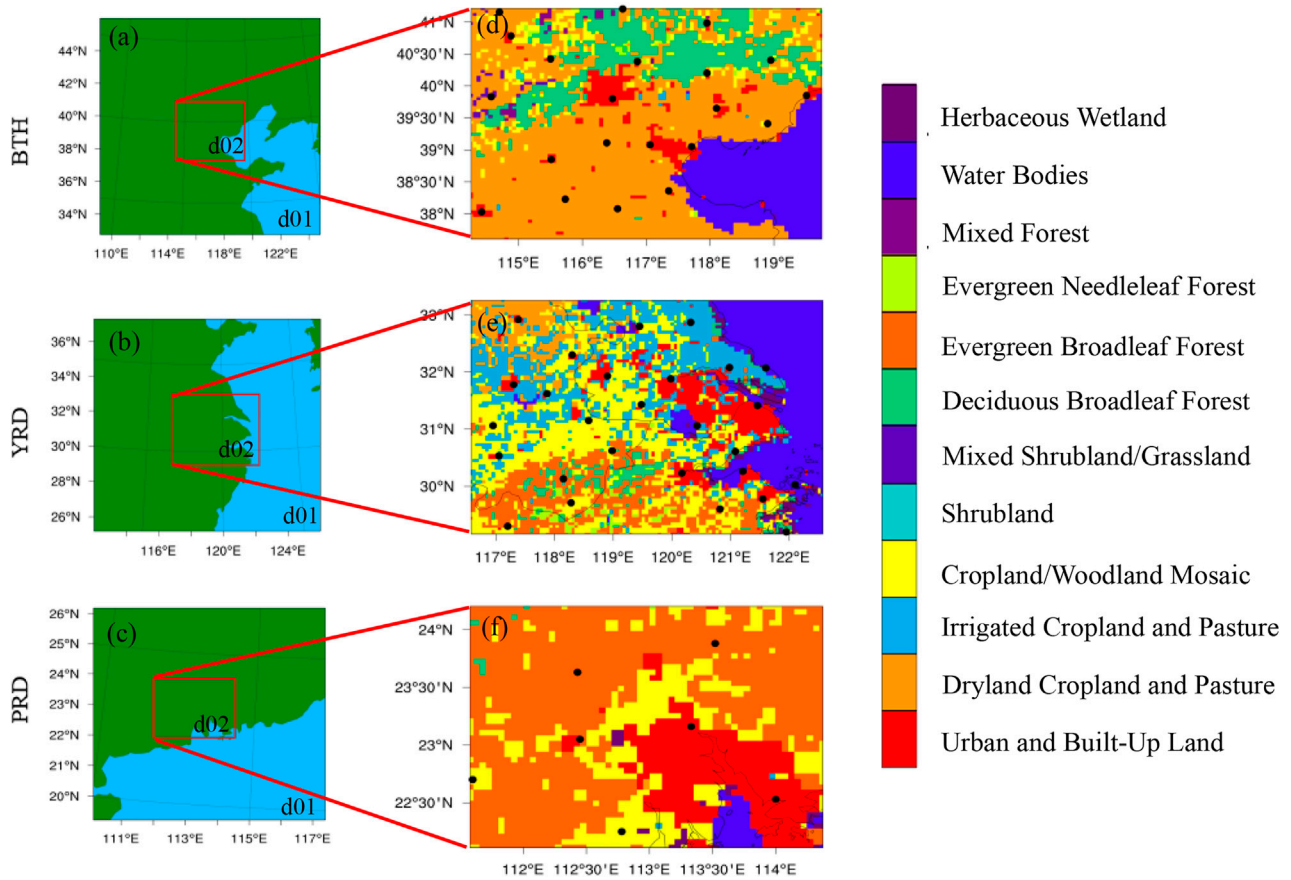

FIGURE 1 | Double-nested model domains used in the study, with D01 as the outer domain and d02 being the innermost domain for **(A)** Beijing-Tianjin-Hebei region (BTH) **(B)** Yangtze River Delta (YRD) and **(C)** Peral River Delta (PRD) respectively. Land-use and land cover categories over BTH, YRD and PRD are shown in **(D–F)**. The black spots in **(D–F)** denote the meteorological observation stations over the three urban agglomerations.

contained 37 terrain-following eta levels from the surface up to 50 hPa. The main physical schemes adopted in this study include the WRF Single-Moment 6-class microphysics scheme (Hong and Lim, 2006), the Kain-Fritsch cumulus scheme (Kain, 2004), the Rapid Radiative Transfer Model for GCM (RRTMG) longwave and shortwave radiation scheme (Iacono et al., 2008), the Yonsei University boundary layer scheme (Hong et al., 2006), and the Noah land surface model (Chen and Dudhia, 2001) which is coupled with the single-layer UCM.

Atmospheric initial and lateral boundary conditions for driving the WRF model were taken from the bias-corrected CESM CMIP5 datasets (with a horizontal resolution of 0.9° × 1.25° in latitudinal and longitudinal directions) at 6-h intervals (https://rda.ucar.edu/datasets/ds316.1/). Compared with other CMIP5 models, CESM can reasonably reproduce the global temperature and precipitation distribution (Knutti and Sedlacek 2013), especially in China (Chen and Frauenfeld, 2014). For the future projection, a low-medium scenario (i.e., RCP45) was selected, which is corresponding to moderate emissions with a range of technologies and strategies for reducing GHG emissions (Thomson et al., 2011).

Moreover, the daily mean surface air temperature (SAT) retrieved from the Earth System Grid data portal was used to estimate the timing of 1.5 and 2°C global warming in the CESM projection under RCP4.5 scenario. Relative to the preindustrial period, the timing for 1.5 and 2°C warming is expected in year 2030 and 2047 respectively, based on the CESM CMIP5 projection under RCP4.5 scenario. To investigate future changes in summer HWs over urban agglomerations of eastern China under 1.5 and 2.0°C global warming, we take 1996–2005 as reference time period, 2025–2034 as 1.5°C warming time period, and 2042–2051 as 2°C warming time period in this study. Then three sets of 10-year dynamical downscaling experiments have been conducted, with WRF driven by the CESM simulation and projection results, i.e., 1) a historical downscaling run during 1996–2005 (Hereafter "Exp HIS-run"), with WRF driven by CESM historical simulation during the same period, 2) a scenario run under 1.5°C warming (Hereafter "Exp 1.5-run"), with WRF driven by CESM future projection results during 2025–2034, and 3) a scenario run under 2°C warming (Hereafter "Exp 2.0-run"), with WRF driven by CESM future projection results during 2042–2051. For each experiment, the

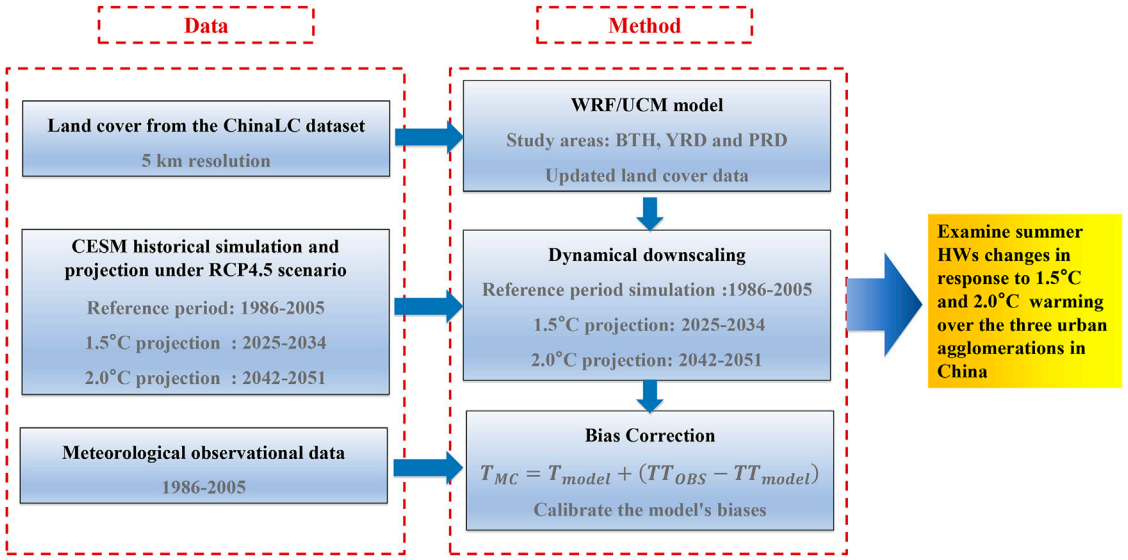

FIGURE 2 | Flow chart for the examination of future changes of summer heat waves over the three urban agglomerations.

model was initiated from 12:00 UTC 31 May and run until 00:00 UTC 1 September each year, with the first 12 h of each run being considered as the spin-up time.

The daily mean temperature (T_{mean}) and maximum temperature (T_{max}) during 1996–2005, which is from the meteorological stations of the China Meteorological Administration (https://data.cma.cn), have been adopted for the evaluation and bias correction of WRF-based dynamical downscaling results. There are 21, 27, and 7 meteorological stations selected in BTH, YRD, and PRD, respectively. These stations include both urban stations and suburban stations in model domain d02 (**Figures 1D–F**).

Land Cover Data

The default land cover data (USGS 24-category) used in the WRF model are based on 1-km Advanced Very High Resolution Radiometer data obtained from 1992 to 1993, which cannot provide up-to-date information. In the present study, a 5-km resolution ChinaLC dataset from 1981 to 2010 was used to represent land cover in the model. Detailed information regarding the data sources and the classification approach can be found in Li et al. (2017) and Yang et al. (2017). When compared with other large-scale land cover datasets, the ChinaLC dataset shows an average overall accuracy of approximately 75%, which is much higher than its counterparts (Xiao et al., 2015; Li et al., 2017). As the resolution of the inner WRF domain was set to 5 km, which is the same as the spatial resolution of ChinaLC data, the land use data in the model can be replaced by the ChinaLC data in the WRF Preprocessing System.

The classification scheme of the ChinaLC dataset is developed based on the International Geosphere-Biosphere Programme (IGBP) land cover classification scheme, which is different from that of the USGS dataset in the WRF model. Before utilizing the ChinaLC dataset, the classification transformation was carried out based on the method used by Liang et al. (2019). A land cover case of the 2010s from the ChinaLC dataset was introduced into the WRF/UCM to represent the land cover over the urban agglomerations. The land cover classifications of the 2010s for the innermost model domains are shown in **Figures 1D–F**. We can see that the main types of land cover in the urban agglomerations present wide divergence in different latitudes, especially for the urban/built-up land (shaded areas in red). However, the urban/built-up land is not the dominant land cover type in urban agglomerations. In the historical scenario, the percentages of urbanized areas in BTH, YRD, and PRD are 4.89, 8.49, and 17.86%, respectively. Despite the varying percentages caused by the different area sizes of selected research regions, the climate characteristics of urban parts are usually very different from those of the suburbs in the regions. Therefore, the response of extreme cases in urban areas to global warming may have been underestimated in previous studies by using the regional average changes.

Definition of Heat Waves

Generally, there are several HW definitions which are based on relative or absolute thresholds, but it is also noted that there is no single HW definition which could be universally accepted (You et al., 2017). Following the heatwave warning criteria used by the China Meteorological Administration (www.cma.gov.cn/en/WeatherWarnings/), we define extreme high temperature with a threshold of 35°C in this study, and the day with $T_{max} \geq 35$°C is defined as a high-temperature day. An HW event is then identified when there are three and more consecutive high-temperature days. Furthermore, three widely used HW indices are adopted for analysis in this study, i.e., the frequency index, which is the number of HWs in the study period; the duration index, which is the sum of the number of high temperature days during the HWs; the intensity index, which refers to the

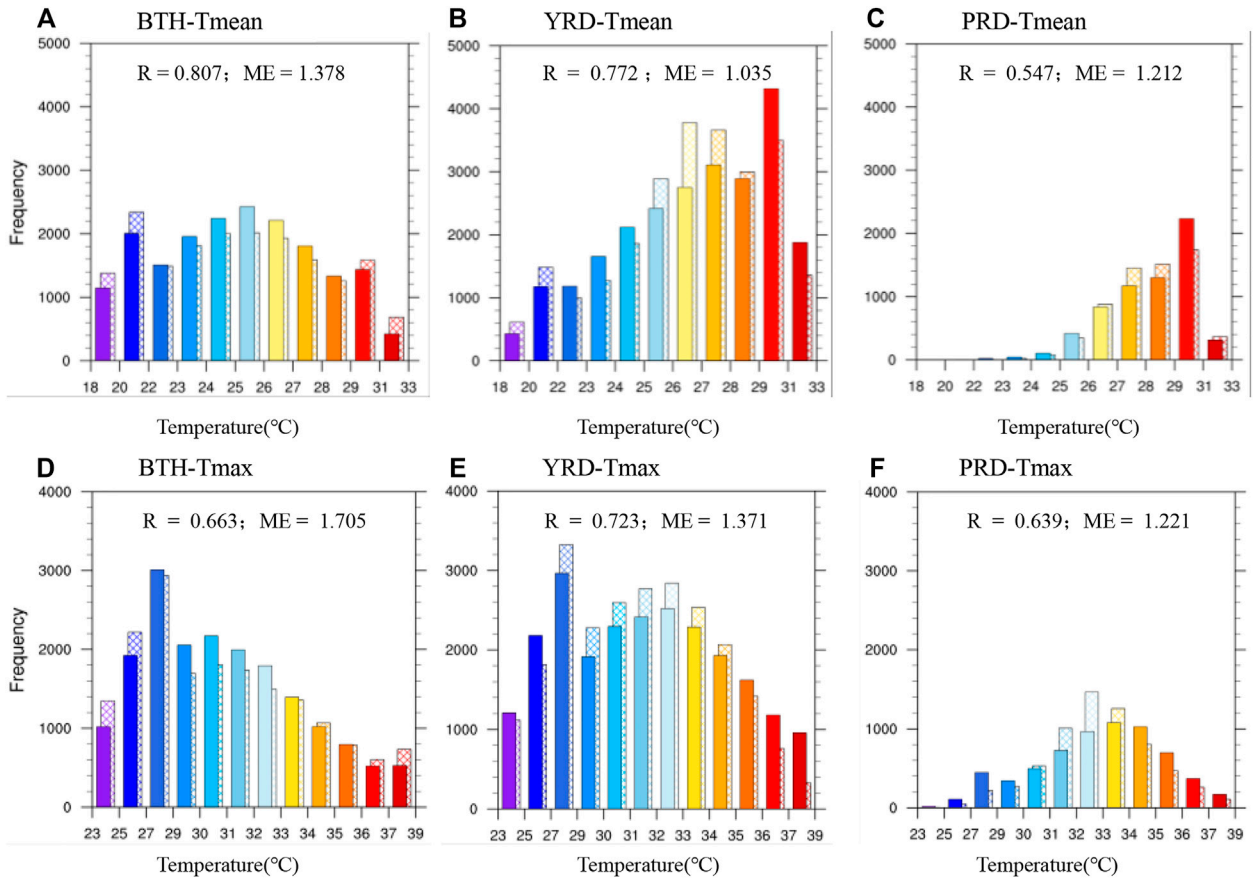

FIGURE 3 | Frequency comparison histogram of T_{mean} and T_{max} between observation data and WRF simulation results during the entire analysis period (JJA of 1996–2005) over **(A,D)** BTH, **(B,E)** YRD, and **(C,F)** PRD (solid color represents observation data, and grids represent WRF simulation results; *R* represents the correlation coefficients, and *ME* represents the mean bias).

cumulative sum of the difference between the daily maximum temperature and the 35°C threshold for all HWs in study period. In this study, we focus on changes of HWs in summer season, so all above three HW indices are calculated for summer season, i.e., June, July and August.

Bias Correction Method

To reduce the model uncertainty of WRF/UCM in simulating the daily mean and maximum temperature, bias correction (BC) for the WRF/UCM-based downscaled T_{max} is needed. Based on the average difference between the observed and simulated T_{mean} and T_{max} during the period 1996–2005, a climatology based bias correction method is applied in this study, just as mentioned in Li et al. (2018).

The bias-corrected temperature for the model (T_{MC}) was calculated as follows:

$$T_{MC} = T_{model} + (TT_{OBS} - TT_{model}) \quad (1)$$

Where T_{model} represents the simulated daily mean/maximum temperature at each grid cell of the model, and ($TT_{OBS} - TT_{model}$) stands for the mean systematic error of the temperature. TT_{OBS} and TT_{model} are the mean values from the observation of all stations and the simulation of model corresponding to the stations during 1996–2005, respectively.

Using the bias corrected temperature results, the future changes of summer HWs in three urban agglomerations have been estimated, and the flow chart of analysis in this study is shown in **Figure 2** as following.

RESULTS

Model Validation

To examine the performance of the WRF/UCM modeling system, the frequency histograms of simulated results versus observed data for Tmean and Tmax are shown in **Figure 3**. All daily values during the entire analysis period (JJA of 1996–2005) from the meteorological stations were used. For BTH, YRD and PRD, the records are 18,900 (92 days × 10 years × 21 stations = 18,900), 24,300 (92 days × 10 years × 27stations = 18,900) and 6,300 (92 days × 10 years × 7 stations = 6,300), respectively. From the frequency of occurrence in different temperature sections, there are good temporal correlations between the bias-corrected model outputs and observations for T_{mean} and T_{max}. The correlation coefficients

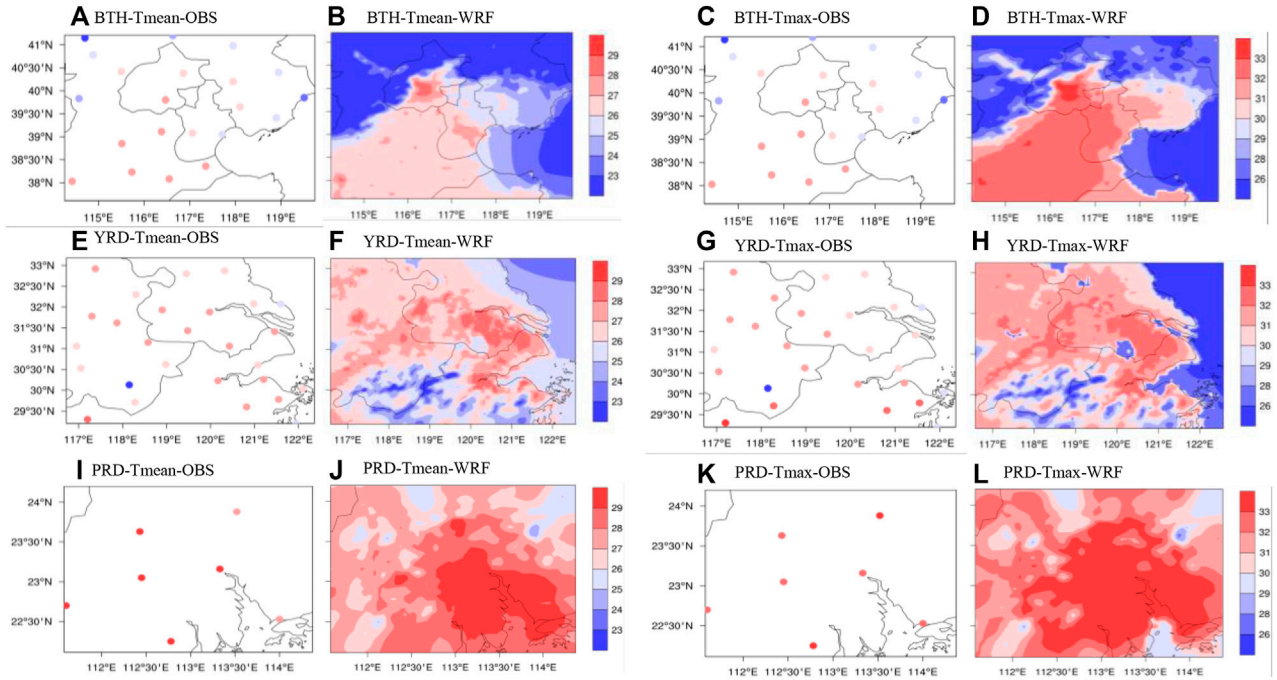

FIGURE 4 | Spatial distributions of averaged T_{mean} and T_{max} of observation data and WRF simulation results during the entire analysis period (JJA of 1996–2005) over **(A–D)** BTH, **(E–H)** YRD, and **(I–L)** PRD.

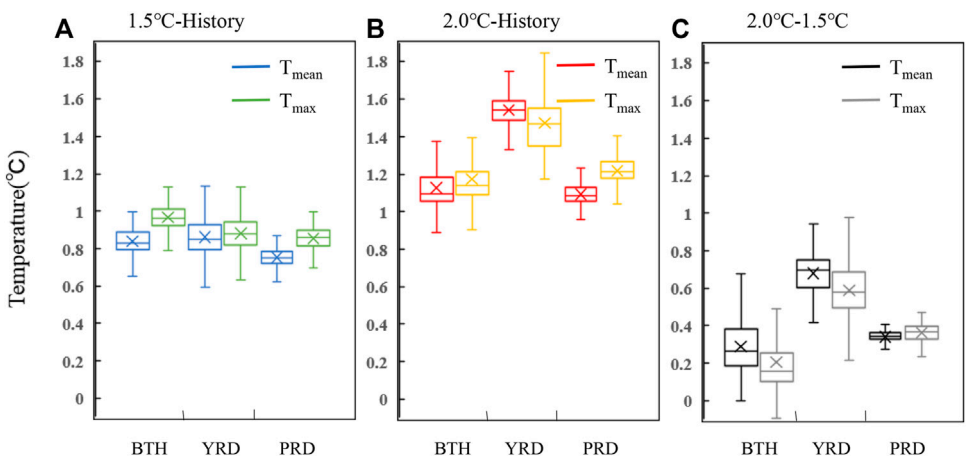

FIGURE 5 | Box diagram of the differences in T_{mean} and T_{max} of the three urban agglomerations over eastern China between **(A)** Exp 1.5-run and Exp HIS-run, between **(B)** Exp 2.0-run and Exp HIS-run, and between **(C)** Exp 2.0-run and Exp 1.5-run ("×" represents the average value, the top horizontal line refers to the maximum value, the bottom horizontal line represents the minimum value, the upper and lower quartile indicate the ranges from 25th to 75th percentile in the packing drawing, and the middle horizontal line represents the median).

are mostly greater than 0.6 for all three urban agglomerations. The mean bias ranges from 1.04 to 1.38 for T_{mean} and from 1.22 to 1.7 for T_{max}. Furthermore, the spatial distributions of summer T_{mean} and T_{max} in observations and bias-corrected model simulations are demonstrated in **Figure 4**. The HIS-run well replicates the observations in JJA with a spatial correlation coefficient of more than 0.6, which indicates that the bias-corrected model outputs capture the climatological features acceptably. The urban heat island effect can be seen, as T_{mean} and T_{max} tend to be higher in the urban areas and lower in the surrounding areas.

In summary, the bias-corrected model outputs can, to a great extent, generate the regional-scale characteristics of the summer temperatures realistically at each selected urban agglomeration faithfully, which suggests the reliability of using WRF downscaling for projecting the HW indices' future changes. We note that a few efforts recently attempted to apply the WRF dynamic downscaling

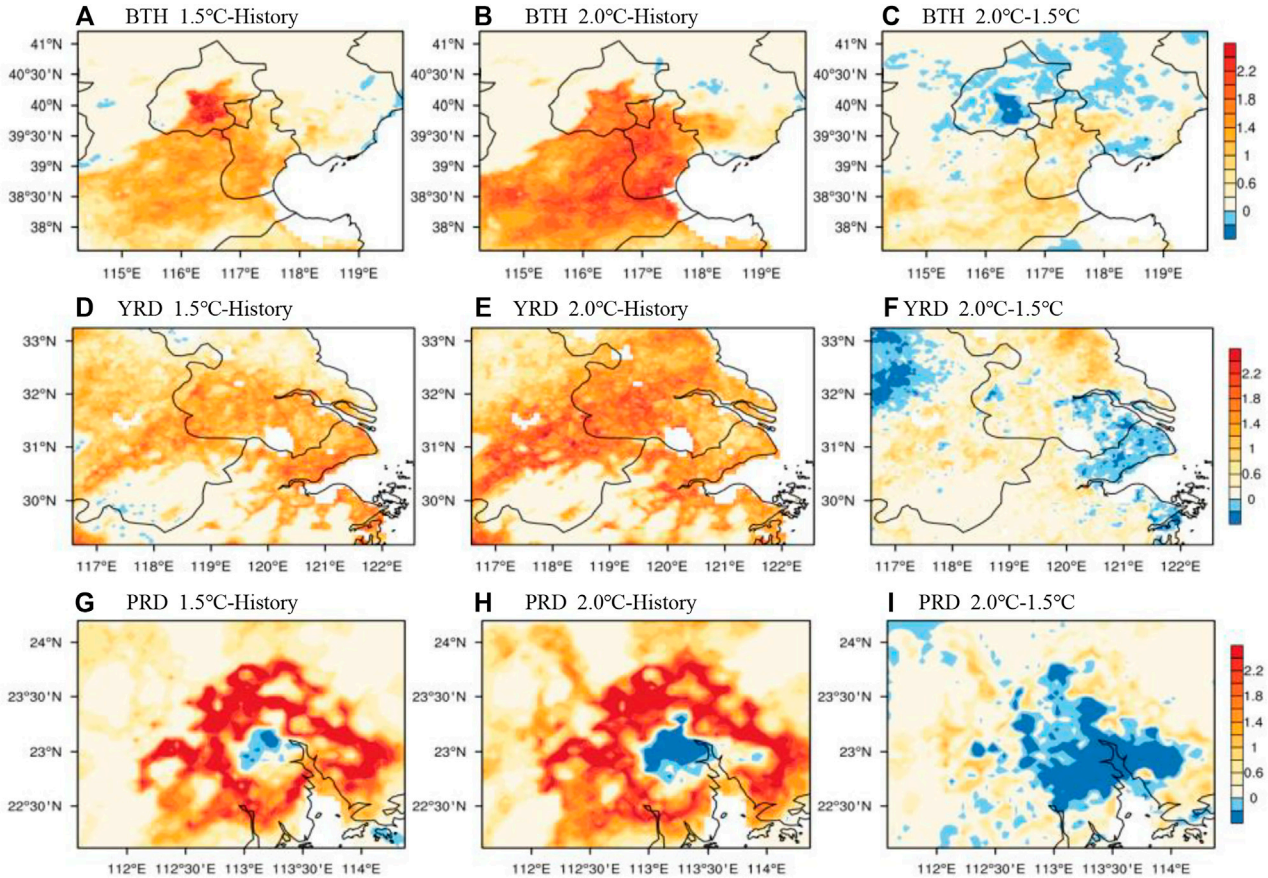

FIGURE 6 | Spatial distributions of the difference in HW frequency over the three urban agglomerations between Exp 1.5-run and Exp HIS-run **(A,D,G)**, between Exp 2.0-run and Exp HIS-run **(B,E,H)**, and between Exp 2.0-run and Exp 1.5-run **(C,F,I)**. The colored area indicates that the change is statistically significant at the 95% confidence level.

method to revisit the regional impacts of global warming (Yamamoto et al., 2018; Ge et al., 2021).

Future Summer Temperature Changes

Figure 5 presents the WRF-projected changes in summer T_{mean} and T_{max} over the three urban agglomerations under 1.5 and 2.0°C warming conditions relative to the historical run. Projected T_{mean} and T_{max} both increase under 1.5 and 2.0°C warming throughout the urban agglomerations. When the warming reaches 1.5°C under RCP4.5, the averaged increasing magnitude of T_{max} are 0.97°C with the inhomogeneous changes range between 0.92 and 1.01°C over BTH region. As for YRD region, the 10-year mean increasing magnitude is 0.88°C, with the range between 0.82 and 0.94°C. The increasing magnitude is smallest over PRD region, with mean magnitude of 0.85°C, maximum T_{max} increase is 0.90°C, and minimum T_{max} increase is 0.82°C. The increasing magnitudes of T_{max} are stronger than those of T_{mean}. It suggests that the number of extreme high temperature events will soar in urban agglomerations. Under the scenario of 2.0°C warming, the changes of summer temperatures will be greater (**Figure 5B**), and the largest increases of T_{mean} and T_{max} occur in YRD.

How the increase from 1.5 to 2.0°C warming impacts on summer temperatures is shown in **Figure 5C**. With this additional 0.5°C temperature rise, T_{mean} will increase by 0.29°C (0.19–0.38°C), 0.68°C (0.6–0.75°C) and 0.34°C (0.33–0.36°C) over BTH, YRD and PRD, respectively, whereas T_{max} can rise by 0.2°C (0.1–0.26°C), 0.59°C (0.5–0.69°C) and 0.36°C (0.33–0.4°C) for BTH, YRD and PRD, respectively. Obviously, the increases of T_{mean} and T_{max} in response to the additional 0.5°C warming are largest in YRD, which implies that by enforcing the agreement on limiting the temperature increase to 1.5°C, the YRD region will benefit more than the other urban agglomerations in terms of reducing extreme hot events. This result is consistent with the results of multi-mode projection on extreme maximum temperature by Yu et al. (2018). Note that the increases of T_{mean} and T_{max} in response to the additional 0.5°C warming in the other urban agglomerations except YRD region is slightly weaker than the additional rise. This may be because our study focuses on summertime when the warming trend will be less significant than winter in China under future global warming (Yang et al., 2021c). In addition, Ge et al. (2021) pointed out that the smaller benefits achieved from the additional 0.5°C warming limit for the WRF projection than CESM.

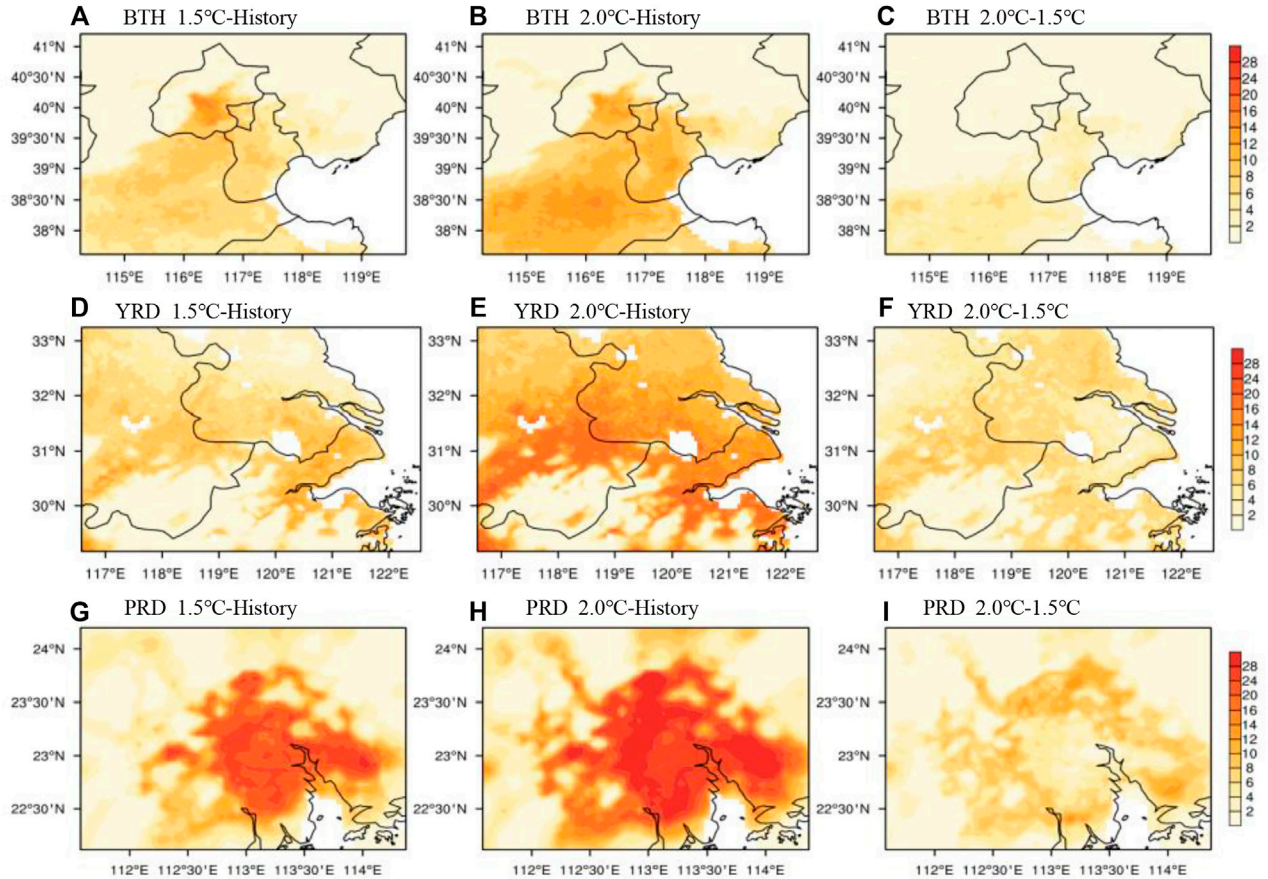

FIGURE 7 | Spatial distributions of the difference in HW duration over the three urban agglomerations between Exp 1.5-run and Exp HIS-run **(A,D,G)**, between Exp 2.0-run and Exp HIS-run **(B,E,H)**, and between Exp 2.0-run and Exp 1.5-run **(C,F,I)**. The colored area indicates that the change is statistically significant at the 95% confidence level.

Future Heat Wave Changes

Figures 6–8 show the spatial distributions of projected future changes in the HWs' frequency, duration, and intensity over the three urban agglomerations. The three indices of summer HWs are enhanced in most areas of the urban agglomerations against the backgrounds of 1.5 and 2.0°C warming. According to the variation diagrams of HW frequency in **Figures 6A,D,G**, the HW frequency is enhanced in almost entire BTH and YRD under the 1.5°C warming scenario. In BTH, the enhancement mainly occurs over the urban underlying surface and the underlying surface of dry cropland to the south of the urban areas, while the urban and cropland/woodland mosaic areas witness most of the HW frequency increases in YRD. As for PRD, the HW frequency decreases in the urban areas of Guangzhou, but increases significantly in the surrounding cities. Under the 2.0°C warming scenario, there is a similar distribution of HW frequency changes, but the range is more extensive, and the intensity is stronger (**Figures 6B,E,H**). With the additional temperature increase of 0.5°C from 1.5 to 2.0°C, the frequency of HWs in metropolitan areas (such as Beijing, Shanghai, Guangzhou) will decrease (**Figures 6C,F,I**). It should be pointed out that the frequency of HWs in our study is defined based on the HW events, so the reduction of frequency may not mean the decrease of high-temperature days, because the increase of HWs' duration may reduce HWs' frequency in the fixed summertime.

The variations of HW duration under different scenarios are illustrated in **Figure 7**. Compared with the historical period, when reaching the warming scenarios of 1.5 and 2.0°C, the urban agglomerations show a ubiquitous characteristic of prolonged HW duration at different latitudes from north to south, and the more southwards the urban agglomerations are located, the larger increases their HW duration will have. In those urban agglomerations, the regions with relatively larger HW duration growth can generally match the regions with higher HW frequency increase shown in **Figure 6**. As can be seen from **Figures 7C,F,I**, with the additional 0.5°C warming, the duration of HWs increases both in the urban areas and in the suburbs. Why does the frequency of HWs in urban areas decrease, while in the suburbs on the contrary (**Figures 6C,F,I**), and the duration of HWs in the suburbs increases more than that in urban areas? It may be because the current urban areas have higher frequency and longer duration of HWs than the suburbs due to the heat island effect. Therefore, under global warming, HWs' frequency

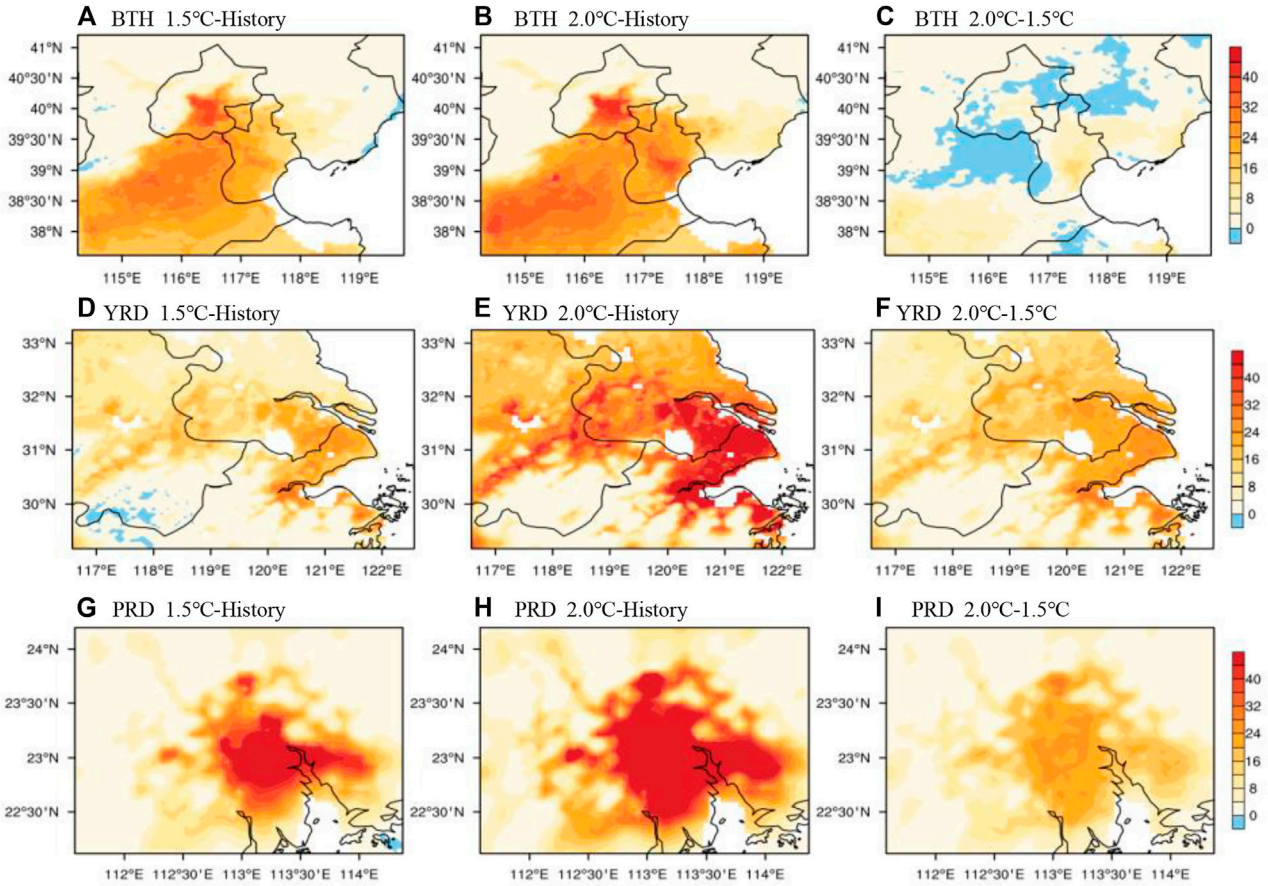

FIGURE 8 | Spatial distributions of the difference in HW intensity over the three urban agglomerations between Exp 1.5-run and Exp HIS-run **(A,D,G)**, between Exp 2.0-run and Exp HIS-run **(B,E,H)**, and between Exp 2.0-run and Exp 1.5-run **(C,F,I)**. The colored area indicates that the change is statistically significant at the 95% confidence level.

TABLE 1 | The values and growth rates of the three HW indices in the three urban agglomerations over eastern China under historical and different warming scenarios.

Heat waves indices	BTH urban agglomeration			YRD urban agglomeration			PRD urban agglomeration		
	Frequency	Duration	Intensity	Frequency	Duration	Intensity	Frequency	Duration	Intensity
History	1.15	5.63	6.81	0.98	6.03	7.28	1.18	6.87	8.15
1.5°C	1.73	9.21	14.76	1.81	11.13	16.25	2.08	14.41	18.78
2.0°C	1.99	10.65	20.56	2.09	16.10	28.52	2.21	18.33	26.96
1.5°C-History growth rate (%)	50.4	63.6	116.7	84.7	84.6	123.2	76.3	109.8	130.4
2.0°C-History growth rate (%)	73.0	89.2	201.9	113.2	167.0	291.8	95.8	166.8	230.8
2.0–1.5°C growth rate (%)	15.0	15.6	39.3	15.5	44.7	75.5	6.3	27.2	43.6

and duration increase within a limited extent in cities, while the suburbs have a greater growth space.

Different from the changes in the frequency and duration of HWs, whether from the historical period to the 1.5 and 2.0°C warming periods or from 1.5 to 2.0°C warming, large increases of HW intensity are mainly concentrated over the urban underlying surface (**Figure 8**). This implies that the urban population will face stronger HWs in the future.

Furthermore, the future changes in the area-average frequency, duration, and intensity of HWs in each urban agglomeration are summarized in **Table 1**. It can be seen from the table that, under any scenario, the more southward the urban agglomerations are, the higher frequency, longer duration, and greater intensity their HWs will have, since the HW indices are related to the geographical latitudes of the urban agglomerations. Under the 1.5°C warming scenario, the frequency, duration and intensity of HWs are increased respectively by 50.4, 63.6, and 116.7% in BTH, 84.7, 84.6, and 123.2% in YRD, and 76.3, 109.8, and 130.4% in PRD compared with the historical period. Among the three HWs indices, the intensity grows the most. The

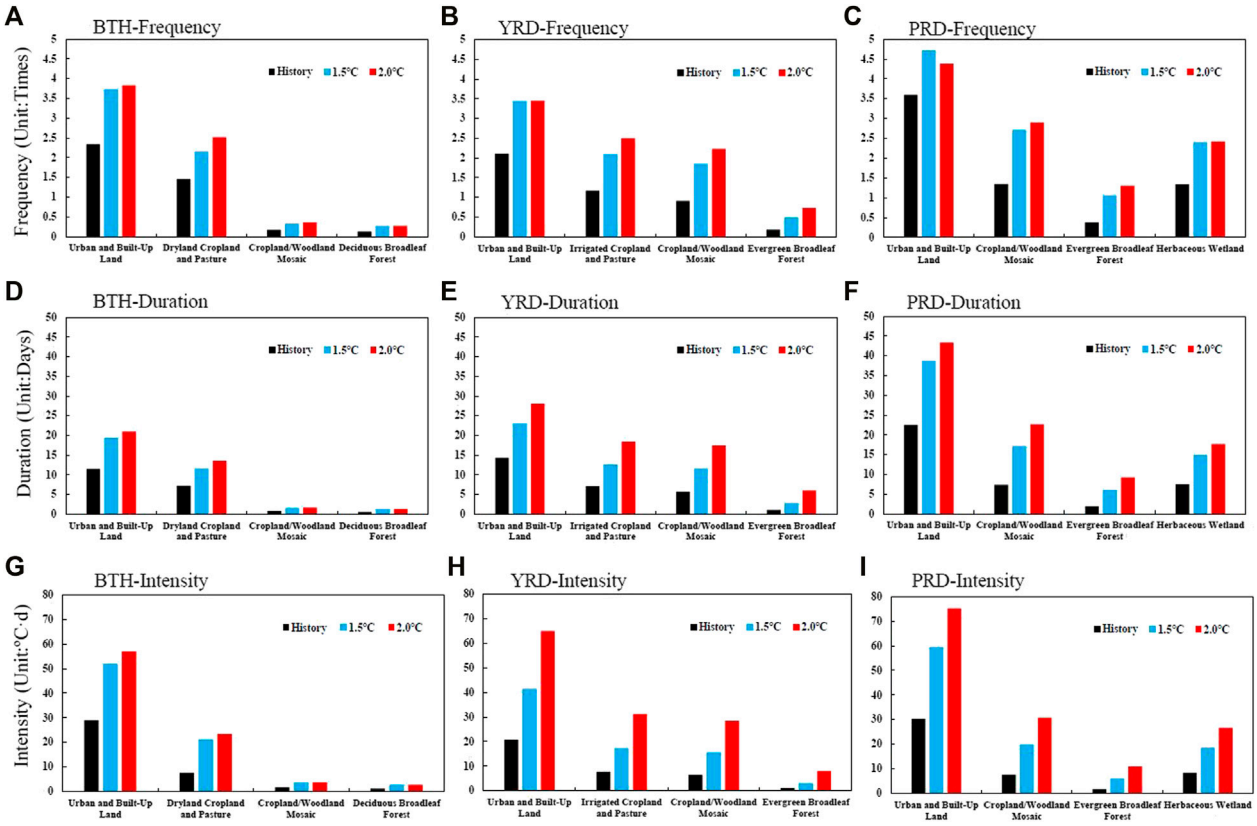

FIGURE 9 | Area averages of HW frequency **(A)**, **(B)**, **(C)**, duration **(D)**, **(E)**, **(F)** and intensity **(G)**, **(H)**, **(I)** over four major underlying surfaces in each urban agglomeration (black represents the historical period, blue represents the 1.5°C warming period and red represents the 2.0°C warming period).

additional warming of 0.5°C from 1.5 to 2.0°C will result in 15.5, 44.7, and 75.5% increases in the frequency, duration, and intensity of HWs in YRD, which are the largest among those of the three urban agglomerations.

Difference in Heat Wave Risks Between Urban and Non-Urban Areas

From the spatial distribution figures concerning the future changes in HWs' frequency, duration, and intensity, we can see large spatial differences in each urban agglomeration, which mainly lie between the urban and non-urban underlying surfaces. Four major land cover types were selected to analyze their HW index values in each urban agglomeration in detail. **Figure 9** shows the area-average HW frequency, duration, and intensity values of different land cover types in each urban agglomeration. Compared with other major land cover types, the urban areas have much higher frequency, duration, and intensity of HWs. The response of HW indices to the warming is more robust in the urban areas, especially under 1.5°C warming climate. In the scenario of 1.5°C warming, the HWs' frequency, duration and intensity in urban areas of BTH are 3.73, 19.36, and 51.98 respectively. Compared to the respective values of HW indices over the dryland cropland and pasture, which are the biggest among those of non-urban land cover types in BTH, the above values in urban areas are 60, 68, and 144% higher. In YRD, the HW frequency, duration, and intensity in urban areas are 3.44, 22.96, and 41.49 respectively, and those values are 65, 83 and 140% higher than the respective greatest values for non-urban land cover, which all belong to the irrigated cropland and pasture in this case. The HW frequency, duration, and intensity in the urban areas of PRD are 4.71, 38.74, and 59.54 respectively, which are 74, 126, and 200% higher than those of the cropland and woodland mosaic, the largest among the respective values for non-urban land cover. In PRD, the differences in the values of HW indices between urban and non-urban areas are particularly significant. The foregoing results thus suggest a much graver future risk of HWs in urban areas than in non-urban areas.

CONCLUSION AND DISCUSSIONS

Urban areas are more vulnerable to HWs due to the combined impacts of global climate change and their own local climate effects. In this study, the high-resolution downscaling results of WRF/UCM have been used to investigate the future changes of summer HWs under 1.5 and 2.0°C global warming over three

urban agglomerations of eastern China. The results indicate that the WRF/UCM model can capture the basic features of summer temperature across urban agglomerations.

The results of downscaling projection based on the WRF/UCM show that the influence ranges of HWs in summer are significantly expanded, and the values of HWs indices are significantly increased compared with the data of the historical period. The growth rates of the three HWs indices can reach more than 50% in the 1.5°C warming period, and can even be higher than 70% in the 2.0°C warming period, during which the growth rate of HW intensity is more than 200%. An additional 0.5°C temperature increase from 1.5 to 2.0°C has the most significant impact on the future HWs of the YRD urban agglomeration; particularly, the HW intensity therein can increase by 75.5%, which is far higher than the other urban agglomerations.

The downscaled changes of HWs in the three urban agglomerations under the future warming of 1.5–2.0°C are qualitatively consistent with previous conclusions derived from statistically downscaled results of 19 CMIP5 models under RCP4.5 (Yu et al., 2017), although the magnitude of changes differs due to difference in extreme events definition and climate models used for projection (Li et al., 2018; Sun et al., 2019). But all results suggest that urban agglomerations would go through very extreme heat waves events if there is no climate change mitigation strategy being taken in the remainder of the 21st century.

It is noted that the possible changes of the HWs across three urban agglomerations in this study are under transient warming condition using CESM projection results. There has recent interest in understanding the differences of future changes of climate extremes between stabilized and transient warming situation (Sun et al., 2019; King et al., 2020; Ge et al., 2021). King et al. (2020) pointed out that there are substantial differences of temperature changes between transient and quasi-equilibrium states, relative to differences between the 1.5 and 2 °C global warming limits. Therefore, it is worthy of in-depth study of the differences in HWs between transient and equilibrium climates, which is of great significance for managing the risks of climate change.

On the other hand, the projections or statistically downscaled data based on coarse-resolution global climate system models used the regional averaged results to represent the future climate change in urban agglomerations, which is insufficient in urban areas (Bounoua et al., 2015; Zhao et al., 2021). This results derived from WRF/UCM model downscaled data demonstrate the warming response in urban areas is more prominent, compared with other major land cover types in each urban agglomeration. In the scenario of 1.5°C warming, the difference of HWs between urban and non-urban areas is particularly significant in PRD. Based on the CMIP6 data sets under all future scenarios, the greatest heat risk considering population or economy is projected in the PRD region (Chou et al., 2021; Zhang et al., 2021), which is consistent with our projections. The results should provide further scientific support for the mitigation and adaption of the future HWs risk in mega-cities.

However, only RCP4.5 was used in our analysis and various RCPs may cause uncertainties of the result. Uncertainties from the projections of various global models can also be another source of the uncertainties of the results. In addition, accurate land cover information is also important. It is necessary to perform further investigation to reduce the uncertainty in our results for better supporting the mitigation and adoption of the future HWs risk in the urban areas.

DATA AVAILABILITY STATEMENT

The original contributions presented in the study are included in the article/Supplementary Material, further inquiries can be directed to the corresponding author.

AUTHOR CONTRIBUTIONS

HM and ZL designed the study. HM and YW performed the downscaling simulations and the data analysis. All authors contributed to the writing of the manuscript.

FUNDING

This work was jointly supported by China National Key R&D Program (2017YFA0603804), the National Natural Science Foundation of China (42021004, 42175032) and the "Earth System Science Numerical Simulator Facility" (EarthLab).

REFERENCES

Bounoua, L., Zhang, P., Mostovoy, G., Thome, K., Masek, J., Imhoff, M., et al. (2015). Impact of Urbanization on US Surface Climate. *Environ. Res. Lett.* 10, 084010. doi:10.1088/1748-9326/10/8/084010

Chen, F., and Dudhia, J. (2001). Coupling an Advanced Land Surface-Hydrology Model with the Penn State-NCAR MM5 Modeling System. Part I: Model Implementation and Sensitivity. *Mon. Wea. Rev.* 129, 569–585. doi:10.1175/1520-0493(2001)129<0569:caalsh>2.0.co;2

Chen, L., and Frauenfeld, O. W. (2014). A Comprehensive Evaluation of Precipitation Simulations over China Based on CMIP5 Multimodel Ensemble Projections. *J. Geophys. Res. Atmos.* 119, 5767–5786. doi:10.1002/2013jd021190

Chen, L., Ma, Z., Li, Z., Wu, L., Flemke, J., and Li, Y. (2018). Dynamical Downscaling of Temperature and Precipitation Extremes in China under Current and Future Climates. *Atmosphere-Ocean* 56 (1), 55–70. doi:10.1080/07055900.2017.1422691

Chen, Y., and Li, Y. (2017). An Inter-comparison of Three Heat Wave Types in China during 1961-2010: Observed Basic Features and Linear Trends. *Sci. Rep.* 7, 45619. doi:10.1038/srep45619

Chou, J., Sun, M., Dong, W., Zhao, W., Li, J., Li, Y., et al. (2021). Assessment and Prediction of Climate Risks in Three Major Urban Agglomerations of Eastern China. *Sustainability* 13, 13037. doi:10.3390/su132313037

Coumou, D., and Robinson, A. (2013). Historic and Future Increase in the Global Land Area Affected by Monthly Heat Extremes. *Environ. Res. Lett.* 8 (3), 034018. doi:10.1088/1748-9326/8/3/034018

Dian-Xiu, Y., Ji-Fu, Y., Zheng-Hong, C., You-Fei, Z., and Rong-Jun, W. (2014). Spatial and Temporal Variations of Heat Waves in China from 1961 to 2010. *Adv. Clim. Change Res.* 5, 66–73.

Fang, C. (2015). Important Progress and Future Direction of Studies on China's Urban Agglomerations. *J. Geogr. Sci.* 25 (8), 1003–1024. doi:10.1007/s11442-015-1216-5

Frich, P., Alexander, L., Della-Marta, P., Gleason, B., Haylock, M., Klein Tank, A., et al. (2002). Observed Coherent Changes in Climatic Extremes during the Second Half of the Twentieth century. *Clim. Res.* 19 (3), 193–212. doi:10.3354/cr019193

Ge, J., Qiu, B., Wu, R., Cao, Y., Zhou, W. D., Zhou, W., et al. (2021). Does Dynamic Downscaling Modify the Projected Impacts of Stabilized 1.5°C and 2°C Warming on Hot Extremes Over China? *Geophys. Res. Lett.* 48. doi:10.1029/2021GL092792

Grossman-Clarke, S., Schubert, S., and Fenner, D. (2017). Urban Effects on Summertime Air Temperature in Germany under Climate Change. *Int. J. Climatol.* 37, 905–917. doi:10.1002/joc.4748

Gong, P., Li, X. C., and Zhang, W. (2019). 40-Year (1978–2017) Human Settlement Changes in China Reflected by Impervious Surfaces From Satellite Remote Sensing. *Science Bulletin* 64 (11), 756–763.

Hong, S.-Y., Noh, Y., and Dudhia, J. (2006). A New Vertical Diffusion Package with an Explicit Treatment of Entrainment Processes. *Monthly Weather Rev.* 134, 2318–2341. doi:10.1175/mwr3199.1

Hong, S. Y., and Lim, J. J. (2006). The WRF Single-Moment 6-Class Microphysics Scheme (WSM6). *J. Korean Meteorol. Soc.* 42 (2), 129–151.

Hua, W., Dong, X., Liu, Q., Zhou, L., Chen, H., and Sun, S. (2021). High-Resolution WRF Simulation of Extreme Heat Events in Eastern China: Large Sensitivity to Land Surface Schemes. *Front. Earth Sci.* 9, 770826. doi:10.3389/feart.2021.770826

Iacono, M. J., Delamere, J. S., Mlawer, E. J., Shephard, M. W., Clough, S. A., and Collins, W. D. (2008). Radiative Forcing by Long-Lived Greenhouse Gases: Calculations with the AER Radiative Transfer Models. *J. Geophys. Res.* 113, D13103. doi:10.1029/2008JD009944

IPCC (2014). "Part A: Global and Sectoral Aspects. Contribution of Working Group II to the Fifth Assessment Report of the Intergovernmental Panel on Climate Change," in *Climate Change 2014: Impacts, Adaptation, and Vulnerability* (Cambridge, United Kingdom and New York, NY: Cambridge University Press) 1132.

Kain, J. S. (2004). The Kain-Fritsch Convective Parameterization: An Update. *J. Appl. Meteorol.* 43, 170–181. doi:10.1175/1520-0450(2004)043<0170:tkcpau>2.0.co;2

King, A. D., Lane, T. P., Henley, B. J., and Brown, J. R. (2020). Global and Regional Impacts Differ between Transient and Equilibrium Warmer Worlds. *Nat. Clim. Chang.* 10, 42–47. doi:10.1038/s41558-019-0658-7

Knutti, R., and Sedláček, J. (2013). Robustness and Uncertainties in the New CMIP5 Climate Model Projections. *Nat. Clim Change* 3 (4), 369–373. doi:10.1038/nclimate1716

Kovats, R. S., and Hajat, S. (2008). Heat Stress and Public Health: A Critical Review. *Annu. Rev. Public Health* 29, 41–55. doi:10.1146/annurev.publhealth.29.020907.090843

Kusaka, H., and Kimura, F. (2004). Coupling a Single-Layer Urban Canopy Model with a Simple Atmospheric Model: Impact on Urban Heat Island Simulation for an Idealized Case. *J. Meteorol. Soc. Jpn.* 82, 67–80. doi:10.2151/jmsj.82.67

Kusaka, H., Kondo, H., Kikegawa, Y., and Kimura, F. (2001). A Simple Single-Layer Urban Canopy Model for Atmospheric Models: Comparison with Multi-Layer and Slab Models. *Boundary-Layer Meteorology* 101, 329–358. doi:10.1023/a:1019207923078

Lesk, C., Rowhani, P., and Ramankutty, N. (2016). Influence of Extreme Weather Disasters on Global Crop Production. *Nature* 529 (7584), 84–87. doi:10.1038/nature16467

Li, D., Zhou, T., Zou, L., Zhang, W., and Zhang, L. (2018). Extreme High-Temperature Events Over East Asia in 1.5°C and 2°C Warmer Futures: Analysis of NCAR CESM Low-Warming Experiments. *Geophys. Res. Lett.* 45, 1541–1550. doi:10.1002/2017gl076753

Li, H., Xiao, P., Feng, X., Yang, Y., Wang, L., Zhang, W., et al. (2017). Using Land Long-Term Data Records to Map Land Cover Changes in China Over 1981-2010. *IEEE J. Sel. Top. Appl. Earth Observations Remote Sensing* 10 (4), 1372–1389. doi:10.1109/jstars.2016.2645203

Liang, Y. X., Ma, H. Y., Jiang, Z. H., Bao, Y. T., and Li, H. J. (2019). Impact Assessment of Changes in Agricultural and Natural Vegetation Mosaics on Near-Surface Meteorological fields in the Yangtze River Delta. *J. Meteorol. Sci.* 39 (1), 23–33. doi:10.3969/2018jms.0013 (in Chinese).

McMichael, A. J., and Lindgren, E. (2011). Climate Change: Present and Future Risks to Health, and Necessary Responses. *J. Intern. Med.* 270 (5), 401–413. doi:10.1111/j.1365-2796.2011.02415.x

Meehl, G. A., and Tebaldi, C. (2004). More Intense, More Frequent, and Longer Lasting Heat Waves in the 21st century. *Science* 305 (5686), 994–997. doi:10.1126/science.1098704

Oke, T. R. (1982). The Energetic Basis of the Urban Heat Island. *Q.J Royal Met. Soc.* 108, 1–24. doi:10.1002/qj.49710845502

Pachauri, R. K., Allen, M. R., Barros, V. R., Broome, J., Cramer, W., Christ, R., et al. (2014). *Climate Change 2014: Synthesis Report. Contribution of Working Groups I, II and III to the Fifth Assessment Report of the Intergovernmental Panel on Climate Change*. Geneva, Switzerland: IPCC, 151.

Perkins, S. E. (2015). A Review on the Scientific Understanding of Heatwaves—Their Measurement, Driving Mechanisms, and Changes at the Global Scale. *Atmos. Res.* 164-165, 242–267. doi:10.1016/j.atmosres.2015.05.014

Ren, G., and Zhou, Y. (2014). Urbanization Effects on Trends of Extreme Temperature Indices of National Stations over mainland China, 1961–2008. *J. Clim.* 27, 2340–2360. doi:10.1175/jcli-d-13-00393.1

Seneviratne, S. I., Donat, M. G., Mueller, B., and Alexander, L. V. (2014). No Pause in the Increase of Hot Temperature Extremes. *Nat. Clim Change* 4 (3), 161–163. doi:10.1038/nclimate2145

Skamarock, W. C., and Klemp, J. B. (2008). A Time-Split Nonhydrostatic Atmospheric Model for Weather Research and Forecasting Applications. *J. Comput. Phys.* 227 (7), 3465–3485. doi:10.1016/j.jcp.2007.01.037

Stone, B., Hess, J. J., and Frumkin, H. (2010). Urban Form and Extreme Heat Events: Are Sprawling Cities More Vulnerable to Climate Change Than Compact Cities? *Environ. Health Perspect.* 118 (10), 1425–1428. doi:10.1289/ehp.0901879

Su, Q., and Dong, B. (2019a). Projected Near-Term Changes in Three Types of Heat Waves over China under RCP4.5. *Clim. Dyn.* 53, 3751–3769. doi:10.1007/s00382-019-04743-y

Su, Q., and Dong, B. (2019b). Recent Decadal Changes in Heat Waves over China: Drivers and Mechanisms. *J. Clim.* 32 (14), 4215–4234. doi:10.1175/jcli-d-18-0479.1

Sun, C., Jiang, Z., Li, W., Hou, Q., and Li, L. (2019). Changes in Extreme Temperature over China when Global Warming Stabilized at 1.5 °C and 2.0 °C. *Sci. Rep.* 9. doi:10.1038/s41598-019-50036-z

Sun, Y., Zhang, X., Ren, G., Zwiers, F. W., and Hu, T. (2016). Contribution of Urbanization to Warming in China. *Nat. Clim Change* 6 (7), 706–709. doi:10.1038/nclimate2956

Sun, Y., Zhang, X., Zwiers, F. W., Song, L., Wan, H., Hu, T., et al. (2014). Rapid Increase in the Risk of Extreme Summer Heat in Eastern China. *Nat. Clim Change* 4 (12), 1082–1085. doi:10.1038/nclimate2410

Thomson, A. M., Calvin, K. V., Smith, S. J., et al. (2011). RCP4.5: A Pathway for Stabilization of Radiative Forcing by 2100. *Climatic Change* 109 (1–2), 77–94. doi:10.1007/s10584-011-0151-4

Wang, L., Li, C., Ying, Q., Cheng, X., Wang, X., Li, X., et al. (2012). China's Urban Expansion from 1990 to 2010 Determined with Satellite Remote Sensing. *Chin. Sci. Bull.* 57, 2802–2812. doi:10.1007/s11434-012-5235-7

Wu, J., Han, Z., Xu, Y., Zhou, B., and Gao, X. (2020). Changes in Extreme Climate Events in China Under 1.5 °C-4 °C Global Warming Targets: Projections Using an Ensemble of Regional Climate Model Simulations. *J. Geophys. Res. Atmos.* 125. doi:10.1029/2019JD031057

Xiao, P., Li, H., Yang, Y., Wang, L., and Wang, X. (2015). "Land-use Changes in China during the Past 30 Years," in *Land-Use Changes in China* (Singapore: World Scientific), 11–49. doi:10.1142/9789814651783_0002

Yamamoto, M., Kasai, M., Okaze, T., Hanaoka, K., and Mochida, A. (2018). Analysis of Climatic Factors Leading to Future Summer Heatstroke Risk Changes in Tokyo and Sendai Based on Dynamical Downscaling of Pseudo Global Warming Data Using WRF. *J. Wind Eng. Ind. Aerodynamics* 183, 187–197. doi:10.1016/j.jweia.2018.10.001

Yang, X., Zeng, G., Zhang, S., Hao, Z., and Iyakaremye, V. (2021a). Relationship between Two Types of Heat Waves in Northern East Asia and Temperature Anomalies in Eastern Europe. *Environ. Res. Lett.* 16, 024048. doi:10.1088/1748-9326/abdc8a

Yang, X., Zhou, B., Xu, Y., and Han, Z. (2021b). CMIP6 Evaluation and Projection of Temperature and Precipitation over China. *Adv. Atmos. Sci.* 38, 817–830. doi:10.1007/s00376-021-0351-4

Yang, Y., Lin, Z., Luo, L., Zhang, Y., and Li, Z. (2021c). Inhomogeneous Trends in the Onset Date of Extreme Hot Days in China over the Last Five Decades. *Atmos. Oceanic Sci. Lett.* 14, 100080. doi:10.1016/j.aosl.2021.100080

Yang, Y., Xiao, P., Feng, X., and Li, H. (2017). Accuracy Assessment of Seven Global Land Cover Datasets over China. *ISPRS J. Photogrammetry Remote Sensing* 125, 156–173. doi:10.1016/j.isprsjprs.2017.01.016

You, Q. L., Jiang, Z. H., Kong, L., Wu, Z., Bao, Y., Kang, S., et al. (2017). A Comparison of Heat Wave Climatologies and Trends in China Based on Multiple Definitions. *Clim. Dyn.* 48, 3975–3989. doi:10.1007/s00382-016-3315-0

Yu, R., Zhai, P., and Lu, Y. (2018). Implications of Differential Effects between 1.5 and 2 °C Global Warming on Temperature and Precipitation Extremes in China's Urban Agglomerations. *Int. J. Climatol* 38, 2374–2385. doi:10.1002/joc.5340

Yu, Y., Shao, Q., Lin, Z., and Kang, I.-S. (2021). Characteristics Analysis and Synoptic Features of Event-Based Regional Heatwaves over China. *J. Geophys. Res. Atmospheres* 126, e2020JD033865. doi:10.1029/2020jd033865

Zhang, G., Zeng, G., Liang, X.-Z., and Huang, C. (2021). Increasing Heat Risk in China's Urban Agglomerations. *Environ. Res. Lett.* 16, 064073. doi:10.1088/1748-9326/ac046e

Zhao, L., Oleson, K., Bou-Zeid, E., Krayenhoff, E. S., Bray, A., Zhu, Q., et al. (2021). Global Multi-Model Projections of Local Urban Climates. *Nat. Clim. Change* 11, 152–157. doi:10.1038/s41558-020-00958-8

Conflict of Interest: The authors declare that the research was conducted in the absence of any commercial or financial relationships that could be construed as a potential conflict of interest.

frontiers in Environmental Science

BRIEF RESEARCH REPORT
published: 18 February 2022
doi: 10.3389/fenvs.2022.810342

Do Electric Vehicles Mitigate Urban Heat? The Case of a Tropical City

Gianluca Mussetti[1]*, *Edouard L. Davin*[1,2], *Jonas Schwaab*[1], *Juan A. Acero*[3], *Jordan Ivanchev*[4], *Vivek Kumar Singh*[3], *Luxi Jin*[5] and *Sonia I. Seneviratne*[1]

[1]Institute for Atmospheric and Climate Science, ETH Zurich, Zurich, Switzerland, [2]Wyss Academy for Nature, Climate and Environmental Physics, Oeschger Centre for Climate Change Research, University of Bern, Bern, Switzerland, [3]CENSAM, Singapore-MIT Alliance for Research and Technology (SMART), Singapore, Singapore, [4]TUMCREATES, Singapore, Singapore, [5]Geography Department, Humboldt University of Berlin, Berlin, Germany

On top of their well known positive impact on air quality and CO_2 emissions, electric vehicles generate less exhaust heat compared to traditional vehicles thanks to their high engine efficiency. As such, electric vehicles have the potential to mitigate the excessive heat in urban areas—a problem which has been exacerbated due to urbanisation and climate change. Still, the heat mitigation potential of electric vehicles has not been fully understood. Here, we combine high-resolution traffic heat emission inventories with an urban climate model to simulate the impact of the fleet electrification to the near-surface air temperature in the tropical city of Singapore. We show that a full replacement of traditional internal combustion engine vehicles with electric vehicles reduces the near-surface air temperature by up to 0.6°C. The heat mitigation potential is highest during the morning traffic peak and over areas with the largest traffic density. Interestingly, the reduction in exhaust heat emissions due to the fleet electrification during the evening traffic peak hardly leads to a reduction of near-surface air-temperatures, which is attributed to the different atmospheric conditions during morning and evening. This study presents a new quantification of the city-wide impact of electric vehicles on the air temperature in a tropical urban area. The results may support policy-makers toward designing holistic solutions to address the challenge of climate change adaptation and mitigation in cities.

Keywords: urban climate, electric vehicles, heat mitigation, urban heat island, Singapore

OPEN ACCESS

Edited by:
Chenghao Wang,
Stanford University, United States

Reviewed by:
Isabella Capel-Timms,
University College London, United Kingdom
Paul Osmond,
University of New South Wales, Australia

***Correspondence:**
Gianluca Mussetti
mussetti.gianluca@gmail.com

Specialty section:
This article was submitted to Interdisciplinary Climate Studies, a section of the journal Frontiers in Environmental Science

Received: *06 November 2021*
Accepted: *17 January 2022*
Published: *18 February 2022*

Citation:
Mussetti G, Davin EL, Schwaab J, Acero JA, Ivanchev J, Singh VK, Jin L and Seneviratne SI (2022) Do Electric Vehicles Mitigate Urban Heat? The Case of a Tropical City. Front. Environ. Sci. 10:810342. doi: 10.3389/fenvs.2022.810342

1 INTRODUCTION

The combined effect of climate change and the urban heat island challenges the living conditions in cites, with consequences on human health, the economy and ecosystems (Revi et al., 2014). Cities are asked to take an active role in mitigating their contribution to global warming and associated climate change by reducing their CO_2 emissions (Hsu et al., 2020). At the same time, they need to implement local measures to adapt to warmer conditions (hereinafter heat mitigation), which are inevitable even with the most optimistic CO_2 emission pathways (IPCC, 2014).

Heat mitigation in cities involves interventions in one of the following aspects, which are the main drivers of the urban heat island: urban materials, urban form, vegetation and anthropogenic heat (Oke et al., 2017). Anthropogenic heat emissions are produced by building heating, ventilation and cooling (HVAC), vehicular traffic and human metabolism (Sailor, 2011; Sun et al., 2018). Several studies have been performed on the impact of measures on HVAC on the air temperature in urban areas (Salamanca et al., 2014; Takane et al., 2019; Jin et al., 2020). By contrast, the urban climate impact of measures on vehicular traffic is yet mostly unexplored (Zhu et al., 2017).

The vehicular market is experiencing a radical change, with a growing number of electric vehicles (EVs). The quickly increasing share of EVs can be attributed to technological advances and supportive policies that include financial incentives to buy them (IEA, 2020). Such policies are motivated by the long-recognised environmental benefits of EVs (Hardman et al., 2017) which include their positive impact on air quality (Liang et al., 2019) and CO_2 emissions (Wolfram and Lutsey, 2016). Importantly, EVs are also expected to reduce the amount of exhaust heat released in the urban environment. The reduced exhaust heat in EVs compared to internal combustion engine (ICE) vehicles is due to the higher energy efficiency of EVs, i.e., the amount of energy which is transferred to the drive system. The energy efficiency of EVs is about 80–90%, while those of ICE vehicles is of about 13–20% (Muneer and García, 2017). Accordingly, a substantial fleet electrification (i.e., increasing share of EVs) is expected to reduce the amount of exhaust heat released by vehicles into the atmosphere. However, it is still unclear to what extent a reduced amount of exhaust heat from vehicles would translate into spatio-temporal changes in near-surface air temperature. Such knowledge is essential when assessing how an increased share of EVs could reduce the urban heat and its adverse impacts.

A first estimation of the heat mitigation potential of EVs has been derived by simply scaling the literature data on the contribution of traffic to the urban heat island intensity (Li et al., 2015). Using this approach, that study found that a full conversion to EVs could reduce the average urban heat island intensity by approx. 1°C (Li et al., 2015). Although the approach is interesting, the main problem with this estimation is that surface and canopy-layer urban heat island intensity data have been mixed. Given that the surface temperature shows much larger variability than the canopy-layer air temperature (Oke et al., 2017), these results are likely overestimated. Moreover, the authors did not investigate on spatial and temporal patterns of the impact.

Currently, the Cooling Singapore project (Cooling Singapore, 2021) is performing an in-depth investigation on the urban climate impact of vehicular traffic in the city-state of Singapore. A preliminary modelling study shows that vehicular traffic has a small but considerable warming effect in the urban area of Singapore (Singh et al., 2022). Employing the Weather Research and Forecasting (WRF) model (Skamarock et al., 2005; Chen et al., 2011), previous studies found that traffic contributes up to 1.1°C to near-surface air temperature and a full transition to EVs could produce a reduction up to 0.9°C. Further studies are needed to corroborate the results and to understand the mechanisms which drive the spatial and temporal variability of these effects.

In order to bridge this knowledge gap, this study investigates the impact of vehicular traffic on near-surface temperature using high-resolution urban climate modelling and high-resolution data on heat emissions from vehicular traffic. The heat mitigation induced by a full fleet electrification is quantified and compared to that of replacing individual air conditioning (AC) units with centralised AC units—another technological measures to reduce anthropogenic heat emissions in cities. The study focuses on the city-state island of Singapore. Located one degree north of the equator, the city-state island of Singapore experiences a tropical wet climate with abundant rainfall, high and uniform temperatures, and high humidity all year round. Singapore has the largest population density in the world and an abundant share of its territory (45%) is built-up (Yee et al., 2011; Gaw et al., 2019). It comes as no surprise that the anthropogenic heat is one of the largest contributor in the surface energy balance in Singapore. While buildings are responsible for the largest share (49–83%) of the total anthropogenic heat emission, exhaust heat from traffic makes up to one third in residential areas (Quah and Roth, 2012).

2 MATERIALS AND METHODS

2.1 Model Set-Up

The simulations are performed using the regional climate model COSMO-CLM (Rockel et al., 2008), coupled with a multi-layer urban canopy model (Schubert et al., 2012). The model also includes a building energy model (Jin et al., 2021), which computes the anthropogenic heat generation due to indoor space cooling. A summary of the model setup is provided in the **Supplementary Table S1**. The simulations were performed for the period 01–30 April 2016 and the first 5 days were discarded as spin-up time. The model is applied using three nested domains with horizontal resolution of 0.1° (~10 km), 0.02° (~2 km) and 0.004° (~400 m) (**Supplementary Figure S1**). Initial and boundary conditions are provided by the ERA5 reanalysis (Copernicus Climate Change Service, 2017), and used to drive the coarsest model domain. Land use information for the year 2016 are derived from ESA CCI land cover (ESA, 2017). The information regarding the urban area is derived using a combination of high-resolution datasets and parameters that were derived from literature. Specifically, the urban canopy parameters were generated using a 3D city model including all buildings in Singapore (courtesy of A*STAR, Singapore) and a high-resolution urban land cover map (Gaw et al., 2019). The datasets were transformed into model-ready urban canopy parameters using the python tool UCPgenerator (Mussetti, 2019; Mussetti et al., 2020). An overview of the most important urban canopy parameters is given in **Supplementary Figure S2**. Thermo-physical properties of urban materials follow the values proposed by previous studies (Demuzere et al., 2017), which are representative of a low-rise residential area in Singapore (**Supplementary Table S2**). It should be noted that this is a simplification, since material properties can vary between districts with different building functions and types.

The building energy model used a target indoor temperature of 25°C and a constant operation throughout the day. As a default, it was assumed that the exhaust heat due to indoor space cooling is released at the height of the corresponding floor (Jin et al., 2020). This model option corresponds to the case of individual (split) AC units for each floor. Further information on the AC set-up is given in **Supplementary Table S3**. An additional simulation has been performed (AC scenario) were it is assumed that 25% of the indoor space cooling uses centralised units with exhaust heat

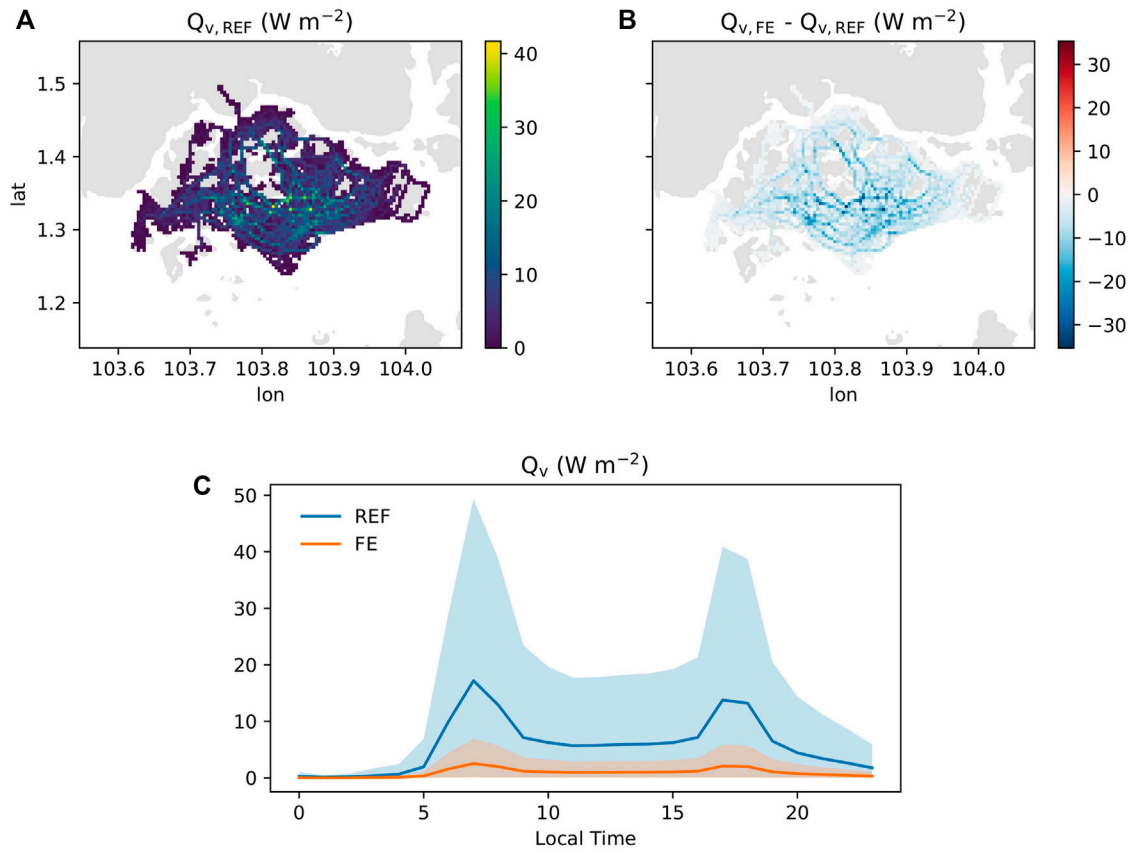

FIGURE 1 | Sensible heat emissions from vehicles (Q_v). **(A)** shows the spatial distribution of the daily-averaged Q_v in the scenarios REF (current vehicles composition); **(B)** shows the difference between FE (full fleet electrification) and REF; **(C)** shows the diurnal evolution of Q_v in the two scenarios, where solid lines and shaded areas show the mean value and the variability between 5th and 95th percentiles, respectively. The grey area in **(A)** and **(B)** represents land surfaces.

at roof level instead of default split units. The AC scenario is used in the study to represent an additional measure to reduce the (near-surface) exhaust heat emissions.

2.2 Traffic Heat Emissions

The sensible heat flux produced by vehicles (Q_v) is computed using the agent-based traffic simulator CityMoS (TUM CREATE, 2020). CityMoS has been calibrated with trip duration data and validated against speed-band information (Ivanchev and Fonseca, 2020). The travel demand for a typical day is extracted from travel surveys and scaled up for the whole vehicle population using person expansion factors. The demand is used to perform traffic assignment which computes routes for all commuter trips. Based on those routes, congestion levels on every road are estimated and used together with road and vehicle parameters to determine the amount of fuel used by every vehicle on every road segment for different parts of the day (Ivanchev et al., 2020). Agent-based traffic simulations have the advantage to estimate congestion levels, which are hardly captured by traffic counts (Ivanchev et al., 2020). Congestion levels can significantly influence the fuel consumption and thus the amount of heat produced. The amount of heat produced is assumed to be equal to the amount of fuel used and is aggregated for each grid cell (approx. 400 m × 400 m) on an hourly basis. Further information regarding the assumptions on fuel consumption and how it varies with type of vehicle, type of engine and speed are provided in Ivanchev et al. (2020). In summary, CityMoS generates spatial and diurnal temporal distribution of Q_v for a typical day (**Figure 1**). However, it should be noted that variations in traffic density between days in the week and between weekdays and weekend-days are not accounted for.

2.3 Implementation of Traffic Emissions Into Model

Sensible heat flux emission from traffic (Q_v) is released at the lowest model level and generates an increment to the air temperature according to **Eq. 1**:

$$\left(\frac{\delta T}{\delta t}\right)_v = \frac{Q_v}{\rho c_p dz V_c} f_{urb} + \frac{Q_v}{\rho c_p dz} f_{nat}, \quad (1)$$

where $(\frac{\delta T}{\delta t})_v$ is the increment of the air temperature due to traffic emissions (K s^{-1}), Q_v is the sensible heat flux from traffic (W m^{-2}), ρ is the density of the air (kg m^{-3}), c_p is the specific heat capacity of air (kJ kg^{-1} K^{-1}), dz is the height of the first model

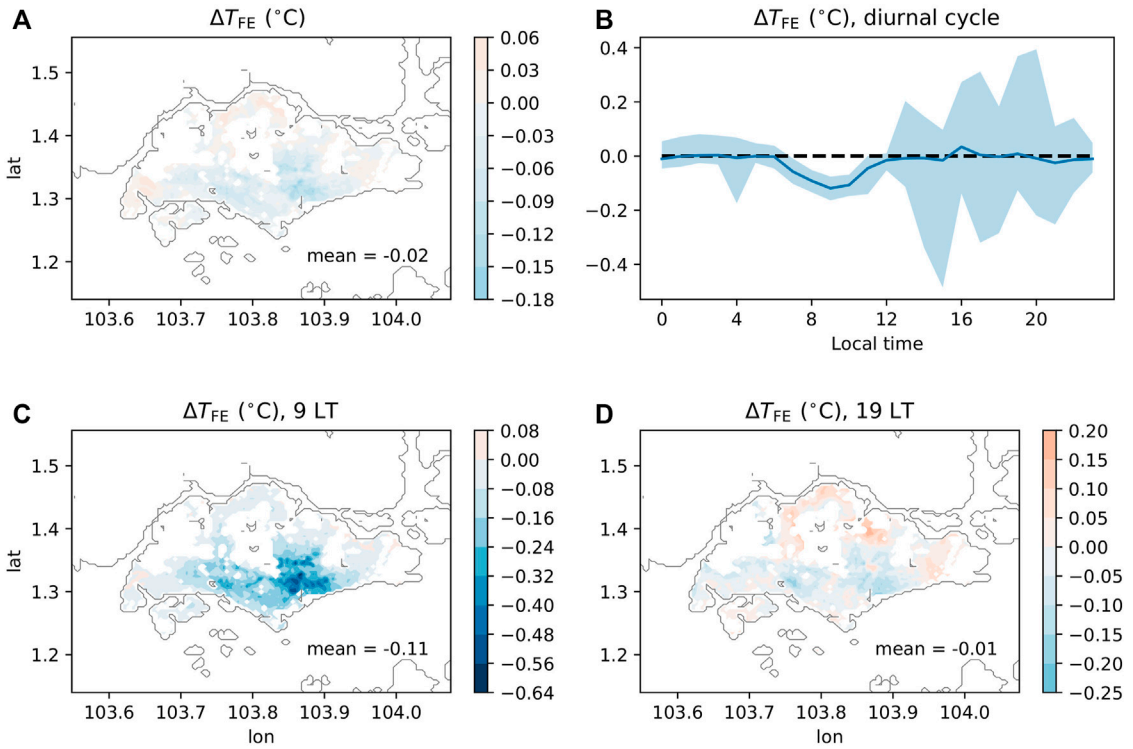

FIGURE 2 | Full electrification of the fleet (FE) mitigates heat, mostly after the morning traffic peak in the central urban area. **(A)** shows the period-average near-surface air temperature difference (ΔT_{FE}, °C) between FE and REF, **(B)** shows the period-average diurnal cycle of ΔT_{FE}, **(C)** shows the period-average T_{FE} at 9 local time (LT) and **(D)** shows the period-average ΔT_{FE} at 19 LT. Only values over the urban area (defined as $f_{urb} > 0.1$) are shown.

level (m), f_{urb} is the urban fraction (-), V_c is a volume correction factor to consider the presence of buildings (-) and f_{nat} is the natural fraction (-), defined as $f_{nat} = 1 - f_{urb}$. **Eq. 1** is added as source term in the equation of energy conservation. Q_v is split between the urban and rural part of the grid cell, which is important since the volume of air in urban grid cells is reduced due to the presence of buildings.

2.4 Model Evaluation

The model results are evaluated against observations of near-surface (2 m) air temperature (T) and 10-m wind speed (u). The evaluation is designed to support a specific model application, which quantifies the impact of heat emissions from traffic on air temperature. As such, this study does not aim to perform a comprehensive model evaluation, which may require using a larger variety of observations and atmospheric variables.

Hourly observations of T and u are provided by the Meteorological Service of Singapore (MSS). From the available sites, only those placed at ground level are used for the evaluation. Observations at roof level have been discarded as recommended by the WMO (Jarraud, 2008). The location of the selected sites is shown in **Supplementary Figure S3**. The model performance is evaluated against the observations using the following metrics: root-mean-square error (RMSE), mean bias error (MBE) and coefficient of determination (r^2). When comparing model results with observations, it is important to keep in mind that the individual sites can be exposed to micro-climatic features. Thus, a specific site is not always representative of the model grid cell and caution is required when interpreting the results of the model evaluation.

The comparison between observed and modelled near-surface air temperature is shown in **Supplementary Figure S4**. The statistical scores are listed in **Supplementary Table S4**. The model is able to reproduce the day-to-day and diurnal variability of T in the majority of the sites. The difference in the diurnal profile of T between sites close to the coast (S102 and S108) and those slightly inland is well modelled. Quantitatively, the comparison indicates a very small MBE, which is found at most sites. Values of RMSE are moderately larger but still within the range of what has been reported in other urban climate modelling studies over Singapore (Mughal et al., 2019; Simón-Moral et al., 2020; Singh et al., 2022). The moderately large RMSE may be due to the strong weather variability associated with the tropical climate (e.g., cloud cover change and precipitation).

The comparison between observed and modelled near-surface wind speed is shown in **Supplementary Figure S5**. The statistical scores are listed in **Supplementary Table S4**. The model is able to reproduce very well both the day-to-day and diurnal variability of u. Importantly, the model simulates well the evolution of the land-sea breeze, which peaks in the afternoon. Quantitatively, the comparison indicates a very small mean bias error (average MBE = $-0.16 \pm 0.3\ m\ s^{-1}$). Strong wind speed events are not

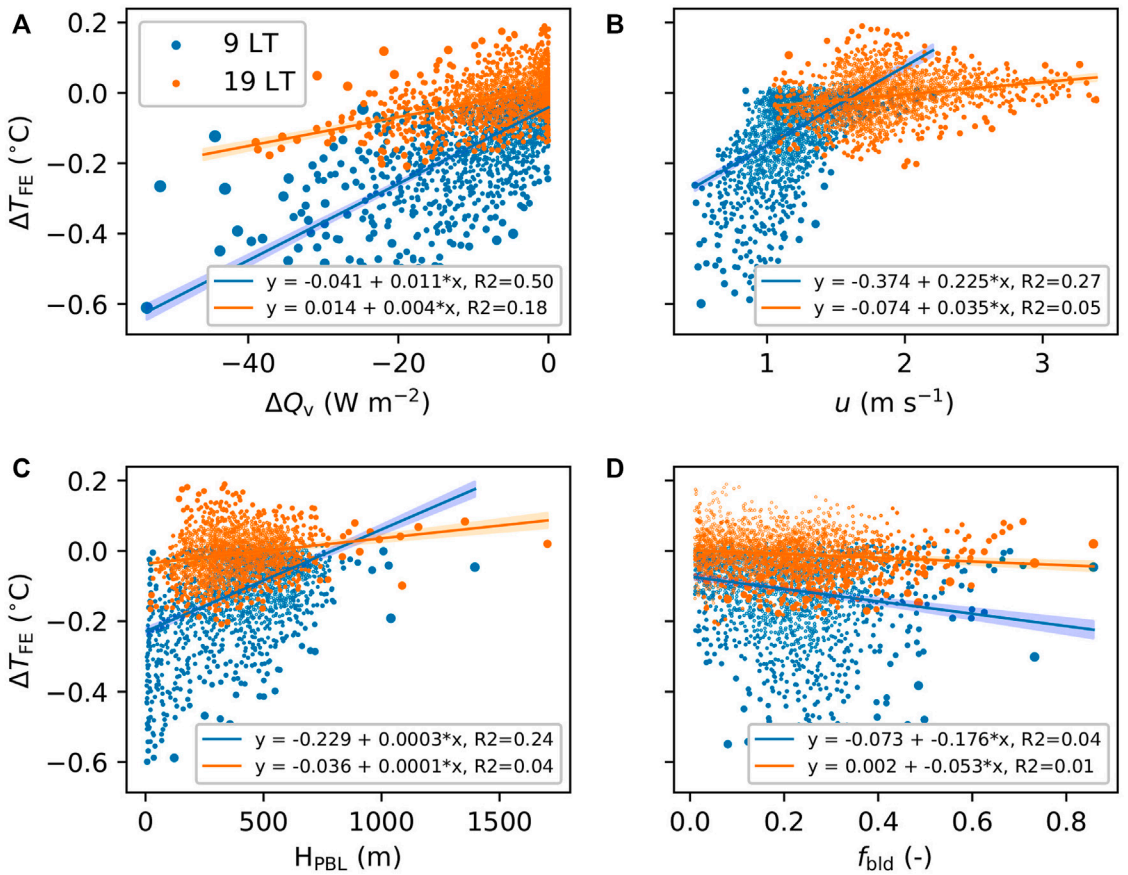

FIGURE 3 | The contrasting response between morning and evening traffic peak may be attributed to changes in atmospheric conditions. Scatter plots of the heat mitigation (ΔT_{FE}) of FE at 9 and 19 LT against the **(A)** reduction in traffic heat emissions (ΔQ_v), **(B)** near-surface wind speed (u), **(C)** boundary layer height (H_{PBL}) and **(D)** fraction of building surfaces (f_{bld}). The plot uses period-average hourly values. The solid lines and shaded areas represent the linear regression and the corresponding confidence intervals (95%), respectively.

always captured by the model, which results in a moderate RMSE (average RMSE = 1.19 ± 0.1 m s^{-1}). Still, the agreement with observations is generally better than what has been reported in other urban climate modelling studies (Mughal et al., 2019).

3 RESULTS

A full electrification of the fleet (FE) produces a reduction in near-surface air temperature compared to current fleet composition (REF) ($\Delta T_{FE} = T_{FE} - T_{REF}$, **Figure 2**). The daily-average ΔT_{FE} is moderate and concentrated over the area with the largest traffic and urban density (max ΔT_{FE} ~−0.2°C). The reduction in the sensible heat emission from traffic (Q_v, **Figure 1**) results in slight warming over areas with low traffic density. Secondary warming effects can be due to slight changes in thermally-driven circulation (e.g., sea-breeze) as well as changes in the local-scale urban heat advection (Bassett et al., 2016; Oke et al., 2017).

The impact of FE is strongly dependent on the time of day (**Figure 2B**). FE has a large impact mostly during and shortly after the morning traffic peak. At 9 LT, FE reduces the near-surface temperature by up to ~0.6°C (**Figure 2C**). Remarkably, FE has no significant impact during and shortly after the evening traffic peak (**Figure 2C**), even though the reduction in Q_v during that time is comparable to that of the morning traffic peak (**Figure 1**).

As shown in **Figures 2B,D** a relatively heterogeneous model response was found in the afternoon, which highlights the model sensitivity to changes in sensible heat flux at the surface. In order to isolate the impact of FE from the internal model variability, statistical significance tests have been applied to the results (**Supplementary Figure S6**). ΔT_{FE} is statistically-significant ($p \leq 0.05$) over the area with highest traffic density during the morning. It is important to remark that the slight afternoon warming over areas with low traffic density is not statistically significant.

It is interesting to explore the conditions that determine the different response to the traffic heat emissions at the morning and evening traffic peaks. The contrasting response between morning and evening traffic peak may be attributed to changes in the atmospheric conditions (**Figure 3**). The heat mitigation (ΔT_{FE})

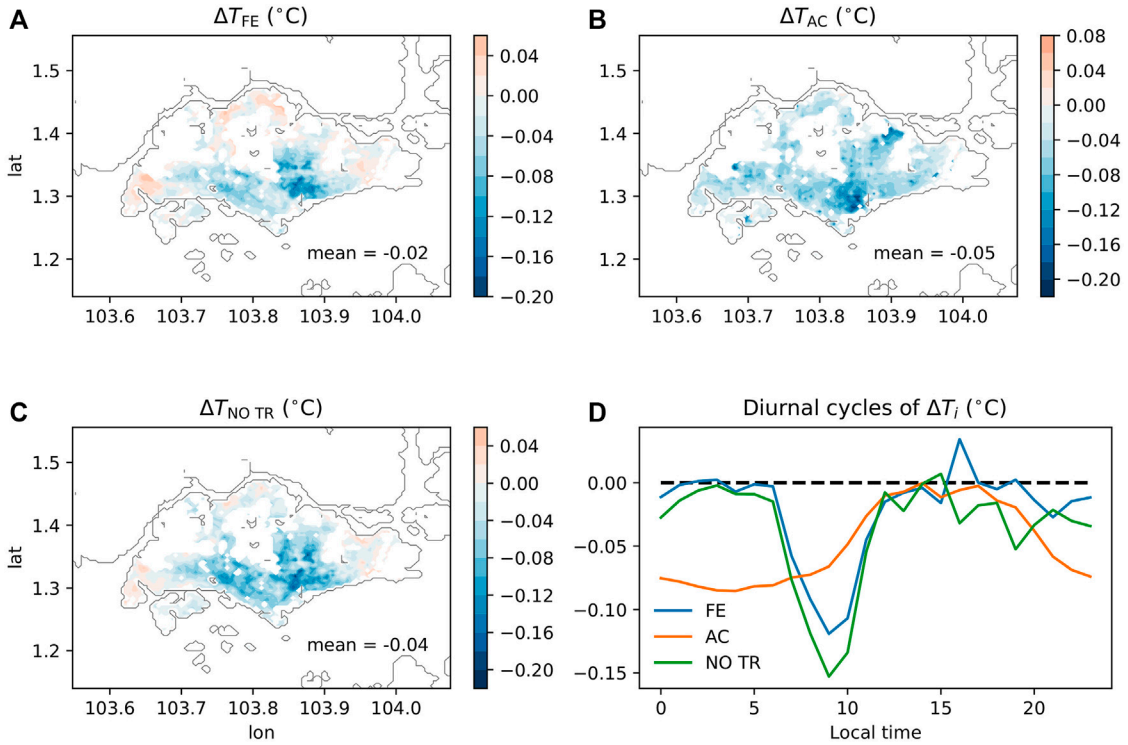

FIGURE 4 | The heat mitigation of FE is more localised than measures on AC, both temporally and spatially. **(A)** shows the period-average near-surface air temperature difference (ΔT_{FE}, °C) due to a full fleet electrification, **(B)** shows the period-average ΔT_{FE} due to an increase in 25% in centralised AC (AC), **(C)** shows the period-average ΔT_{FE} in the case of no traffic (NO TR) and **(D)** shows the period-average diurnal cycle of ΔT_{FE} for the different scenarios.

due to a reduction in traffic heat emissions (ΔQ_v) is threefold in the morning (9 LT) compared to the evening (19 LT). ΔT_{FE} was found to be correlated to the local wind speed (u) and the boundary layer height (H_{PBL}), while urban morphology (f_{bld}) appears to play a minor role. In other words, the reduction in traffic heat emissions has a stronger impact during low wind speed and shallow boundary layer conditions.

The effect of a full fleet electrification (FE) has been compared with that of converting 25% of individual air conditioning (split) units to centralised units with exhaust release at the roof level (AC scenario, **Figure 4**). The heat mitigation (ΔT_{FE}) from the AC scenario is much more uniform over the urban area than that of FE. Both FE and AC result in similar maximum impacts (~0.2°C as daily mean ΔT_{FE}), but the average impact of AC is 2.5 times larger. The most remarkable difference between FE and AC scenarios is their different temporal impact. While FE is only very effective during and shortly after the morning traffic peak, AC has a more homogeneous impact, with an almost constant heat mitigation during the night. The near-constant heat mitigation of AC during night-time may be partially due to the specific set-up with target temperature and constant schedule (see **Section 2.1** and **Supplementary Table S3**). Nevertheless, FE and AC are both unable to reduce the near-surface air temperature during the central hours of the day (12–16 LT).

4 DISCUSSION

4.1 Heat Mitigation Potential of Electric Vehicles

The results of this study indicate that the full fleet electrification (FE) produces a reduction in near-surface air temperature, which is moderate at the daily scale but substantial during the morning traffic peak (up to 0.6°C). In this work, the estimated heat mitigation potential of EVs is lower than what found by Li et al. (2015) but on the same order of what found by Singh et al. (2022). Beside differences in climatic and traffic conditions, we argue that the estimation provided by Li et al. (2015) may overestimate the heat mitigation potential of EVs due to oversimplification of the complex interactions between exhaust heat emissions and atmospheric dynamics.

Our study highlights that the fleet electrification, and in general other measures which reduce the anthropogenic sensible heat emissions (such as the use of centralised AC units), are inefficient in reducing the air temperature during mid-day. The mechanism behind this reduced impact during daytime can be attributed to the specific atmospheric and surface energy balance (SEB) conditions. On the one hand, the boundary layer height (H_{PBL}) determines the vertical column over which the (reduction in) sensible heat (Q) is distributed. Daytime is generally associated with large values of H_{PBL} (Stull, 2012), which

makes even substantial reductions in Q (e.g., anthropogenic heat reductions) mostly ineffective. Additionally, daytime SEB is dominated by the net incoming radiation, which reaches values that are up to 1 order of magnitude larger than those obtained by a FE [500 $W\,m^{-2}$ at noon, according to Roth et al. (2017)]. As such, reducing the air temperature during daytime remains challenging. Interventions on other drivers of the urban heat island are necessary to efficiently reduce the daytime air temperature in tropical climates. Of the possible solutions, increasing the fraction of urban vegetation and applying highly reflective roofs (cool roofs) were found to perform best on daytime heat (Li and Norford, 2016; Schwaab et al., 2021; Wong et al., 2021).

4.2 Limitations and Future Studies

We acknowledge that there are a number of limitations of the study. The impact of local radiative forcing from gaseous and aerosols emissions from vehicular traffic has not been considered here. Previous studies found either small negative (Massoli et al., 2009) and positive (Balkanski et al., 2010) values of radiative forcing due to vehicular traffic emissions. It is therefore still unclear what role traffic-related aerosols play in local thermal conditions.

The model simulations have been performed in the so-called turbulence grey zone, a spatial resolution where the assumptions of some of the physical parameterisation are no longer valid (Honnert et al., 2020). Nevertheless, the use of meso-scale numerical models in the grey-zone is a common practice and may still provide useful results.

Only traffic conditions related to a "typical day" have been used in this study. This assumption is arguably reasonable for calculating monthly averaged impact. However, the impact of variations in traffic density between weekday and weekend, and between different days in the week, was not estimated.

The heat mitigation potential of a full fleet electrification (FE) has been investigated here for a specific city (Singapore)—characterised by its own traffic intensity, (spatio-temporal) traffic pattern and background climate—during an individual month within the dry season. The values of heat mitigation potential of a FE found in this study are directly representative for cities with similar characteristics (e.g., cities in South-East Asia). Cities in different climates, even with similar traffic conditions, may experience slightly different heat mitigation potential from FE due to different atmospheric conditions (e.g., local circulation and boundary layer dynamics) (Stull, 2012). Therefore, further studies are required to consolidate the understanding of the heat mitigation potential of a FE in different traffic and background-climate conditions.

Finally, futures studies would be required to explore how the heat mitigation dynamics of reductions in exhaust heat from traffic (such as FE) correlates with population exposure and, ultimately, how that would contributes to reducing heat-related health risks. It is known that population dynamics have a substantial impact on residents' exposure to urban heat (Yang et al., 2019). Given that vehicular traffic peaks arguably correlate (both spatially and temporally) with commuting patterns, it is therefore possible that the heat mitigation potential of a FE is just delivered at the time and places where most needed.

DATA AVAILABILITY STATEMENT

The data produced with this study is stored in a publicly available repository (Mussetti, 2021). COSMO-CLM is freely available for scientific use to the members of the CLM community. The code of COSMO-DCEP-BEM (Jin et al., 2021) is made freely available to any user with a valid CLM community membership. Traffic heat emission data are available under request to Ivanchev et al. (2020).

AUTHOR CONTRIBUTIONS

GM conceived the work; JI, VS, and JA provided input data and observations; LJ provided the COSMO-DCEP-BEM model; GM conducted the experiments, GM and JS analysed the results. ED, JA, and SS supervised the work. GM wrote the manuscript with contribution from all authors.

FUNDING

The research was funded by the Singapore's National Research Foundation (NRF).

ACKNOWLEDGMENTS

The research was conducted under the Cooling Singapore project. Cooling Singapore is a collaborative project led by the Singapore-ETH Centre (SEC), with the Singapore-MIT Alliance for Research and Technology (SMART), TUMCREATE (established by the Technical University of Munich), the National University of Singapore (NUS), and the Agency for Science, Technology and Research (A*STAR). The authors would like to thank Hee Joo Poh from A*STAR for providing the 3-D city model of Singapore. Lea A. Ruefenacht is greatly acknowledged for managing the project. We thank Muhammad O. Mughal and Gerhard Schmitt for their feedback on the work. The Swiss National Supercomputing Centre (CSCS) is greatly acknowledged for providing computational resources. We thank the two reviewers for their valuable comments.

SUPPLEMENTARY MATERIAL

The Supplementary Material for this article can be found online at: https://www.frontiersin.org/articles/10.3389/fenvs.2022.810342/full#supplementary-material

REFERENCES

Balkanski, Y., Myhre, G., Gauss, M., Rädel, G., Highwood, E. J., and Shine, K. P. (2010). Direct Radiative Effect of Aerosols Emitted by Transport: from Road, Shipping and Aviation. *Atmos. Chem. Phys.* 10, 4477–4489. doi:10.5194/acp-10-4477-2010

Bassett, R., Cai, X., Chapman, L., Heaviside, C., Thornes, J. E., Muller, C. L., et al. (2016). Observations of Urban Heat Island Advection from a High-Density Monitoring Network. *Q.J.R. Meteorol. Soc.* 142, 2434–2441. doi:10.1002/qj.2836

Chen, F., Kusaka, H., Bornstein, R., Ching, J., Grimmond, C. S. B., Grossman-Clarke, S., et al. (2011). The Integrated Wrf/urban Modelling System: Development, Evaluation, and Applications to Urban Environmental Problems. *Int. J. Climatol.* 31, 273–288. doi:10.1002/joc.2158

Cooling Singapore (2021). *Cooling Singapore*.

Copernicus Climate Change Service (C3S) (2017). Era5: Fifth Generation of Ecmwf Atmospheric Reanalyses of the Global Climate. Available at: https://cds.climate.copernicus.eu/cdsapp#!/home (Accessed 08 13.2020

Demuzere, M., Harshan, S., Järvi, L., Roth, M., Grimmond, C. S. B., Masson, V., et al. (2017). Impact of Urban Canopy Models and External Parameters on the Modelled Urban Energy Balance in a Tropical City. *Q.J.R. Meteorol. Soc.* 143, 1581–1596. doi:10.1002/qj.3028

ESA (2017). "Land Cover CCI Product User Guide Version 2," in *Tech. rep., ESA*. Available at: https://maps.elie.ucl.ac.be/CCI/viewer/download/ESACCI-LC-Ph2-PUGv2_2.0.pdf.

Gaw, L. Y.-F., Yee, A. T. K., and Richards, D. R. (2019). A High-Resolution Map of Singapore's Terrestrial Ecosystems. *Data* 4, 116. doi:10.3390/data4030116

Hardman, S., Chandan, A., Tal, G., and Turrentine, T. (2017). The Effectiveness of Financial purchase Incentives for Battery Electric Vehicles - A Review of the Evidence. *Renew. Sustainable Energ. Rev.* 80, 1100–1111. doi:10.1016/j.rser.2017.05.255

Honnert, R., Efstathiou, G. A., Beare, R. J., Ito, J., Lock, A., Neggers, R., et al. (2020). The Atmospheric Boundary Layer and the "gray Zone" of Turbulence: A Critical Review. *J. Geophys. Res. Atmospheres* 125, e2019JD030317. doi:10.1029/2019jd030317

Hsu, A., Tan, J., Ng, Y. M., Toh, W., Vanda, R., and Goyal, N. (2020). Performance Determinants Show European Cities Are Delivering on Climate Mitigation. *Nat. Clim. Chang.* 10, 1015–1022. doi:10.1038/s41558-020-0879-9

IEA (2020). *Global EV Outlook 2020. Tech. Rep.*. Paris: IEA.

IPCC (2014). "Climate Change 2014: Impacts, Adaptation, and Vulnerability," in *Climate Change 2014: Impacts, Adaptation, and Vulnerability. Part A: Global and Sectoral Aspects. Contribution of Working Group II to the Fifth Assessment Report of the Intergovernmental Panel on Climate Change*. Editors C. B. Field, V. R. Barros, D. J. Dokken, K. J. Mach, M. D. Mastrandrea, T. E. Bilir, et al. (Cambridge, United Kingdom and New York, NY, USA: Cambridge University Press), 535–612.

Ivanchev, J., and Fonseca, J. A. (2020). Anthropogenic Heat Due to Road Transport: A Mesoscopic Assessment and Mitigation Potential of Electric Vehicles and Autonomous Vehicles in Singapore. *Tech. rep., ETH Zurich*. doi:10.3929/ethz-b-000401288

Ivanchev, J., Fonseca, J., and Knoll, A. (2020). "Electrification and Automation of Road Transport: Impact Analysis of Heat and Carbon Emissions for singapore," in Proceeding of the 2020 IEEE 23rd International Conference on Intelligent Transportation Systems (ITSC), Rhodes, Greece, 20-23 Sept. 2020 (IEEE), 1–8. doi:10.1109/ITSC45102.2020.9294274

Jarraud, M. (2008). *Guide to Meteorological Instruments and Methods of Observation (Wmo-no. 8)*. Geneva, Switzerland: World Meteorological Organisation. 29.

Jin, L., Schubert, S., Fenner, D., Meier, F., and Schneider, C. (2021). Integration of a Building Energy Model in an Urban Climate Model and its Application. *Boundary-layer Meteorol.* 178, 249–281. doi:10.1007/s10546-020-00569-y

Jin, L., Schubert, S., Hefny Salim, M., and Schneider, C. (2020). Impact of Air Conditioning Systems on the Outdoor thermal Environment during Summer in berlin, germany. *Ijerph* 17, 4645. doi:10.3390/ijerph17134645

Li, C., Cao, Y., Zhang, M., Wang, J., Liu, J., Shi, H., et al. (2015). Hidden Benefits of Electric Vehicles for Addressing Climate Change. *Sci. Rep.* 5, 1–4. doi:10.1038/srep09213

Li, X.-X., and Norford, L. K. (2016). Evaluation of Cool Roof and Vegetations in Mitigating Urban Heat Island in a Tropical City, singapore. *Urban Clim.* 16, 59–74. doi:10.1016/j.uclim.2015.12.002

Liang, X., Zhang, S., Wu, Y., Xing, J., He, X., Zhang, K. M., et al. (2019). Air Quality and Health Benefits from Fleet Electrification in china. *Nat. Sustain.* 2, 962–971. doi:10.1038/s41893-019-0398-8

Massoli, P., Bates, T. S., Quinn, P. K., Lack, D. A., Baynard, T., Lerner, B. M., et al. (2009). Aerosol Optical and Hygroscopic Properties during TexAQS-GoMACCS 2006 and Their Impact on Aerosol Direct Radiative Forcing. *J. Geophys. Res.* 114. doi:10.1029/2008JD011604

Mughal, M. O., Li, X. X., Yin, T., Martilli, A., Brousse, O., Dissegna, M. A., et al. (2019). High-Resolution, Multilayer Modeling of Singapore's Urban Climate Incorporating Local Climate Zones. *J. Geophys. Res. Atmos.* 124, 7764–7785. doi:10.1029/2018JD029796

Muneer, T., and García, I. I. (2017). "The Automobile," in *Electric Vehicles: Prospects and Challenges*. Editors T. Muneer, M. L. Kolhe, and A. Doyle (Elsevier), 1–91. doi:10.1016/B978-0-12-803021-9.00001-X

Mussetti, G., Brunner, D., Henne, S., Allegrini, J., Krayenhoff, E. S., Schubert, S., et al. (2020). COSMO-BEP-Tree v1.0: a Coupled Urban Climate Model with Explicit Representation of Street Trees. *Geosci. Model. Dev.* 13, 1685–1710. doi:10.5194/gmd-13-1685-2020

Mussetti, G. (2021). Data for "Do Electric Vehicles Mitigate Urban Heat? *The case a Trop. city*". doi:10.5281/zenodo.5788965

Mussetti, G. (2019). *UCPgenerator v1.1*. doi:10.5281/zenodo.3352214

Oke, T. R., Mills, G., Christen, A., and Voogt, J. A. (2017). *Urban Climates*. Cambridge University Press. doi:10.1017/9781139016476

Quah, A. K. L., and Roth, M. (2012). Diurnal and Weekly Variation of Anthropogenic Heat Emissions in a Tropical City, singapore. *Atmos. Environ.* 46, 92–103. doi:10.1016/j.atmosenv.2011.10.015

Revi, A., Satterthwaite, D. E., Aragón-Durand, F., Corfee-Morlot, J., Kiunsi, R. B., Pelling, M., et al. (2014). "Urban Areas," in *Climate Change 2014: Impacts, Adaptation, and Vulnerability. Part A : Global and Sectoral Aspects. Contribution of Working Group II to the Fifth Assessment Report of th e Intergovernmental Panel on Climate Change*. Editors C. B. Field, V. R. Barros, D. J. Dokken, K. J. Mach, M. D. Mastrandrea, T. E. Bilir, et al. (Cambridge, United Kingdom and Ne w York, NY, USA: Cambridge University Press), 535–612.

Rockel, B., Will, A., and Hense, A. (2008). The Regional Climate Model Cosmo-Clm (Cclm). *metz* 17, 347–348. doi:10.1127/0941-2948/2008/0309

Roth, M., Jansson, C., and Velasco, E. (2017). Multi-year Energy Balance and Carbon Dioxide Fluxes over a Residential Neighbourhood in a Tropical City. *Int. J. Climatol.* 37, 2679–2698. doi:10.1002/joc.4873

Sailor, D. J. (2011). A Review of Methods for Estimating Anthropogenic Heat and Moisture Emissions in the Urban Environment. *Int. J. Climatol.* 31, 189–199. doi:10.1002/joc.2106

Salamanca, F., Georgescu, M., Mahalov, A., Moustaoui, M., and Wang, M. (2014). Anthropogenic Heating of the Urban Environment Due to Air Conditioning. *J. Geophys. Res. Atmos.* 119, 5949–5965. doi:10.1002/2013jd021225

Schubert, S., Grossman-Clarke, S., and Martilli, A. (2012). A Double-canyon Radiation Scheme for Multi-Layer Urban Canopy Models. *Boundary-layer Meteorol.* 145, 439–468. doi:10.1007/s10546-012-9728-3

Schwaab, J., Meier, R., Mussetti, G., Seneviratne, S., Bürgi, C., and Davin, E. L. (2021). The Role of Urban Trees in Reducing Land Surface Temperatures in European Cities. *Nat. Commun.* 12, 1–11. doi:10.1038/s41467-021-26768-w

Simón-Moral, A., Dipankar, A., Roth, M., Sánchez, C., Velasco, E., and Huang, X. Y. (2020). Application of MORUSES Single-layer Urban Canopy Model in a Tropical City: Results from Singapore. *QJR Meteorol. Soc.* 146, 576–597. doi:10.1002/qj.3694

Singh, V. K., Mughal, M. O., Martilli, A., Acero, J. A., Ivanchev, J., and Norford, L. K. (2022). Numerical Analysis of the Impact of Anthropogenic Emissions on the Urban Environment of singapore. *Sci. Total Environ.* 806, 150534. doi:10.1016/j.scitotenv.2021.150534

Skamarock, W. C., Klemp, J. B., Dudhia, J., Gill, D. O., Barker, D. M., Wang, W., et al. (2005). *A Description of the Advanced Research WRF Version 2. Tech. Rep.* Boulder, CO: National Center For Atmospheric Research Boulder Co Mesoscale and Microscale.

Stull, R. B. (2012). *An Introduction to Boundary Layer Meteorology*, Vol. 13. Springer Science & Business Media. doi:10.1007/978-94-009-3027-8

Sun, R., Wang, Y., and Chen, L. (2018). A Distributed Model for Quantifying Temporal-Spatial Patterns of Anthropogenic Heat Based on Energy Consumption. *J. Clean. Prod.* 170, 601–609. doi:10.1016/j.jclepro.2017.09.153

Takane, Y., Kikegawa, Y., Hara, M., and Grimmond, C. S. B. (2019). Urban Warming and Future Air-Conditioning Use in an Asian Megacity: Importance of Positive Feedback. *Npj Clim. Atmos. Sci.* 2, 1–11. doi:10.1038/s41612-019-0096-2

TUM CREATE (2020). CityMoS. Available at: http://citymos.net.

Wolfram, P., and Lutsey, N. (2016). "Electric Vehicles: Literature Review of Technology Costs and Carbon Emissions," in *Tech. Rep.* (Washington, DC, USA: ICCT).

Wong, N. H., Tan, C. L., Kolokotsa, D. D., and Takebayashi, H. (2021). Greenery as a Mitigation and Adaptation Strategy to Urban Heat. *Nat. Rev. Earth Environ.* 2, 166–181. doi:10.1038/s43017-020-00129-5

Yang, J., Hu, L., and Wang, C. (2019). Population Dynamics Modify Urban Residents' Exposure to Extreme Temperatures across the United States. *Sci. Adv.* 5, eaay3452. doi:10.1126/sciadv.aay3452

Yee, A. T. K., Corlett, R. T., Liew, S., and Tan, H. T. (2011). The Vegetation of singapore—an Updated Map. *Gardens' Bull. Singapore* 63, 205–212.

Zhu, R., Wong, M. S., Guilbert, É., and Chan, P.-W. (2017). Understanding Heat Patterns Produced by Vehicular Flows in Urban Areas. *Sci. Rep.* 7, 1–14. doi:10.1038/s41598-017-15869-6

Conflict of Interest: The authors declare that the research was conducted in the absence of any commercial or financial relationships that could be construed as a potential conflict of interest.

frontiers in Environmental Science

ORIGINAL RESEARCH
published: 09 March 2022
doi: 10.3389/fenvs.2022.862310

Integrating Ecosystems and Socioeconomic Systems to Identify Ecological Security Pattern and Restoration Strategy in a Rapidly Urbanizing Landscape

Jieqi Tan[1], *Hui Li*[2] *and Wei Lin*[2]*

[1]The Bartlett Center for Advanced Spatial Analysis, University College London, London, United Kingdom, [2]College of Forestry and Landscape Architecture, South China Agricultural University, Guangzhou, China

The rapid process of urbanization has been accompanied by a disordered expansion of construction land, which has resulted in the degradation of ecosystem services. The identification of ecological security patterns (ESPs) is an important means to coordinating human-land relationships and carrying out ecological restoration strategies, which are of great significance to protecting ecological sustainability. However, previous studies have ignored the mutual impact of urbanization and ecological protection, which leads to the contradiction between them and useless of ESPs. This paper takes a rapidly urbanizing metropolitan area as an example. Ecological sources were identified based on the integration of ecosystem services and socioeconomic indicators by the Ordered Weighted Averaging (OWA) method, which considers the trade-off between ecosystems and socioeconomic systems. The Linkage Mapper tool was used to extract ecological corridors, and thus ecological barrier points and pinch points were identified to implement ecological restoration. ESPs included 158 ecological sources according to the results. In more detail, the ecological sources and corridors were mainly distributed in the area dominated by ecosystem indicators, whereas the central urban area contributed less ecological sources, which indicates that the trade-off between ecosystems and socioeconomic systems has a significant impact on the construction of ESPs. Specifically, 406 ecological corridors were classified into different resistance levels to extract 433.26 km^2 barrier points and 458.51 km^2 pinch points. The study also proposed primary and secondary ecological restoration strategies for medium-, high- and low-resistance corridors based on the optimization of ESPs, which could not only improve ecosystem quality, but also fulfil the demands of human well-being. The integration of ecosystems and socioeconomic systems improves the existing methods for identifying ecological sources and restoration priority areas, and provides a scientific basis for balancing the development of urbanization and ecological protection in metropolitan regions.

Keywords: ecological security pattern, ecosystem services, socioeconomic system, trade-off, OWA method, Guangzhou

OPEN ACCESS

Edited by:
Zhaowu Yu,
Fudan University, China

Reviewed by:
Yanxu Liu,
Beijing Normal University, China
Haiwei Yin,
Nanjing University, China

****Correspondence:***
Wei Lin
gis_xifan@163.com

Specialty section:
This article was submitted to Environmental Informatics and Remote Sensing, a section of the journal Frontiers in Environmental Science

Received: *25 January 2022*
Accepted: *18 February 2022*
Published: *09 March 2022*

Citation:
Tan J, Li H and Lin W (2022) Integrating Ecosystems and Socioeconomic Systems to Identify Ecological Security Pattern and Restoration Strategy in a Rapidly Urbanizing Landscape. Front. Environ. Sci. 10:862310. doi: 10.3389/fenvs.2022.862310

1 INTRODUCTION

Along with the continuous urbanization of recent decades, disorderly expansion of urban construction land and significant loss of ecological land have restricted the sustainability of urban development (Feist et al., 2017; Peng et al., 2018; Zhai and Huang, 2022). Within a coupled human and natural system, the quantity and quality of the ecosystem services are impacted by anthropogenic disturbances, which affects regional landscape patterns and ecological security (Peng et al., 2017b). As a result, how to ensure the structural stability and functional security of natural ecosystems for sustainable urban development is an urgent issue (Li et al., 2015; Cumming and Allen, 2017; Serra-Llobet and Hermida, 2017). The construction of ecological security patterns (ESPs) was proposed to develop a method for improving ecological security. The ESPs, an interconnected ecological network composed of different ecosystems, is an effective approach to support biological species, maintain natural ecological processes and promote ecosystem services, as well as to achieve regional ecological sustainability (Su et al., 2016; Peng et al., 2018; Fu et al., 2020).The concept of ESPs was derived from landscape ecological planning in the 1990s (Yu, 1996). Many scholars have studied ESPs on different scales from the perspective of landscape ecology and urban planning (Peng et al., 2017b; Peng et al., 2018).

Landscape elements of key significance for ensuring regional ecological processes and ecosystem services, such as ecological sources, ecological corridors and strategic points, are all focused on ESPs (Dong et al., 2021; Gao et al., 2021). Therefore, the basic research paradigm of "identification of ecological sources, construction of resistance surfaces, and extraction of ecological corridors" has been gradually formed (Zhang et al., 2017). The strategy for selecting ecological source areas is fundamental to the construction of an ESPs, which is mainly conducted through assessing the ecological sensitivity, ecological importance or connectivity (Su et al., 2016) (Zhang et al., 2017). The method of identification of ecological sources has changed from the direct selection of nature reserves to the evaluation of ecosystem services that affect regional ecological security (Peng et al., 2017a; Wu et al., 2018). The integration of multiple ecosystem services, such as water yield and biodiversity protection, has been applied to source identification (Peng et al., 2018; Fu et al., 2020).

Integrating various components of coupled human and natural systems is necessary to address complex interconnections and to identify effective solutions to sustainability challenges (Liu et al., 2015). However, ecosystem services and human activities are seldom considered jointly in the assessment of ESPs (Wang et al., 2019); most studies have not adequately considered the ability to fulfill people's demand for ecosystem services when identifying sources of ESPs, which still focus on ecological patches as the supplier of ecosystem services, ignoring the interaction between ecosystems and human socioeconomic systems (Zhang et al., 2017). These ecological patches with the ability to fulfill human demand (e.g., cultural ecosystem services) is essential to consider when evaluating their capacity to form part of the source area.

It is worth noting that previous studies that considered an integrated valuation approach weighting various overlapping types of ecosystem services, may have overlooked the relationships (trade-offs or synergies) between these services. This may have either induced space competition among multiple ecosystem services or undermined the causal interrelationship among multiple ecosystem services (Dai et al., 2017; Zhao et al., 2020; Pan and Li, 2021). There is thus an urgent need to study and balance the trade-offs among multiple ecosystem services in decision-making processes (Zhang et al., 2015). One of the multicriteria evaluation methods, the ordered weighted averaging (OWA) operator, was first developed in the context of fuzzy set theory (Yager, 1988). The use of the OWA method has proven to be an effective approach in decision-making processes, and proposed a set of scientific and flexible planning methods to balance multiple conflicting ecosystem services in ESPs construction processes (Zhao et al., 2020; Pan and Li, 2021). Moreover, increasing economic development has led to urbanization in previous undeveloped areas (Deng et al., 2021), and caused many ecological and environmental problems in the meanwhile. The increasing ecosystem services may lead to the control of the development of urbanization (Li et al., 2022). These are issues needed to be discussed, the mutual impact of urbanization and ecological protection has not been considered and the trade-off between ecosystems and the socioeconomic system is still unclear. To address this gap, socioeconomic indicators should be considered to integrate with ecosystem services in order to construct the ESPs. Therefore, the OWA method was introduced to resolve the contradiction between ecological protection and urbanization decisions in this study. The optimization of ESPs in most of the current studies focused on the improvement of the evaluation process (Peng et al., 2018; Wang et al., 2019). However, there was little research on optimization after the establishment of ESPs (Fu et al., 2020). ESPs can provide a practicable way for ecological restoration to spatially identify key landscape elements; existing studies have identified key restoration areas in ecological corridors, pinch points, break and barrier points (Wang et al., 2018; Fang et al., 2020), and put forward zoning ecological restoration solutions (Ying et al., 2019; Ni et al., 2020). In addition, the ecological restoration of a coupled ecosystem and socioeconomic system based on ESPs is still in its infancy.

In recent years, Guangzhou has grown rapidly and has spread in a disorderly manner (Fan et al., 2018), and the ecological land has been seriously damaged, which seriously affects the welfare of the residents (Zhang et al., 2020). Hence, the Municipality government of Guangzhou proposed a framework of ecological networks and corridors in the metropolitan area and municipal administrative area according to ecological civilization construction planning (2016–2020). There have been similar approaches to constructing an ecological network of Guangzhou and to improving environmental protection under rapid urbanization (Zhao et al., 2017; Yang et al., 2018). However, previous approaches focused solely on ecological elements, such as forest land, natural reserves and the habitats of crucial species, without using an ecosystem service importance evaluation. The

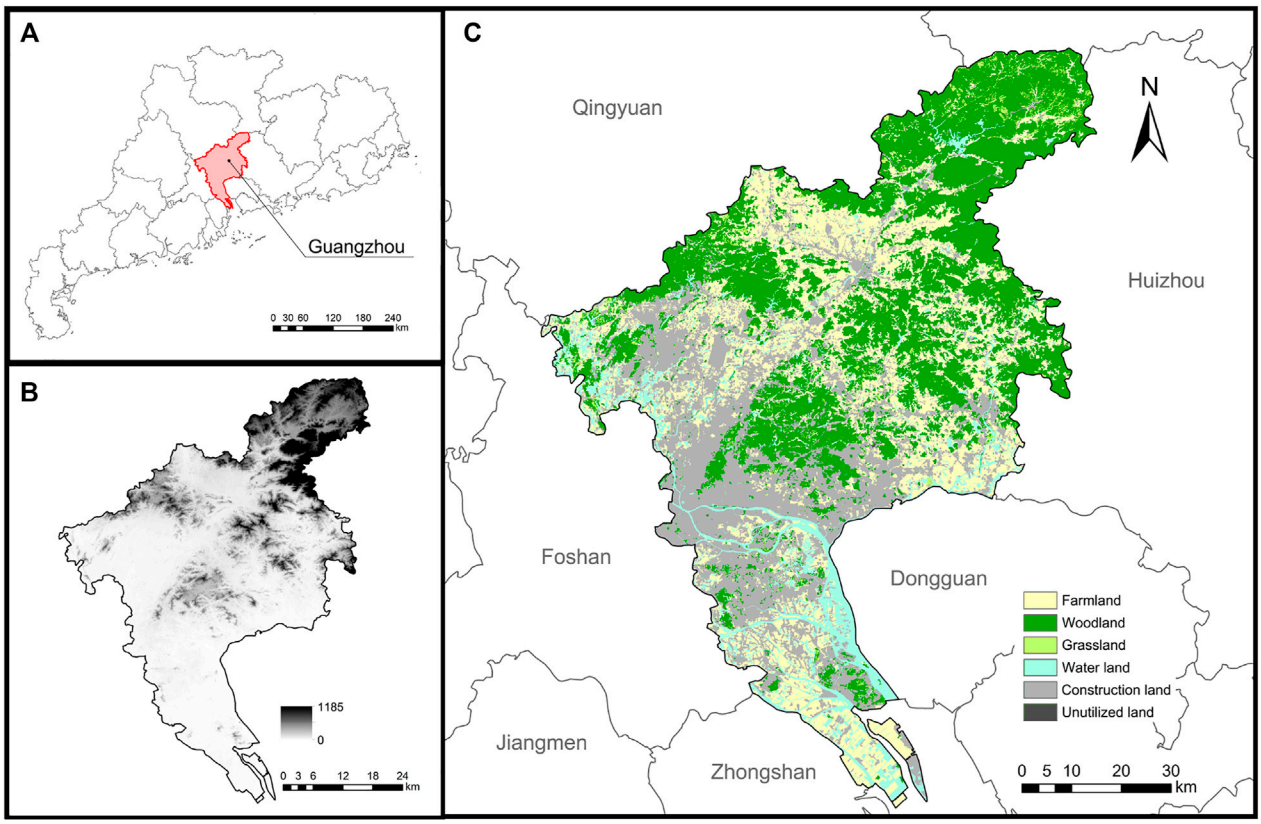

FIGURE 1 | (A)is the site of the study area, **(B)** is the elevation of the study area, **(C)** is land cover types of the study area.

studies mentioned above only assessed the landscape connectivity, failing to consider both the importance of ecosystem services and socioeconomic indicators, as well as restoration strategies. Therefore, it is urgent to move the process of ecological protection and restoration forward in order to identify key restoration regions for Guangzhou based on the optimization of the ESPs.

Based on the above considerations, the research objectives were to identify ecological sources by comprehensively evaluating the integration between ecosystem and socioeconomic indicators, to build ESPs based on the lowest cost path and identify the barrier point and pinch point for the corridors and to propose the optimization of the ecological restoration regions on the basis of ESPs.

2 MATERIALS AND METHODS

2.1 Study Area

Guangzhou is the central city in the Guangdong-Hong Kong-Macao Greater Bay Area, with a total area of 7434.4 km^2. There are eleven municipal districts in Guangzhou (**Figure 1**). Having a topographical structure of densely forested mountains, the northern area is the ecological supporting area of Guangzhou. The central area, with its topography of hilly and basins, is the location of the socioeconomic center. Besides, the southern area is also a potential area for the future development of construction land due to the plain topography. With the rapid socioeconomic development of Guangzhou in the past decade, the construction land has expanded rapidly and the population has grown about 500,000 people per year. Therefore, Guangzhou has become one of the cities where the conflict between urban development and the ecological environment is most prominent in the Greater Bay Area (Li et al., 2021).

2.2 Data

The basic data in this study mainly include: 1) the 2020 Globe Land 30M surface coverage dataset from Globe Land http://www.globallandcover.com/; 2) the 2020 GDEMV2 30M resolution digital elevation data from NASA https://search.earthdata.nasa.gov/search/; 3) Guangdong Province 30M resolution soil erodibility factor dataset from National Science and Technology Infrastructure Platform - National Earth System Science Data Center http://www.geodata.cn; 4) 2020 MODIS MOD13Q1 NDVI 16-days data from NASA https://modis.gsfc.nasa.gov/data/; 5) 2020 monthly values of basic elements of China's international exchange station for meteorological radiation and monthly values of China's ground climate data from the National Meteorological Science Data Center http://data.cma.cn/; 6) 2020 national urban road dataset from Gaode Map https://www.amap.com; 7) 2020 Guangzhou city POI data from Gaode Map https://www.amap.com; 8) NPP/VIIRS annual

TABLE 1 | Assessment methods.

Indicator	Method	Calculation
Carbon Fixation	To study the metabolic capacity of the ecosystem, the net primary productivity is used to characterize the Carbon fixation Yang et al. (2016). Carnegie Ames Stanford (CASA) model	NPP(i,t) = APAR(i,t) × $\xi(i, t)$; NPP(i,t) is the net primary productivity on-grid i in time period t; APAR(i,t) is the photosynthetically active radiation index on-grid i in time period t, and $\xi(i, t)$ is the light energy conversion rate on-grid i in time period t
Water Yield	The Water Balance Method Casagrande et al. (2021)	WY = P–ET–D; WY is the annual water yield; P is annual precipitation; ET indicates the annual evapotranspiration; D is the surface runoff, which is the product of surface runoff coefficient and precipitation Wang et al. (2020)
Soil Conservation	RUSLE Erosion Model Ye and Shi (2021)	A = R× K× LS× C× P; A is the erosion amount of soil; PA is the erosion amount of soil; R is the rainfall erosion factor; K is the soil erodibility factor; LS is the slope length slope factor; C is the vegetation cover and management factor, and P is the soil conservation measure factor. Among them, the rainfall erosion factor (R) is set as a constant due to the small difference of precipitation in the study area, and the P and C coefficients will refer to the research results of related literature
Habitat Quality	Habitat Quality module of the InVEST model Liu et al. (2021)	
Cultural Ecosystem Service	Recreation services, accessibility, and historical heritage services Yu et al. (2018); Marina et al. (2020) demonstrate the level of cultural resources in the study area, so the study identifies the potential for sustainable cultural development through this index	CS = 0.9L+0.1CH; L = 0.2LU+0.5P+0.15RD+0.15 PT; CS is the value of cultural services; L is the value of recreation and leisure; CH is the value of spiritual and cultural resources, calculated by estimation of historical and cultural facilities in the study area. LU is the type of land use coverage; P is the service of the parks in the study area, which is quantified with reference to the evaluation of Guangzhou city parks in "Guangzhou City Park Directory" "Guangzhou City Green Space System Plan (2020–2035)". RD is road density, and PT is public transport station distribution density, which is quantified by kernel density estimation to POI data of public transport stations Yang and Li (2021); Bing et al. (2021)
Landuse Development Degree		The ratio of construction land to the total land area in the study unit. This study quantifies the degree of land use development by the ratio of built-up land to total land area within a 100 m grid Peng et al. (2017a)
Population Density	Worldpop 100 m population density raster dataset	There are significant differences in population density and nighttime lighting index between different areas. Therefore, the study will take the logarithm of the two indicators PD and NL Gong et al. (2019)
Nighttime Lighting	NPP/VIIRS annual nighttime lighting index	

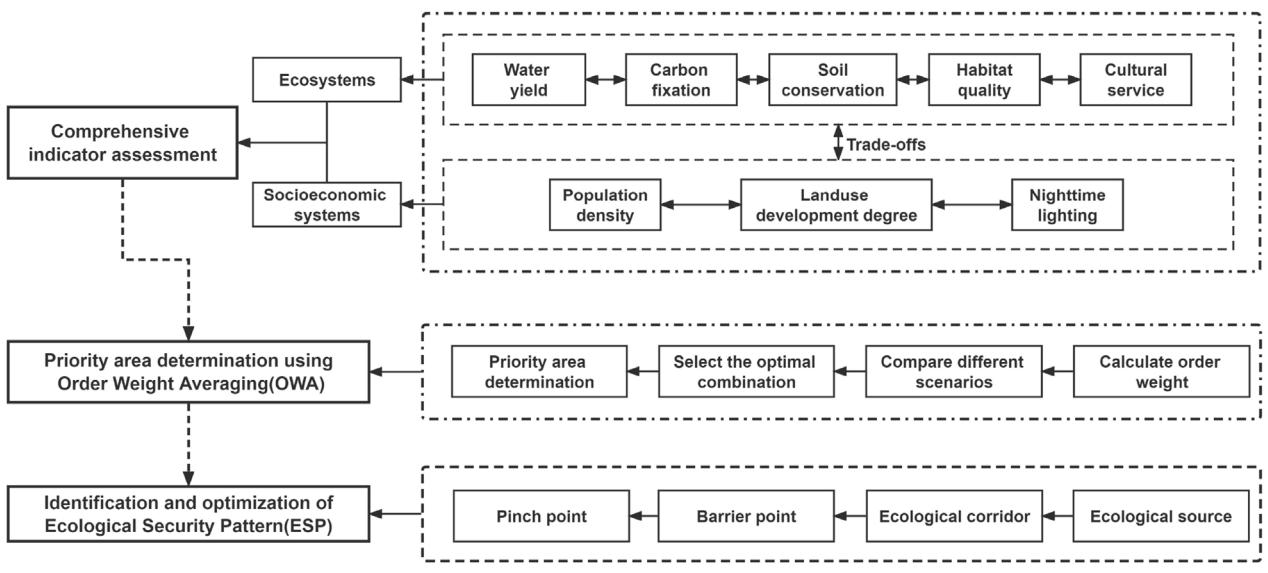

FIGURE 2 | The research framework.

nighttime lighting index sourced from National Oceanic and Atmospheric Administration https://ncc.nesdis.noaa.gov/VIIRS/; 9) 100 m population density raster dataset for 2020 sourced from worldpop https://www.worldpop.org/; (10) Guangzhou City Park Directory http://lyylj.gz.gov.cn/attachment/6/6806/6806818/7295517.pdf

3 METHODOLOGY

3.1 Indicator Assessment

As shown in **Table 1** and **Figure 2**, The assessment of the importance of ecosystem services is the basis for the construction of ESPs. In terms of the topography and land cover types of Guangzhou, the study area is facing some ecological problems of soil erosion, massive destruction of native vegetation, habitat fragmentation and the decline of water yield. Therefore, ecosystem services of Soil Conservation (SC), Habitat Quality (HQ) and Water Yield (WY) were selected as indicators and Carbon Fixation (CF) was also selected because it is a quantitative approach to the delineation of ecological redline for ecological protection in planning. In the meanwhile, due to the incomplete parks and recreation system and increasing demands of cultural ecosystem service in the study area, Cultural Service (CS) was also selected as ecosystem indicators. On the other hand, the degree of Land-use Development (LD), Population Density (PD) and Nighttime Data (NT) were selected to represent the socioeconomic system (Ding et al., 2019).

3.2 Correlation Analysis

According to the previous study, ecosystem and socioeconomic indicator trade-offs and synergies were based on linear data fitting, which can show the direction and intensity of interactions between each of the two indicators (Li et al., 2020). In this study, we first used Pearson correlation analysis to form a correlation matrix by using the GGally package in R, version 4.1.1 The values of eight types of indicators were randomly extracted from a total of 50,000 locations at the scale of the study area. The Pearson correlation coefficients between two indicators were calculated and tested for significance. When the correlation coefficient between two indicators is positive, there was synergy between them. When the correlation coefficient is negative, there were trade-offs between the indicators (Chen et al., 2021). The magnitude of its absolute value reflects the degree of trade-offs or synergy between the indicators. Complex trade-offs may exist among different indicators of the same factor, while specific trade-offs may exist between the ecosystem and socioeconomic system.

3.3 Multicriteria Evaluation

Multicriteria evaluation (MCE) can measure and evaluate regional suitability by weighing multiple relationships (Valente and Vettorazzi, 2008). The OWA method can weigh different decision objectives to determine the optimal decision by performing spatial operations on each evaluation metric. OWA method presents different decision sets by considering the trade-off relationships between different criteria (Chen et al., 2021). OWA method can weigh different decision objectives to determine the optimal decision by controlling each evaluation indicator for spatial operations and balance multiple conflicting indicators in the decision-making process. By considering the trade-offs between different criteria, different decision scenarios were simulated and different decision sets were presented. The formula is as follows (Zhao et al., 2020):

$$OWA\left(x_{ij}\right) = \sum_{i=1}^{n} w_i s_{ij}, \left(w_i \in [0,1], \sum_{i}^{n} w_i = 1, i \text{ and } j = 1,2,3,\ldots,n \right) \quad (1)$$

where x_{ij} is the standardized comprehensive evaluation index value; s_{ij} is the sequence value arranged in descending order by x_{ij} through the size of the attribute value; w_i is the order weight arranged in descending order by x_{ij} through the size of the attribute value; n is the number of indicators.

According to different decision risks, the bit-order weights generated and the trade-offs obtained based on the bit-order weights under various decision risks were calculated as follows:

$$w_i = Q_{RIM}\left(\frac{i}{n}\right) - Q_{RIM}\left(\frac{i-1}{n}\right), i = 1,2,3,\ldots,n \quad (2)$$

$$\mathrm{Q_{RIM}}\,(r) = r^{\alpha}, \alpha \in (0,\infty) \quad (3)$$

$$\text{trade-off} = 1 - \sqrt{\frac{n\sum_i^n \left(w_i - \frac{1}{n}\right)^2}{n-1}}, 0 \le \text{trade-off} \le 1 \quad (4)$$

In the formula, Q_{RIM} is the monotonical rule function; w_i is the number of the bit order; n is the number of indicators; α is the decision risk coefficient under different decisions.

In this study, seven decision scenarios (α of 0.001,0.1,0.5,1,2,10,1000)were presented, It shows that under the decision scenario of $\alpha < 1$, ecology space will be restricted protected or even reach the scenario of Complete Protection. On the other hand, changes in decision making from $\alpha = 1$ to $\alpha =$ 1,000 gradually shows the scenario of developing with the risk of ecological destruction (Li et al., 2022). In the process of OWA method, eight evaluation indicators were min-max normalized from 0 to 1 and ranked in descending order by the mean size of the normalized values to obtain the rank order weights of each indicator. The decision risk level was ordered into seven types, and a total of eight decision scenarios were dynamically generated for different decision levels. By multiplying the rank order weights of each indicator with the weighted weight values of the eight assessment indicators and their indicator values, comprehensive ecosystem and socioeconomic evaluation maps can be obtained under different scenarios. The top 20% of each scenario were identified as ecological priority areas based on the comprehensive evaluation map (Chen et al., 2021). By comparing the degree of trade-off in different scenarios, the scenario with the highest degree of trade-off was selected as the optimal scenario. In this scenario, ecological conservation and socioeconomic development will be in dynamic balance, and the city will be in a state of effective conservation while developing (Li et al., 2022).

3.4 Building the Ecological Security Pattern

3.4.1 Ecological Source

In this study, ecological sources were identified by combining ecosystem and socioeconomic system. Ecological priority areas of a certain size are essential for the material and energy connection of the ecological network (Cui et al., 2020). Referring to previous studies and the actual situation of Guangzhou (Long et al., 2018),

our study integrated and screened all $\geq 1km^2$ areas from ecological priority areas as ecological sources (Mao et al., 2020).

3.4.2 Ecological Corridor

Urban ecological corridors connect ecological sources in the urban system network (Mao et al., 2020). The resistance surface is the key to influencing material and energy flow between ecological sources. Therefore, the resistance surface value was determined based on the comprehensive evaluation value of the ecosystem and socioeconomic system. In particular, we normalized the integrated assessment value raster to calculate the resistance of the raster with the following equation (Peng et al., 2018).

$$R_i = 1000 \times (1 - A_i) \quad (5)$$

where R_i is the surface value of resistance in grid i; A_i is the comprehensive evaluation value in grid i.

In the next step, the least-cost path was calculated by the Linkage Mapper tool and set the maximum cost-weight distance as 20,000 (Xu et al., 2021a). Linkage Mapper filters the optimal corridors from the source to the neighboring source to map the optimal paths by simulating the minimum cost distance accumulated by ecosystem services (Song and Qin, 2016). This study identifies each ecological corridor's average resistance level by the ratio of the cost-weighted distance of each least-cost path to the Euclidean distance between sources. The corridor ratios were separated by the natural breakpoint method into extremely high resistance, high resistance, medium resistance, low resistance, and extremely low resistance (Su et al., 2021).

3.4.3 Barrier Point Analysis

Barrier points are high-resistance areas that prevent ecological corridors from connecting to the ecological source (Pan and Wang, 2021). In this study, the Barriers Mapper function in the Linkage Mapper tool was used to identify ecological barriers by setting 250, 500, 750 and 1000 m as the search radius. Five intervals were set based on the identification results by the natural breakpoint method, and the highest-value interval was selected as the barrier point (Wang et al., 2022).

3.4.4 Pinch Point Analysis

Ecological pinch point is a high-flow, key node in the ecological process, that should be protected as a priority. Pinch points play an important role in ecological connectivity, being in areas of high resistance and making a large contribution to connecting ecological corridors (Peng et al., 2018). Pinch points can be identified using the Pinch point Mapper function in the Linkage Mapper tool. In this study, the analysis results were divided by the natural breakpoint method. The category with the highest current values (which means the least average resistance distance) is extracted as the ecological pinch point (Zhu et al., 2020).

4 RESULTS

4.1 Indicator Assessment

The normalization result of each indicator value was shown in **Figure 3**. The high values of HQ and SC were located in the northern area and river around the southern area, and therefore would be rich in biodiversity and high soil retention. Besides, the high value of CF was concentrated in the northern area due to the high vegetation cover and woodland there. What's more, there was a relatively low WY capacity due to the effects of high urbanization in the central area. By contrast WY was generally at high value in the northern and southern areas because of abundant precipitation and the impact of rivers in the study area. However, compared with other ecosystem indicators, the high value areas of the CS are situated sporadically in the large forest parks and landscape areas from northern and central area in hilly. In addition, the indicators from the socioeconomic system including LD, PD and NL were highly similar. Their high value was concentrated in the highly urbanized areas in the central area and the southern area under rapid development (Ding et al., 2019).

4.2 Correlation Analysis

The study calculated the correlation coefficients among the comprehensive evaluation indicators (**Figure 4**).The correlation coefficients between ecosystem indicators generally showed a positive correlation. Most indicators' correlation indices were concentrated in the range of 0.1–0.5. The correlation between CF-WY (0.544) and CF-HQ (0.705) showed a significantly positive correlation, indicating synergies between these two relationships, while CS weakly correlated with WY and SC at 0.012 and 0.037, respectively. On the other hand, the data revealed significant positive correlations between the socioeconomic indicators.

Overall, all indicators show negative correlation between ecosystem and socioeconomic system, which indicates that there was an apparent trade-off relationship between them.

4.3 OWA Method for Different Scenarios

As shown from **Table 2**, with the increase in the decision risk coefficient, the rank order weight of high-level comprehensive evaluation indexes decreases continuously. In contrast, the rank order weight of low-level comprehensive evaluation indicators increases continuously.

Under different scenarios, the top 20% of the comprehensive evaluation value was selected as the ecological priority area. Consequently, the map of ecological priority areas under different scenarios was shown (**Figure 5**). From the seven different types of scenarios (**Table 3**), it can be seen that the decision result was optimistic at $\alpha = 0.001,0.1,0.5$. The high-value areas were mainly concentrated in the north and south of the study area, and most of the land types in the ecological priority protection areas were woodlands. Obviously, this type of scenario makes it difficult to develop construction land and maybe not easy to meet the growing population needs of megacities. Meanwhile, the criterion weights of all indicators in this study were 0.125 when $\alpha = 1$. The high-value areas were evenly distributed throughout the study area, and the ecological priority areas were mainly forest land at that time. Moreover, farmland, water area and construction area occupy part of the ecological priority area. The comprehensive evaluation weighting value was the

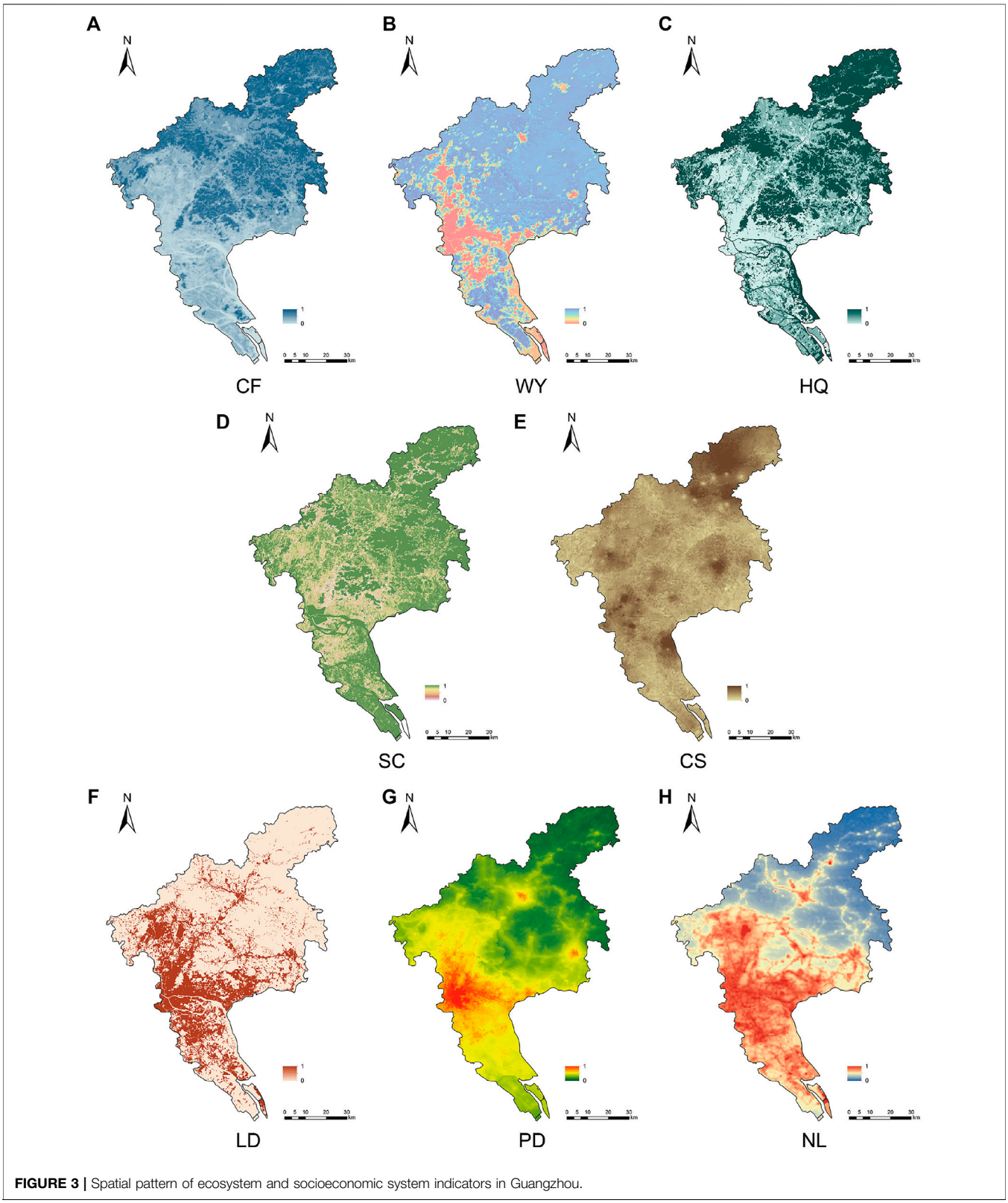

FIGURE 3 | Spatial pattern of ecosystem and socioeconomic system indicators in Guangzhou.

largest when $\alpha = 1$. However, when $\alpha = 2,10,1000$, the decision result was pessimistic. The high-value area was concentrated in the central area, and the ecological priority protection area was mainly dominated by construction land. The indicator of the socioeconomic system currently dominates the comprehensive evaluation indicator, and the area was at a high-risk level. As

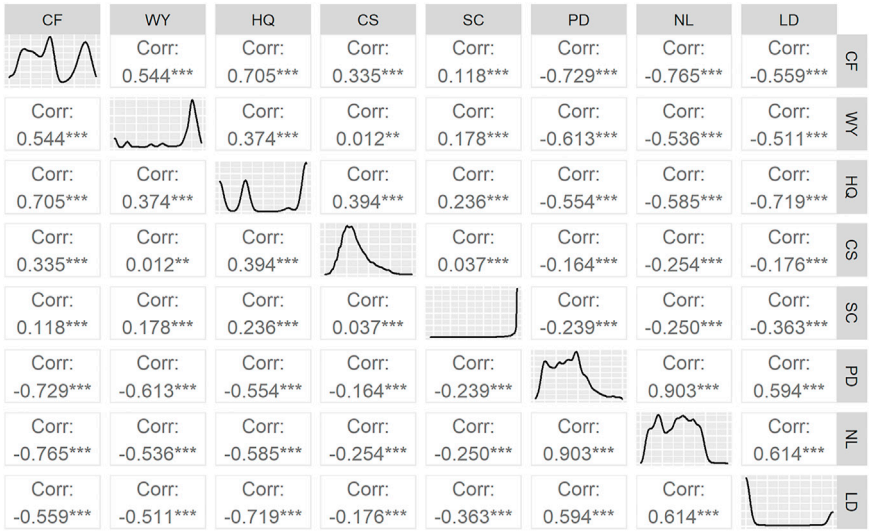

FIGURE 4 | Correlation matrix.

TABLE 2 | Bit order weight operators under different decision risk scenarios.

Scenario	1	2	3	4	5	6	7
α	0.0001	0.1	0.5	1	2	10	1,000
w_1	0.9998	0.8123	0.3536	0.1250	0.0156	0.0000	0.0000
w_2	0.0001	0.0583	0.1464	0.1250	0.0469	0.0000	0.0000
w_3	0.0000	0.0360	0.1124	0.1250	0.0781	0.0001	0.0000
w_4	0.0000	0.0265	0.0947	0.1250	0.1094	0.0009	0.0000
w_5	0.0000	0.0211	0.0835	0.1250	0.1406	0.0081	0.0000
w_6	0.0000	0.0176	0.0755	0.1250	0.1719	0.0472	0.0000
w_7	0.0000	0.0151	0.0694	0.1250	0.2031	0.2068	0.0000
w_8	0.0000	0.0133	0.0646	0.1250	0.2344	0.7369	1.0000
trade-off	0.0002	0.2134	0.7280	1.0000	0.7835	0.2723	0.0000

the ecological risk gradually increases, the ecological priority area changes from green space, woodland and grassland, to farmland and construction areas.

4.4 The Ecological Security Pattern of Guangzhou

4.4.1 Ecological Source

By simulating the decision risk of each scenario in the OWA method, the result (α = 1), with the highest trade-off was selected as the final scenario. Therefore, the comprehensive evaluation was shown in **Figure 6A** and resistance surface was shown in **Figure 6B** based on the final scenario. In this study, spots of more than 1 km^2 were selected as ecological sources of the study area.

According to **Figure 7**, the number of ecological sources was 158 and the total area of ecological sources was 1,085.34km^2, accounting for 15.03% of the total area of Guangzhou.

From the spatial layout, most ecological sources were distributed in the northern area, accounting for 84.91% of the total area of ecological sources.

The ecological sources in the central area account for 8.88% of the total area of ecological sources. This revealed the fragmentation of green space caused by the expansion of urban construction areas in the central area of Guangzhou, as there were relatively few ecological sources with eligible area and high comprehensive evaluation values.

Moreover, the area of ecological sources in the southern part accounts for 6.21% of the total area of ecological sources. The ecosystem values were much lower than those of the northern part of the study area, where woodland was the main land cover type. The socioeconomic system indicators were lower than those of the central area due to the lack of urbanization activities and population density, which results in a low overall evaluation value. Ecological sources were spatially scattered, and the area of individual sources was small.

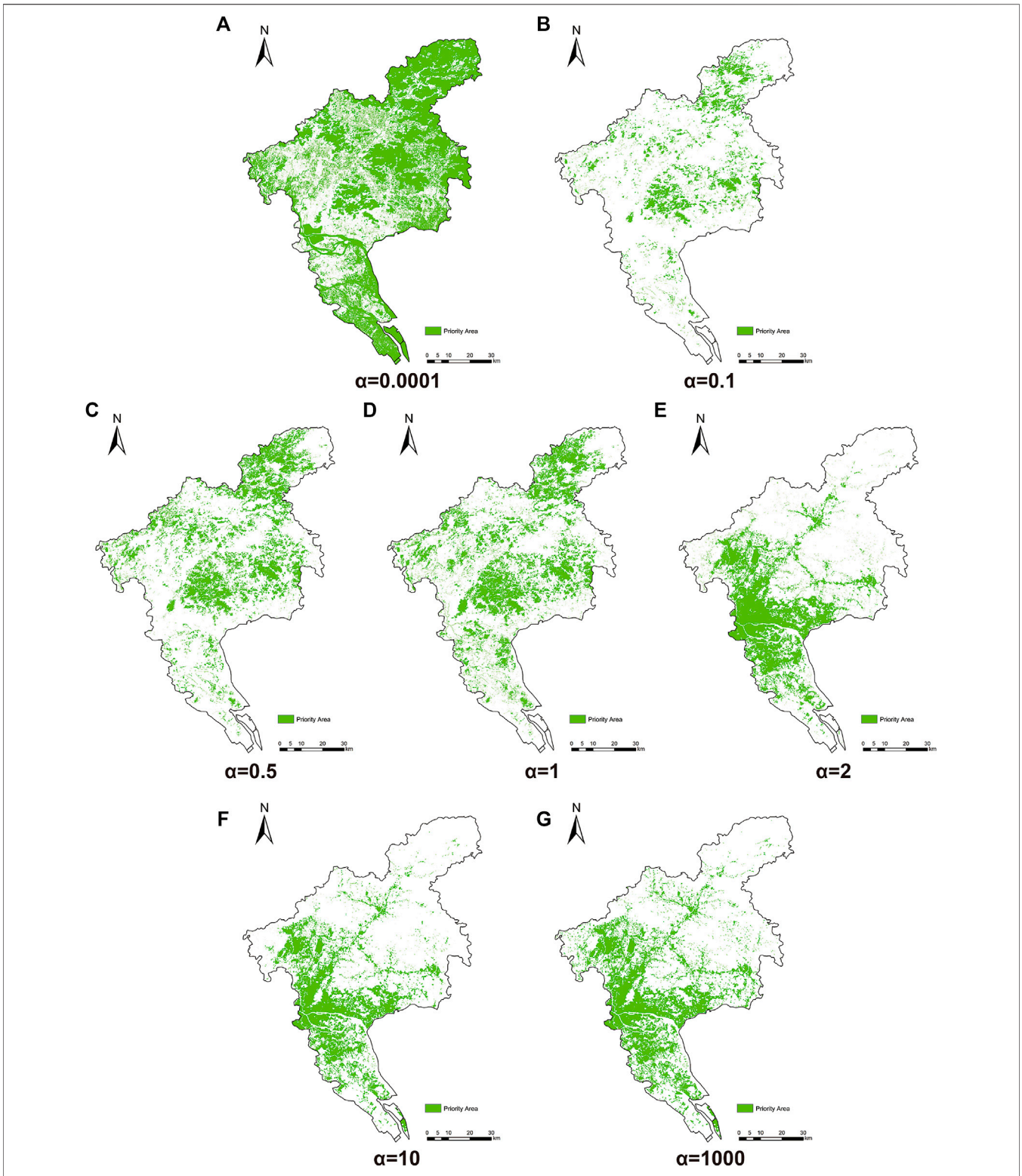

FIGURE 5 | Ecological priority area of different scenarios in Guangzhou.

Most of the ecological sources were woodland, accounting for 85.58% of the total area of ecological sources, with a small proportion of water land and construction land. Due to the trade-offs between ecosystem and socioeconomic system, the sources in the northern and southern area were mostly dominated by ecosystem indicators. Moreover, the

TABLE 3 | Changes in the proportion of land use in ecological priority areas under different scenarios.

α	Farmland (%)	Woodland (%)	Grassland (%)	Waterland (%)	Constructionland (%)
0.000 1	21.73	52.90	3.29	17.24	4.85
0.1	0.00	93.36	0.15	6.49	0.00
0.5	0.05	93.05	0.70	6.20	0.00
1	1.23	85.58	1.16	6.29	5.73
2	2.00	5.76	0.48	1.52	90.25
10	0.33	0.22	0.05	0.10	99.30
1,000	0.77	0.30	0.08	0.13	98.71

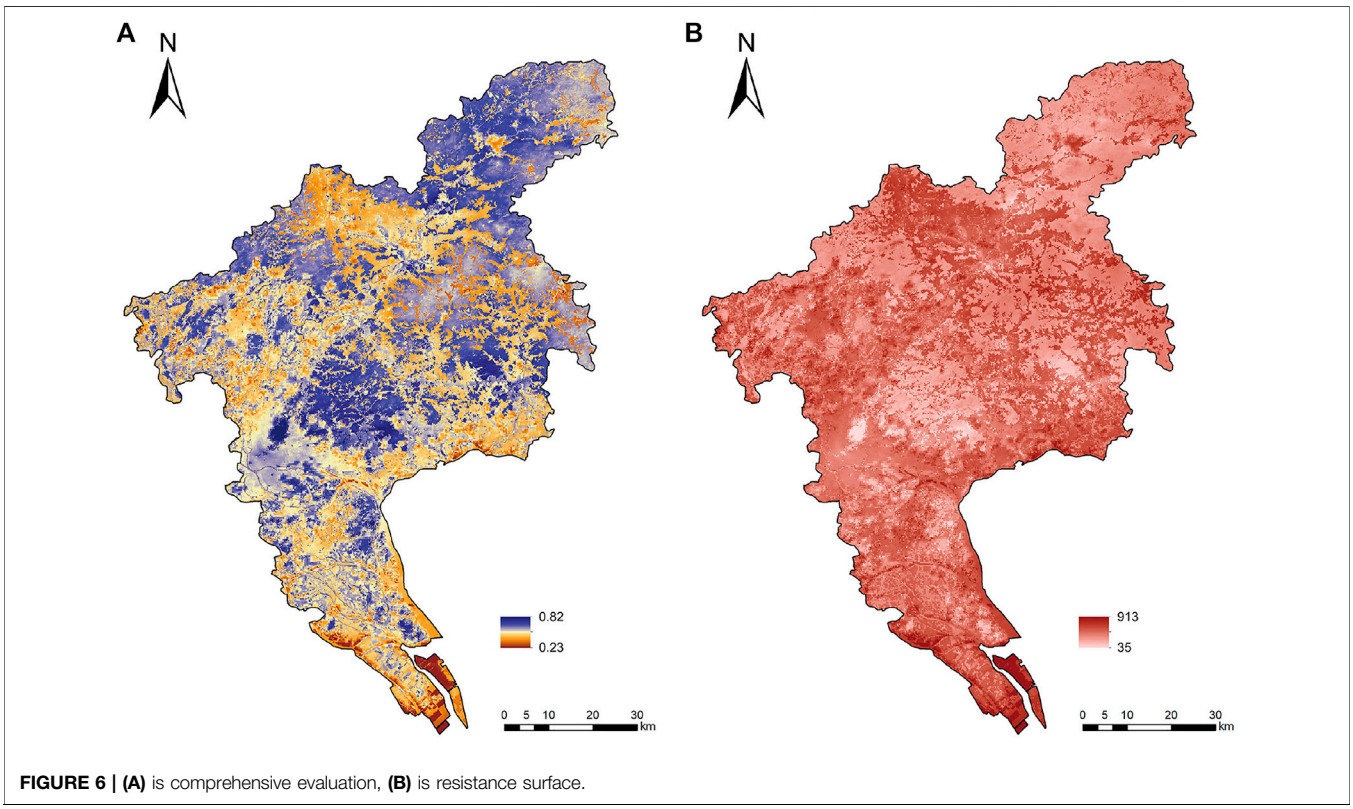

FIGURE 6 | (A) is comprehensive evaluation, **(B)** is resistance surface.

ecological sources in the central urban area were generally dominated by economic indicators.

4.4.2 Ecological Corridor

In total, 406 major ecological corridors with a total length of 1520 km and an average length of 3.3 km were identified in Guangzhou. As shown in **Figure 7**, the ecological corridor in Guangzhou was uniformly distributed, changing from dense in the northern area to sparse in the southern area.

The northern area in Guangzhou has the largest number of ecological corridors, with 334 in total. There was a short average corridor length due to the dense and continuous distribution of ecological sources. Some of the smaller ecological sources connect the northern area through dense, low-cost-distance corridors, occupying most of the area. Therefore, most of the northern corridor could maintain the connectedness of the whole area. There was the lowest number of ecological corridors in the central area, at 30. The spatial layout of corridors in this area was in a circular radial shape. The socioeconomic system index-driven ecological sources link the northern and southern parts, increasing ecological space connectedness in the central zone. However, the average cost distance of corridors in the region was much higher. There were 41 ecological corridors in the southern area. Due to the remote distance between ecological sources, the average distance of corridors was relatively long, and they have a higher cost distance. The southern area was in its initial development stage, and the socioeconomic conditions were far lower than the central area.

Overall, 30 extremely high-, 65 high-, 161 medium-, 147 low- and 2 extremely low-resistance corridors were identified. Extremely high- and high-resistance corridors were normally distributed in the north area, at extremely close distances among the ecological sources. However, the intervening patches of extremely low ecological value significantly reduce

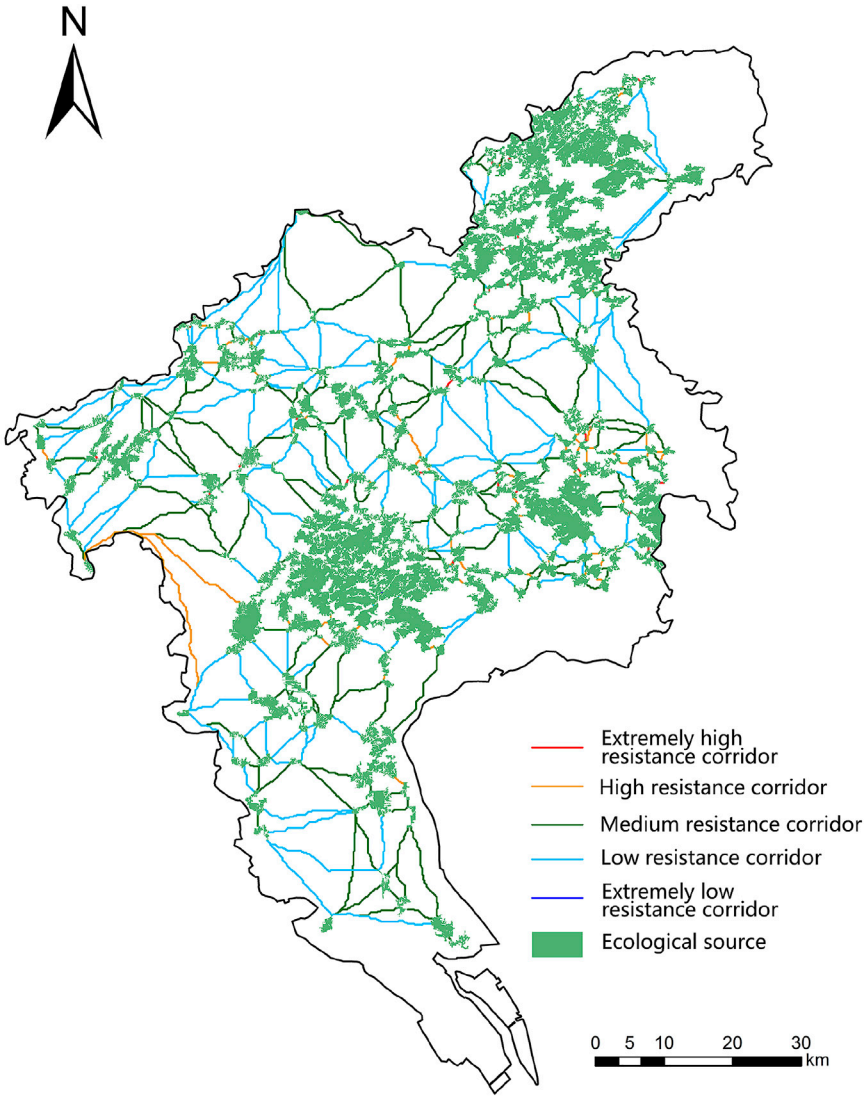

FIGURE 7 | Ecological source and corridor.

the connectedness of the corridor between two sources. Furthermore, medium-resistance corridors were generally located in two ecological sources with longer cost-weighted distances. The complex and various land-use types have an impact on the overall resistance of the corridor.

4.4.3 Barrier Point Analysis

Comparing the results of the different radii, the four different radii have a similar range of barriers. The search results from a smaller radius can accurately search for a higher barrier score in the fine area in the corridor. Therefore, a 250 m radius was selected to identify ecological barrier point and the total area was 433.26 km^2 (**Figure 8A**).

Most of the ecological barrier points were located in the farmland and construction land. When it comes to the spatial layout, there were a large number of scattered barrier points in the northern part of the study area, and it would be very difficult to completely remove them in the future. In the central and southern areas, there were large-scale barrier points. Corridor connectivity can be significantly improved by removing barrier points in this area. Ecological restoration measures should be recommended for optimization.

4.4.4 Pinch Point Analysis

The results (**Figure 8B**) show that the ecological pinch points were mainly located in the northern area. Pinch points were mostly situated in woodland, with a small amount in farmland and construction land. On the other hand, in the southern area, the proportion of pinch points in farmland and construction land was significantly higher.

The narrow pinch point area acts as a catalyst for corridor connectively when the relatively high-resistance patches spread around the area. However, the analysis of ecological corridors with different resistance types shows that although the study

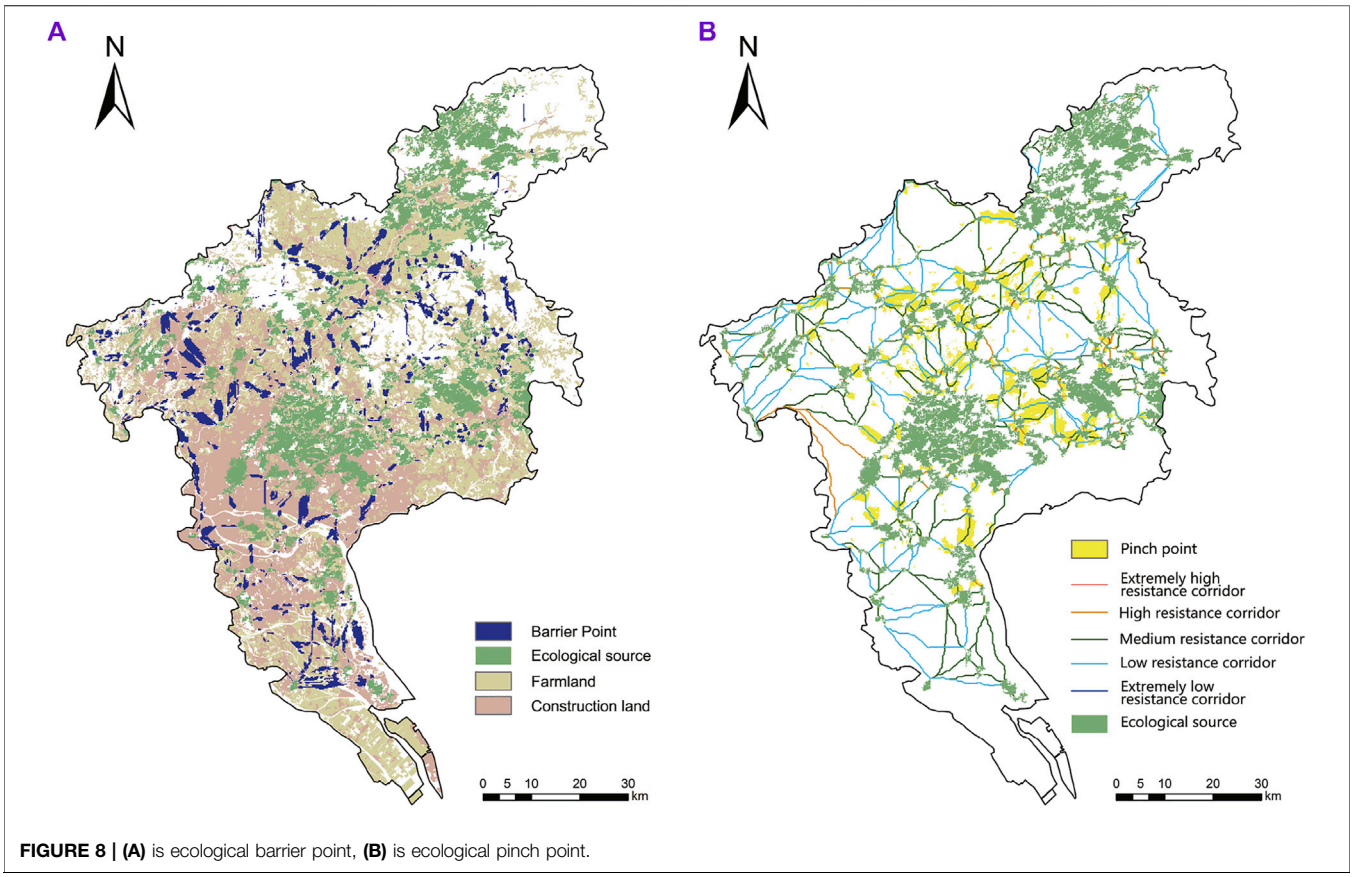

FIGURE 8 | (A) is ecological barrier point, **(B)** is ecological pinch point.

identifies high-value pinch points, they were mostly in low-resistance corridors. Medium- and high-resistance corridors were impeded by the disorderly encroachment of construction land in the northern and southern areas, resulting in the fragmentation of green space and farmland patches. The fragmented areas were highly mixed with various land-use types, and therefore contribute less to connectivity.

5 DISCUSSION

5.1 Significance for Integration of Ecosystem and Socioeconomic System

Previous studies directly select forest patches or habitat areas of wild animals as source areas, but the subjective interference in this selection method was large. Although good accessibility was considered in this selection method, the results only identified ecological patches as the sources of Guangzhou (Yang et al., 2018). Therefore, the high comprehensive value areas in other land-use types tend to be ignored. Furthermore, by changing the selection criteria of sources, the importance of core patches could also be quantitatively evaluated based on the structure of ecosystem and ecological sensitivity (Peng et al., 2017a; Su et al., 2022). The ecosystem services-based ESPs were regarded as an effective method for strengthening the integrity of ecosystems and socioeconomic systems (Fan et al., 2021). It is reasonable to rank patches based on their multifunction of providing key ecosystem services, however, the interaction between the ecosystem and human socioeconomic system cannot be neglected due to the role of ESPs in figuring out the contradiction between ecological land protection and urban development.

We proposed a comprehensive selection method containing five crucial ecosystem services in Guangzhou; aside from regulation and provision ecosystem services, cultural services were also included to quantify the importance of ecological areas. To understand the relationship between ecosystem and socioeconomic system, several scenarios based on the OWA method were compared to identify the ecological sources. Our approach identified the demand for human well-being and the ability to provide effective services (Peng et al., 2017a). Green space and parks in the central part of Guangzhou were also extracted, although the patches were fragmented due to the expansion of construction land. Specifically, a small proportion of construction land also extracted due to the trade-offs between ecosystem and socioeconomic system, which can be identified as the strategic points in the ESPs. Our selection method, therefore, is more conducive to the identification of ecological sources.

In the context of global climate change and anthropogenic disturbances, socioeconomic development will lead to more prominent eco-environmental problems (Liu, 2016). Aiming to solve problems of ecological security,the Guangzhou government has carried out a series of projects and plans such as ecological protection redline, however, these “bottom-line” policies mainly

concerned ecological space while neglected the human-land contradiction in metropolitan area (Xu et al., 2021b), or neglect the potential crucial patches outside the ecological protection redline (Ye et al., 2018). To address this gap, this study considered both the ecosystem and socioeconomic system to construct the ESPs. It is worth noting that the most ecological sources were distributed in the hilly area with woodland, which tend to be threatened by unforeseeable human activities. It should be of great concern to integrate ecosystem and socioeconomic system to deal with future climate changes and sustainable development.

5.2 Limitations and Challenges

Previous studies mostly used the artificial discrimination method to eliminate results directly, but it was not easy to determine the ecological sources (Fu et al., 2020). In this study, the ecological sources were selected under the specified threshold, and as a result, ecological sources in the southern and central areas of Guangzhou were much less abundant than in the northern area. Several important "green core" areas such as Dafu Mountain, Seagull Island, and Huang Shan lu forest park were identified. Some important patches such as Nansha wetland in the southern area were eliminated due to their small area, though they may have potential value in other ecosystem services. Future study is still needed to determine the rationality of the threshold, and the assessment indexes need to be enhanced to make sure that the ecological sources are in their best state.

Referring to related studies, the selection of ecosystem indicators is mainly based on support, cultural and regulating services. However, the farmland is usually contributed to the provision of ecosystem services and may be underestimated when the study does not select food production as an indicator (Xu et al., 2014). As a result, high-quality farmland in the southern area may not be highly valued, leading to a reduction in ecological sources in the south. Therefore, the range of evaluation indicators could be expanded in future studies, which could add into the integration of ecosystem and socioeconomic system relationships in comparison with the results of current studies.

The connectivity of heterogeneous landscapes can be effectively identified by the least-cost path. However, the identification of corridor importance merits further discussion (Song and Qin, 2016). Circuit theory can provide multiple potential corridors and contribute to identifying corridors of priority importance (Liu et al., 2021; Pan and Wang, 2021), but it is not possible to intuitively investigate corridor movement pathways and connectivity because of random-walk (LaPoint et al., 2013). Therefore, we use the intuitive least-cost path to describe the priority of each corridor and ratio of cost-weighted distance to length to determine the relative resistance. This could be more flexible in researching corridor connectivity. However, compared with circuit theory it is still insufficient in identifying the importance of multiple pathways (McRae et al., 2008).

Different ecological corridor widths have an impact on the identification of ecological barrier points and pinch points. Consequently, they can provide the scientific basis for the definition of ecological restoration and protection areas in ecological corridors (Hou et al., 2021). An agreement regarding the widths of different ecological corridors has not yet been reached (Peng et al., 2017c). Therefore, determining the widths of corridors is an essential point in the implementation of ESPs (Zhai and Huang, 2022). However, this has not been discussed due to the constraints of the study, but should be considered in future research.

5.3 Optimization and Restoration

Different strategies should be proposed depending on the land-use types of different areas. For the northern areas dominated by the ecosystems, it is necessary to consider this area as the role of the ecological supporting area and focus on ecological conservation strategy. Ecological protection areas such as forest parks should be strictly protected, while appropriate recreational services should be provided as rationally direct ecological resources. For the central area, which is dominated by socioeconomic systems, small green spaces should be constructed and distributed throughout the area. Moreover, green spaces should be designed to deliver recreational and cultural characteristics, balancing ecosystem values with socioeconomic system values. In addition, in the southern area, which is a potential area for urban construction in Guangzhou according to Territorial Spatial Planning, the expansion of construction land should be rationally restricted to prevent the shrinkage of ecological space. Strategies such as exposure to green space and ecological greenways (Zhang et al., 2021), which can deliver different kinds of ecosystem services and enhance the multifunctionality of corridors, are recommended to integrate complementary ecosystem connectivity (Carlier and Moran, 2019).

Corridors play an important role in the maintenance of ecological processes (Peng et al., 2018). Furthermore, in order to implement ecological restoration in ecological corridors, the areas of barriers points and pinch points should be given more priority (Peng et al., 2018). Medium-to-high-resistance ecological corridors should be set as priority areas for future ecological restoration. Ecological restoration should start by prioritizing the removal of ecological barriers. In urban spaces, corridors should be connected by road green belts and greenways. It is possible to improve the corridor barrier points by enriching the green space with various types, vegetation species and vertical structures. Furthermore, the barrier point can be also improved by combining green and blue spaces to form an ecological network and green infrastructure (Yu et al., 2020), which simultaneously contribute to human well-being and sustainable climate adaption planning (Ignatieva et al., 2011; Monteiro et al., 2020; Yang et al., 2020; Yu et al., 2021). When it comes to the connectedness of farmland, high-standard farmland should be interpenetrated by building connecting channels within the space which could interfere with the corridor's connectivity.

Ecological pinch points should be a conservation priority, including strategies to maintain and recover the areas (Castilho et al., 2015). It is necessary to integrate the fragmented patches through land consolidation, which can integrate different spaces with various land-use types in a unified way and carry out spatial reconfiguration. Low-resistance ecological corridors should

be flexibly maintained. These scattered barrier points can be set as secondary areas for ecological restoration and can be gradually improved by nature-based solutions (Bush and Doyon, 2019). In the future, the area needs to avoid being divided into fragmented spaces. Throughout the stages of development, these areas should be centrally classified by a unified authority, which will also facilitate maintenance at a later stage.

6 CONCLUSION

Although previous studies have identified ecological security patterns based on multiple ecosystem services, traditional methods only identified what were considered "ecological patches" as the suppliers, and lacked integration between ecosystems and the socioeconomic systems. This study selected comprehensive evaluation indicators including ecosystems and socioeconomic systems to identify ecological sources, introducing the OWA method from the perspective of trade-off. The highest trade-off scenario was selected and, finally, the ecological sources and resistance surfaces were identified.

There were 158 ecological sources with an area of 1,085.34 km^2 and 406 ecological corridors with a total length of 1506 km in Guangzhou. The pattern of ecological sources and corridors from various areas were influenced by the dominant ecosystem or socioeconomic system, which indicates that the trade-off between ecosystem and socioeconomic system has a significant impact on the construction of ESPs. Moreover, ecological barrier points and pinch points with total areas of 433.26 and 458.51 km^2, respectively, were recognized to implement ecological restoration. This study also proposed primary ecological restoration strategies for medium- and high-resistance corridors. A large number of scattered barrier points were located in the northern area and large-scale barrier points were generally situated in the central and southern areas. Therefore, restoration strategies including enriching vegetation types and vertical structures and building green belts and greenways should be proposed to restore large-scale barriers points. When it comes to pinch points, land consolidation strategies such as construction land reclamation and farmland preservation should be implemented in medium- and high-resistance corridors, while buffer zones should be constructed to enhance the resilience of low-resistance corridors. This could achieve the win-win scenario of preserving ecological space while furthering urban development.

The integration of ecosystems and the socioeconomic systems was used as a fundamental basis to improve the existing methods of constructing ecological security patterns. The proposed ecological restoration solutions based on this method contribute to the overall improvement of the connectivity of the ESPs, offering a reference for balancing the development of urbanization and ecological protection in other metropolitan areas.

DATA AVAILABILITY STATEMENT

Information about the existing publicly accessible datasets is contained within the article, further inquiries can be directed to the corresponding author.

AUTHOR CONTRIBUTIONS

Conceptualization, WL JT, and HL; methodology, WL and JT; data analysis, JT; validation, WL and JT; investigation, WL; resources, WL; writing—original draft preparation, JT and WL; writing—review and editing, WL and HL; visualization, JT; supervision, WL and HL; project administration, HL; funding acquisition, HL All authors have read and agreed to the published version of the manuscript.

FUNDING

This research was financially supported by the National Natural Science Foundation of China (No. 52078222), and the Key Research Project of Department of Education of Guangdong Province (No. 2020ZDZX1033).

ACKNOWLEDGMENTS

The authors are grateful to the reviewers and editors for their detailed comments and valuable suggestions.

REFERENCES

Bing, Z., Qiu, Y., Huang, H., Chen, T., Zhong, W., and Jiang, H. (2021). Spatial Distribution of Cultural Ecosystem Services Demand and Supply in Urban and Suburban Areas: A Case Study from Shanghai, china. *Ecol. Indic.* 127, 107720. doi:10.1016/j.ecolind.2021.107720

Bush, J., and Doyon, A. (2019). Building Urban Resilience with Nature-Based Solutions: How Can Urban Planning Contribute? *Cities* 95, 102483. doi:10.1016/j.cities.2019.102483

Carlier, J., and Moran, J. (2019). Landscape Typology and Ecological Connectivity Assessment to Inform Greenway Design. *Sci. Total Environ.* 651, 3241–3252. doi:10.1016/j.scitotenv.2018.10.077

Casagrande, E., Recanati, F., Rulli, M. C., Bevacqua, D., and Melià, P. (2021). Water Balance Partitioning for Ecosystem Service Assessment. A Case Study in the Amazon. *Ecol. Indic.* 121, 107155. doi:10.1016/j.ecolind.2020.107155

Castilho, C. S., Hackbart, V. C. S., Pivello, V. R., and dos Santos, R. F. (2015). Evaluating Landscape Connectivity for Puma Concolor and panthera Onca Among atlantic forest Protected Areas. *Environ. Manage.* 55, 1377–1389. doi:10.1007/s00267-015-0463-7

Chen, T., Li, P., and Wang, Q. (2021). Identification of Ecological Security Patterns in Chengdu-Chongqing Urban Agglomeration Based on Multi-Scenario Decision Making and Ecosystem Service Trade-Offs. *Chin. Environ. Sci.*, 1–23. doi:10.19674/j.cnki.issn1000-6923.20210324.001

Cui, L., Wang, J., Sun, L., and Lv, C. (2020). Construction and Optimization of green Space Ecological Networks in Urban Fringe Areas: A Case Study with the

Urban Fringe Area of Tongzhou District in Beijing. *J. Clean. Prod.* 276, 124266. doi:10.1016/j.jclepro.2020.124266

Cumming, G. S., and Allen, C. R. (2017). Protected Areas as Social-Ecological Systems: Perspectives from Resilience and Social-Ecological Systems Theory. *Ecol. Appl.* 27, 1709–1717. doi:10.1002/eap.1584

Dai, E.-f., Wang, X.-l., Zhu, J.-j., and Xi, W.-m. (2017). Quantifying Ecosystem Service Trade-Offs for Plantation forest Management to Benefit Provisioning and Regulating Services. *Ecol. Evol.* 7, 7807–7821. doi:10.1002/ece3.3286

Deng, C., Liu, J., Nie, X., Li, Z., Liu, Y., Xiao, H., et al. (2021). How Trade-Offs between Ecological Construction and Urbanization Expansion Affect Ecosystem Services. *Ecol. Indic.* 122, 107253. doi:10.1016/j.ecolind.2020.107253

Ding, Y., Zhang, L., and Zeng, X. (2019). The Construction of an Ecological Function Network and its Application in the Greater bay Area, china. *J. Ecol. Rural Environ.* 35, 573–581. doi:10.19741/j.issn.1673-4831.2018.0244

Dong, J., Jiang, H., Gu, T., Liu, Y., and Peng, J. (2021). Sustainable Landscape Pattern: a Landscape Approach to Serving Spatial Planning. *Landscape Ecol.* 37, 31–42 .doi:10.1007/s10980-021-01329-0

Fan, S., Chen, X., Ren, H., Shen, W., Rongbo, X., Zhang, Q., et al. (2018). Landscape Structure and Network Characteristics of the Greenway System in Guangzhou City, south china. *Landscape Ecol. Eng.* 15, 25–35. doi:10.1007/s11355-018-0358-x

Fan, F., Liu, Y., Chen, J., and Dong, J. (2021). Scenario-based Ecological Security Patterns to Indicate Landscape Sustainability: a Case Study on the Qinghai-Tibet Plateau. *Landscape Ecol.* 36, 2175–2188. doi:10.1007/s10980-020-01044-2

Fang, Y., Wang, J., Huang, L.-y., and Zhai, T.-l. (2020). Determining and Identifying Key Areas of Ecosystempreservation and Restoration for Territorial Spatial Planning Based on Ecological Security Patterns: A Case Study of Yantai City. *J. Nat. Res.* 35, 190. doi:10.31497/zrzyxb.20200116

Feist, B. E., Buhle, E. R., Baldwin, D. H., Spromberg, J. A., Damm, S. E., Davis, J. W., et al. (2017). Roads to Ruin: Conservation Threats to a sentinel Species across an Urban Gradient. *Ecol. Appl.* 27, 2382–2396. doi:10.1002/eap.1615

Fu, Y., Shi, X., He, J., Yuan, Y., and Qu, L. (2020). Identification and Optimization Strategy of County Ecological Security Pattern: A Case Study in the Loess Plateau, china. *Ecol. Indic.* 112, 106030. doi:10.1016/j.ecolind.2019.106030

Gao, J., Du, F., Zuo, L., and Jiang, Y. (2021). Integrating Ecosystem Services and Rocky Desertification into Identification of Karst Ecological Security Pattern. *Landscape Ecol.* 36, 2113–2133. doi:10.1007/s10980-020-01100-x

Gong, J., Liu, D., Zhang, J., Xie, Y., Cao, E., and Li, H. (2019). Tradeoffs/synergies of Multiple Ecosystem Services Based on Land Use Simulation in a Mountain-basin Area, Western china. *Ecol. Indic.* 99, 283–293. doi:10.1016/j.ecolind.2018.12.027

Hou, Q., Du, Y., Dong, W., Zeng, Z., Zhang, L., Duan, Y., et al. (2021). Smart City Oriented Ecological Corridor Layout of Sanshui River basin in Arid Area of Loess Plateau. *Sustainable Energ. Tech. Assess.* 44, 100993. doi:10.1016/j.seta.2021.100993

Ignatieva, M., Stewart, G. H., and Meurk, C. (2011). Planning and Design of Ecological Networks in Urban Areas. *Landscape Ecol. Eng.* 7, 17–25. doi:10.1007/s11355-010-0143-y

LaPoint, S., Gallery, P., Wikelski, M., and Kays, R. (2013). Animal Behavior, Cost-Based Corridor Models, and Real Corridors. *Landscape Ecol.* 28, 1615–1630. doi:10.1007/s10980-013-9910-0

Li, C., Zheng, H., Li, S., Chen, X., Li, J., Zeng, W., et al. (2015). Impacts of Conservation and Human Development Policy across Stakeholders and Scales. *Proc. Natl. Acad. Sci.* 112, 7396–7401. doi:10.1073/pnas.1406486112

Li, Z., Deng, X., Jin, G., Mohmmed, A., and Arowolo, A. O. (2020). Tradeoffs between Agricultural Production and Ecosystem Services: A Case Study in Zhangye, Northwest china. *Sci. Total Environ.* 707, 136032. doi:10.1016/j.scitotenv.2019.136032

Li, X., Xiao, J., Wang, J., Wu, J., and Long, N. (2021). Research on the Evaluation and Application of Natural Resources Assets for Ecological Restoration: A Case Study of Guangzhou City. *Acta Ecol. Sin.* 42, 1192–1202.

Li, H., Yao, Y., Yang, X., Dong, X., Yang, J., Ma, Z., et al. (2022). Simulating Ecologucal Security Pattern in the Xiong'an New Area Based on the Multicriteria Evaluation of AHP-OWA. *Acta Ecol. Sin.* 42 (1), 1–11. doi:10.5846/stxb202010162642

Liu, J., Mooney, H., Hull, V., Davis, S. J., Gaskell, J., Hertel, T., et al. (2015). Systems Integration for Global Sustainability. *Science* 347, 1258832. doi:10.1126/science.1258832

Liu, Z., Huang, Q., and Yang, H. (2021). Supply-demand Spatial Patterns of Park Cultural Services in Megalopolis Area of Shenzhen, china. *Ecol. Indicators* 121, 107066. doi:10.1016/j.ecolind.2020.107066

Liu, G. (2016). Formation and Evolution Mechanism of Ecological Security Pattern in Southwest china. *Acta Ecol. Sin.* 36, 7088–7091. doi:10.5846/stxb201611212364

Long, N., Huang, H., Li, X., Wu, J., and Lei, D. (2018). A Research on Urban Ecological Corridors Network Planning of Megacities: A Case Study of Guangzhou. *Urban. Architect.* 3, 53–57. doi:10.19892/j.cnki.csjz.2018.03.010

Mao, C., Dai, L., Qi, L., Wang, Y., Zhou, W., Zhou, L., et al. (2020). Constructing Ecological Security Pattern Based on Ecosystem Services: A Case Study in Liaohe River basin, Liaoning Province, china. *Acta Ecol. Sin.* 40, 6486–6494. doi:10.5846/stxb201909191954

Marina, L. S., Antonio, T. C., and Mercedes, L. G. d. P. (2020). The Potential Role of Cultural Ecosystem Services in Heritage Research through a Set of Indicators. *Ecol. Indic.* 117, 106670. doi:10.1016/j.ecolind.2020.106670

McRae, B. H., Dickson, B. G., Keitt, T. H., and Shah, V. B. (2008). Using Circuit Theory to Model Connectivity in Ecology, Evolution, and Conservation. *Ecology* 89, 2712–2724. doi:10.1890/07-1861.1

Monteiro, R., Ferreira, J. C., and Antunes, P. (2020). Green Infrastructure Planning Principles: An Integrated Literature Review. *Land* 9, 525. doi:10.3390/land9120525

Ni, Q., Hou, H., Ding, Z., Li, Y., and Li, J. (2020). Ecological Remediation Zoning of Territory Based on the Ecological Security Pattern Recognition: Taking Jiawang District of Xuzhou City as an Example. *J. Nat. Res.* 35, 204. doi:10.31497/zrzyxb.20200117

Pan, J., and Li, L. (2021). Optimization of Ecological Security Pattern in Gansu Section of the Yellow River basin Using OWA and Circuit Model. *Trans. Chin. Soc. Agric. Eng.* 37, 259–268. doi:10.11975/j.issn.1002-6819.2021.03.031

Pan, J., and Wang, Y. (2021). Ecological Security Evaluation and Ecological Pattern Optimization in Taolai River basin Based on CVOR and Circuit Theory. *Acta Ecol. Sin.* 41, 2582–2595. doi:10.5846/stxb202005111183

Peng, J., Yang, Y., Xie, P., and Liu, Y. (2017a). Zoning for the Construction of green Space Ecological Networks in Guangdong Province Based on the Supply and Demand of Ecosystem Services. *Acta Ecol. Sin.* 37, 4562–4572. doi:10.1016/j.chnaes.2016.12.002

Peng, J., Zhao, H., Liu, B., and Wu, J. (2017b). Research Progress and prospect on Regional Ecological Security Pattern Construction. *Geogr. Res.* 36, 407. doi:10.11821/dlyj201703001

Peng, J., Zhao, H., and Liu, Y. (2017c). Urban Ecological Corridors Construction: A Review. *Acta Ecol. Sin.* 37, 23–30. doi:10.1016/j.chnaes.2016.12.002

Peng, J., Yang, Y., Liu, Y., Hu, Y., Du, Y., Meersmans, J., et al. (2018). Linking Ecosystem Services and Circuit Theory to Identify Ecological Security Patterns. *Sci. Total Environ.* 644, 781–790. doi:10.1016/j.scitotenv.2018.06.292

Serra-Llobet, A., and Hermida, M. A. (2017). Opportunities for green Infrastructure under ecuador's New Legal Framework. *Landscape Urban Plann.* 159, 1–4. doi:10.1016/j.landurbplan.2016.02.004

Song, L., and Qin, M. (2016). Identification of Ecological Corridors and its Importance by Integrating Circuit Theory. *Chin. J. Appl. Ecol.* 27, 3344–3352. doi:10.13287/j.1001-9332.201610.035

Su, Y., Chen, X., Liao, J., Zhang, H., Wang, C., Ye, Y., et al. (2016). Modeling the Optimal Ecological Security Pattern for Guiding the Urban Constructed Land Expansions. *Urban For. Urban Green.* 19, 35–46. doi:10.1016/j.ufug.2016.06.013

Su, J., Yin, H., and Kong, F. (2021). Ecological Networks in Response to Climate Change and the Human Footprint in the Yangtze River delta Urban Agglomeration, china. *Landscape Ecol.* 36, 2095–2112. doi:10.1007/s10980-020-01129-y

Su, X., Shen, Y., Xiao, Y., Liu, Y., Cheng, H., Wan, L., et al. (2022). Identifying Ecological Security Patterns Based on Ecosystem Services Is a Significative Practice for Sustainable Development in Southwest china. *Front. Ecol. Evol.* 9, 810204. doi:10.3389/fevo.2021.810204

Valente, R. d. O. A., and Vettorazzi, C. A. (2008). Definition of Priority Areas for forest Conservation through the Ordered Weighted Averaging Method. *For. Ecol. Manage.* 256, 1408–1417. doi:10.1016/j.foreco.2008.07.006

Wang, M., Hou, X., and Wang, J. (2018). Resilience Mechanism and Practical Insights from Water-Related Physical Form in Jiangnan Based on Traditional

Ecological Wisdom. *Landcape Archit. J.* 25, 52–57. doi:10.14085/j.fjyl.2018.06.0052.06

Wang, D., Chen, J., Zhang, L., Sun, Z., Wang, X., Zhang, X., et al. (2019). Establishing an Ecological Security Pattern for Urban Agglomeration, Taking Ecosystem Services and Human Interference Factors into Consideration. *PeerJ* 7, e7306. doi:10.7717/peerj.7306

Wang, L., Feng, X., Chang, Q., Liu, H., and Wang, J. (2020). Pattern Construction of Habitat Network for Urban green Space Based on the Compound Model of InVEST and MCR. *Chin. Landscape Archit.* 36, 113–118. doi:10.19775/j.cla.2020.06.0113

Wang, X., Zhao, P., Zhao, Y., Song, W., and Liu, X. (2022). Identification of key areas of land space ecological protection and restoration based on the pattern of ecological security in Guangdong, Hong Kong and Macau. *Acta Ecol. Sin.* 1–12, 450–461. doi:10.5846/stxb202011072848

Wu, J., Ma, H., and Peng, J. (2018). Improving Urban Ecological Security Pattern Based on Functional Nodes-Key Corridors: A Case Study of Shenzhen City. *Prog. Geogr.* 37, 1663–1671. doi:10.18306/dlkxjz.2018.12.008

Xu, L., Yin, H., Li, Z., and Li, S. (2014). Land Ecological Security Evaluation of Guangzhou, china. *Int. J. Environ. Res. Public Health* 11, 10537–10558. doi:10.3390/ijerph111010537

Xu, C., Cheng, L., Su, J., Yin, H., and Guo, Y. (2021a). Developing Regional Ecological Networks along the Grand Canal Based on an Integrated Analysis Framework. *J. Resour. Ecol.* 12, 801–813. doi:10.5814/j.issn.1674-764x.2021.06.008

Xu, C., Meng, N., Zhang, Y., Xie, S., Han, B., Su, Z., et al. (2021b). Urban Ecological Conservation Redlines Delineation and Management: A Case Study of macao Special Administrative Region. *Acta Ecol. Sin.* 41, 9103–9117. doi:10.5846/stxb202105071200

Yager, R. (1988). On Ordered Weighted Averaging Aggregation Operators in Multicriteria Decisionmaking. *IEEE Trans. Syst. Man, Cyber.* 18, 183–190. doi:10.1109/21.87068

Yang, Y., and Li, Q. (2021). Distribution Pattern and its Formation Mechanism of Public Recreational Space Based on POI Data: A Case Study of the Main Urban Area of Changsha City. *Mod. Urban Res.* 3, 91–97. doi:10.3969/j.issn.1009-6000.2021.03.013

Yang, X., Zhou, Z., Li, J., Fu, X., Mu, X., and Li, T. (2016). Trade-offs between Carbon Sequestration, Soil Retention and Water Yield in the Guanzhong-Tianshui Economic Region of china. *J. Geogr. Sci.* 26, 1449–1462. doi:10.1007/s11442-016-1337-5

Yang, Z., Jiang, Z., Guo, C., Yang, X., Xu, X., Li, X., et al. (2018). Construction of Ecological Network Using Morphological Spatial Pattern Analysis and Minimal Cumulative Resistance Models in Guangzhou City, china. *Chin. J. Appl. Ecol.* 29, 3367–3376. doi:10.13287/j.1001-9332.201810.019

Yang, G., Yu, Z., Jørgensen, G., and Vejre, H. (2020). How Can Urban Blue-green Space Be Planned for Climate Adaption in High-Latitude Cities? a Seasonal Perspective. *Sustain. Cities Soc.* 53, 101932. doi:10.1016/j.scs.2019.101932

Ye, L., and Shi, Z. (2021). Analysis of RUSLE Model Parameter Acquisition Methods Based on Domestic Literature. *Yunnan Geogr. Environ. Res.* 33, 45–51. doi:10.3969/j.issn.1001-7852.2021.02.006

Ye, X., Zou, C., Liu, G., Lin, N., and Xu, M. (2018). Main Research Contents and Advances in the Ecological Security Pattern. *Acta Ecol. Sin.* 38, 53–57. doi:10.5846/stxb201701110083

Ying, L., Wang, J., and Zhou, Y. (2019). Ecological-environmental Problems and Solutions in the Minjiang River basin, Fujian Province, china. *Acta Ecol. Sin.* 39, 8857–8866. doi:10.5846/stxb201905291106

Yu, L., Liu, J., Li, T., and Zhu, H. (2018). Research Progress of Urban Public Recreational Space in china. *Acta Geogr. Sin.* 73, 1923–1941. doi:10.11821/dlxb201810008

Yu, Z., Yang, G., Zuo, S., Jørgensen, G., Koga, M., and Vejre, H. (2020). Critical Review on the Cooling Effect of Urban Blue-Green Space: A Threshold-Size Perspective. *Urban For. Urban Green.* 49, 126630. doi:10.1016/j.ufug.2020.126630

Yu, Z., Zhang, J., and Yang, G. (2021). How to Build a Heat Network to Alleviate Surface Heat Island Effect? *Sustain. Cities Soc.* 74, 103135. doi:10.1016/j.scs.2021.103135

Yu, K. (1996). Security Patterns and Surface Model in Landscape Ecological Planning. *Landscape Urban Plann.* 36, 1–17. doi:10.1016/S0169-2046(96)00331-3

Zhai, T., and Huang, L. (2022). Linking MSPA and Circuit Theory to Identify the Spatial Range of Ecological Networks and its Priority Areas for Conservation and Restoration in Urban Agglomeration. *Front. Ecol. Evol.* 10. doi:10.3389/fevo.2022.828979

Zhang, L., Fu, B., Lü, Y., and Zeng, Y. (2015). Balancing Multiple Ecosystem Services in Conservation Priority Setting. *Landscape Ecol.* 30, 535–546. doi:10.1007/s10980-014-0106-z

Zhang, L., Peng, J., Liu, Y., and Wu, J. (2017). Coupling Ecosystem Services Supply and Human Ecological Demand to Identify Landscape Ecological Security Pattern: A Case Study in Beijing–Tianjin–Hebei Region, china. *Urban Ecosyst.* 20, 1–14. doi:10.1007/s11252-016-0629-y

Zhang, Y., Hu, Y., and Zhuang, D. (2020). A Highly Integrated, Expansible, and Comprehensive Analytical Framework for Urban Ecological Land: A Case Study in Guangzhou, china. *J. Clean. Prod.* 268, 122360. doi:10.1016/j.jclepro.2020.122360

Zhang, J., Yu, Z., Cheng, Y., Sha, X., and Zhang, H. (2021). A Novel Hierarchical Framework to Evaluate Residential Exposure to green Spaces. *Landscape Ecol.* Available at: https://link.springer.com/article/10.1007/s10980-021-01378-5. doi:10.1007/s10980-021-01378-5

Zhao, K., Li, X., and Yuan, N. (2017). From American "greenway" to European Greenway: The Construction of Ecological Network in Urban and Rural Space—a Case Study of Zengcheng District of Guangzhou. *Chin. Landscape Archit.* 33, 82–87.

Zhao, W., Han, Z., Yan, X., and Zhong, J. (2020). Ecological Security pattern construction based on multi-scenario trade-off of ecosystem services: A Case Study of wafangdian, Dalian. *J. Nat. Res.* 35, 546. doi:10.31497/zrzyxb.20200304

Zhu, J., Su, J., Haiwei, Y., and Fanhua, K. (2020). Construction of xuzhou Ecological network based on comprehensive sources identification and multi-scale nesting. *J. Nat. Res.* 35, 1986–2001. doi:10.31497/zrzyxb.20200817

Conflict of Interest: The authors declare that the research was conducted in the absence of any commercial or financial relationships that could be construed as a potential conflict of interest.

Publisher's Note: All claims expressed in this article are solely those of the authors and do not necessarily represent those of their affiliated organizations, or those of the publisher, the editors and the reviewers. Any product that may be evaluated in this article, or claim that may be made by its manufacturer, is not guaranteed or endorsed by the publisher.

frontiers in Environmental Science

ORIGINAL RESEARCH
published: 16 March 2022
doi: 10.3389/fenvs.2022.808026

A Synoptic Framework for Forecasting the Urban Rainfall Effect Using Composite and K-Means Cluster Analyses

Jordan McLeod[1] *and Marshall Shepherd*[2]*

[1]Department of Earth Sciences, University of South Alabama, Mobile, AL, United States, [2]Department of Geography, University of Georgia, Athens, GA, United States

Observational and numerical modeling studies continue to affirm the existence of the "urban rainfall effect" (URE), or a discernible anomaly in warm season precipitation due to urbanization. However, the literature has been lacking a progression towards the predictability of the URE. Atlanta, Georgia has consistently appeared in the literature because of its well-studied urban rainfall anomalies. Using the Multi-sensor Precipitation Estimates (MPE) dataset and the ERA-Interim reanalysis dataset, an 18-year period (2002–2019) is examined. Three similar but distinct methods are used to define urban rainfall days (URDs), or periods when the precipitation in the urbanized areas of Atlanta are greater than the surrounding rural areas. A combination of compositing, wind rose, and *k*-means cluster analyses are employed to extract the synoptic framework supportive of the URE in Atlanta, Georgia. The synoptic-scale compositing analysis reveals that there are a consistent set of meteorological ingredients that are needed to produce an URD, including weaker-than-average southwesterly-to-northwesterly flow at 700 hPa, copious amounts of moisture throughout the tropospheric column, and a background low-level convergent flow. Composite atmospheric soundings reveal that there is enhanced moisture throughout the tropospheric column on URDs, leading to marginal instability that favors localized convection across the Atlanta metropolitan area. The study also provides clarity on how often the URE is present (roughly 8% of the time) during warm season days across the Atlanta metropolitan area. Taken together, this synoptic framework will aid in the forecasting of the URE in Atlanta and can be easily applied to other cities.

Keywords: urban, rainfall, synoptic, Atlanta, K-means, MPE, reanalysis

OPEN ACCESS

Edited by:
Ashish Sharma, University of Illinois at Urbana-Champaign, United States

Reviewed by:
Zhonghua Zheng, Columbia University, United States
Debanjana Das, University of Texas at Austin, United States

***Correspondence:**
Marshall Shepherd
marshgeo@uga.edu

Specialty section:
This article was submitted to Atmosphere and Climate, a section of the journal Frontiers in Environmental Science

Received: *02 November 2021*
Accepted: *15 February 2022*
Published: *16 March 2022*

Citation:
McLeod J and Shepherd M (2022) A Synoptic Framework for Forecasting the Urban Rainfall Effect Using Composite and K-Means Cluster Analyses. Front. Environ. Sci. 10:808026. doi: 10.3389/fenvs.2022.808026

1 INTRODUCTION

More than half of the global population lives in urban spaces, and that number may exceed 65% by 2025 (Shepherd et al., 2013). The literature chronicles how urban environments modify weather and hydroclimate (Seto and Shepherd, 2009; Debbage and Shepherd, 2019). Like urban heat islands, urban effects on the hydroclimate have increasingly become well-understood. For decades, a scholarly question loomed regarding the role of urbanization on precipitation processes (Landsberg, 1956; Shepherd et al., 2002; Mitra and Shepherd, 2016). A host of investigators

employed field campaigns (Shepherd et al., 2013), remote sensing platforms and long-term observations (Shepherd et al., 2002; Mote et al., 2007; Jin and Shepherd, 2008; Mitra et al., 2012; McLeod et al., 2017; Johnson and Shepherd, 2018), or numerical weather models (Schmid and Niyogi, 2013; Debbage and Shepherd, 2019) to answer the following fundamental questions:

> Can cities, via urban landscapes and/or associated aerosol processes, initiate or modify precipitating cloud systems?
>
> If so, what processes are of first-order significance in urban-influenced precipitating storms?

Liu and Niyogi (2019) recently established, with some degree of conclusiveness, that urbanization affects rainfall processes. Key findings from their meta-analysis established or confirmed several long-standing issues within the urban hydrometeorological community. While historical studies from the METROMEX (i.e., Metropolitan Meteorological Experiment) era argued that urban effects on rainfall are primarily downwind of the city, their analysis revealed that urbanization modifies rainfall in distinct spatial patterns around the central business district of a city: 18% downwind, 16% over the city, 2% on the left, and 4% on the right relative to storm direction. This is consistent with work by other investigators as well (Ashley et al., 2012; Bentley et al., 2012) and an important step in establishing what Shepherd et al. (2010) called the "urban rainfall effect," or URE. The URE is a broad term that captures the various ways that the urban environment modifies the initiation or modification of precipitation processes.

While the concept of the URE has been established for many cities using a variety of methodological approaches, the predictability of urban-generated rainfall remains largely unexplored. Previous studies (e.g., Bentley et al., 2012) have shown that the URE occurs most frequently during periods of weak synoptic flow, and McLeod et al. (2017) revealed that the magnitude and spatial pattern of urban-induced rainfall around Atlanta, Georgia was dependent on the synoptic flow regime. In addition, Dixon and Mote (2003) have shown that low-level moisture, rather than the intensity of the urban heat island, was the most significant predictor of urban-generated convection for the city of Atlanta. However, only a limited effort has been focused on identifying which meteorological variables in the synoptic-scale environment most effectively distinguish days exhibiting the URE. Bentley et al. (2012) revealed that a synoptic environment characterized by moderate thermodynamic instability was most favorable for producing urban convection and rainfall over Atlanta. Herein, the research was motivated by the following questions: (1) Can urban-generated rainfall be predicted with satisfactory skill for a city that has a strong URE during the warm season, such as Atlanta, GA? and (2) If so, which suite of meteorological variables can be used to most effectively distinguish days with a detectable URE from those days lacking a URE signal?

This paper provides a potentially "first of its kind" attempt at establishing a framework for predicting the URE. Building upon the work of McLeod et al. (2017), we use the city of Atlanta as a testbed for the analysis. **Section 2** will provide an overview of the data and methodology, and **Section 3** presents results. **Section 4** summarizes key conclusions and potential pathways forward.

2 MATERIALS AND METHODS

2.1 Data

One novel aspect of this study is the use of the Multi-sensor Precipitation Estimates (MPE) dataset to create a database of urban rainfall days (URDs). MPE (Fulton et al., 1998; Seo, 1998; Seo et al., 2010) is a gridded precipitation product that blends Doppler radar estimates and observations from station gauges. The use of this gridded dataset offers a more complete representation of precipitation across the study region, which is particularly important given the convective nature of precipitation during the warm season. The network of station gauges across northern Georgia is not be able to adequately capture convective precipitation totals at the local scale, but Doppler radar provides estimated precipitation totals that can aid in filling these coverage gaps. Our analysis spanned the period 2002–2019 (18 years), which reflects the availability of MPE data. The spatial resolution is approximately 4 km × 4 km, while the temporal resolution is defined as a hydrologic day, or the 24-h period extending from 1200 UTC to 1200 UTC. The high spatial resolution reflects another important reason for using the MPE dataset in this study. It is important to acknowledge that typical inaccuracies associated with Doppler radar (e.g., bright band contamination, Z-R relationships, spatial coverage, precipitation type, and range issues) and station gauges (e.g., wind, siting, and undercatch) will affect the precipitation estimates analyzed in this study (Smith et al., 1996; Sieck et al., 2007; Seo et al., 2010).

The ERA-Interim reanalysis dataset (Dee et al., 2011) is employed to construct synoptic-scale composite maps of the following meteorological variables: 500 hPa geopotential heights, 700 hPa vertical velocity, 700 hPa wind speed, 2-m dew point temperature, integrated vapor transport, precipitable water, and 1,000 hPa divergence. This dataset is produced from a 4-dimensional variational (4D-Var) analysis of observations over a 12-h analysis window. The spatial resolution is 0.75° × 0.75° (80 km × 80 km), and the temporal resolution is 6-hourly (0000, 0600, 1200, 1800 UTC), which was further aggregated to the daily scale for this study. The period of record used for the ERA-Interim reanalysis is the same as that of the MPE dataset.

The ERA-Interim reanalysis is also used to create a daily database of 700 hPa wind speed and direction over the metropolitan area of Atlanta. Shepherd et al. (2002) noted that the 700 hPa level can be used for defining prevailing wind flow in urban climatology studies. The average of four ERA-Interim reanalysis grid cells centered over the Atlanta area (32.75–34.25°N, 83.5–85°W) was used to develop the wind climatology. While the 700 hPa wind climatology could have been developed from atmospheric sounding data collected from nearby Peachtree City, GA (KFFC; located about 25 miles southwest of downtown Atlanta), there are a few advantages

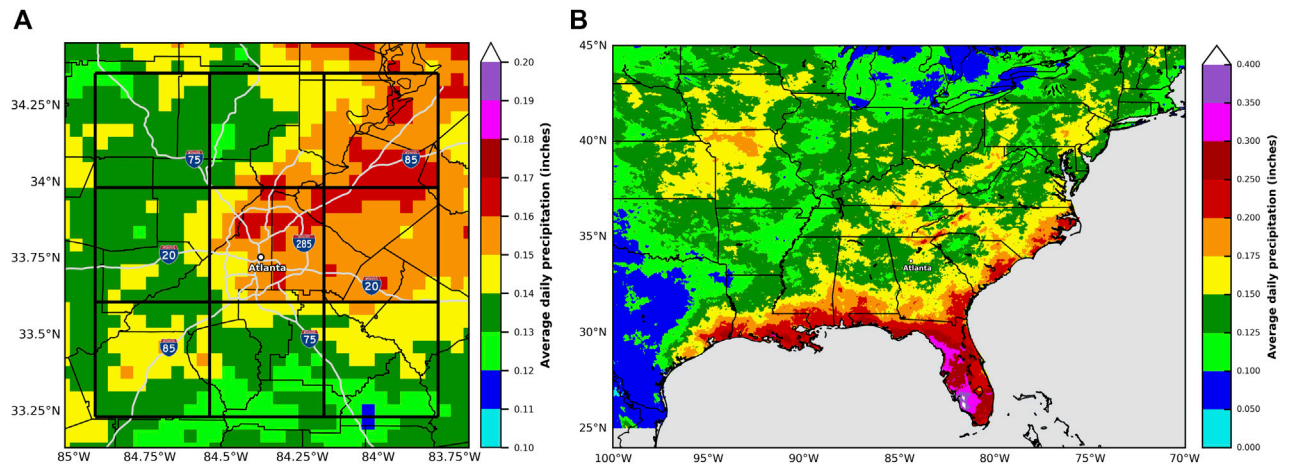

FIGURE 1 | (A) Mean daily precipitation during meteorological summer (JJA, 2002–2019). The 9-cell gridded framework is indicated by the black-outlined boxes. **(B)** Same for the entire southeastern U.S.

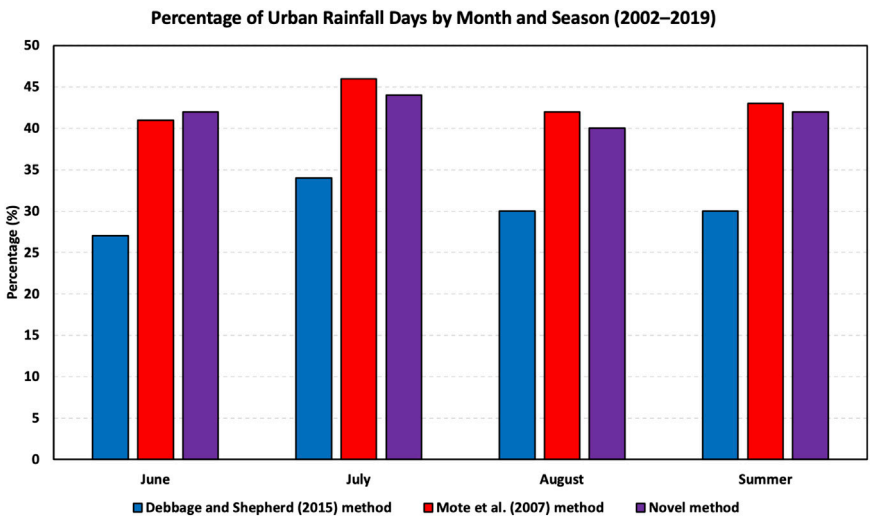

FIGURE 2 | Percentage of urban rainfall days by month and season (2002–2019) for the three different methods employed in this study.

to using the reanalysis data. First, atmospheric sounding data is only collected twice (1200 UTC and 0000 UTC) per day, whereas the 6-hourly resolution of the reanalysis dataset provides a more precise daily average of 700 hPa winds. In addition, the gridded reanalysis data can be used to compute a more spatially representative average of the 700 hPa wind field across the Atlanta metropolitan area, while the sounding data provides a more localized, point-based estimate of 700 hPa winds.

The third key dataset used in this study is the archive of atmospheric soundings provided by the University of Wyoming's Department of Atmospheric Science (University of Wyoming, 2020). During the 18-year period from 2002 to 2019, sounding data were gathered at KFFC for every day during meteorological summer (JJA). However, only soundings launched at 0000 UTC each day were collected since we are only interested in the most convectively active portion of the day. Because each sounding has a different number of observations at unique pressure levels, a linear interpolation scheme had to be applied to pressure, air temperature, dew point temperature, and wind components. Thus, composite soundings were constructed from these interpolated values, similar to Schroeder et al. (2016).

2.2 Methods

The analysis in this study was restricted to the core of the convective season, which we define as meteorological summer (JJA). Previous scholars (e.g., Hand and Shepherd, 2009; Mote et al., 2007) have noted that there is less large-scale atmospheric forcing and more locally-forced convective activity during this period of time. Similar to Hand and Shepherd (2009) and McLeod et al. (2017), a geographic framework with nine

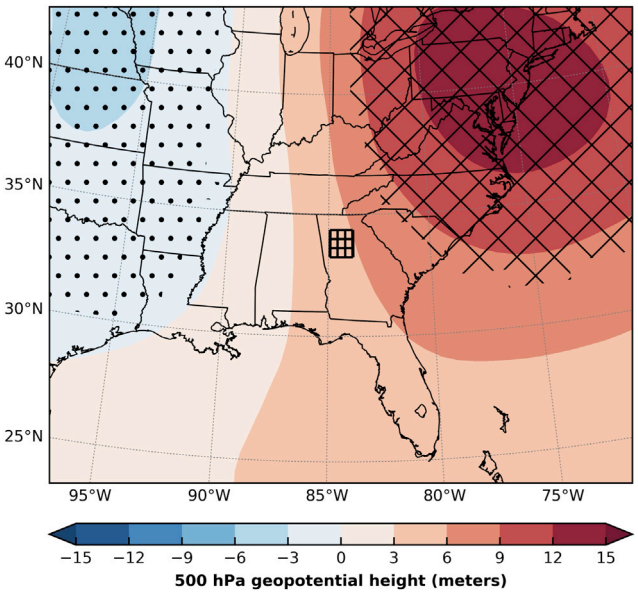

FIGURE 3 | Composite anomaly map of 500 hPa geopotential height for URDs compared to non-URDs. Cross hatching (dot hatching) indicates height anomalies that are at least 1 standard deviation greater (lower) than the sample mean. The 9-cell gridded framework centered on Atlanta is indicated by the black-outlined boxes.

equally-sized grid cells is applied to the city of Atlanta, Georgia. Specifically, the grid is centered on downtown Atlanta, with the central MPE pixel located at approximately 33.77°N and 84.39°W. Each grid cell is 9 × 9 MPE pixels, or approximately 36 km × 36 km. Thus, the total grid is 27 × 27 MPE pixels, or approximately 108 × 108 km. The approximate geographic bounds of the total grid are as follows: 33.23–34.36°N and 84.93–83.80°W. **Figure 1** shows the average daily precipitation across the Atlanta metropolitan area from 2002 to 2019, coupled with an overlay of the grid cell framework. Similar to Figure 3 in McLeod et al. (2017), the urban enhancement of summer precipitation over and downwind of Atlanta can be readily observed in **Figure 1A**. Climatologically, the entire 9-grid region is within a maritime tropical regime, so the enhancement of warm season rainfall (yellow, orange, and red shading) over and to the east of the central business district of Atlanta is indicative of the URE and consistent with previous literature (Shepherd et al., 2002; Mote et al., 2007). **Figure 1B** shows the average daily precipitation during summer over a broader region of the central and eastern United States. The urban enhancement of precipitation is still clearly visible over and downwind of the Atlanta metropolitan area. These figures serve as the foundation for all analyses conducted in this study.

Recent studies are increasingly refining what "downwind" means within the context of these studies. Earlier studies from the METROMEX era (see Shepherd et al., 2013 for a review) and into the early 2000s (Shepherd et al., 2002) operated under the assumption of a "fixed" downwind region based on climatology. McLeod et al. (2017) and Schmid and Niyogi (2013) have found that the URE is strongly a function of the prevailing wind regime such that the "downwind" effect may vary around the urban area.

For each day during the study period, the average precipitation amount was computed for each of the nine grid cells centered on the Atlanta metropolitan area. In order to define an URD, two methods were selected from previous studies and one novel method was devised. Three methods were used in this study to account for sensitivity in selecting URDs, with the goal of creating a more robust, comprehensive definition of an URD. The first method was adapted from Debbage and Shepherd (2015), who established that the intensity of an urban heat island was equal to the minimum temperature averaged over the urban area minus the minimum temperature averaged over the rural area. Similarly, we define an URD as the average precipitation over the central urban grid cell minus the precipitation averaged across the remaining 8 "rural" grid cells. Thus, an URD is observed when this relationship is positive, or the average precipitation over the central urban grid cell exceeds the average precipitation across the remaining 8 "rural" grid cells. The second method was adapted from Mote et al. (2007), who compared radar-based precipitation data over an urban grid cell centered on Atlanta with a more rural grid cell located immediately to the west. We use the same procedure for our second method for defining an URD, where an URD is observed when the average precipitation over the central urban grid cell exceeds the average precipitation over the more rural grid cell located to the west. Finally, a novel third method was created to test whether the average precipitation observed across the urban core, eastern, and northeastern grid cells were greater than the average precipitation over the remaining six grid cells. McLeod et al. (2017) showed that the greatest rainfall anomalies occur climatologically in the urban core, eastern, and northeastern grid cells due to the prevailing southwesterly-to-northwesterly mid-tropospheric wind flow during the summer. Therefore, an URD would occur if the precipitation averaged across the urban core, eastern, and northeastern grid cells exceeded that of the remaining six grid cells. This novel third method is customized for the Atlanta metropolitan area, but future work could explore whether this method can be used for other regions, depending on the local mid-tropospheric wind pattern.

Figure 2 shows the percentage of URDs by month and season for the three different methods. The first method based on Debbage and Shepherd (2015) is clearly the most conservative of the three methods, as only 30 percent of all summer days from 2002 to 2019 are classified as URDs. In contrast, over 40 percent of all summer days are classified as URDs for the Mote et al. (2007) and novel methods. Similar monthly patterns emerge among the three methods, as all three observe their greatest percentage of URDs during July. The Debbage and Shepherd (2015) and Mote et al. (2007) methods record their least percentage of URDs during June, while the novel method records its least percentage of URDs during August.

A HYSPLIT (Hybrid Single-Particle Lagrangian Integrated Trajectory) backward trajectory analysis was conducted for the 99th percentile and greater URDs (n = 17 days), based on the novel method of defining URDs (Stein et al., 2015; Rolph et al.,

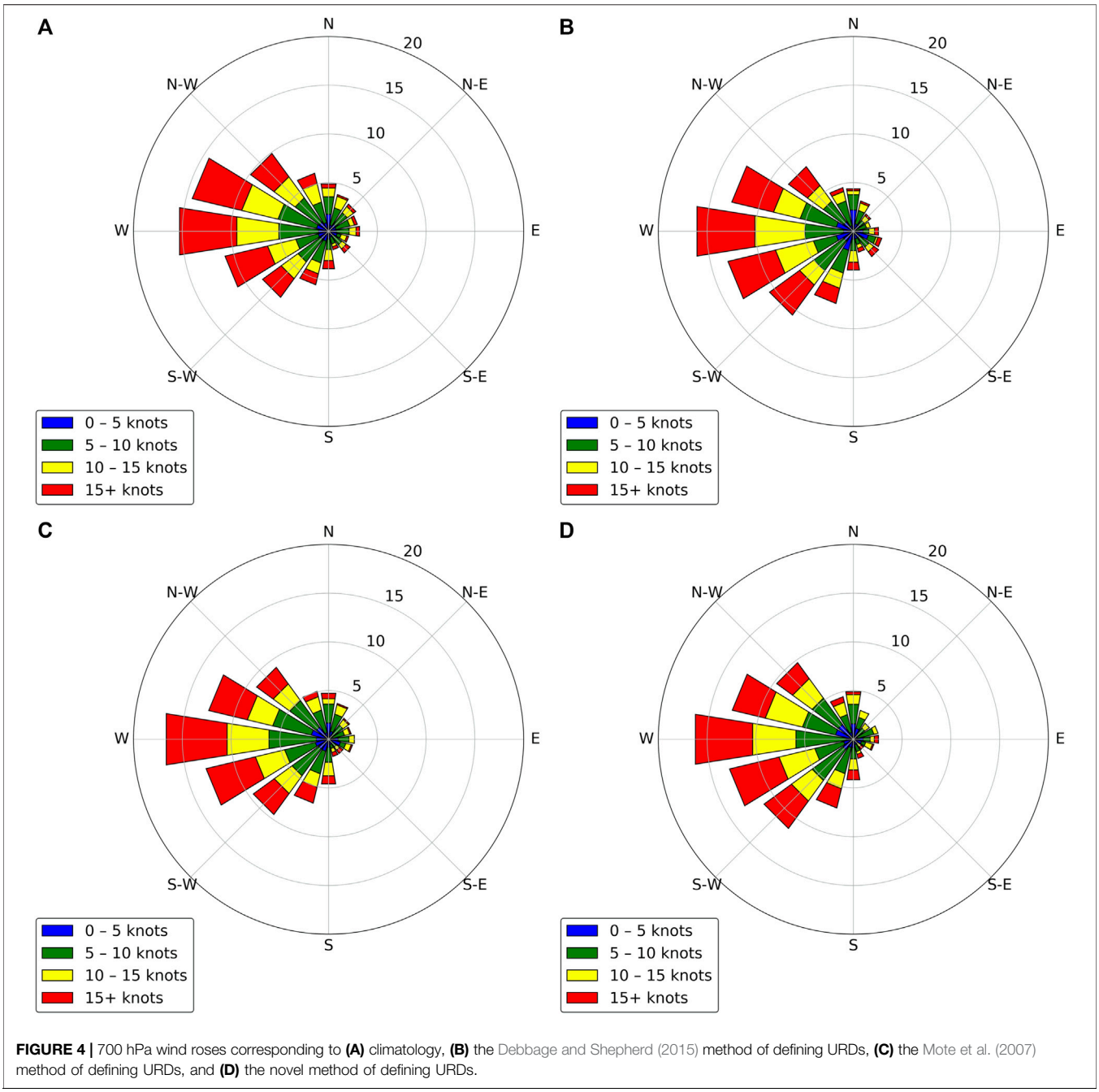

FIGURE 4 | 700 hPa wind roses corresponding to **(A)** climatology, **(B)** the Debbage and Shepherd (2015) method of defining URDs, **(C)** the Mote et al. (2007) method of defining URDs, and **(D)** the novel method of defining URDs.

2017). Each trajectory was initialized over Atlanta and run backward in time for a total of 72 h using the North American Regional Reanalysis (NARR) dataset. Three distinct trajectories initialized at 10 m, 500 m, and 1,500 m above ground level were computed for each daily simulation. Finally, the hourly latitude and longitude coordinates for all of the 17 trajectory simulations were averaged together to form single composite trajectories at the three heights above ground level.

Zhang et al. (2020) used a *k*-means cluster analysis in their assessment of urbanization and rainfall variability. However, the cluster analysis was used for categorizing the intensity of urbanization. Herein, a *k*-means cluster analysis was performed on the daily MPE data spanning each summer (JJA) season from 2002 to 2019, resulting in a total of 1,652 days for analysis. This sample of 1,652 days was partitioned into 8 clusters, in which each daily observation is assigned to the cluster with the nearest mean. Thus, the precipitation values for each pixel depicted in **Figure 12** represent the nearest means, or the centers of each cluster. A total of 8 clusters was chosen to provide enough variability in the cluster partitioning so that an urban signal could be detected. A sensitivity analysis was conducted by selecting 7 and 9 clusters, but the results were generally similar to the analysis using 8 clusters. Because the urban signal was more

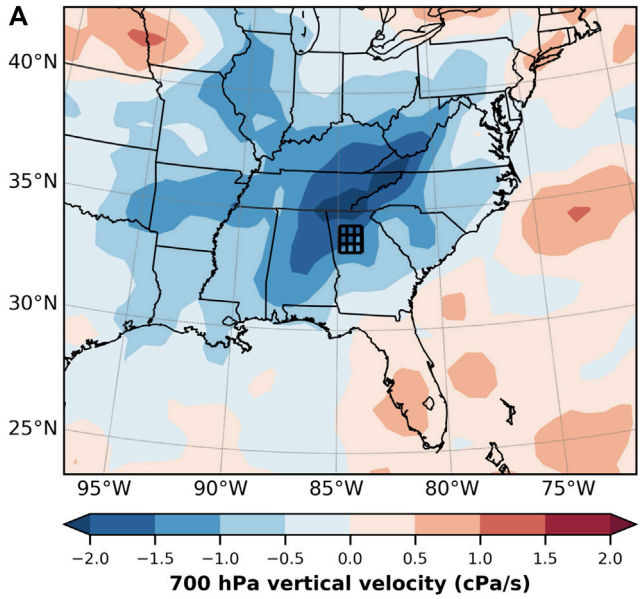

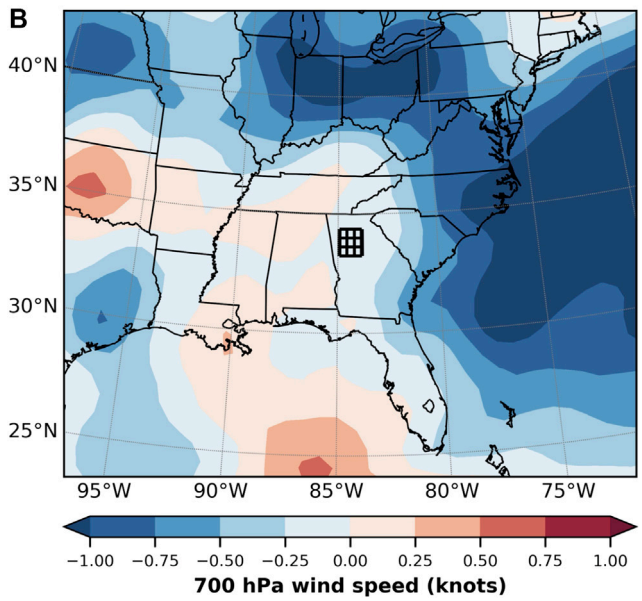

FIGURE 5 | Composite anomaly map of **(A)** 700 hPa vertical velocity and **(B)** 700 hPa wind speed for URDs compared to non-URDs. The 9-cell gridded framework centered on Atlanta is indicated by the black-outlined boxes.

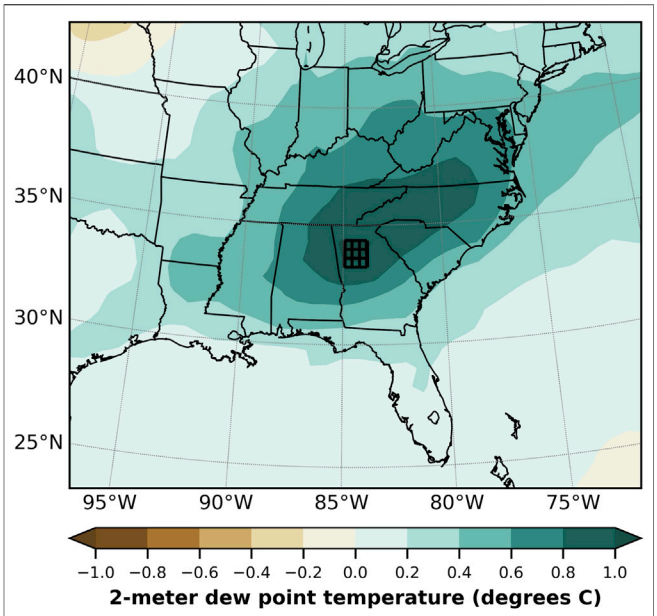

FIGURE 6 | Composite anomaly map of 2-m dew point temperature for URDs compared to non-URDs. The 9-cell gridded framework centered on Atlanta is indicated by the black-outlined boxes.

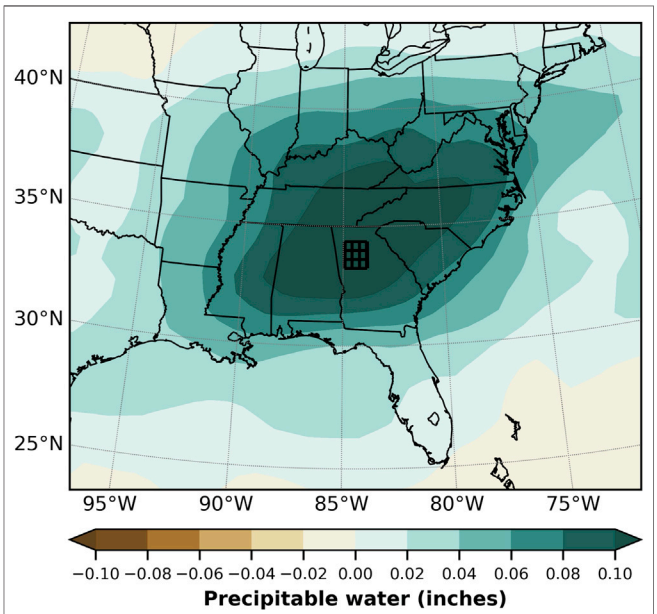

FIGURE 7 | Composite anomaly map of precipitable water for URDs compared to non-URDs. The 9-cell gridded framework centered on Atlanta is indicated by the black-outlined boxes.

robust in the 8-cluster analysis, it was chosen for further examination.

3 RESULTS

3.1 Synoptic-Scale Composites

The synoptic-scale compositing analysis reveals that there are a consistent set of meteorological ingredients that are needed to produce an URD. Because the three methods produce very similar composite maps across all seven meteorological variables, only the maps for the most conservative method (i.e., Debbage and Shepherd, 2015) are displayed in the corresponding figures below. It is important to note that the anomalies for each map were calculated as the difference between the average of all URDs and non-URDs during 2002–2019. While

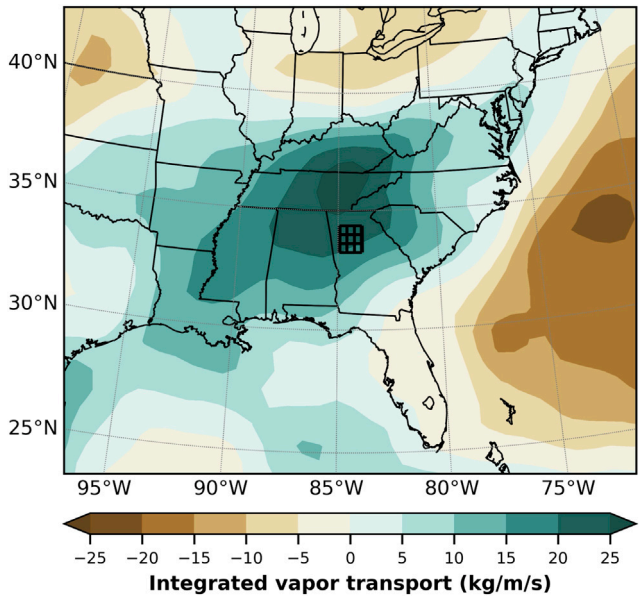

FIGURE 8 | Composite anomaly map of integrated vapor transport for URDs compared to non-URDs. The 9-cell gridded framework centered on Atlanta is indicated by the black-outlined boxes.

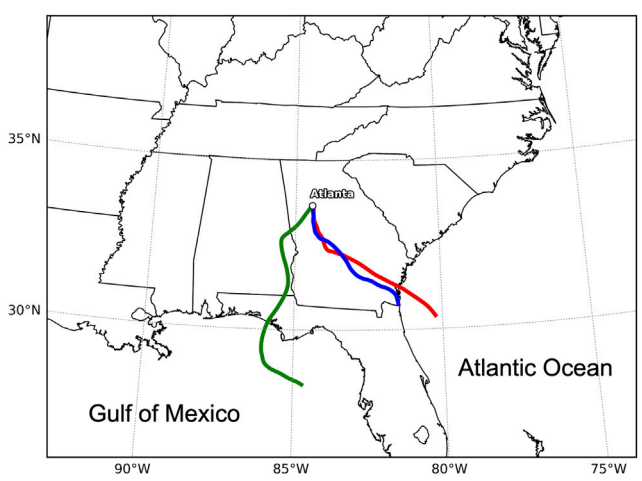

FIGURE 9 | HYSPLIT backward trajectory analysis for the 99th percentile and greater URDs ($n = 17$ days). The trajectories are color-coded as follows: 10 m above ground level (red line), 500 m above ground level (blue line), and 1,500 m above ground level (green line).

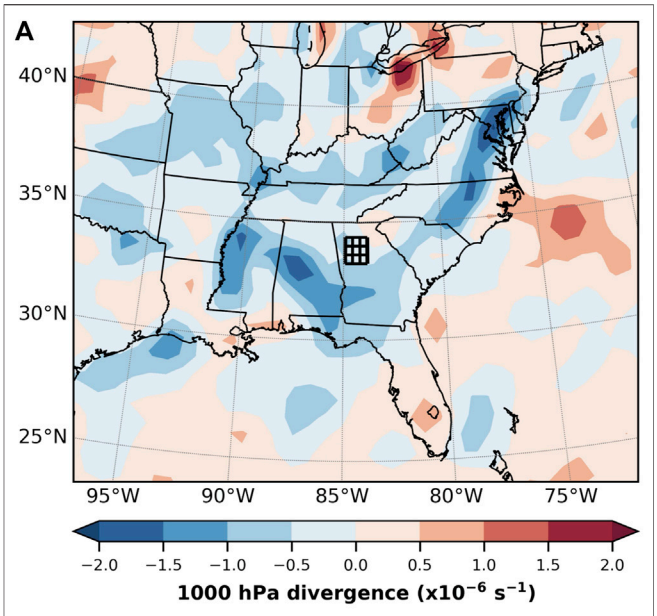

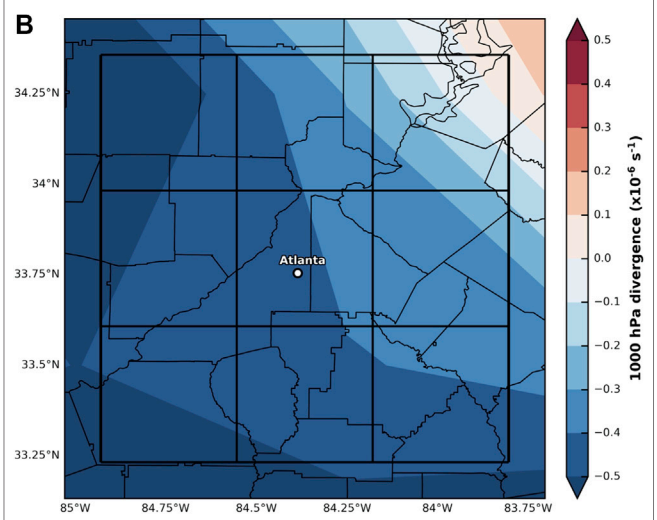

FIGURE 10 | Composite anomaly map of 1,000 hPa divergence for URDs compared to non-URDs across the Southeast region **(A)** and the metropolitan Atlanta area **(B)**. The 9-cell gridded framework centered on Atlanta is indicated by the black-outlined boxes.

the magnitude of the anomalies may appear small, it is likely just a function of the time of year being analyzed (i.e., summer) and the mesoscale nature of the precipitation pattern under examination.

In **Figure 3**, the composite map for 500 hPa geopotential heights indicates that Atlanta is caught between weak negative anomalies to the west and stronger positive anomalies to the northeast. Both the negative height anomalies over the Great Plains and the positive height anomalies over the Mid-Atlantic and Northeast U.S. are statistically significant based on a Z-score test. This anomaly pattern should promote west-southwesterly flow and advection over the Atlanta area, which is consistent with the wind rose analysis presented in **Figure 4**. **Figure 5A** shows that negative anomalies of 700 hPa vertical velocity are present over the Atlanta metropolitan area, indicating upward motion is occurring downstream of the weakly negative 500 hPa height anomalies over the Central Plains region. **Figure 5B** indicates that slightly weaker-than-average 700 hPa winds are present over Atlanta. This is consistent with the results of McLeod et al. (2017), who found that positive rainfall anomalies over the urban core of Atlanta are often associated with weaker-than-average 700 hPa winds. Low-level moisture is anomalously high

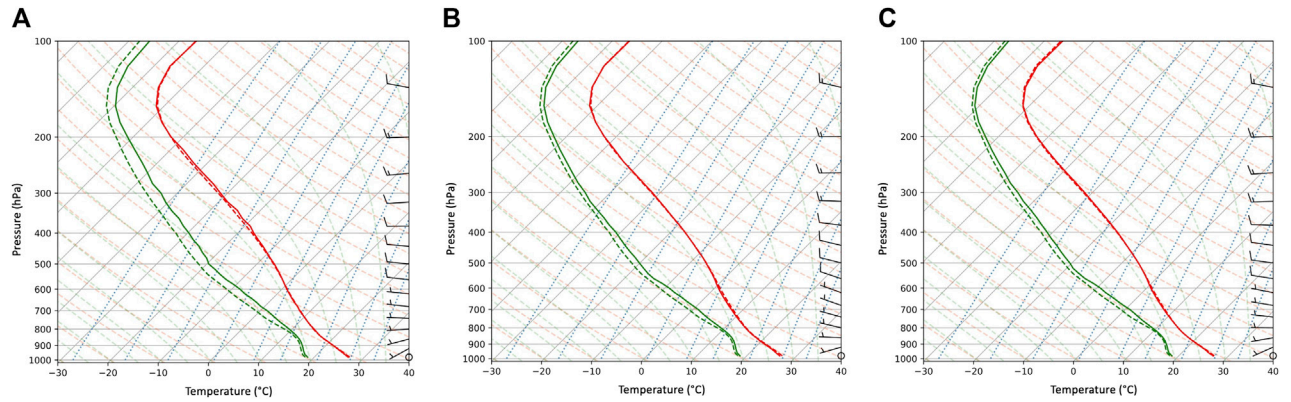

FIGURE 11 | Composite soundings corresponding to **(A)** the Debbage and Shepherd (2015) method of defining URDs, **(B)** the Mote et al. (2007) method of defining URDs, and **(C)** the novel method of defining URDs. Each sounding has a set of dashed and solid air temperature (red) and dew point temperature (green) lines. The dashed lines represent the climatological mean sounding for every June–August day during 2002–2019, while the solid lines represent only the URDs.

over the Atlanta area, as depicted in **Figure 6**. Dixon and Mote (2003) found that low-level moisture was more important than UHI intensity in producing urban-generated precipitation over Atlanta. In addition, **Figures 7**, **8** reveal that positive anomalies of precipitable water and integrated vapor transport are present across the Atlanta metropolitan area during URDs. Thus, the entire atmospheric column is moister compared to average, which is supported by the composite sounding analysis shown later in **Figure 10**. Schroeder et al. (2016) found that for extreme urban flooding, precipitable water values were typically in the 1–3% range of historical values.

In **Figure 9**, a HYSPLIT backward trajectory analysis is presented for the 99th percentile and greater URDs (n = 17 days), according to the novel method of defining URDs. It is clear that the most extreme URDs are characterized by low-level moisture transport from the Atlantic Ocean, while mid-level moisture transport occurs from the Gulf of Mexico. This deep-layer moisture transport from two subtropical bodies of water supports the positive anomalies in both precipitable water and integrated vapor transport that were shown over the Atlanta area in **Figures 7**, **8**.

Given that the synoptic environment on URDs are supportive for convection, a composite of 1,000 hPa divergence was conducted. **Figure 10** shows that a broad area of convergence is present on URDs as compared to non-URDs. We hypothesize that the background convergent flow is a condition supportive of convective forcing at the meso-gamma scale associated with the urban environment itself. Shepherd el al. (2010) and Debbage and Shepherd (2019) found evidence of enhanced low-level convergence in their modeling studies of urban-enhanced convective precipitation.

The compositing results suggests that a synoptic urban convective regime (SUCR) represents a baseline environment supportive of the urban rainfall effect. However, additional analysis is required to add credibility to the SUCR hypothesis.

3.2 Wind Rose Analysis

In **Figure 4**, 700 hPa wind roses for the three methods of defining URDs (**Figures 4B–D**) are compared against the climatological wind rose for all summer days during 2002–2019 (**Figure 4A**). While it is evident that the climatological wind rose is nearly identical to the other three wind roses, there are some important points that can be made with respect to URDs. First, URDs can occur under any wind direction at 700 hPa, but they are most commonly observed when the flow is southwesterly-to-northwesterly. Indeed, over 50% of URDs for any of the three methods observed southwesterly-to-northwesterly flow at 700 hPa. McLeod et al. (2017) captured this finding when describing the urban rainfall signature around Atlanta as "flow regime dependent." In addition, URDs can occur under a wide range of 700 hPa wind speeds, but they most commonly occur when wind speeds are between 5 and 10 knots. Around one-third of URDs for any of the three methods observed 700 hPa wind speeds between 5 and 10 knots. McLeod et al. (2017) showed that slower 700 hPa wind speeds were more effective at producing positive precipitation anomalies directly over the Atlanta urban core, while faster wind speeds tended to be associated with enhanced precipitation downwind of the Atlanta urban core.

3.3 Composite Atmospheric Soundings

Figure 11 presents composite atmospheric soundings for all URDs identified using each of the three methods. Each sounding has a set of dashed and solid air temperature and dew point temperature lines. The dashed lines represent the climatological mean sounding for every June–August day during 2002–2019, while the solid lines represent only the URDs. The air temperature lines are mostly on top of each other, indicating very little difference between URDs and climatology. However, the dew point temperature lines for URDs are consistently warmer and closer to the air temperature lines, when compared against climatology. The atmosphere during URDs is thus more moist compared to the climatological average summer day, and this enhanced moisture can be found throughout the tropospheric column. Finally, the wind profiles reveal that flow is predominately westerly throughout much of the atmospheric column, with an increase in speed as pressure decreases with height.

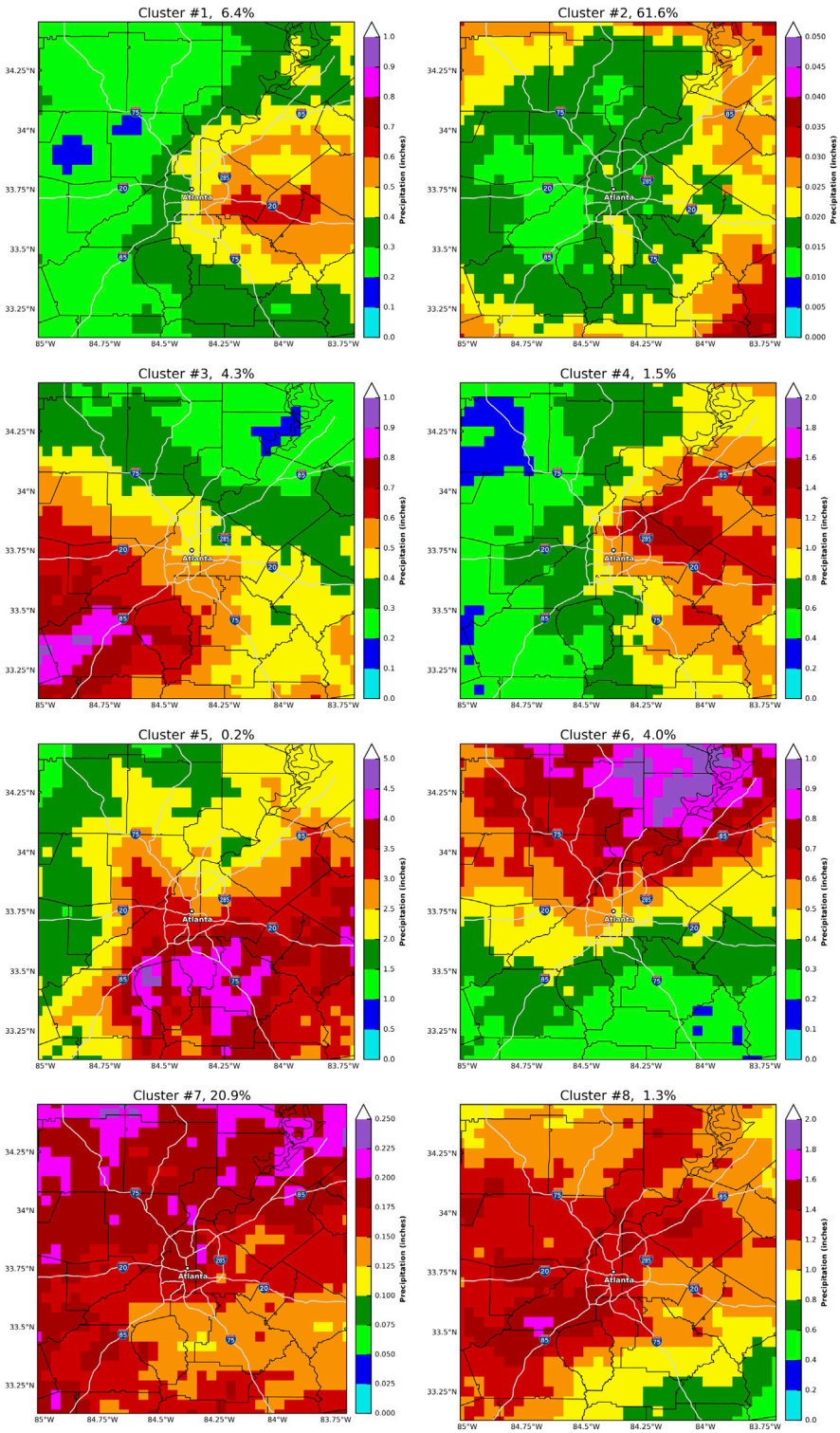

FIGURE 12 | *K*-means cluster maps (1–8), with the percentage of days associated with each cluster located at the top of each map.

These soundings indicate marginal instability, or the condition when localized convection is favored over widespread thunderstorm activity. The urban environment of Atlanta via the heat island and convergent forcing can more effectively initiate convection during periods of weak instability when the mesoscale dominates any synoptic-scale processes. These

findings are strongly supported by Dixon and Mote (2003), who also performed a comparison of soundings between UHI-induced precipitation events and their climatological study period. While they found that both air temperature and dew point temperature differed significantly between UHI-induced precipitation days and average days, the differences for dew point temperature were much greater in magnitude, particularly in the bottom half of the troposphere (Dixon and Mote, 2003). This led them to conclude that low-level moisture, rather than UHI intensity, is the dominant factor controlling the occurrence of urban-generated convection.

3.4 K-Means Cluster Analysis

Figures 12A–H show the results of the *k*-means cluster analysis, with the 8 clusters mapped across the Atlanta, GA region. Over 60% of the sample corresponds to days with relatively minimal precipitation (Cluster #2), which is consistent with the summertime climatology of thunderstorm activity across the Atlanta metropolitan area (Rose et al., 2008; Bentley et al., 2012). Most days during the summer are characterized by little to no convective precipitation. The next highest (~20%) percentage of days occurs in Cluster #7, where the greatest precipitation occurs over northern portions of the region and within the urban core of Atlanta. This cluster provides some indication of an urban rainfall effect over the I-285 corridor of Atlanta, but the most compelling evidence of an urban rainfall effect can be found in Clusters #1 and #4. Though collectively occurring only about 8% of the time, these two clusters reveal a pronounced urban rainfall signal, as precipitation is maximized immediately over and downwind (i.e., to the east) of downtown Atlanta. Taken together, the results of this cluster analysis confirm that the urban rainfall effect can be readily detected in the summertime precipitation climatology across the Atlanta metropolitan area.

4 DISCUSSION

Overall, this study has moved the literature a step forward towards the predictability of the urban rainfall effect. Using a combination of synoptic compositing, wind rose, and *k*-means cluster analyses, a set of ingredients supportive of the urban rainfall effect in the Atlanta area are presented as representative of a synoptic urban convective regime (SUCR):

- Primarily southwesterly-to-northwesterly flow at 700 hPa
- Weaker-than-average winds at 700 hPa
- Weakly negative (strongly positive) 500 hPa height anomalies to the west (northeast)
- Anomalously moist surface and atmospheric column
- Background low-level convergent flow

Our analysis, possibly for the first time, also quantifies how often the urban rainfall effect occurs during the warm season. The *k*-means cluster analysis suggests that the urban rainfall effect is detectable in about 8% of the sample days.

Ultimately, the urban rainfall effect will need to be a part of detailed predictive capabilities by forecasters and modeling systems. This study has laid a basic foundation for understanding the synoptic-scale environment that is supportive of the urban rainfall effect. This could provide some initial guidance for forecasters on large-scale conditions in order to refine localized precipitation or lightning guidance around cities. Future regional modeling studies can evaluate our findings by conducting simulations of case days representative of this synoptic urban convective regime under varying urban landscape scenarios. A limitation of this study is the focus on one geographic region. Future studies should consider other cities and methodologies like self-organizing maps.

DATA AVAILABILITY STATEMENT

Publicly available datasets were analyzed in this study. The MPE database can be found here: http://convection.meas.ncsu.edu:8080/thredds/catalog/ncep/mpe/netcdf/stage4/catalog.html. The ERA-Interim reanalysis dataset can be found here: https://www.ecmwf.int/en/forecasts/datasets/reanalysis-datasets/era-interim. The University of Wyoming atmospheric sounding data can be found here: http://weather.uwyo.edu/upperair/sounding.html. The HYSPLIT backward trajectory data can be found here: https://www.ready.noaa.gov/HYSPLIT_traj.php.

AUTHOR CONTRIBUTIONS

MS and JM contributed equally to the development of this manuscript including analysis and interpretation. JM generated much of the data analysis and MS conducted the interpretation and writing. JM also assisted with writing and interpretation.

FUNDING

This research was funded by NASA Grant 80NSSC20K1268.

ACKNOWLEDGMENTS

The authors acknowledge the NASA Interdisciplinary Science Program (NASA IDS). We particularly acknowledge the guidance of Kathy Hibbert and Aaron Pina. We also extend a special acknowledgment to Gail Skafronick-Jackson.

REFERENCES

Ashley, W. S., Bentley, M. L., and Stallins, J. A. (2012). Urban-Induced Thunderstorm Modification in the Southeast United States. *Climatic Change* 113 (2), 481–498. doi:10.1007/s10584-011-0324-1

Bentley, M. L., Stallins, J. A., and Ashley, W. S. (2012). Synoptic Environments Favourable for Urban Convection in Atlanta, Georgia. *Int. J. Climatol.* 32 (8), 1287–1294. doi:10.1002/joc.2344

Debbage, N., and Shepherd, J. M. (2015). The Urban Heat Island Effect and City Contiguity. *Comput. Environ. Urban Syst.* 54, 181–194. doi:10.1016/j.compenvurbsys.2015.08.002

Debbage, N., and Shepherd, J. M. (2019). Urban Influences on the Spatiotemporal Characteristics of Runoff and Precipitation during the 2009 Atlanta Flood. *J. Hydrometeorology* 20 (1), 3–21. doi:10.1175/jhm-d-18-0010.1

Dee, D. P., Uppala, S. M., Simmons, A. J., Berrisford, P., Poli, P., Kobayashi, S., et al. (2011). The ERA-Interim Reanalysis: Configuration and Performance of the Data Assimilation System. *Q.J.R. Meteorol. Soc.* 137, 553–597. doi:10.1002/qj.828

Dixon, P. G., and Mote, T. L. (2003). Patterns and Causes of Atlanta's Urban Heat Island-Initiated Precipitation. *J. Appl. Meteorol.* 42, 1273–1284. doi:10.1175/1520-0450(2003)042<1273:pacoau>2.0.co;2

Fulton, R. A., Breidenbach, J. P., Seo, D. J., Miller, D. A., and O'Bannon, T. (1998). The WSR-88D Rainfall Algorithm. *Weather Forecast.* 13 (2), 377–395. doi:10.1175/1520-0434(1998)013<0377:twra>2.0.co;2

Hand, L., and Shepherd, J. M. (2009). An Investigation of Warm Season Spatial Rainfall Variability in Oklahoma City: Possible Linkages to Urbanization and Prevailing Wind. *J. Appl. Meteorology Climatology* 48, 251–269. doi:10.1175/2008JAMC2036.1

Jin, M., and Shepherd, J. M. (2008). Aerosol Relationships to Warm Season Clouds and Rainfall at Monthly Scales over east China: Urban Land versus Ocean. *J. Geophys. Res. Atmospheres* 113 (D24), 1–12. doi:10.1029/2008jd010276

Johnson, B., and Shepherd, J. M. (2018). An Urban-Based Climatology of winter Precipitation in the Northeast United States. *Urban Clim.* 24, 205–220. doi:10.1016/j.uclim.2018.03.003

Landsberg, H. E. (1956). The Climate of Towns. *Man's Role in Changing the Face of the Earth* 2, 584–606.

Liu, J., and Niyogi, D. (2019). Meta-Analysis of Urbanization Impact on Rainfall Modification. *Sci. Rep.* 9 (1), 7301–7314. doi:10.1038/s41598-019-42494-2

McLeod, J., Shepherd, M., and Konrad, C. E., II (2017). Spatio-Temporal Rainfall Patterns Around Atlanta, Georgia and Possible Relationships to Urban Land Cover. *Urban Clim.* 21, 27–42. doi:10.1016/j.uclim.2017.03.004

Mitra, C., and Shepherd, M. (2016). "Urban Precipitation: A Global Perspective," in *The Routledge Handbook of Urbanization and Global Environment Change*. Editors K. C. Seto and W. Solecki (London, United Kingdom: Routledge), 152–168. Chapter 11.

Mitra, C., Shepherd, J. M., and Jordan, T. (2012). On the Relationship between the Premonsoonal Rainfall Climatology and Urban Land Cover Dynamics in Kolkata City, India. *Int. J. Climatol.* 32 (9), 1443–1454. doi:10.1002/joc.2366

Mote, T. L., Lacke, M., and Shepherd, J. M. (2007). Radar Signatures of the Urban Effect on Precipitation Distribution: a Case Study for Atlanta, Georgia. *Geophys. Res. Lett.* 34 (20), L20710. doi:10.1029/2007GL031903

Rolph, G., Stein, A., and Stunder, B. (2017). Real-Time Environmental Applications and Display System: Ready. *Environ. Model. Softw.* 95, 210–228. doi:10.1016/j.envsoft.2017.06.025

Rose, L. S., Stallins, J. A., and Bentley, M. L. (2008). Concurrent Cloud-To-Ground Lightning and Precipitation Enhancement in the Atlanta, Georgia (United States), Urban Region. *Earth Interactions* 12 (11), 1–30. doi:10.1175/2008EI265.1

Schmid, P. E., and Niyogi, D. (2013). Impact of City Size on Precipitation-modifying Potential. *Geophys. Res. Lett.* 40 (19), 5263–5267. doi:10.1002/grl.50656

Schroeder, A., Basara, J., Shepherd, J. M., and Nelson, S. (2016). Insights into Atmospheric Contributors to Urban Flash Flooding across the United States Using an Analysis of Rawinsonde Data and Associated Calculated Parameters. *J. Appl. Meteorology Climatology* 55 (2), 313–323. doi:10.1175/JAMC-D-14-0232.1

Seo, D.-J. (1998). Real-Time Estimation of Rainfall fields Using Radar Rainfall and Rain Gage Data. *J. Hydrol.* 208, 37–52. doi:10.1016/S0022-1694(98)00141-3

Seo, D.-J., Seed, A., and Delrieu, G. (2010). "Radar and Multisensor Rainfall Estimation for Hydrologic Applications," in *Rainfall: State of the Science (Geophysical Monograph Series)*. Editors F. Y. Testik and M. Gebremichael (Washington, DC: American Geophysical Union), 191, 79–104. doi:10.1029/2010gm000952

Seto, K. C., and Shepherd, J. M. (2009). Global Urban Land-Use Trends and Climate Impacts. *Curr. Opin. Environ. Sustainability* 1 (1), 89–95. doi:10.1016/j.cosust.2009.07.012

Shepherd, J. M., Andersen, T., Strother, C., Horst, A., Bounoua, L., and Mitra, C. (2013). Urban Climate Archipelagos: A New Framework for Urban Impacts on Climate. IEEE Earthzine. Available at: https://earthzine.org/urban-climate-archipelagos-a-new-framework-for-urban-impacts-on-climate/ (Accessed May 6, 2020).

Shepherd, J. M., Pierce, H., and Negri, A. J. (2002). Rainfall Modification by Major Urban Areas: Observations from Spaceborne Rain Radar on the TRMM Satellite. *J. Appl. Meteorology* 41 (7), 689–701. doi:10.1175/1520-0450(2002)041<0689:rmbmua>2.0.co;2

Shepherd, J. M., Carter, M., Manyin, M., Messen, D., and Burian, S. (2010). The Impact of Urbanization on Current and Future Coastal Convection: A Case Study for Houston. Environ. *Environ. Plann. B Plann. Des.* 37, 284–304. doi:10.1068/b34102t

Sieck, L. C., Burges, S. J., and Steiner, M. (2007). Challenges in Obtaining Reliable Measurements of point Rainfall. *Water Resour. Res.* 43 (1), 1–23. doi:10.1029/2005WR004519

Smith, J. A., Seo, D. J., Baeck, M. L., and Hudlow, M. D. (1996). An Intercomparison Study of NEXRAD Precipitation Estimates. *Water Resour. Res.* 32 (7), 2035–2045. doi:10.1029/96WR00270

Stein, A. F., Draxler, R. R., Rolph, G. D., Stunder, B. J. B., Cohen, M. D., and Ngan, F. (2015). NOAA's HYSPLIT Atmospheric Transport and Dispersion Modeling System. *Bull. Amer. Meteorol. Soc.* 96, 2059–2077. doi:10.1175/BAMS-D-14-00110.1

University of Wyoming (2020). Weather. Dept. Of Atmospheric Science. University of Wyoming. Available online at http://weather.uwyo.edu/upperair/sounding.html (Accessed April 25, 2020).

Zhang, L. L., Chen, X. H., and Lai, R. Y. (2020). Urban Signatures of Sub-Daily Extreme Precipitation Events Over a Metropolitan Region. *Atmos. Res.* 246 (1), 105204. doi:10.1016/j.atmosres.2020.105204

Conflict of Interest: The authors declare that the research was conducted in the absence of any commercial or financial relationships that could be construed as a potential conflict of interest.

frontiers | Frontiers in Environmental Science

ORIGINAL RESEARCH
published: 02 May 2022
doi: 10.3389/fenvs.2022.872282

Analyzing the Spatial Distribution of LST and Its Relationship With Underlying Surfaces in Different Months by Classification and Intersection

*Xiao Wei and Xiao-Jun Wang**

Department of Landscape Architecture, School of Architecture, Southeast University, Nanjing, China

OPEN ACCESS

Edited by:
Zhaowu Yu,
Fudan University, China

Reviewed by:
Manob Das,
University of Gour Banga, India
Bao-Jie He,
Chongqing University, China

***Correspondence:**
Xiao-Jun Wang
xjworking@163.com

Specialty section:
This article was submitted to Environmental Informatics and Remote Sensing, a section of the journal Frontiers in Environmental Science

Received: *09 February 2022*
Accepted: *30 March 2022*
Published: *02 May 2022*

Citation:
Wei X and Wang X-J (2022) Analyzing the Spatial Distribution of LST and Its Relationship With Underlying Surfaces in Different Months by Classification and Intersection. Front. Environ. Sci. 10:872282. doi: 10.3389/fenvs.2022.872282

Urban heat islands (UHIs) have become one of the most critical issues around the world, especially in the context of rapid urbanization and global climate change. Extensive research has been conducted across disciplines on the factors related to land surface temperature (LST) and how to mitigate the UHI effect. However, there remain deficiencies in the exploration of LST changes across time and their relationship with underlying surfaces in different temperature ranges. In order to fill the gap, this study compared the LST of each month by using the quantile classification method taking the Landsat 8 images of Nanjing on May 18th, July 21st, and October 9th in 2017 as the subject and then calculated the differences between July and May as well as that between July and October by an intersection tool taking the LST classes of July as the baseline. Additionally, the spatial pattern of each temperature class and intersection area was analyzed with the help of several landscape metrics, and the land contribution index (LCI) was utilized to better quantify the thermal contribution of each underlying surface to the area. The results indicated that the difference between months mainly reflected in the medium temperature area, especially between July and October, in which landscape patterns illustrated a trend of fragmentation and decentralization. The proportions of underlying surfaces in different types of intersection revealed the distinction of their warming and cooling degrees over time, in which the warming degree of other rigid pavement was higher in the warming process from May to July, and the cooling degree of buildings was greater in the cooling process from July to October. The LCI of each underlying surface in the entire study area was different from that in each temperature class, indicating that underlying surfaces had distinguished thermal contributions in different temperature ranges. This study is expected to fill the gap in previous studies and provide a new perspective on the mitigation of UHI.

Keywords: land surface temperature, spatial distribution, urban heat island, underlying surfaces, classification, intersection, land contribution index

INTRODUCTION

The global climate change has become an indisputable fact. According to the report Climate Change 2021: Fundamentals of Natural Science released by the IPCC in August 2021, "The temperature of the past 10 years is likely to be the highest in 125,000 years. . .extreme high temperatures (including heat waves) continue to increase in frequency and intensity over most land areas of the world" (Veal, 2021). More than 356,000 heat-related deaths were reported in 2019, according to the Lancet, and that number is likely to increase with the rise in global temperature (Ebi et al., 2021; Jay et al., 2021).

With the expansion of the global population, urban areas are expected to absorb virtually all of the future growth of the world's population as well as provide necessary resources and services, leading to more rapid urbanization than ever before (Desa, 2019). However, it is accompanied by a series of urban issues, among which the UHIs effect has attracted the most attention. Due to the energy imbalance caused by changing underlying surfaces and increased anthropogenic heat in urban areas (Oke, 1982), UHIs would bring not only an unpleasant thermal comfort experience (He et al., 2020) but also a series of social equality, energy consumption, and ecological environment issues (He et al., 2022). Heat waves pose a great threat to human health, especially to vulnerable groups in cities (Markevych et al., 2017). It not only directly threatens human health through high temperature but also indirectly increases the incidence of respiratory diseases, and cardiovascular and cerebrovascular diseases (Anderson and Bell, 2011; Xu et al., 2020). In hot weather, people have to increase the frequency of indoor air conditioning and other refrigeration appliances, resulting in higher energy consumption. In turn, the heat discharged from these devices to outdoor spaces will aggravate the local heat island effect and reinforce a vicious circle (Xu et al., 2019). Particularly, high temperatures would affect the economic production of certain industries and increase excess spending on electricity, water, cooling facilities, healthcare, and medical services (He et al., 2022). More seriously, rising temperature could lead to environmental pollution and drought (Makhelouf, 2009; Mazdiyasni and AghaKouchak, 2015; Van Ryswyk et al., 2019), with significant negative effects on plant growth and wildlife habitat, further worsening ecosystems (United Nations, 2021).

UHIs effect is usually quantified in terms of temperature differences between urban and rural areas or between heat islands, cold islands, and their surroundings. The distinction

TABLE 1 | Measurement methods of the UHI effect in the literature (Wang et al., 2020).

Number	Index	Calculation method
1	Surface UHI (Rasul et al., 2015)	SUHI = T_u–T_r, SUCI = T_r–T_u, where SUHI = surface urban heat island, SUCI = surface urban cool island, T_u = mean LST of urban or core, and T_r = mean LST of rural buffer. A 10-km buffer zone around the city is used here to define the reference "rural" surface temperature
2	Surface UHI intensity (Li and Zhou, 2019)	SUHII = mean (LST_{urban})–mean (LST_{buffer}), SUHII was calculated as the difference of mean LST between the urban area and its buffer zone, in which the buffer zone is delineated with the equal size of the corresponding urban area
3	UHI intensity index (Huang et al., 2019)	UHIER = $\Delta T/T_s$=(T_i–T_s)/T_s, UHIER refers to the UHI intensity index, expressed in relative LST in the area and ΔT represents the difference between the LST of the i-th pixel (T_i) and the mean LST of rural areas (T_s)
4	Urban cool island (Kong et al., 2014)	UCI = ΔT=(T_i– $\bar{T}$) ($\Delta T \leq 0$), where $\bar{T} = \sum_1^n T_i/n$, that is to say, the summary of each pixel's land surface temperature (T_i) divided by the total number of pixels in the study area
5	Cooling intensity of UGS (Yu et al., 2018)	Defining the cooling effect of greenspace patches as the LST difference between the patch and its surrounding urban area. Defining the maximum cooling extent as the distance between the edge of the greenspace and the first turning point of a temperature drop compared with the greenspace's temperature. This turning point is the maximum ΔLST, which refers to as the cooling intensity
6	Greenspace cool island cooling capability (Zhang Y et al., 2017)	UCI = ΔT=(T_i– $\bar{T}$) (ΔT<0), where T_i is the LST of a given pixel and $\bar{T}$ is the corresponding mean LST CS = A_UCI_i–A_GCI_i(ΔT<0), where CS represents the GCI cooling capability; A_UCI and A_GCI represent the areas of UCI and GCI, respectively; and i is the ID of the corresponding grid
7	Greenspace cool island (Du et al., 2017)	GCI effect is evaluated by the LST difference between greenspaces and their surroundings. From the edge of a greenspace, and its surrounding buffer is sliced into annulus-shaped areas with a fixed width. 1) GCI range (GR): The distance between the first turning point of the temperature curve and the edge of greenspace. The unit is km. 2) Temperature drop amplitude (TA): The LST drop between the turning point and greenspace interior. The unit is °C. 3) Temperature gradient (TG): The gradient (temperature drop with unit distance) of surrounding LST. The unit is °C/km
8	Greenspace cooling island intensity (Zhang X et al., 2017)	GSCI = $\Delta T = T_u$–T_{gs}, where T_{gs} is the daily average LST_m for a certain UGS interior and T_u is the daily average land surface temperature measured by temperature and humidity probes LST_m in the external 10 m buffer of the corresponding UGS
9	Surface urban cool island (Chen et al., 2014)	Surface UCI was represented by the minimum LST of each urban green patch
10	Surface UHI intensity (Liu et al., 2016)	SUHII was defined as the mean LST difference between the urban region and its surrounding suburban area. A threshold of impervious surfaces percentage (60%) was used to separate the ISA percentage map into dense-intensity and low-intensity impervious surface areas. The urban border was produced by aggregating the dense impervious surfaces regions with an aggregation distance of 1 km. The region within the delineated border was considered an urban area, while the outside of it was defined as the suburban area

lies in the definition of a rural area or the scope of the surrounding environment. This article summarizes the commonly used methods for calculating the UHI effect, as listed in **Table 1**. Apparently, many scholars have proposed a variety of calculation methods according to their research focus, which is helpful to understand the UHI effect from different perspectives but will possibly lead to contradictory results that are not universal across regions (Huang et al., 2018; Peng et al., 2018; Li and Zhou, 2019). The Local Climate Zone scheme proposed by Stewart and Oke addresses this issue and standardizes the surface structure and cover description, thereby standardizing urban and suburban/rural sites for temperature comparison (Oke and Stewart, 2012), which is a very useful tool for studying the UHI effect across regions. However, the LCZ requires a large amount of detailed information about the study sites through survey and assessment, which is more suitable for an in-depth study of surface properties and their relationship with the UHI effect (Das and Das, 2020; Zhao et al., 2021). In this study, which focuses on the qualitative research of LST and underlying surface types at an early stage, a more feasible and replicable way is applied to classify the LST into several classes based on the quantile method, which may help diminish the error between different definitions of UHI intensity.

A number of research studies have discussed the annual and seasonal variations of LST as well as its driving factors, including the local climate (Zhou et al., 2016), terrain (Abbas et al., 2021), urbanization level (Chao et al., 2020), land use types (Zhou et al., 2014; Guha and Govil, 2020; Guha et al., 2021), landscape metrics (Masoudi and Tan, 2019; Zhang and Wang, 2020), biotope types (Vulova and Kleinschmit, 2019), building morphology (Chen et al., 2021), and tree canopy (Elmes et al., 2017). But most of them place emphasis on high-temperature areas while neglecting medium-temperature areas, and mainly aim at a specific time while barely analyzing it from a continuous-time sequence. To better understand the formation mechanism of urban climate and the roles of various factors, it is of great significance to investigate the changing trend of temperature at all ranges over time.

It has come to an agreement that underlying surfaces play a leading role in the formation of a UHI (Zhang X. et al., 2017; Stanganelli and Gerundo, 2017; Huang et al., 2019), in which natural surfaces like urban green spaces (UGS) and water bodies can effectively alleviate the UHI (Zhao et al., 2011; Sun et al., 2019; Erdem et al., 2021). Due to photosynthesis, evapotranspiration, and shadowing effects, vegetation in the UGS influences the physical environment of cities by selectively absorbing and reflecting incident radiation, and regulating latent and sensible heat exchange (Oke, 1987). At the same time, the water bodies could absorb and store more heat because of their high specific heat capacity (Ghosh and Das, 2018; Dudorova and Belan, 2019). It should be noticed that their cooling effect has thresholds regarding the size, shape, connectivity, complexity (composition and configuration), seasonal and diurnal difference, latitude, and climate difference (Yu Z. et al., 2020). However, most studies study the relationship between surface temperature and underlying surface focusing on the whole area, while little attention is paid to the differences within the area; in other words, areas with different temperature ranges may have various performances due to different thermal properties.

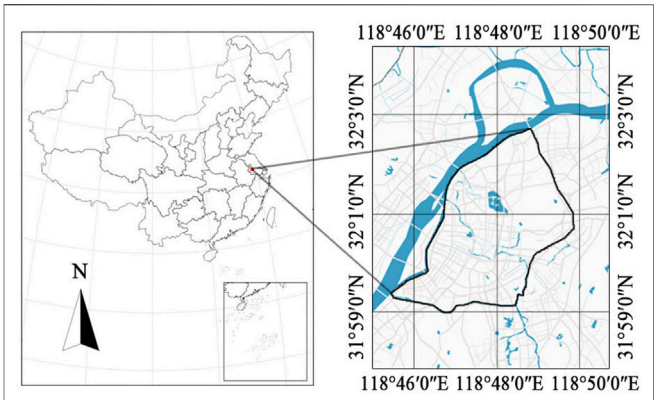

FIGURE 1 | Location of the study area.

Based on the aforementioned discussion, the previous studies have a few deficiencies in the neglect of the LST change from a continuous-time sequence, and its relationship with the underlying surface in different temperature ranges. In order to make up for those deficiencies, this study uses the quantile method to classify the LST of different months into several classes for better normalized research and uses an intersection tool to compare the difference in spatial distribution between months. In addition, the thermal contribution of different underlying surfaces in different LST classes and its variation with time are analyzed. This article is a great reference for cities going through rapid urbanization and attempting to integrate natural elements into urban centers as it takes Nanjing as the research subject due to its predominant geological location and typical urban morphology in China. In summary, this article focuses on addressing the following two issues: (1) how the spatial distribution of LST changes in different months and (2) how the thermal contribution of different underlying surfaces changes across time.

MATERIALS AND METHODS

Study Area and Data Source

Nanjing (31°14′–32°37′N, 118°22′–119°14′E) is a megacity in the Yangtze River Delta economic development zone of China with a history of over 1800 years. The total area of Nanjing is approximately 6,587 km^2, and the population of permanent residents is about 9.3 million (Nanjing Bureau of Statistics, 2019). Located in a subtropical monsoon climate zone with four distinct seasons and abundant rainfall, the average temperature of Nanjing is 17.1°C and the total precipitation is 1,294.4 mm in 2020 (Nanjing Bureau of Statistics, 2019). The topography of Nanjing comprises low mountains, hills, plains, rivers, and lakes, with elevations ranging from 7 to 448 m a.s.l. This study selected approximately 280 square kilometers in the city center

TABLE 2 | Weather condition of the selected days and detailed information of the Landsat 8 images.

Date	Air temperature	Weather condition	Cloud cover of the images (%)	The acquisition time of the images (GMT)
May 18th	18–30°C	Cloudy to sunny	6.64	02:36:34
July 21st	29–38°C	Sunny to cloudy	1.12	02:36:58
October 9th	22–29°C	Sunny	0.07	02:37:22

area of Nanjing for study (shown in **Figure 1**), which is bounded by large rivers and main roads in the city, including the Yangtze River, the Qinhuai New River, the Round City Highway, and the Ningluo Highway.

Three clear Landsat 8 images with little cloud are downloaded from the USGS Data Center (https://earthexplorer.usgs.gov/) for study, and the acquisition dates are May 18th, July 21st, and October 9th in 2017, respectively. Weather conditions of the selected dates and detailed information on the data sets are listed in **Table 2**. ENVI 5.3 software is applied to perform the data preprocessing including geometric correction, radiometric calibration, atmospheric correction, and clipping of the study area.

Classification of the Underlying Surfaces

The underlying surface of the study area is divided into four types based on the Landsat data and Baidu Map, namely, UGS, water bodies, buildings, and other rigid pavements. As the research area is in the urban center with little bare land or farmland, except for UGS, water bodies, and buildings, other rigid pavements mainly include open squares and roads.

First, the modified normalized difference water index (MNDWI) is used to extract water from the image, which is proved to be more accurate than the original normalized differential water index (Xu, 2006). The thresholds of each underlying surface are determined based on the original Landsat 8 images and Baidu map after repeated tests of different thresholds and manual calibration. In this study, the threshold of MNDWI is determined as 0.20. Second, the normalized differential vegetation index (NDVI) is used to extract UGSs from the image (Weng et al., 2004). Removing water bodies obtained from the previous steps, the threshold value of 0.35 is used for UGS identification. Third, all the water bodies and UGS are removed, which leaves only the impervious surface. Based on the building footprint information acquired from the Baidu map using Python (Sun et al., 2020), buildings are extracted from the impervious surface. Finally, the remaining pixels are classified as other rigid pavements. As a result, the four types of underlying surface map of the study area are complete. The equations of MNDWI and NDVI are as follows:

$$\mathrm{MNDWI} = (\mathrm{GREEN} - \mathrm{MIR})/(\mathrm{GREEN} + \mathrm{MIR}), \quad (1)$$

$$\mathrm{NDVI} = (\mathrm{NIR} - \mathrm{RED})/(\mathrm{NIR} + \mathrm{RED}), \quad (2)$$

where GREEN, MIR, NIR, and RED correspond to the value of bands 3, 6, 5, and 4 of Landsat 8 images, respectively.

Retrieval of Land Surface Temperature

This study applied the radiative transfer equation (RTE) to calculate the LST, which is based on the thermal infrared radiative transfer equation by removing the influence of atmosphere on thermal radiation in the process of radiative transfer to accurately obtain the surface temperature (Yu et al., 2014). The RTE has wide applicability and can be applied to the thermal infrared remote sensing data on any sensor; especially, it can achieve the highest LST accuracy in environments with high atmospheric water vapor (Sekertekin, 2019). The calculation is based on **Eq. 3**:

$$L_\lambda = [\varepsilon B(T_s) + (1-\varepsilon)L\downarrow]\tau + L\uparrow, \quad (3)$$

where L_λ is the brightness value of thermal infrared radiation received by the satellite sensor, ε is the surface emissivity, T_s is the real surface temperature (Kelvin), $B(T_s)$ is the brightness temperature, τ is the atmospheric transmittance in the thermal infrared band, and$L\downarrow$ and $L\uparrow$ are the atmospheric downward and upward radiation brightness, respectively. The last three parameters can be obtained on one of the NASA websites (http://atmcorr.gsfc.nasa.gov/) by inputting the acquisition time and central latitude and longitude. Using **Eq. 4**, the LST can be calculated as follows:

$$T_s = \frac{K_2}{\ln\left(\frac{K_1}{B(T_s)+1}\right)}, \quad (4)$$

where $K_1 = 774.89\,W/(m^2 \cdot sr \cdot \mu m)$ and $K_2 = 1321.08\,K$ for the Landsat TM images.

Analysis of Temperature Pattern

Classification Method of LST

The commonly used classification method of LST is the mean–standard deviation method (Sun et al., 2020), which divides different temperature classes according to the mean value and standard deviation of LST in the research area. However, this method may classify more areas as moderate and a much smaller proportion as hot. Taking the LST in July as an example and using the mean–standard deviation method to classify the temperature, the proportion of moderate temperature was 42.29%, and that of high temperature was only 0.49%. In addition, the proportion of each temperature class may vary a lot when comparing different months. Therefore, in order to minimize the error of comparison between months, the quantile method is used to sort all pixels in a certain order and then divide them according to a percentage (Sun et al., 2020). As a result,

TABLE 3 | Selected landscape metrics (Marks, 1995).

Landscape metrics	Abbreviation	Description
Percentage of landscape	PLAND	Proportional abundance of the corresponding patch type in the landscape (unit: %)
Patch density	PD	Number of patches of the corresponding patch type divided by total landscape area (unit: number per km2)
Mean patch area	AREA_MN	Total patch area of the corresponding patch type divided by patch number (unit: ha)
Mean Euclidean nearest neighbor distance	ENN_MN	Mean distance to the nearest neighboring patch of the same type based on the edge-to-edge distance (unit: m)
Aggregation index	AI	Number of like adjacencies involving the corresponding class, divided by the maximum possible number of like adjacencies involving the corresponding class, which is achieved when the class is maximally clumped into a single, compact patch; multiplied by 100 (unit: %)

the data amount of each temperature class, namely, the area of each temperature class is the same. In this study, the LST is divided into seven classes, from low to high, namely, extremely low-temperature class, low-temperature class, sub-low-temperature class, medium-temperature class, sub-high-temperature class, high-temperature class, and extremely high-temperature class. For the sake of concise expression, cls_1 to cls_7 is used as the abbreviation of each class, in which the cls_1 is the extremely low-temperature class and cls_7 is the extremely high-temperature class. The steps are to import the raster map of LST into ArcGIS, and use the quantile method in the reclassify tool to classify the raster into seven classes.

Landscape Pattern of Temperature Class

Five landscape metrics were selected to calculate the landscape pattern of different temperature classes as different types of patches (shown in **Table 3**). The coefficient of variation (CV) of the landscape metric is calculated to intuitively compare the differences between each temperature class in different months. The calculation method of CV is the standard deviation divided by average value, which is not affected by scale and dimension, and can be used to reflect the dispersion degree of a group of data (Lee and Stat, 1994). Similarly, different types of intersection areas are taken as patches to calculate the landscape pattern of each intersection area.

Spatial Distribution of Temperature Class

The overlap degree in each class of July and May as well as that of July and October is calculated by taking the LST classes of July as the baseline using the intersect tool in ArcGIS, in which the overlapped areas of the same class and different classes are subdivided. The higher the overlap degree of the same class in 2 months, the higher the similarity of the LST distribution in these 2 months. Meanwhile, the proportion of different underlying surfaces in each overlapped area is calculated to analyze the reasons for these differences. Then, the overlapped types of different temperature classes are divided into cold–hot overlapped type and hot–cold overlapped type. The cold–hot overlapped type refers to the area belonging to the lower temperature class in July that overlap with that belonging to the higher temperature class in another month, and the hot–cold overlapped type is the opposite. Moreover, the difference between the two overlapped types in different temperature classes is analyzed.

Calculation of the Land Contribution Index

In order to clarify the thermal impact of each underlying surface in different areas, the land contribution index (LCI) introduced by Huang et al. (2019) is calculated for comparison. The LCI is a quantitative indicator for determining the thermal contribution of the respective underlying surface to the temperature change of the entire area. It considers the temperature difference of each underlying surface and its proportion to the area into consideration shown as follows:

$$LCI = (T_i - T_m) \times P_i \ , \ i = 1, 2, 3, 4 \tag{5}$$

where T_i is the average temperature of the *i-th* underlying surface, T_m is the average temperature of the research area, i represents four kinds of underlying surfaces, and P_i refers to the proportion of the *i-th* underlying surface to the entire area. The LCI of each underlying surface in the whole research area and each temperature class as well as in the different overlapped types area are calculated, respectively. An LCI $\geq$ 0 means that the corresponding underlying surface has a positive effect on the temperature rise of the area. On the contrary, an LCI < 0 indicates that the corresponding underlying surface has a positive effect on the temperature drop of the area.

The analysis framework of this study is shown in **Figure 2**. In short, the LST of each month is classified into different classes, and then the LST classes of July are intersected with those of the other 2 months and categorized into different types. Meanwhile, the landscape pattern and underlying surface of each temperature class and intersection area are analyzed.

RESULTS

Classification of LST in Different Months

LST Classes in Different Months

The LST classes in different months and the temperature range in each class are shown in **Figure 3**; **Table 4**. The temperature is highest in July, followed by May and then October. It is clear that the distribution of LST classes in different months has similar patterns in general. The cold island effect is significant near Zijin Mountian, Xuanwu Lake, Mufu Mountain, and other large mountains and water bodies. In May, the heat island effect is more prominent in the northwest area, while it aggregates in the city center area in July. However, in October, the heat islands are

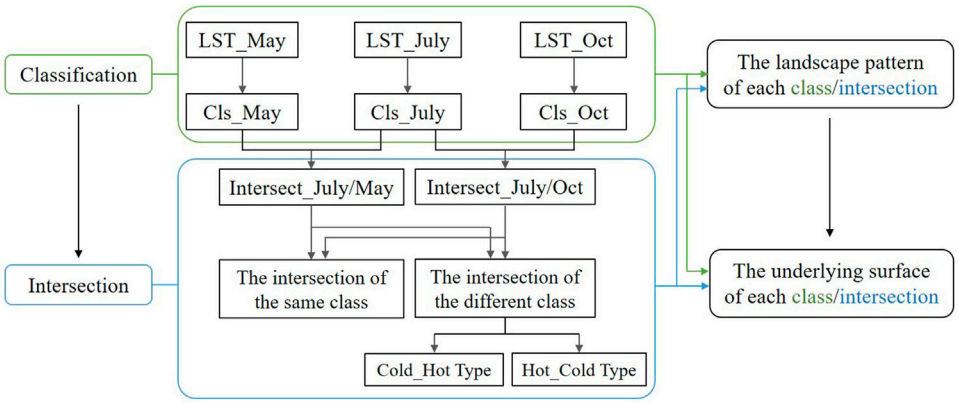

FIGURE 2 | Analysis framework.

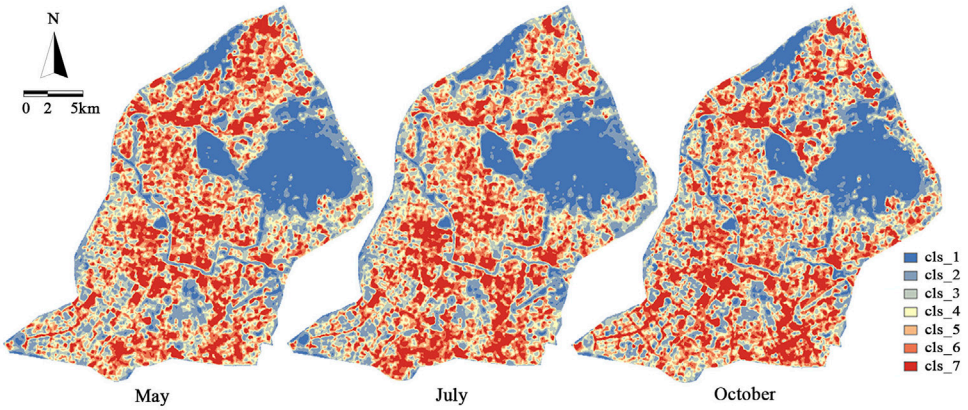

FIGURE 3 | LST classes in different months.

relatively small and scattered in the central area but more intense in the southeast and southwest areas.

Landscape Pattern of Each LST Class in Different Months

The variation coefficients of different LST classes in each month are shown in **Table 5**. The specific value of each landscape metric is shown in **Supplementary Appendix Table A1**. The larger the CV is, the higher the dispersion degree of this set of data is, that is, the greater difference in the landscape metric of this LST class in different months. According to the result, the CV of PD, AREA_MN, and ENN_MN are the highest in cls_1, that is, the extremely low-temperature class, while the CV of PLAND and AI are much smaller. It is indicated that the density, area, and distance

TABLE 4 | Temperature range of each temperature class in different months (unit: °C).

LST class	May	July	Oct
cls_1	27.71–33.96	29.46–35.98	23.02–27.22
cls_2	33.97–36.89	35.99–39.19	27.23–28.71
cls_3	36.90–38.03	39.20–40.56	28.72–29.45
cls_4	38.04–38.88	40.57–41.48	29.46–30.03
cls_5	38.89–39.64	41.49–42.31	30.04–30.60
cls_6	39.65–40.59	42.32–43.32	30.61–31.43
cls_7	40.60–51.85	43.33–52.86	31.44–44.04

TABLE 5 | CV of landscape metrics of different temperature classes in 3 months (unit: %).

	PLAND	PD	AREA_MN	ENN_MN	AI
cls_1	0.08	27.08	24.90	8.65	0.48
cls_2	0.27	14.51	13.09	3.31	1.92
cls_3	2.05	17.33	18.22	8.20	3.45
cls_4	1.17	18.96	17.23	5.69	2.95
cls_5	0.52	14.08	13.81	3.01	1.98
cls_6	1.50	5.46	4.21	1.19	0.52
cls_7	1.13	5.63	5.81	0.49	0.33

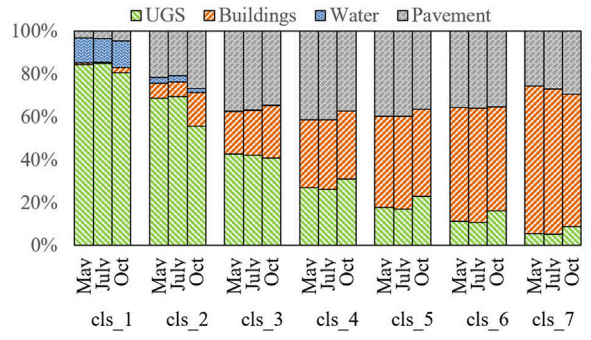

FIGURE 4 | Underlying surfaces of different temperature classes in 3 months.

of patches in the extremely cold area vary greatly from month to month, while the proportion and aggregation degree of patches have no remarkable difference. The CV of cls_6 and cls_7, that is, the high-temperature area and the extremely high-temperature area, is relatively small in all landscape metrics, that is to say, the landscape pattern of the hot area in different months is close to each other. Moreover, cls_3 and cls_4, that is, the sub-low-temperature area and the medium-temperature area, show a higher degree of variances in all metrics, while cls_2 and cls_5, that is, the low-temperature area and the sub-high-temperature area, show a lower degree of difference. In general, the landscape pattern of each temperature class in 3 months present great differences in the area with the lowest temperature and the area with the medium temperature, while there is little difference in the area with high temperature, that is, the area with strong heat island intensity.

Particularly, PLAND has the smallest CV among the 5 landscape metrics, which is reasonable due to the principle of the quantile classification method applied in this study. The CV of PD and AREA_MN is the largest, especially in the cls_1 to cls_5 areas, in which the CV of cls_1 is the largest. Combined with actual data, in October, the PD is always the highest and the AREA_MN is always the lowest among 3 months in all classes. Meanwhile, the difference between July and May is small, in which the PD in July is the lowest and the AREA_MN in July is the highest or slightly lower than in May.

With regard to the ENN_MN, the CV of ENN_MN is the highest in cls_1 and cls_3, while lowest in cls_7. The value of ENN_MN in July is the highest in cls_1 to cls_5, while slightly lower than that in other months in cls_6 and cls_7. The CV of AI is generally small, among which the CV of cls_3 is the highest and cls_7 is the lowest. In cls_2 to cls_5, where the CV is relatively high, AI in October is the smallest, and AI in July is the largest. Only in cls_4, AI in May is slightly higher than that in July.

In conclusion, the difference in landscape patterns between May and July is small but more obvious between July and October, especially the PD and AREA_MN are significantly varied among 3 months. The discrepancy is mostly reflected in the extremely cold area and the area with medium temperature, while not so remarkable in the hot area. Based on the meaning and the concrete value of each landscape metric, it is demonstrated that the LST classes in October are a large number of small patches densely distributed compared with the other 2 months, while LST classes in July and May are quite the opposite.

Underlying Surfaces of Each LST Class in Different Months

The type of the underlying surfaces and their proportions in each LST class is calculated as shown in **Figure 4**. With the rising temperature, the proportion of UGS in each LST class reduces gradually, while the proportion of buildings increases. The proportion of other rigid pavement first increases then slightly reduces. Water bodies are mainly distributed in cls_1 and cls_2, especially in the former. In the extremely low-temperature class, the proportion of UGS is the highest, more than 80%, followed by water, around 11%, and the proportion of buildings is the lowest, which is 2.48% in October and less than 1% in May and July. In the extremely high-temperature class, the proportion of UGS is the lowest, ranging from 5 to 8%; buildings account for more than 60%, and other rigid pavement accounts for about 27%.

By comparing the proportion of underlying surfaces in the same LST class between different months, it is shown that there is a slight variance between May and July, which is between 0 and 1.31%, while the high difference of up to 13.67% is found between July and October.

As for each underlying surface, the proportion of UGS in cls_1 to cls_3 in October is significantly lower than that in the other 2 months, while in cls_4 to cls_7, it is completely the opposite. In cls_1 to cls_3, the proportion of buildings in October is higher than that in May and July. In cls_4, the proportion of buildings in 3 months is the same, and in cls_5 to cls_7, the proportion of buildings is lower than that in May and July. The water bodies are mainly distributed in cls_1 and cls_2, in which the proportion of water bodies in cls_1 is higher in October than that in the other 2 months, while in cls_2, it is just the reverse. As for the other rigid pavements, the proportion in cls_1, cls_2, and cls_7 is the highest in October, while in cls_3 to cls_6, the proportion in October is the lowest among 3 months.

LCI of Each Underlying Surface

The LCI of each underlying surface in the entire area and each temperature class is shown in **Figure 5**. **Figure 5A** shows the LCI of each underlying surface in the entire area and **Figures 5B–D** show the LCI of each underlying surface in each temperature class of May, July, and October, respectively. It is clear that UGS and water are the prominent cooling surfaces, while buildings and pavement are the opposite. Because the research area is the central part of the city with mountains and lakes, such as Zijin Mountain and Xuanwu Lake, which play a remarkable role in cooling the area, the LCI of UGS and water are significantly high in this study, especially in July, reaching up to 0.94 for UGS. The LCI of each underlying surface in July is the highest and lowest in October, indicating that the underlying surfaces have a more obvious impact on LST in the summer.

However, there are a few differences comparing LCI between each temperature class. In cls_1, only the LCI of water is a negative number and has the highest value; UGS, buildings, and pavement are all positive numbers. In cls_2, the LCI of water lowers a lot, and the LCI of UGS turns to be negative with the highest value. That is to say, the water bodies are prominent in mitigating heat in the extremely

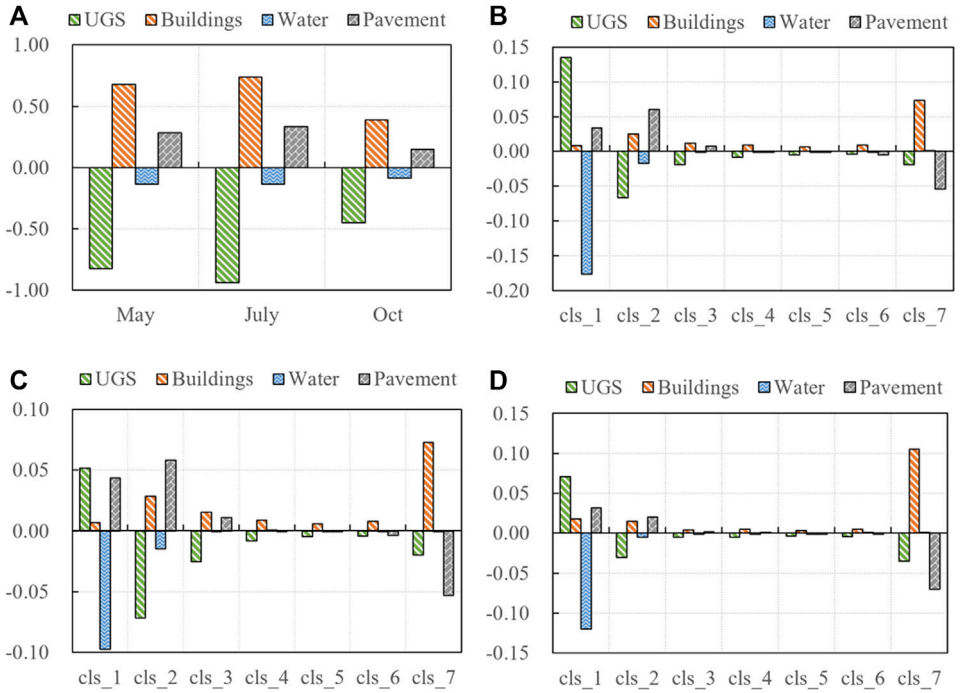

FIGURE 5 | LCI of each underlying surface in the whole area **(A)** and in each LST class in May **(B)**, July **(C)**, and October **(D)**.

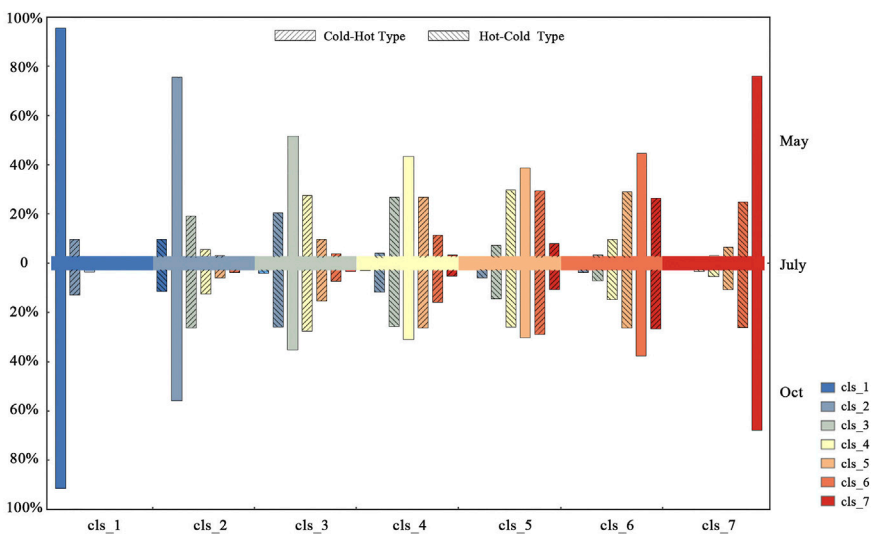

FIGURE 6 | Proportions of overlapped areas in different temperature classes in different months.

low-temperature area, while the cooling effect of UGS is more significant in the low-temperature area. The LCI in cls_3 to cls_6 is much lower than that in the first two classes. In cls_7, buildings have the highest positive value, while the other surfaces have negative value, meaning that buildings are the dominant heating surfaces in the highest temperature area, and even the pavement contributes to a cooling impact compared with buildings in this area. In general, water bodies have a positive effect on cooling down the corresponding area, and buildings have a significant warming effect in all classes, while the cooling effect of UGS is more remarkable in cls_2 to cls_6, especially in cls_2. As for the other rigid pavement, its thermal contribution is warming up the area in cls_1 to cls_3, then turning to cool down the area in cls_4 to cls_7, and the high values are in cls_2 and cls_7. Comparing different

months, it is indicated that the LCI of each underlying surface in May is the highest in cls_1, cls_2, and cls_4 to cls_6. In cls_3, the highest LCI is in July, and in cls_7, it is in October. It is shown that the thermal contribution of each underlying surface in different temperature classes is distinguished in different months.

Intersection of Each LST Class in Different Months

Proportion of Each Intersection Area

Taking the LST classes of July as the benchmark, the intersection of each class between May and July (intersection_July/May) as well as July and October (intersection_July/Oct) are analyzed, respectively, as shown in **Figure 6**. The colors in the figure represent different LST classes, in which the color red means high temperature and the color blue means low temperature. The middle column in the figure is the LST class in July, and the upper and lower sides illustrate the LST classes of May and October that overlap with the corresponding class of July and their proportions, respectively. For example, 48.86% of cls_3 in July overlaps with cls_3 in May, which is the overlap of the same class in these 2 months. Apart from that, the overlap of the different classes represents the differences in the spatial distribution of LST between the 2 months. Particularly, 17.75% of cls_3 in July overlaps with cls_2 in May that can be grouped into hot-cold overlapped type, simply expressed as Jcls3_Mcls2, and 24.85% of cls_3 in July overlap with the cls_4 in May, which is a cold–hot overlapped type, abbreviated as Jcls3_Mcls4.

It is indicated that the overlap degree of the same LST class is higher (58.03%) in the intersection_July/May, while lower (47.12%) in the intersection_July/Oct. As for each LST class, the overlap degree of cls_1, that is, the extremely low-temperature area, is the highest, reaching 92.82% in the intersection_July/May and 88.69% in the intersection_July/Oct. As temperature rises, the overlap degree of the same class first decreases and then increases, presenting a U-shaped trend. The overlap degree of cls_7 is the second highest, 73.18% in the intersection_July/May and 65.01% in the intersection_July/Oct. The overlap degree of cls_5 is the lowest, only 36.00% in the intersection_July/May and 27.54% in the intersection_July/Oct.

The overlapped areas of different LST classes are mainly distributed in one or two adjacent classes before and after this specific class, that is, the cold–hot type and hot–cold type defined in this study. Along with the rising temperature, the proportion of the overlapped area of different temperature classes first increased and then decreased slightly, reaching the highest ratio in cls_5 (27.14%). In the lower temperature class, the cold–hot type is more prevalent, and in the higher temperature class, the hot–cold type is dominant.

In general, the spatial distribution of extremely low-temperature area, low-temperature area, and extremely high-temperature area is similar in different months, while the greatest differences among different months are reflected in the medium temperature area, mainly cls_3 to cls_6, which is the sub-low-temperature area, medium-temperature area, high-temperature area, and sub-high-temperature area.

Landscape Pattern of Each Intersection Area

Taking the intersection area of different classes as the research focus, the landscape metrics of cold–hot and hot–cold overlapped types in the intersection_July/May are compared with those in the intersection_July/Oct, as shown in **Table 6**. Based on the results, it is indicated that PLAND in the intersection_July/Oct is higher than that in the intersection_July/May, coinciding with the conclusion in the last section. PD of the intersection_July/Oct is much lower than that in the intersection_July/May, while the AREA_MN and AI are the opposite, demonstrating that the difference of the LST class between July and October is presented in larger patches and is more aggregated in the spatial distribution. As for the ENN_MN, the hot–cold type in the intersection_July/Oct is higher than that in the intersection_July/May; however, the cold–hot type is lower than that in the latter, revealing that the distance of the patches in different overlapped types varies a lot in different months.

Furthermore, comparing the difference between the two overlapped types, it is found that the PLAND of the cold–hot type is higher than the hot–cold type in both intersection areas of July/May and July/Oct, indicating that the differences among 3 months can be more categorized into cold–hot type, that is, the colder area in July overlaps with the warmer area in the other 2 months. The PD of the cold–hot type is lower than that in the hot–cold type in the intersection_July/May and higher than that in the latter in the intersection_July/Oct, while the AREA_MN, ENN_MN, and AI are quite the opposite. On the whole, in the intersection_July/May, the patches of cold–hot type are relatively large with a small number and are more aggregated with a longer distance to each other. However, in the intersection_July/Oct, the patches of cold–hot type are relatively small with a large number and are less aggregated with a shorter distance to each other.

Underlying Surfaces of Each Intersection Area

The proportions of each underlying surface in the overlapped area of the intersection_July/May are compared with those of the intersection_July/Oct. The results of different overlapped types are shown in **Figure 7**. It is clear that the differences between the cold–hot overlapped type and the hot–cold overlapped type are obvious. For the hot–cold overlapped type, the proportion of UGS in the intersection_July/May is significantly higher than that in the intersection_July/Oct, while the proportion of buildings is remarkably lower than that in the latter. The proportion of other rigid pavement is

TABLE 6 | Landscape metrics of each intersection area.

Month	Type	PLAND	PD	AREA_MN	ENN_MN	AI
July/May	Hot–cold	22.01	40.14	2.49	88.24	69.06
	Cold–hot	23.01	37.75	2.64	89.10	72.46
July/Oct	Hot–cold	26.85	22.90	4.37	94.66	75.31
	Cold–hot	28.13	25.18	3.97	87.60	73.79

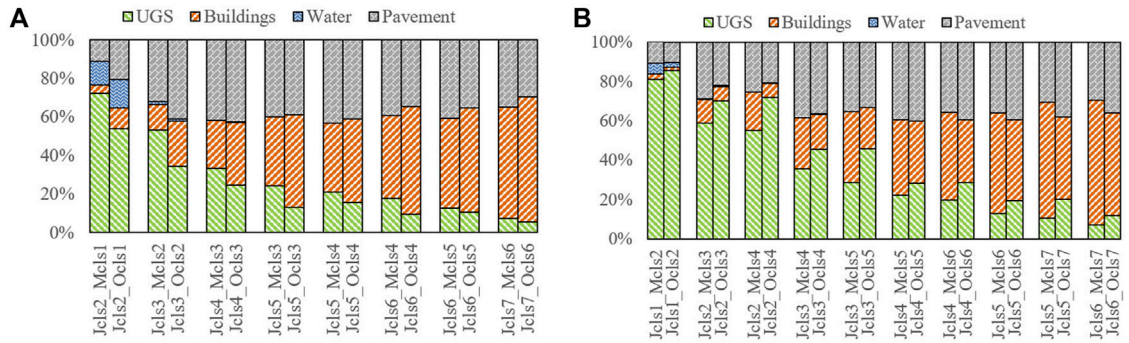

FIGURE 7 | Underlying surfaces of **(A)** hot–cold overlapped type and **(B)** cold–hot overlapped type in different intersections.

TABLE 7 | Proportions of underlying surfaces in different overlapped types.

	July–May		July–Oct	
	Cold–hot (%)	Hot–cold (%)	Cold–hot (%)	Hot–cold (%)
UGS	26.77	25.91	37.32	18.64
Buildings	39.13	35.50	28.48	43.41
Water	0.35	0.80	0.25	0.95
Pavement	33.75	37.79	33.95	37.00

lower than that in the latter in cls_2 to cls_4 but higher than that in the latter in the following temperature LST classes. Quite the opposite, in the cold–hot overlapped type, the proportion of UGS in the intersection_July/May is significantly lower than that in intersection_July/Oct, and the proportion of buildings is higher than that in the latter. The proportion of other rigid pavement is higher than that in the latter in cls_1 to cls_3 and lower than that in the latter in the other LST classes.

Furthermore, the two overlapped types of different LST classes can be regarded as the differences along with the overall warming or cooling process from May to July to October. From May to July, although the overall temperature has increased, the warming degree of the hot–cold overlapped area is higher than that of other areas, so its LST class in May upgrades when it is in July. Similarly, the cold–hot overlapped type indicates that the warming degree of this area is relatively low, resulting in the downgrading of its LST class. Combined the proportion of each underlying surface in the areas of different overlapped types (**Table 7**), it is shown that from May to July, buildings account for the most in the cold–hot type and higher than that in the hot–cold type, revealing that buildings have lower warming degree in some extent. The proportion of other rigid pavement is the highest in the hot–cold type and higher than that in the cold–hot type, indicating the warming degree of other rigid pavement is relatively high. In addition, the proportion of water bodies in the hot–cold type is much higher than that in the cold–hot type, demonstrating that water bodies have higher warming degrees from May to July.

In the same way, the hot–cold overlapped area can be regarded as the cooling degree of this area is higher than other areas in the process of overall cooling process from July to October, so its LST class downgrades. The cold–hot overlapped type indicates that the cooling degree of this area is lower leading to the upgrading of its LST class. Based on the underlying surface in the intersection_July/Oct, it is shown that the ratio of UGS in the cold–hot overlapped type is significantly higher than that in the hot–cold overlapped area, and the proportions of the building, water bodies as well as other rigid pavements are lower than the latter, suggesting that the last three kinds of underlying surfaces account for more in the area of higher cooling degree, while UGS has a lower cooling degree.

DISCUSSION

Spatial Differences of LST Among Three Months

In previous studies, annual and seasonal variation of LST is one of the basic research on urban climate (Peng et al., 2018; Zhang and Wang, 2020; Shi et al., 2021). However, most studies focus on the high or low temperature in the area, namely, the heat islands and cold islands, and little attention is paid to the medium temperature area. According to the aforementioned results, here is a small difference in the high and low temperature areas between different months, while there is a noticeable difference in the medium temperature area. Specifically, the overlap degree of the same LST class in July and May is higher than that in July and October. The highest degree of overlap is in the extremely low-temperature area, followed by the extremely high-temperature area. Along with the increase in temperature, the overlap degree of the same LST class will decrease first and then increase, showing a U-shape change trend, indicating that the distribution of the cold and the hot islands in the city is similar in different months, while that of medium-temperature area significantly differs. One plausible reason is that the LST of medium-temperature area is not only dependent on its ground and spatial feature but also influenced by surrounding heat and cold islands. Although the spatial pattern of heat and cold islands may not significantly change over 3 months, their ability or extent to regulate their surroundings fluctuates over time (Yu et al., 2019; Yu K. et al., 2020).

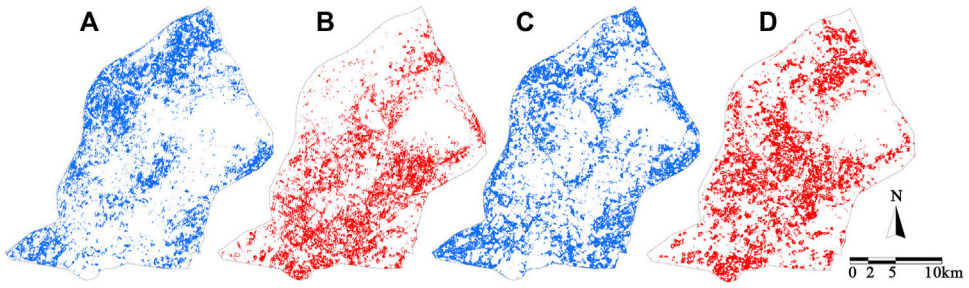

FIGURE 8 | Spatial distribution of the **(A)** cold–hot type in the intersection_July/May, **(B)** hot–cold type in the intersection_July/May, **(C)** cold–hot type in the intersection_July/Oct, and **(D)** hot–cold type in the intersection_July/Oct.

In this study, the LST differences across time are subdivided into cold–hot and hot–cold overlapped types, and the distinctions between those two types turns out to be significant, in which the cold–hot type accounts for more in both intersections of July/May and July/Oct. Furthermore, in the intersection_July/May, the patches of cold–hot type are relatively large with a small number and more aggregated with a longer distance to each other. However, in the intersection_July/Oct, the landscape pattern of the cold–hot type is quite the opposite. According to the spatial distribution of different overlapped types shown in **Figure 8**, in the intersection_July/May, most of the cold–hot type areas are distributed densely in the northwest of the research area, and other small parts are scattered in the central area, along the southeast edge and the southwest corner. On the contrary, the hot–cold type areas are mainly located in the east and south of the study area, especially aggregated in the south of Zijin Mountain. In the intersection_July/Oct, the cold–hot type areas are mostly distributed along the surrounding boundary of the study area, while the hot–cold type areas occupy the majority of the city center. In other words, there is a difference in the warming and cooling degrees within the research area, and it needs to be further explored.

Temperature Changes of Different Underlying Surfaces

The main reason for the LST difference lies in the variances of underlying surfaces (Liu et al., 2013; Guo et al., 2020; Parvez et al., 2021). It is concluded that UGS and water bodies contribute the most in the cool area, while buildings and other rigid pavements account for the most in the hot area, in which buildings are the dominant factor. However, it is worth noting that UGS occupies around 5% even in the highest temperature area, indicating that UGS may not always be the cold island, and its surrounding environment should be taken into consideration (Yuan et al., 2021). Combined with the LCI of each underlying surface, the results show that the performance of the underlying surface in the whole region is different from that in different temperature classes, indicating that the role of each underlying surface in different temperature areas is different. Both UGS and water bodies contribute a cooling effect to the area, and the LCI of UGS is higher than that of water bodies, but the cooling effect of the latter is more significant in the extremely cool area, while UGS plays a dominant role in the cool area. Previous studies have investigated the cooling effect of UGS and water bodies. Some studies have come to the same conclusion that the LCI of UGS is higher than that of water bodies (Tarawally et al., 2018), while others have obtained the opposite results due to the different research scale (Huang et al., 2019), but few research has further investigated the thermal contribution of underlying surface in different temperature classes. According to Wang et al. (2019), the impact of urban water bodies on the LST does vary across different LCZ types, which supports the aforementioned conclusion to a certain extent. Therefore, specific mitigation and adaption efforts should be made according to the actual conditions.

By comparing the underlying surfaces between different months, it is found that there is little difference between the underlying surface in May and July, but a significant difference between the underlying surface in July and October. In summary, water bodies contribute more to the cooling effect in October, while the contribution degree of UGS in October is relatively lower than that in the other 2 months. In addition, other rigid pavements contribute more to high temperature in October. Furthermore, there are great differences between the two overlapped types. In the hot–cold overlapped type, the proportion of UGS in the intersection_July/May is significantly higher than that in the intersection_July/Oct, while that of the building is significantly lower than that of the latter. The proportion of other rigid pavements is lower than that of the latter in cls_2 to cls_4 but higher than that of the latter in the following LST class. However, in the cold–hot overlapped type, it is totally the opposite case.

Combining with the meaning of the cold–hot and hot–cold overlapped types, that is, the warming and cooling degrees of different underlying surfaces, it is concluded that the warming degree of buildings is relatively low, while other rigid pavements and water bodies have a higher warming degree in certain areas in the warming process from May to July. In the cooling process from July to October, the cooling degree of UGS in some areas is low, while that of buildings, water bodies, and other rigid pavement is higher, especially buildings. Zhang et al. (2021) defined the urban surface heating rate (SHR) as the

change in LST per percentage of impervious surface area (ISA) and the urban surface cooling rate (SCR) as the change in LST per percentage of fractional vegetation cover (FVC). They also concluded that the trend of SHR and SCR, along with the percent of ISA and FVC, had remarkable seasonal differences. The difference is that Zhang et al. (2021) considered the specific heating and cooling rate of the underlying surface and its variation trend with temperature within a day, while this study focuses on the heating and cooling degrees of each underlying surface and its variation trend across time. Moreover, the former research did not distinguish the impervious surface between buildings and other rigid pavements, which is proved to have great differences in the influence of the UHI formation in this study.

Implications, Limitations, and Future Research

This study may provide a new perspective on mitigating the UHI effect at the different stages of LST change. In addition to focusing on the UHIs effect at a particular time, temperature changes before and after that particular time, may help understand the formation of the heat island effect. From July to October, the landscape pattern of low- and medium-temperature areas exhibits a trend of fragmentation and decentralization, while the high-temperature area does not significantly change. Conversely, if heat island patches could be more fragmented and decentralized, their intensity might be reduced. Yu et al. (2021) came to a similar conclusion in the research of heat networks, that is, when links and pinch points are blocked, SUHI connectivity is reduced, thus breaking the network and significantly alleviating the SUHI effect. Therefore, effective cooling measures should be taken in high-risk and key areas to prevent corridor connectivity. In other words, heat patches are prevented from being aggregated and linked by fragmenting them into small patches and breaking the linkages. Similarly, Wang et al. (2017) pointed out that large temperature contrasts between adjacent patches and fragmental patches are recommended for heat release.

Considering the significant relationship between LST and underlying surfaces, it is essential to optimize the spatial distribution of underlying surfaces. This study reveals that UGS and water bodies show distinguished thermal contributions to the different temperature classes, which means that the more specific mitigation and adaption efforts should be carried out under different circumstances. It seems that water bodies contribute the highest cooling effect to the coolest area, while UGS has a sustained cooling effect from a cool to a hot area. With limited resources, there might be relative thresholds for both UGS and water bodies to fulfill a win–win cooling efficiency in the whole area (Yu Z. et al., 2020; Wu et al., 2020). Previous studies have generally regarded buildings and other rigid pavements together as impervious surfaces and examined their positive impact on temperature rise (Liu et al., 2016). However, it turns out that buildings contribute the most to the highest temperature area, while other rigid pavement has a relative cooling effect in the same area, even though its thermal contribution in the whole area is the opposite. Therefore, it may be a feasible method to explore more about the properties of other rigid pavements and enhance their cooling effect in high-temperature areas.

There are a few limitations that need to be mentioned. First, this study selects May, July, and October as the representative of different seasons that could be haphazard due to unpredictable weather events. Second, the underlying surfaces are classified based on the Landsat image with 30 m resolution in order to coincide with the LST data, but it is not enough for more detailed research on the characteristics of each underlying surface. Third, this study focuses on the impact of different underlying surface types on LST variation, while other factors such as the vegetation volume in different seasons, energy consumption, and other indexes related to production activities are not involved.

Future studies will detail the characteristics of different underlying surfaces, for example, building height and density, greenspace morphology, the area and shape of water bodies, the impervious rate of other rigid pavement, and the influence of the surrounding environment. Furthermore, the spatial differences between cold–hot and hot–cold overlapped types and their distribution regularities will be thoroughly analyzed based on the detailed aforementioned factors. It is believed that it can provide applicable references for future urban design.

CONCLUSION

Taking the LST of Nanjing in different months as an example, this study divided temperature into different classes by using the quantile method and then compared the spatial distribution of each LST class in different months. The results indicate that there is a small difference in the distribution of heat and cold islands between months, while a major difference in medium-temperature area. In particular, the spatial pattern of each LST class illustrates a trend of fragmentation and decentralization from July to October. Further analysis of the intersection of each LST class in different months shows that the overlap degree of the low-temperature area and high-temperature area is higher than that of the medium-temperature area. The overlapped area of different LST classes is divided into hot–cold and cold–hot types. In the process of temperature change from May to July and October, different overlapped types can be regarded as different cooling degrees in different areas to a certain extent. It turns out that the warming degree of other rigid pavements is higher in the warming process from May to July, and the cooling degree of buildings is greater in the cooling process from July to October. Meanwhile, the thermal contribution of each underlying surface is different among LST classes, so it is necessary to formulate more targeted strategies. This study provides a new perspective for the mitigation of UHI based on the comprehensive understanding of the temperature change from a continuous-

time sequence, expecting to be a reference for sustainable urban design in the future.

DATA AVAILABILITY STATEMENT

The original contributions presented in the study are included in the article/**Supplementary Material**, further inquiries can be directed to the corresponding author.

AUTHOR CONTRIBUTIONS

XW collected the data, performed data analysis, and developed the draft manuscript as well as the tables and figures. X-JW guided the conceptualization of the study and provided instructions on the research method and revision of the manuscript.

FUNDING

This research was funded by the National Natural Science Foundation of China (50978054 and 51878144).

SUPPLEMENTARY MATERIAL

The Supplementary Material for this article can be found online at: https://www.frontiersin.org/articles/10.3389/fenvs.2022.872282/full#supplementary-material

REFERENCES

Abbas, A., He, Q., Jin, L., Li, J., Salam, A., Lu, B., et al. (2021). Spatio-Temporal Changes of Land Surface Temperature and the Influencing Factors in the Tarim Basin, Northwest China. *Remote Sensing.* 13 (19), 3792. doi:10.3390/rs13193792

Anderson, G. B., and Bell, M. L. (2011). Heat Waves in the United States: Mortality Risk during Heat Waves and Effect Modification by Heat Wave Characteristics in 43 U.S. Communities. *Environ. Health Perspect.* 119 (2), 210–218. doi:10.1289/ehp.1002313

Chao, Z., Wang, L., Che, M., and Hou, S. (2020). Effects of Different Urbanization Levels on Land Surface Temperature Change: Taking Tokyo and Shanghai for Example. *Remote Sensing.* 12 (12), 2022. doi:10.3390/rs12122022

Chen, A., Yao, X. A., Sun, R., and Chen, L. (2014). Effect of Urban green Patterns on Surface Urban Cool Islands and Its Seasonal Variations. *Urban For. Urban Green.* 13 (4), 646–654. doi:10.1016/j.ufug.2014.07.006

Chen, Q., Cheng, Q., Chen, Y., Li, K., Wang, D., and Cao, S. (2021). The Influence of Sky View Factor on Daytime and Nighttime Urban Land Surface Temperature in Different Spatial-Temporal Scales: A Case Study of Beijing. *Remote Sensing.* 13 (20), 4117. doi:10.3390/rs13204117

Das, M., and Das, A. (2020). Assessing the Relationship Between Local Climatic Zones (Lczs) and Land Surface Temperature (Lst) – a Case Study of Sriniketan-Santiniketan Planning Area (Sspa), West Bengal, India. *Urban Clim.* 32, 100591. doi:10.1016/j.uclim.2020.100591

Desa, U. (2019). *World Population Prospects 2019: Highlights*. New York, NY: United Nations Department for Economic and Social Affairs.

Du, H., Cai, W., Xu, Y., Wang, Z., Wang, Y., and Cai, Y. (2017). Quantifying the Cool Island Effects of Urban green Spaces Using Remote Sensing Data. *Urban For. Urban Green.* 27, 24–31. doi:10.1016/j.ufug.2017.06.008

Dudorova, N. V., and Belan, B. D. (2019). "The Role of Evaporation and Condensation of Water in the Formation of the Urban Heat Island," in 25th International Symposium On Atmospheric and Ocean Optics - Atmospheric Physics).

Ebi, K. L., Capon, A., Berry, P., Broderick, C., de Dear, R., Havenith, G., et al. (2021). Hot Weather and Heat Extremes: Health Risks. *The Lancet.* 398 (10301), 698–708. doi:10.1016/s0140-6736(21)01208-3

Elmes, A., Rogan, J., Williams, C., Ratick, S., Nowak, D., and Martin, D. (2017). Effects of Urban Tree Canopy Loss on Land Surface Temperature Magnitude and Timing. *Isprs J. Photogrammetry Remote Sensing.* 128, 338–353. doi:10.1016/j.isprsjprs.2017.04.011

Erdem, U., Cubukcu, K. M., and Sharifi, A. (2021). An Analysis of Urban Form Factors Driving Urban Heat Island: the Case of Izmir. *Environ. Dev. Sustain.* 23 (5), 7835–7859. doi:10.1007/s10668-020-00950-4

Ghosh, S., and Das, A. (2018). Modelling Urban Cooling Island Impact of green Space and Water Bodies on Surface Urban Heat Island in a Continuously Developing Urban Area. *Model. Earth Syst. Environ.* 4 (2), 501–515. doi:10.1007/s40808-018-0456-7

Guha, S., Govil, H., Gill, N., and Dey, A. (2021). A Long-Term Seasonal Analysis on the Relationship between LST and NDBI Using Landsat Data. *Quat. Int.* 575-576, 249–258. doi:10.1016/j.quaint.2020.06.041

Guha, S., and Govil, H. (2020). Seasonal Impact on the Relationship between Land Surface Temperature and Normalized Difference Vegetation index in an Urban Landscape. *Geocarto Int.*, 1–21. doi:10.1080/10106049.2020.1815867

Guo, A., Yang, J., Sun, W., Xiao, X., Xia Cecilia, J., Jin, C., et al. (2020). Impact of Urban Morphology and Landscape Characteristics on Spatiotemporal Heterogeneity of Land Surface Temperature. *Sustainable Cities Soc.* 63, 102443. doi:10.1016/j.scs.2020.102443

He, B.-J., Ding, L., and Prasad, D. (2020). Relationships Among Local-Scale Urban Morphology, Urban Ventilation, Urban Heat Island and Outdoor thermal comfort under Sea Breeze Influence. *Sustainable Cities Soc.* 60, 102289. doi:10.1016/j.scs.2020.102289

He, B.-J., Wang, J., Zhu, J., and Qi, J. (2022). Beating the Urban Heat: Situation, Background, Impacts and the Way Forward in China. *Renew. Sustainable Energ. Rev.* 161, 112350. doi:10.1016/j.rser.2022.112350

Huang, M., Cui, P., and He, X. (2018). Study of the Cooling Effects of Urban Green Space in Harbin in Terms of Reducing the Heat Island Effect. *Sustainability.* 10 (4), 1101. doi:10.3390/su10041101

Huang, Q., Huang, J., Yang, X., Fang, C., and Liang, Y. (2019). Quantifying the Seasonal Contribution of Coupling Urban Land Use Types on Urban Heat Island Using Land Contribution Index: A Case Study in Wuhan, China. *Sustainable Cities Soc.* 44, 666–675. doi:10.1016/j.scs.2018.10.016

Jay, O., Capon, A., Berry, P., Broderick, C., de Dear, R., Havenith, G., et al. (2021). Reducing the Health Effects of Hot Weather and Heat Extremes: from Personal Cooling Strategies to green Cities. *The Lancet.* 398 (10301), 709–724. doi:10.1016/s0140-6736(21)01209-5

Kong, F., Yin, H., James, P., Hutyra, L. R., and He, H. S. (2014). Effects of Spatial Pattern of Greenspace on Urban Cooling in a Large Metropolitan Area of Eastern China. *Landscape Urban Plann.* 128, 35–47. doi:10.1016/j.landurbplan.2014.04.018

Lee, E. W. T., and Stat, A. (1994). "Transformation of the Coefficient of Variation," in Spring Meeting of the Eastern-North-American-Region of the Biometric-Society), 355–358.

Li, X., and Zhou, W. (2019). Optimizing Urban Greenspace Spatial Pattern to Mitigate Urban Heat Island Effects: Extending Understanding from Local to the City Scale. *Urban For. Urban Green.* 41, 255–263. doi:10.1016/j.ufug.2019.04.008

Liu, K., Gao, W., Gu, X. F., and Gao, Z. Q. (2013). "The Relation between the Urban Heat Island Effect and the Underlying Surface LUCC of Meteorological Stations," in Conference on Remote Sensing and Modeling of Ecosystems for Sustainability X).

Liu, K., Su, H., Li, X., Wang, W., Yang, L., and Liang, H. (2016). Quantifying Spatial-Temporal Pattern of Urban Heat Island in Beijing: An Improved Assessment Using Land Surface Temperature (LST) Time Series Observations from LANDSAT, MODIS, and Chinese New Satellite GaoFen-

1. *IEEE J. Sel. Top. Appl. Earth Observations Remote Sensing.* 9 (5), 2028–2042. doi:10.1109/jstars.2015.2513598

Makhelouf, A. (2009). The Effect of Green Spaces on Urban Climate and Pollution. *Iranian J. Environ. Health Sci. Eng.* 6 (1), 35–40. Available at: https://ijehse.tums.ac.ir/index.php/jehse/article/view/190.

Markevych, I., Schoierer, J., Hartig, T., Chudnovsky, A., Hystad, P., Dzhambov, A. M., et al. (2017). Exploring Pathways Linking Greenspace to Health: Theoretical and Methodological Guidance. *Environ. Res.* 158, 301–317. doi:10.1016/j.envres.2017.06.028

Marks, K. M. B. J. (1995). *FRAGSTATS: Spatial Pattern Analysis Program for Quantifying Landscape Structure*. Portland, OR: USDA Forest Service.

Masoudi, M., and Tan, P. Y. (2019). Multi-year Comparison of the Effects of Spatial Pattern of Urban green Spaces on Urban Land Surface Temperature. *Landscape Urban Plann.* 184, 44–58. doi:10.1016/j.landurbplan.2018.10.023

Mazdiyasni, O., and AghaKouchak, A. (2015). Substantial Increase in Concurrent Droughts and Heatwaves in the United States. *Proc. Natl. Acad. Sci. U.S.A.* 112 (37), 11484–11489. doi:10.1073/pnas.1422945112

Nanjing Bureau of Statistics (2019). *Statistical Yearbook of Nanjing*. Nanjing, China: China Statistics Press.

Oke, T. R. (1982). The Energetic Basis of the Urban Heat Island. *Q.J R. Met. Soc.* 108 (455), 1–24. doi:10.1002/qj.49710845502

Oke, T. R. (1987). *Boundary Layer Climates*. London ; New York: Methuen.

Parvez, I. M., Aina, Y. A., and Balogun, A.-L. (2021). The Influence of Urban Form on the Spatiotemporal Variations in Land Surface Temperature in an Arid Coastal City. *Geocarto Int.* 36 (6), 640–659. doi:10.1080/10106049.2019.1622598

Peng, J., Jia, J., Liu, Y., Li, H., and Wu, J. (2018). Seasonal Contrast of the Dominant Factors for Spatial Distribution of Land Surface Temperature in Urban Areas. *Remote Sensing Environ.* 215, 255–267. doi:10.1016/j.rse.2018.06.010

Rasul, A., Balzter, H., and Smith, C. (2015). Spatial Variation of the Daytime Surface Urban Cool Island during the Dry Season in Erbil, Iraqi Kurdistan, from Landsat 8. *Urban Clim.* 14, 176–186. doi:10.1016/j.uclim.2015.09.001

Sekertekin, A. (2019). Validation of Physical Radiative Transfer Equation-Based Land Surface Temperature Using Landsat 8 Satellite Imagery and SURFRAD *In-Situ* Measurements. *J. Atmos. Solar-Terrestrial Phys.* 196, 105161. doi:10.1016/j.jastp.2019.105161

Shi, L., Ling, F., Foody, G. M., Yang, Z., Liu, X., and Du, Y. (2021). Seasonal SUHI Analysis Using Local Climate Zone Classification: A Case Study of Wuhan, China. *Int. J. Environ Res Public Health.* 18 (14), 7242. doi:10.3390/ijerph18147242

Stanganelli, M., and Gerundo, C. (2017). Understanding the Role of Urban Morphology and Green Areas Configuration during Heat Waves. *Int. J. Agric. Environ. Inf. Syst.* 8 (2), 50–64. doi:10.4018/ijaeis.2017040104

Stewart, I. D., and Oke, T. R. (2012). Local Climate Zones for Urban Temperature Studies. *Bull. Am. Meteorol. Soc.* 93 (12), 1879–1900. doi:10.1175/bams-d-11-00019.1

Sun, L., Tang, L., Shao, G., Qiu, Q., Lan, T., and Shao, J. (2020). A Machine Learning-Based Classification System for Urban Built-Up Areas Using Multiple Classifiers and Data Sources. *Remote Sensing.* 12 (1), 91. doi:10.3390/rs12010091

Sun, Y., Gao, C., Li, J., Wang, R., and Liu, J. (2019). Quantifying the Effects of Urban Form on Land Surface Temperature in Subtropical High-Density Urban Areas Using Machine Learning. *Remote Sensing.* 11 (8), 959. doi:10.3390/rs11080959

Tarawally, M., Xu, W., Hou, W., and Mushore, T. (2018). Comparative Analysis of Responses of Land Surface Temperature to Long-Term Land Use/Cover Changes between a Coastal and Inland City: A Case of Freetown and Bo Town in Sierra Leone. *Remote Sensing.* 10 (1), 112. doi:10.3390/rs10010112

United Nation (2021). The Impact of Disasters and Crises on Agriculture and Food Security. *Food Agric. Org. Unit Nations.* 8, 94–95. Available at: http://www.fao.org/3/cb3673en/cb3673en.pdf.

Van Ryswyk, K., Prince, N., Ahmed, M., Brisson, E., Miller, J. D., and Villeneuve, P. J. (2019). Does Urban Vegetation Reduce Temperature and Air Pollution Concentrations? Findings from an Environmental Monitoring Study of the Central Experimental Farm in Ottawa, Canada. *Atmos. Environ.* 218, 116886. doi:10.1016/j.atmosenv.2019.116886

Veal, A. J. (2021). Book Notes. *World Leis. J.* 63 (4), 443–444. doi:10.1080/16078055.2021.2008646

Vulova, S., and Kleinschmit, B. (2019). "Therma Lbehavior and its Seasonal and Diurnal Variability of Urban green Infrastructure in a Mid-latitude City - Berlin," in 2019 Joint Urban Remote Sensing Event (JURSE). doi:10.1109/jurse.2019.8809011

Wang, X., Wei, X., and Zou, H. (2020. Research Progress About the Impact of Urban Green Space Spatial Pattern on Urban Heat Island *Ecol. Environ. Sci.* 29 (9), 1904–1911. doi:10.16258/j.cnki.1674-5906.2020.09.024

Wang, Y., Zhan, Q., and Ouyang, W. (2019). How to Quantify the Relationship between Spatial Distribution of Urban Waterbodies and Land Surface Temperature? *Sci. Total Environ.* 671, 1–9. doi:10.1016/j.scitotenv.2019.03.377

Wang, Y., Zhan, Q., and Ouyang, W. (2017). Impact of Urban Climate Landscape Patterns on Land Surface Temperature in Wuhan, China. *Sustainability.* 9 (10), 1700. doi:10.3390/su9101700

Weng, Q., Lu, D., and Schubring, J. (2004). Estimation of Land Surface Temperature-Vegetation Abundance Relationship for Urban Heat Island Studies. *Remote Sensing Environ.* 89 (4), 467–483. doi:10.1016/j.rse.2003.11.005

Wu, J., Yang, S., and Zhang, X. (2020). Interaction Analysis of Urban Blue-Green Space and Built-Up Area Based on Coupling Model-A Case Study of Wuhan Central City. *Water.* 12 (8), 2185. doi:10.3390/w12082185

Xu, G., Chen, L., Chen, Y., Wang, T., Shen, F.-H., Wang, K., et al. (2020). Impact of Heatwaves and Cold Spells on the Morbidity of Respiratory Diseases: A Case Study in Lanzhou, China. *Phys. Chem. Earth, Parts A/B/CParts A/B/C.* 115, 102825. doi:10.1016/j.pce.2019.102825

Xu, H. (2006). Modification of Normalised Difference Water index (NDWI) to Enhance Open Water Features in Remotely Sensed Imagery. *Int. J. Remote Sensing.* 27 (14), 3025–3033. doi:10.1080/01431160600589179

Xu, X., Liu, S., Sun, S., Zhang, W., Liu, Y., Lao, Z., et al. (2019). Evaluation of Energy Saving Potential of an Urban green Space and its Water Bodies. *Energy and Buildings.* 188-189, 58–70. doi:10.1016/j.enbuild.2019.02.003

Yu, K., Chen, Y., Liang, L., Gong, A., and Li, J. (2020). Quantitative Analysis of the Interannual Variation in the Seasonal Water Cooling Island (WCI) Effect for Urban Areas. *Sci. Total Environ.* 727, 138750. doi:10.1016/j.scitotenv.2020.138750

Yu, Z., Yang, G., Zuo, S., Jørgensen, G., Koga, M., and Vejre, H. (2020). Critical Review on the Cooling Effect of Urban Blue-green Space: A Threshold-Size Perspective. *Urban For. Urban Green.* 49, 126630. doi:10.1016/j.ufug.2020.126630

Yu, K., Chen, Y., Wang, D., Chen, Z., Gong, A., and Li, J. (2019). Study of the Seasonal Effect of Building Shadows on Urban Land Surface Temperatures Based on Remote Sensing Data. *Remote Sensing.* 11 (5), 497. doi:10.3390/rs11050497

Yu, X., Guo, X., and Wu, Z. (2014). Land Surface Temperature Retrieval from Landsat 8 TIRS-Comparison between Radiative Transfer Equation-Based Method, Split Window Algorithm, and Single Channel Method. *Remote Sensing.* 6 (10), 9829–9852. doi:10.3390/rs6109829

Yu, Z., Guo, X., Zeng, Y., Koga, M., and Vejre, H. (2018). Variations in Land Surface Temperature and Cooling Efficiency of green Space in Rapid Urbanization: The Case of Fuzhou City, China. *Urban For. Urban Green.* 29, 113–121. doi:10.1016/j.ufug.2017.11.008

Yu, Z., Zhang, J., and Yang, G. (2021). How to Build a Heat Network to Alleviate Surface Heat Island Effect? *Sustainable Cities Soc.* 74, 103135. doi:10.1016/j.scs.2021.103135

Yuan, B., Zhou, L., Dang, X., Sun, D., Hu, F., and Mu, H. (2021). Separate and Combined Effects of 3D Building Features and Urban green Space on Land Surface Temperature. *J. Environ. Manage.* 295, 113116. doi:10.1016/j.jenvman.2021.113116

Zhang, S. N., and Wang, P. (2021). "Impact of Urban Form on Land Surface Temperature (LST) Based Seasonal Characteristics: Empirical Study from Nanjing," in 6th International Conference on Advances in Energy Resources and Environment Engineering (ICAESEE)).

Zhang, X., Wang, D., Hao, H., Zhang, F., and Hu, Y. (2017). Effects of Land Use/Cover Changes and Urban Forest Configuration on Urban Heat Islands in a Loess Hilly Region: Case Study Based on Yan'an City, China. *Int. J. Environ Res Public Health.* 14 (8), 840. doi:10.3390/ijerph14080840

Zhang, Y., Zhan, Y., Yu, T., and Ren, X. (2017). Urban green Effects on Land Surface Temperature Caused by Surface Characteristics: A Case Study of Summer Beijing Metropolitan Region. *Infrared Phys. Technology* 86, 35–43. doi:10.1016/j.infrared.2017.08.008

Zhang, Y., Balzter, H., and Li, Y. (2021). Influence of Impervious Surface Area and Fractional Vegetation Cover on Seasonal Urban Surface Heating/Cooling Rates. *Remote Sensing.* 13 (7), 1263. doi:10.3390/rs13071263

Zhao, C., Fu, G., Liu, X., and Fu, F. (2011). Urban Planning Indicators, Morphology and Climate Indicators: A Case Study for a north-south Transect of Beijing, China. *Building Environ.* 46 (5), 1174–1183. doi:10.1016/j.buildenv.2010.12.009

Zhao, Z., Sharifi, A., Dong, X., Shen, L., and He, B.-J. (2021). Spatial Variability and Temporal Heterogeneity of Surface Urban Heat Island Patterns and the Suitability of Local Climate Zones for Land Surface Temperature Characterization. *Remote Sensing.* 13 (21), 4338. doi:10.3390/rs13214338

Zhou, D., Zhang, L., Li, D., Huang, D., and Zhu, C. (2016). Climate-vegetation Control on the Diurnal and Seasonal Variations of Surface Urban Heat Islands in China. *Environ. Res. Lett.* 11 (7), 074009. doi:10.1088/1748-9326/11/7/074009

Zhou, W., Qian, Y., Li, X., Li, W., and Han, L. (2014). Relationships between Land Cover and the Surface Urban Heat Island: Seasonal Variability and Effects of Spatial and Thematic Resolution of Land Cover Data on Predicting Land Surface Temperatures. *Landscape Ecol.* 29 (1), 153–167. doi:10.1007/s10980-013-9950-5

Conflict of Interest: The authors declare that the research was conducted in the absence of any commercial or financial relationships that could be construed as a potential conflict of interest.

frontiers | Frontiers in Environmental Science

BRIEF RESEARCH REPORT
published: 30 June 2022
doi: 10.3389/fenvs.2022.918076

Influence of Multi-Scale Meteorological Processes on $PM_{2.5}$ Pollution in Wuhan, Central China

Yucong Miao[1], Xinxuan Zhang[1], Huizheng Che[1]* and Shuhua Liu[2]*

[1]State Key Laboratory of Severe Weather & Key Laboratory of Atmospheric Chemistry of CMA, Chinese Academy of Meteorological Sciences, Beijing, China, [2]Department of Atmospheric and Oceanic Sciences, School of Physics, Peking University, Beijing, China

Heavy $PM_{2.5}$ (particulate matter with an aerodynamics diameter less than 2.5 μm) pollution frequently happens in Wuhan under unfavorable meteorological conditions. To comprehensively understand the complex impact of both regional-scale synoptic forcing and local-scale processes within the planetary boundary layer (PBL) on air quality in Wuhan, this study analyzed long-term $PM_{2.5}$ concentration measurement, near-surface and upper-air meteorological observations from March 2015 to February 2019, in combination with the Modern-Era Retrospective Analysis for Research and Applications version 2 (MERRA-2). We found that in winter the day-to-day change of $PM_{2.5}$ pollution level in Wuhan was governed by the synoptic warm/cold advection, in addition to the high emissions of pollutants. The synoptic condition can largely determine both the vertical development of PBL and horizontal transport of pollutants. When a high-pressure system is located to the north of Wuhan at the 900-hPa level, the induced warm advection above 1,000 m can enhance the thermal stability of lower troposphere and inhibit the development of daytime PBL, leading to a decreased dispersion volume for pollutants. Meanwhile, within the PBL the pollutants emitted from Henan, Shandong, and Anhui provinces can be transported to Wuhan, further worsening the pollution. Our results highlight the importance of coordinated pollution controls in Central China and adjacent north regions under the unfavorable synoptic condition.

Keywords: $PM_{2.5}$ pollution, synoptic condition, regional transport, planetary boundary layer, multi-scale processes

OPEN ACCESS

Edited by:
Ashish Sharma, University of Illinois at Urbana-Champaign, United States

Reviewed by:
Zhenxing Shen, Xi'an Jiaotong University, China
Yuanjian Yang, Nanjing University of Information Science and Technology, China

****Correspondence:***
Yucong Miao
miaoyucong@yeah.net
Huizheng Che
chehz@cma.gov.cn

Specialty section:
This article was submitted to Atmosphere and Climate, a section of the journal Frontiers in Environmental Science

Received: *12 April 2022*
Accepted: *13 June 2022*
Published: *30 June 2022*

Citation:
Miao Y, Zhang X, Che H and Liu S (2022) Influence of Multi-Scale Meteorological Processes on $PM_{2.5}$ Pollution in Wuhan, Central China. Front. Environ. Sci. 10:918076. doi: 10.3389/fenvs.2022.918076

INTRODUCTION

Wuhan, the capital city of Hubei province, is one of most populated and heaviest polluted cities in China (Miao et al., 2019; Xiao et al., 2020; Tao et al., 2021). It is a major industrial and commercial city in Central China, with a population of more than ten million. Due to the high level of urbanization and industrialization, and associated huge consumptions of energy and resources, anthropogenic air pollution has become one of most critical environmental issues in Wuhan (Miao et al., 2019). The $PM_{2.5}$ (particulate matter with an aerodynamics diameter less than 2.5 μm) pollution events have been frequently reported under unfavorable meteorological conditions (e.g., Lu et al., 2019; Miao and Liu, 2019; Tao et al., 2021), threatening the health of citizens (Pope and Dockery, 2006).

The city is crossed by the transportation routes of road, rail, and river from almost every direction, linking the north, south, west, and east parts of China. This unique geographical location

(**Supplementary Figure S1**) makes it subject to the influence of air masses/pollutants moved from every direction (Mbululo et al., 2019; Miao et al., 2019). For example, during a pollution episode in November 2017, large amounts of aerosols were transported to Wuhan from North China along with the movement of cold air masses (Xiao et al., 2020). Similar processes have also been reported by Hu et al. (2021) and Lu et al. (2019). In addition to these trans-boundary transport processes, the local-scale planetary boundary layer (PBL) also plays a critical role in the formation of $PM_{2.5}$ pollution (Liu et al., 2018; Mbululo et al., 2019; Xiao et al., 2020). Because the PBL governs the vertical exchange of energy, matter, and heat between surface and upper free atmosphere, the height of boundary layer (BLH) is widely used to quantify the volume for pollutant dispersion and dilution (Stull, 1988; Miao and Liu, 2019). Within the PBL, near-surface inversion layer and calm wind condition were often found to be associated with the $PM_{2.5}$ pollution in Wuhan (Mbululo et al., 2019; Miao and Liu, 2019). Although the importance of regional-scale synoptic condition (Xiao et al., 2020) or local-scale PBL thermal structure (Miao and Liu, 2019) for the $PM_{2.5}$ pollution in Wuhan has been pointed out, the connection between these multi-scale atmospheric processes and their integrated effects on pollution are not yet clear understood, particularly in the heavily polluted winter.

In order to comprehensively understand the pollution formation mechanism in Wuhan and elucidate the environmental impact of multi-scale meteorological processes, we collected and analyzed long-term $PM_{2.5}$ concentration measurement, near-surface and upper-air meteorological observations from March 2015 to February 2019, in combination with the Modern-Era Retrospective Analysis for Research and Applications version 2 (MERRA-2).

DATA AND METHOD

In this study, hourly $PM_{2.5}$ concentration data from March 2015 to February 2019 in Wuhan were collected from nine monitoring sites in Wuhan (**Supplementary Figure S1B**), which are operated by the China National Environmental Monitoring Center (CNEMC). We first calculated the daily concentrations for each $PM_{2.5}$ monitoring site, and then averaged the concentrations of all sites to derive the daily values. Besides, both ground-level and upper-air meteorological observations were obtained from a station (114.05°E, 30.60°N) in Wuhan, which is operated by the China Meteorological Administration. The ground-level meteorological parameters were recorded hourly. The sounding balloon was launched twice a day at 08: 00 LT (00:00 UTC) and 20:00 LT (12:00 UTC), which can provide fine-resolution vertical profiles of temperature, humidity, wind, and pressure (Miao et al., 2015).

To complement these above-mentioned discrete observations to gain further insight into the nature of $PM_{2.5}$ pollution, we analyzed the MERRA-2 data in this study, which is the latest atmospheric reanalysis of the modern satellite era developed by NASA's Global Modeling and Assimilation Office (Gelaro et al., 2017). In the vertical dimension, there are 72 model levels from surface to 0.01-hPa level. The MERRA-2 dataset was used as an alternative to derive the daily maximum BLH in the afternoon (Miao et al., 2022). We estimated the BLH as the level at which the potential temperature (PT) first exceeds the minimum PT within the PBL by 1.5 K (Nielsen-Gammon et al., 2008; Miao et al., 2021). Based on the meteorological fields (e.g., pressure, temperature) derived from MERRA-2, we employed the T-mode principal component analysis (T-PCA) (Huth et al., 2008) to identify the typical synoptic conditions associated with the polluted and clean conditions in Wuhan. The T-PCA studied region covered Central China and its adjacent regions, in a range from 110 to 121°E and 26 to 37°N. The T-PCA has been widely used to untangle the relationships between regional-scale background meteorological conditions and local-scale weather phenomena or pollution processes (e.g., Miao et al., 2018; Yan et al., 2019; Li et al., 2021), which has proven to be a reliable objective classification method due to its high temporal and spatial stability in the classified results (Philipp et al., 2010; Zhang et al., 2012; Ye et al., 2016). The detailed information of the T-PCA can be found in previous studies of Huth et al. (2008) and Philipp et al. (2010). After identifying the typical synoptic conditions, the spatial distributions of $PM_{2.5}$ concentration could be revealed on the basis of the Chinese Air Quality Reanalysis (CAQRA), which is the assimilation dataset of surface observations from the CNEMC using the ensemble Kalman filter and Nested Air Quality Prediction Modeling System (Kong et al., 2021).

Besides, 48-h backward trajectories of air masses were simulated using the Hybrid Single Particle Lagrangian Integrated Trajectory model (HYSPLIT) (Draxler and Hess, 1998) and MERRA-2 data, which can help to recognize the transport pathways of pollutants (Sun et al., 2017). For each day during the study period, a 48-h backward trajectory was calculated with ending time at 20:00 LT, and the trajectory ending point was set above the meteorological station in Wuhan (114.05°E, 30.60°N, 100 m above ground level). Based on the simulated backward trajectories, we calculated the map of potential source contribution function (PSCF) (Mbululo et al., 2019; Sun et al., 2017) for the $PM_{2.5}$ pollution in Wuhan. The PSCF value in the ij-th grid was calculated as Pij/Nij, in which the Nij was the number of endpoints that fall in the ij-th grid and the Pij was the number of "polluted" trajectory endpoints in the same grid. The "polluted" trajectory was usually determined according to a threshold value of pollutants' concentration. In this study, we calculated the PSCF with a resolution of 0.5° × 0.5°.

RESULTS AND DISCUSSION

Overall Characteristics of $PM_{2.5}$ Pollution in Wuhan

During the study period from March 2015 to February 2019, prominent seasonal variation of $PM_{2.5}$ concentration in Wuhan can be observed (**Supplementary Figure S2**). The maximum seasonally average $PM_{2.5}$ concentration was 86.5 μg m^{-3} in winter (Dec-Jan-Feb), significantly higher than the average concentrations in other seasons, which were 55.3 μg m^{-3} in

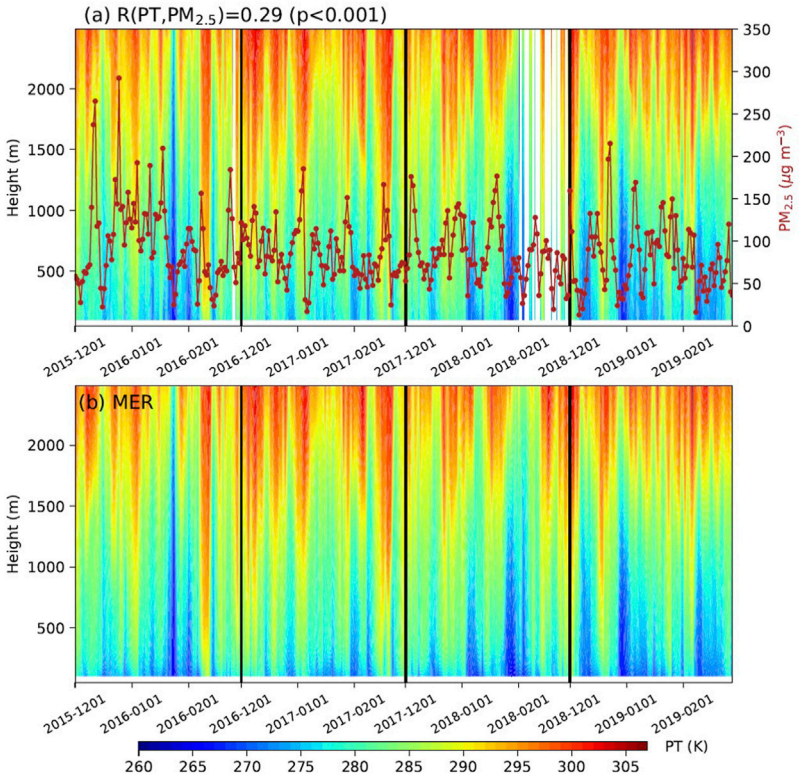

FIGURE 1 | Time-height sections of potential temperature (PT) in winter from December 2015 to February 2019 in Wuhan, derived from **(A)** radiosonde measurements and **(B)** MERRA-2 at 08:00 LT. In **(A)**, the time series of daily $PM_{2.5}$ concentration (red line and dots) is also shown, and the correlation coefficient between the daily concentration and 850-hPa PT is 0.29 ($p < 0.001$). The correlation coefficient between the measured PT profiles and MERRA-2 PT profiles is 0.99 ($p < 0.001$).

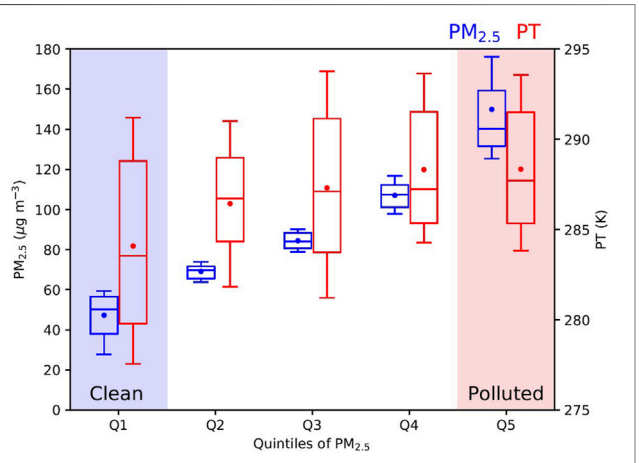

FIGURE 2 | Boxplot showing the changes of daily $PM_{2.5}$ concentration (blue) and 850-hPa PT (red) in Wuhan during winter on the days of different quintiles of $PM_{2.5}$ concentration (Q1 to Q5). The PTs shown were derived from the radiosonde measurements at 08:00 LT, and the measurements of rainy days (24-h accumulated precipitation greater than 0.5 mm) were excluded. The central box represents the values from the lower to upper quartile (25th to 75th percentile). The vertical line extends from the 0th percentile to the 90th percentile value. The middle solid line represents the median, and the dot represents the mean value.

spring (Mar-Apr-May), 31.0 μg m^{-3} in summer (Jun-Jul-Aug), and 49.1 μg m^{-3} in autumn (Sep-Oct-Nov). Therefore, we focused on the wintertime $PM_{2.5}$ pollution in Wuhan. Because most pollution events in winter occurred on the dry conditions, we excluded the rainy days (i.e., 24-h accumulated precipitation greater than 0.5 mm) in this study. In total, the measurements of 260 days in winter were analyzed.

The day-to-day variation of $PM_{2.5}$ concentration in Wuhan is shown in **Figure 1A**. It was found that higher $PM_{2.5}$ concentrations were often associated with warmer atmosphere above 1,000 m. Comparing the 850-hPa PT with daily $PM_{2.5}$ concentration in Wuhan, a significant positive correlation ($R = 0.29$, $p < 0.001$) can be found. To further understand the relationship between 850-hPa PT and $PM_{2.5}$ pollution level, we grouped both variables into five bins according to the quintile values of $PM_{2.5}$ concentration (**Figure 2**). Binning is an effective approach to isolate the expected variability from sampling uncertainty (Seidel et al., 2010; Miao et al., 2018). There was a pronounced increasing trend in the 850-hPa PT along with the deterioration of $PM_{2.5}$ pollution from the first quintile to the fifth quintile, with a spearman correlation coefficient of 0.99 ($p < 0.001$) between the averages of binned PTs and $PM_{2.5}$ concentrations. This relationship between the 850-hPa PT and $PM_{2.5}$ concentration is consistent with the previous study in Central China (Miao et al., 2018). Specifically, the first quintile of $PM_{2.5}$ concentration ranged from 20.3 of

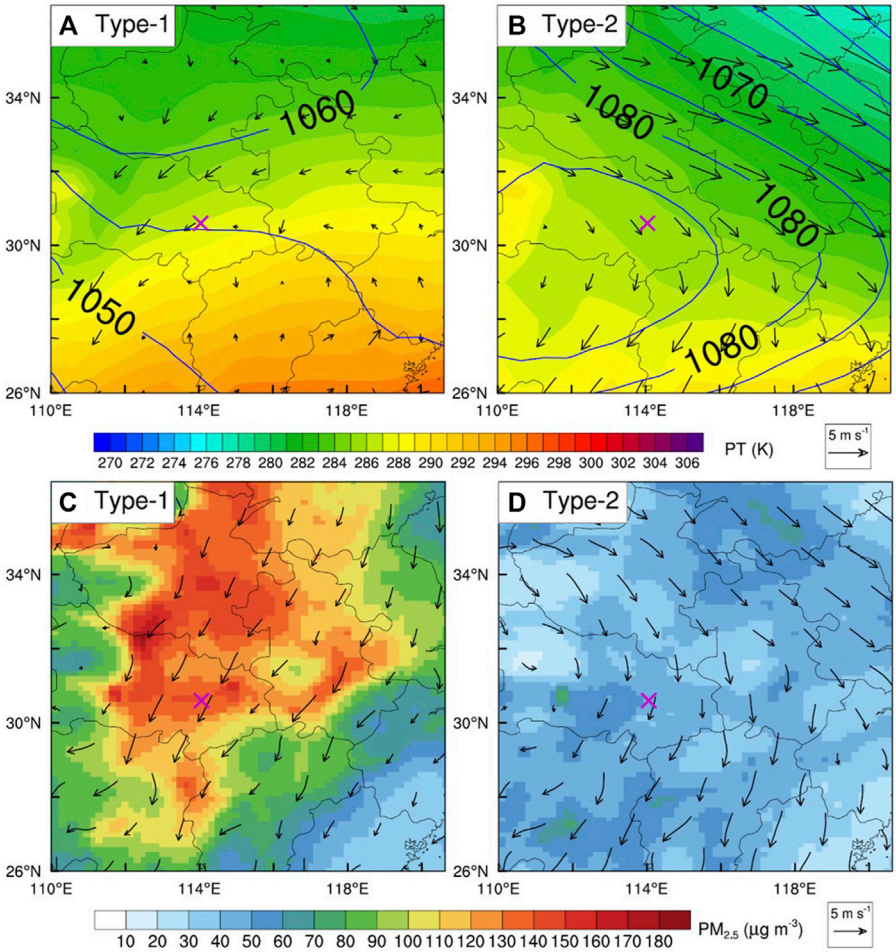

FIGURE 3 | Typical synoptic patterns associated with **(A)** polluted and **(B)** clean conditions in Wuhan, and the corresponding **(C,D)** near-surface $PM_{2.5}$ concentration and wind fields. In **(A,B)**, the synoptic patterns were identified using the T-PCA on the basis of daily MERRA-2 850-hPa PT fields, overlaid with geopotential height and wind vector fields at the 900-hPa level. In **(C,D)**, the $PM_{2.5}$ concentration and wind fields were derived from the CAQRA data, and only the data on the polluted or clean days were averaged for the specific type of synoptic pattern.

61.5 μg m^{-3}, corresponding to the 850-hPa PT within a range from 269 to 296 K, while the fifth quintile of $PM_{2.5}$ concentration (121.4–292.3 μg m^{-3}) was relevant to higher PT (280–299 K). The elevated warming above 1,000 m was also reported in the pollution episode in Wuhan during November 2017 (Xiao et al., 2020), which may enhance the thermal stability in lower troposphere, suppress the development of PBL, and limit the dispersion and dilution of pollutants (Miao et al., 2019; Wang et al., 2020). Such a physical mechanism will be systematically elucidated in the following section by combining synoptic classification and PBL structure analysis. In the rest, we referred the first and fifth quintiles to the clean and polluted conditions in Wuhan, respectively.

In addition to the thermal structure, significant difference in the wind profiles between the clean and polluted conditions can also be observed (**Supplementary Figure S3B**); the clean condition featured north or northwesterly winds at the height between 700 and 1,200 m, while the polluted condition was associated with relatively weaker northeasterly winds. All these above-mentioned differences of PT, wind speed and direction in Wuhan were well reproduced by MERRA-2 (**Figure 1** and **Supplementary Figure S3**). Thus, it would be reliable to explore the underlying physical processes in Wuhan using MERRA-2.

Influence of Synoptic Condition and PBL Structure

Because the change of $PM_{2.5}$ pollution in Wuhan was closely related to the variation of 850-hPa PT, we used the daily 850-hP PT fields derived from MERRA-2 as the T-PCA input data, and eight types of synoptic pattern were objectively classified (**Supplementary Figure S4**). Among these identified synoptic types, Type-1 was predominantly relevant to the $PM_{2.5}$ pollution days, and Type-2 was in relation to the clean condition (**Supplementary Figure S5**). These two synoptic types were the most occurred conditions in Central China, accounted for 74.5% of the total (**Supplementary Figure S4**). Under the control of Type-2, Wuhan was influenced by a cold advection from the northwest (**Figure 3B**). By contrast, Wuhan was under the

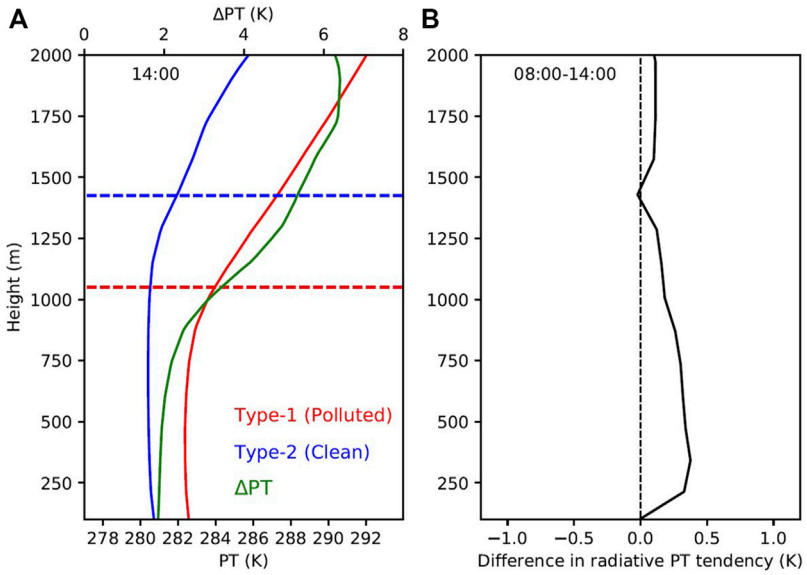

FIGURE 4 | (A) Averaged PT profiles at 14:00 LT in Wuhan on the polluted (in red) and clean (in blue) days under the typical synoptic types and their difference (in green), and **(B)** the difference in the PT tendency due to radiation between the polluted and clean days from 08:00 to 14:00 LT. All the PT profiles shown are derived from MERRA-2, and the BLHs at 14:00 LT were denoted by the dashed lines in **(A)**.

influence of a 900-hPa high-pressure system in the north of city when Type-1 happened, leading to weak northeasterly winds and input of warmer air masses from the east to Wuhan (**Figure 3A**). The elevated warm advection can significantly increase PT above 1,000 m (**Figure 4A**), and strengthen the thermal inversion above the PBL, leading to a depressed PBL in the afternoon. Specifically, the average BLH at 14:00 LT was merely around 1,100 m in Wuhan under the control of Type-1, significantly shallower than the average BLH of Type-2 (1,400 m). Such a depression of BLH decreased the dispersion volume for pollutants (Stull, 1988; Li et al., 2021; Miao et al., 2022), leading to an increased $PM_{2.5}$ concentration in Wuhan.

In addition to the regional-scale synoptic forcing, the radiative effect of aerosol can also modulate the PBL thermal structure (Wang et al., 2018; Miao et al., 2020), which might be another cause of PBL depression in the afternoon. Based on the temperature tendency due to radiation derived from MERRA-2, the PBL thermal modulation caused by the aerosol radiative effect at 14:00 LT can be approximately estimated, which is calculated as the difference of 6-h accumulated radiative temperature tendency (08:00 to 14:00 LT) between the polluted and clean days (**Figure 4B**). From 08:00 to 14:00 LT, the aerosol radiative effect can increase the PT of the upper and middle portions of PBL by 0.2–0.4 K, however, it cannot explain the pronounced difference (around 4–6 K) near the PBL top between the polluted and clean days (**Figure 4A**). It indicates that the depression of afternoon PBL on the pollution days in Wuhan is primarily caused by the synoptic forcing (**Figure 3**), although the aerosol radiative effect (**Figure 4B**) may further suppress the development of PBL to some extent (Miao et al., 2019).

The synoptic condition not only modulates the PBL structure, but also determines the transport pathways of pollutants (Ye et al., 2016; Xiao et al., 2020). Because the day-to-day variation of $PM_{2.5}$ concentration in Wuhan can be well duplicated by CAQRA (**Supplementary Figure S6**), we derived the near-surface spatial distributions of $PM_{2.5}$ concentration and wind from CAQRA (**Figures 3C,D**). Under the influence of Type-1, grids with $PM_{2.5}$ concentration greater than 120 μg m^{-3} not only can be found in Wuhan, but also in the north upstream regions (**Figure 3C**), including Henan, Anhui, and Shandong provinces. When influencing by the large-scale northerly prevailing winds, the massive pollutants in Henan, Anhui, and Shandong provinces can be easily transported to Wuhan. Such a transport of pollutants from north under the Type-1 must be partly responsible for the formation of heavy $PM_{2.5}$ pollution in Wuhan.

To further validate the regional transport from north, we derived the PSCF map for $PM_{2.5}$ pollution in Wuhan on the basis of HYSPLIT backward trajectories. The trajectories ending on the $PM_{2.5}$ pollution days were identified as the "polluted" trajectories. In addition to the local emissions, the potential source regions for the heavy $PM_{2.5}$ pollution in Wuhan included the north part of Anhui, the east part of Henan, and the west part of Shandong (**Supplementary Figure S7**), which are well consistent with the CAQRA $PM_{2.5}$ concentration fields of Type-1 (**Figure 3C**). It indicates that the transport of pollutants from Henan, Anhui, and Shandong provinces is critical to the formation of heavy $PM_{2.5}$ pollution in Wuhan. Therefore, to achieve a pollution-free environment, coordinated controls between Wuhan and its north upstream regions should be implemented when the unfavorable synoptic condition happens.

In short, the synoptic condition governs the wintertime $PM_{2.5}$ pollution in Wuhan *via* both vertical depression of BLH (**Figures 3A**, **4**) and horizontal transport of pollutants (**Figure 3C**). When there is a high-pressure system located to the north of Wuhan at

the 900-hPa level, the elevated warm advection above 1,000 m can enhance the thermal stability in lower troposphere and inhibit the development of daytime PBL, leading to a decreased dispersion volume for pollutants in Wuhan. Meanwhile, within the PBL the pollutants emitted from the north provinces (i.e., Henan, Shandong, and Anhui) can be transported to Wuhan, further worsening the pollution. These multi-scale meteorological processes are critical to the frequent occurrence of $PM_{2.5}$ pollution in Wuhan during winter, in addition to the high emissions of pollutants.

CONCLUSION

Our results improve the understanding of $PM_{2.5}$ pollution formation mechanism in the populated Central China, as well as the environmental impacts of multi-scale meteorological conditions during winter. We find that synoptic warm/cold air advection is critical to the formation of air pollution in Wuhan, because it governs both the vertical development of PBL and horizontal transport of pollutants. When a high-pressure system is located to the north of Wuhan at the 900-hPa level, the elevated warm advection above 1,000 m can enhance the thermal stability in lower troposphere and inhibit the development of daytime PBL in Wuhan. Meanwhile, the pollutants emitted from the adjacent Henan, Shandong, and Anhui provinces can be transported to Wuhan, further worsening the pollution. This study highlights the importance of coordinated pollution controls in Central China and its adjacent north regions under the unfavorable synoptic condition.

Besides, although this study has emphasized the impact of physical processes on the $PM_{2.5}$ pollution in Wuhan, the chemical processes within the PBL also should not be deemphasized, which merits further experimental, observational, and numerical investigations.

DATA AVAILABILITY STATEMENT

Publicly available datasets were analyzed in this study. This data can be found here: The MERRA-2 datasets analyzed for this study are archived by the National Aeronautics and Space Administration of the United States (https://gmao.gsfc.nasa.gov/reanalysis/MERRA-2/). The air quality measurements analyzed are archived by the China National Environmental Monitoring Center (http://www.cnemc.cn/). The meteorological measurements analyzed are archived by the China Meteorological Administration (http://data.cma.cn/). The CAQRA datasets analyzed can be found in the Science Data Bank (https://doi.org/10.11922/sciencedb.00053).

AUTHOR CONTRIBUTIONS

Conceptualization, methodology, formal analysis, writing—original draft, writing—review and editing: YM and HC; visualization, data curation: XZ; supervision: SL.

FUNDING

This study received financial support from the Beijing Nova Program (Z201100006820138), the National Natural Science Foundation of China (42030608, 41875181), and the S&T Development Fund of CAMS (2022KJ001), and the Institute of Heavy Rain of China Meteorological Administration.

SUPPLEMENTARY MATERIAL

The Supplementary Material for this article can be found online at: https://www.frontiersin.org/articles/10.3389/fenvs.2022.918076/full#supplementary-material

REFERENCES

Draxler, R. R., and Hess, G. D. (1998). An Overview of the HYSPLIT_4 Modelling System for Trajectories, Dispersion and Deposition. *Aust. Meteorol. Mag.* 47, 295–308.

Gelaro, R., McCarty, W., Suárez, M. J., Todling, R., Molod, A., Takacs, L., et al. (2017). The Modern-Era Retrospective Analysis for Research and Applications, Version 2 (MERRA-2). *J. Clim.* 30, 5419–5454. doi:10.1175/JCLI-D-16-0758.1

Hu, X. M., Hu, J., Gao, L., Cai, C., Jiang, Y., Xue, M., et al. (2021). Multisensor and Multimodel Monitoring and Investigation of a Wintertime Air Pollution Event Ahead of a Cold Front over Eastern China. *Geophys Res. Atmos.* 126, e2020JD033538. doi:10.1029/2020JD033538

Huth, R., Beck, C., Philipp, A., Demuzere, M., Ustrnul, Z., Cahynová, M., et al. (2008). Classifications of Atmospheric Circulation Patterns. *Ann. N. Y. Acad. Sci.* 1146, 105–152. doi:10.1196/annals.1446.019

Kong, L., Tang, X., Zhu, J., Wang, Z., Li, J., Wu, H., et al. (2021). A 6-Year-Long (2013-2018) High-Resolution Air Quality Reanalysis Dataset in China Based on the Assimilation of Surface Observations from CNEMC. *Earth Syst. Sci. Data* 13, 529–570. doi:10.5194/essd-13-529-2021

Li, Y., Miao, Y., Che, H., and Liu, S. (2021). On the Heavy Aerosol Pollution and its Meteorological Dependence in Shandong Province, China. *Atmos. Res.* 256, 105572. doi:10.1016/j.atmosres.2021.105572

Liu, L., Guo, J., Miao, Y., Liu, L., Li, J., Chen, D., et al. (2018). Elucidating the Relationship between Aerosol Concentration and Summertime Boundary Layer Structure in Central China. *Environ. Pollut.* 241, 646–653. doi:10.1016/j.envpol.2018.06.008

Lu, M., Tang, X., Wang, Z., Wu, L., Chen, X., Liang, S., et al. (2019). Investigating the Transport Mechanism of PM2.5 Pollution during January 2014 in Wuhan, Central China. *Adv. Atmos. Sci.* 36, 1217–1234. doi:10.1007/s00376-019-8260-5

Mbululo, Y., Qin, J., Yuan, Z., Nyihirani, F., and Zheng, X. (2019). Boundary Layer Perspective Assessment of Air Pollution Status in Wuhan City from 2013 to 2017. *Environ. Monit. Assess.* 191, 69. doi:10.1007/s10661-019-7206-9

Miao, Y., Hu, X.-M., Liu, S., Qian, T., Xue, M., Zheng, Y., et al. (2015). Seasonal Variation of Local Atmospheric Circulations and Boundary Layer Structure in the Beijing-Tianjin-Hebei Region and Implications for Air Quality. *J. Adv. Model. Earth Syst.* 7, 1602–1626. doi:10.1002/2015MS000522

Miao, Y., Liu, S., Guo, J., Huang, S., Yan, Y., and Lou, M. (2018). Unraveling the Relationships between Boundary Layer Height and PM2.5 Pollution in China Based on Four-Year Radiosonde Measurements. *Environ. Pollut.* 243, 1186–1195. doi:10.1016/j.envpol.2018.09.070

Miao, Y., Li, J., Miao, S., Che, H., Wang, Y., Zhang, X., et al. (2019). Interaction between Planetary Boundary Layer and PM2.5 Pollution in Megacities in China: a Review. *Curr. Pollut. Rep.* 5, 261–271. doi:10.1007/s40726-019-00124-5

Miao, Y., Che, H., Zhang, X., and Liu, S. (2020). Integrated Impacts of Synoptic Forcing and Aerosol Radiative Effect on Boundary Layer and Pollution in the Beijing-Tianjin-Hebei Region, China. *Atmos. Chem. Phys.* 20, 5899–5909. doi:10.5194/acp-20-5899-2020

Miao, Y., Che, H., Zhang, X., and Liu, S. (2021). Relationship between Summertime Concurring PM2.5 and O3 Pollution and Boundary Layer Height Differs between Beijing and Shanghai, China. *Environ. Pollut.* 268, 115775. doi:10.1016/j.envpol.2020.115775

Miao, Y., Che, H., Liu, S., and Zhang, X. (2022). Heat Stress in Beijing and its Relationship with Boundary Layer Structure and Air Pollution. *Atmos. Environ.* 282, 119159. doi:10.1016/j.atmosenv.2022.119159

Miao, Y., and Liu, S. (2019). Linkages between Aerosol Pollution and Planetary Boundary Layer Structure in China. *Sci. Total Environ.* 650, 288–296. doi:10.1016/j.scitotenv.2018.09.032

Nielsen-Gammon, J. W., Powell, C. L., Mahoney, M. J., Angevine, W. M., Senff, C., White, A., et al. (2008). Multisensor Estimation of Mixing Heights over a Coastal City. *J. Appl. Meteorol. Climatol.* 47, 27–43. doi:10.1175/2007JAMC1503.1

Philipp, A., Bartholy, J., Beck, C., Erpicum, M., Esteban, P., Fettweis, X., et al. (2010). Cost733cat - A Database of Weather and Circulation Type Classifications. *Phys. Chem. Earth, Parts A/B/C* 35, 360–373. doi:10.1016/j.pce.2009.12.010

Pope, C. A., and Dockery, D. W. (2006). Health Effects of Fine Particulate Air Pollution: Lines that Connect. *J. Air & Waste Manag. Assoc.* 56, 709–742. doi:10.1080/10473289.2006.10464485

Seidel, D. J., Ao, C. O., and Li, K. (2010). Estimating Climatological Planetary Boundary Layer Heights from Radiosonde Observations: Comparison of Methods and Uncertainty Analysis. *J. Geophys. Res.* 115, D16113. doi:10.1029/2009JD013680

Stull, R. B. (1988). *An Introduction to Boundary Layer Meteorology*. Editor R. B. Stull (Dordrecht: Springer Netherlands). doi:10.1007/978-94-009-3027-8

Sun, J., Huang, L., Liao, H., Li, J., and Hu, J. (2017). Impacts of Regional Transport on Particulate Matter Pollution in China: a Review of Methods and Results. *Curr. Pollut. Rep.* 3, 182–191. doi:10.1007/s40726-017-0065-5

Tao, M., Huang, H., Chen, N., Ma, F., Wang, L., Chen, L., et al. (2021). Contrasting Effects of Emission Control on Air Pollution in Central China during the 2019 Military World Games Based on Satellite and Ground Observations. *Atmos. Res.* 259, 105657. doi:10.1016/j.atmosres.2021.105657

Wang, Z., Huang, X., and Ding, A. (2018). Dome Effect of Black Carbon and its Key Influencing Factors: A One-Dimensional Modelling Study. *Atmos. Chem. Phys.* 18, 2821–2834. doi:10.5194/acp-18-2821-2018

Wang, Q., Miao, Y., and Wang, L. (2020). Regional Transport Increases Ammonia Concentration in Beijing, China. *Atmosphere* 11, 563. doi:10.3390/atmos11060563

Xiao, Z., Miao, Y., Du, X., Tang, W., Yu, Y., Zhang, X., et al. (2020). Impacts of Regional Transport and Boundary Layer Structure on the PM2.5 Pollution in Wuhan, Central China. *Atmos. Environ.* 230, 117508. doi:10.1016/j.atmosenv.2020.117508

Yan, Y., Miao, Y., Guo, J., Liu, S., Liu, H., Lou, M., et al. (2019). Synoptic Patterns and Sounding-Derived Parameters Associated with Summertime Heavy Rainfall in Beijing. *Int. J. Climatol.* 39, 1476–1489. doi:10.1002/joc.5895

Ye, X., Song, Y., Cai, X., and Zhang, H. (2016). Study on the Synoptic Flow Patterns and Boundary Layer Process of the Severe Haze Events over the North China Plain in January 2013. *Atmos. Environ.* 124, 129–145. doi:10.1016/j.atmosenv.2015.06.011

Zhang, J. P., Zhu, T., Zhang, Q. H., Li, C. C., Shu, H. L., Ying, Y., et al. (2012). The Impact of Circulation Patterns on Regional Transport Pathways and Air Quality over Beijing and its Surroundings. *Atmos. Chem. Phys.* 12, 5031–5053. doi:10.5194/acp-12-5031-2012

Conflict of Interest: The authors declare that the research was conducted in the absence of any commercial or financial relationships that could be construed as a potential conflict of interest.

Publisher's Note: All claims expressed in this article are solely those of the authors and do not necessarily represent those of their affiliated organizations, or those of the publisher, the editors and the reviewers. Any product that may be evaluated in this article, or claim that may be made by its manufacturer, is not guaranteed or endorsed by the publisher.

frontiers | Frontiers in Environmental Science

ORIGINAL RESEARCH
published: 07 July 2022
doi: 10.3389/fenvs.2022.910816

Understanding Growth-Induced Trends in Local Climate Zones, Land Surface Temperature, and Extreme Temperature Events in a Rapidly Growing City: A Case of Bulawayo Metropolitan City in Zimbabwe

Terence Darlington Mushore[1,2]*, *Onisimo Mutanga*[1] *and John Odindi*[1]

[1]*Discipline of Geography, School of Agricultural, Earth and Environmental Sciences, University of KwaZulu-Natal, Pietermaritzburg, South Africa,* [2]*Department of Space Science and Applied Physics, Faculty of Science, University of Zimbabwe, Harare, Zimbabwe*

OPEN ACCESS

Edited by:
Zhaowu Yu,
Fudan University, China

Reviewed by:
Yongzhu Xiong,
Jiaying University, China
Yuanhui Zhu,
Arizona State University, United States

***Correspondence:**
Terence Darlington Mushore
tdmushore@gmail.com

Specialty section:
This article was submitted to Interdisciplinary Climate Studies, a section of the journal Frontiers in Environmental Science

Received: *01 April 2022*
Accepted: *01 June 2022*
Published: *07 July 2022*

Citation:
Mushore TD, Mutanga O and Odindi J (2022) Understanding Growth-Induced Trends in Local Climate Zones, Land Surface Temperature, and Extreme Temperature Events in a Rapidly Growing City: A Case of Bulawayo Metropolitan City in Zimbabwe. Front. Environ. Sci. 10:910816. doi: 10.3389/fenvs.2022.910816

Assessment of the responses of the urban thermal environment to climate is important, especially because of their possible influence on low- and high-temperature extreme events. This study assessed the combination of remotely sensed land surface temperature (LST) and local climate zones (LCZs) with *in situ* air temperature-retrieved extreme temperature indices. It aimed to assess the effect of urban growth on the three-dimensional thermal environment in the Bulawayo metropolitan area, Zimbabwe. LST and LCZ were derived from the Landsat data for 1990, 2005, and 2020, while extreme temperature indices and trends were derived from daily minimum and maximum temperature data from a local weather station. Results showed that the built LCZ expanded at the expense of vegetation-based LCZ. Average LST for each LCZ increased from 1990 to 2020, which was attributed to background warming, while the expansion of high LST areas was associated with LCZ transitions. Although average minimum temperature decreased, cool nights increased, warmest nights remained unchanged, and the lowest minimum increased, the highest minimum temperatures decreased, but the trends were not statistically significant ($p > 0.05$). Indices of daytime warming showed significant changes, which includes an increase in average maximum temperature ($p = 0.002$), increase in lowest maximum temperature ($p = 0$), increase in the number of very warm days ($p = 0.004$), and decrease in the number of cool days ($p = 0$). The significant increase in daytime extremes was attributed to an increase in highly absorbing LCZ and daytime pollution due to industrial activities. The study also concluded that development in water areas or siltation of water bodies has a greater warming effect than other LCZ changes. The findings show that development needs to consider potential effects on the thermal environment and temperature extremes.

Keywords: LCZ, climate change, temperature extremes, hot days, cold nights, extreme climate indices

INTRODUCTION

Urbanization and related anthropogenic activities are causing myriad environmental changes (Grimmond, 2007; Imhoff et al., 2010; Gusso et al., 2014; Nyamekye et al., 2020). Among the changes are land use and land cover (LULC) transformations that alter the near-surface thermal characteristics (e.g., Mbithi et al., 2010; Amiri et al., 2009; Uddin et al., 2010; Nurwanda and Honjo, 2020). Such alterations in thermal characteristics have caused warming-related challenges that include increased heat-related health risks and mortalities and compromised air quality, thereby further worsening health woes (D'Ambrosio Alfano et al., 2013; Harlan and Ruddell, 2011; McMichael et al., 2006). Furthermore, surface warming has been linked with increased energy and water demand for surface, body, and room cooling (Haghighat, 2002; Pérez-Andreu et al., 2018). On the other hand, development-induced activities, such as the growth of industries, produce pollutants that add to the atmospheric composition of greenhouse gases, which in turn increase warming and related effects (Satterthwaite, 2008; Harlan and Ruddell, 2011). Hence, urbanization has the potential to cause a rise in land surface and air temperatures, whose combined effects significantly compromise urban socioeconomic activities and the environment.

Over the years, urban landscape and thermal analysis has benefited from multispectral space-borne remotely sensed datasets, such as the Landsat series, at various spatial and temporal scales (Weng et al., 2007; Jawak and Luis, 2013; Sithole and Odindi, 2015; Odindi et al., 2017). Generally, city-scale analysis is influenced by the heterogeneous nature of urban LULC types that influence thermal characteristics and distinguish them among nearby locations. Fortunately, sensor developments and improved data handling capabilities have enabled a spatially explicit analysis of these changes, even in complex environments (Dousset and Gourmelon, 2003; Meng et al., 2010; Zhou et al., 2012; Vlassova et al., 2014). For instance, sensors, such as the Landsat series, have provided data at 30 m resolution from 1972 to the present (US Geological Survey, 2019), which is capable of revealing the interaction between the land surface and the thermal environment at fine scales. Furthermore, thermal analysis has also been enhanced by the development of the local climate zones (LCZs) approach, which maps cities into categories related to surface and air temperatures (Bechtel et al., 2012; Stewart et al., 2014; Cai et al., 2016, 2017). The LCZs provide a complete overview of human effects on the climate system as they include both effects of land cover and land use (such as industrialization) on the thermal environment (Stewart and Oke, 2012). Understanding the responses of the thermal environment to long-term changes is important not only for monitoring a city's climate but also for assessing the sustainability of its development trajectories.

Among the known impacts of climate change is the intensification of extreme events, such as heat waves, strong winds, heavy precipitation, and prolonged dry spells (Hallegatte and Corfee-Morlot, 2011; Parnell and Walawege, 2011; Goddard and Gershunov, 2020). Small changes in the mean can cause a large change in the likelihood of extreme climate events (Sensoy et al., 2013). For instance, rising temperatures will influence human societies and natural ecosystems with potentially severe effects globally, while the increased heat load in urban areas will harm public health (Sensoy et al., 2013; Geleti et al., 2019). To aid and standardize the analysis, 27 extreme climate indices (precipitation and temperature) have been developed and improved over time (Stenseth et al., 2003; Zubler et al., 2014; Sajjad and Ghaffar, 2019). In line with this, the RClimdex software was developed by the National Climate Data Centre of NOAA to compute the 27 indices of extreme climate using R software. The program provides an easy-to-use software package for the calculation of indices of climate extremes as well as their long-term trends for monitoring and detecting climate change impacts. The indices describe special characteristics of extremes, including amplitude, frequency, and persistence (Toure et al., 2017). They cover a large range of climates and have a large signal-to-noise ratio. Most importantly, they involve the calculation of the number of days in a year exceeding specific thresholds. The indices were found to reveal details hidden in the trends of annual average values. For instance, Kruger (2006) and Kruger and Sekele (2012) observed insignificant trends in annual precipitation and absolute temperatures (maximum and minimum), while extreme precipitation and temperature indices showed significant trends in South Africa. Similarly, a number of studies have indicated strong trends in extreme climate events, especially those related to temperature due to warming (e.g., Kruger, 2006; Mónica and Santos, 2011; Vincent et al., 2011; Athar, 2014; Sein et al., 2018). The indices are of great value, thereby needing application to different types of environments to understand climate trends and their impact.

Although indices have been applied in previous studies, the focus has mainly been on large-scale analysis, such as regional and national (e.g., Kruger, 2006; Vincent et al., 2011; Kruger and Sekele, 2012; Zubler et al., 2014; Rahimi and Hejabi, 2017; Popov et al., 2018; Ogunjo et al., 2021). For instance, Kruger (2006) and Kruger and Sekele (2012) focused on South Africa and observed a rising trend in temperature and precipitation extremes, respectively. On a similar scale, (Vincent et al., 2011) observed significant trends in warming-related extremes and weak trends in precipitation extremes in western India. Recently, Ogunjo et al. (2021) observed rising trends in heat-related extremes and falling trends in cold extremes, such as cold days over Nigeria. While large-scale analysis provides a broader picture, localized analyses are important for area-specific and dynamic adaptation and mitigation strategies and activities. This is important, especially in urban areas of developing countries, where rapid development activities and population growth are influencing climate, thereby worsening the potential for harsh extreme events, especially those related to warming. However, to the best of our knowledge, studies that focus on extreme climate events, especially those related to temperature in urban areas, are scarce. Furthermore, there is a paucity of studies that relate urban growth to trends in extreme climate events, especially in developing countries, despite the projected growth and climate patterns. The growth of cities, which has occurred over the years, has changed the spatial structure of LCZs, and the responses of

the thermal environment to these long-term changes need to be monitored and understood. The impact of climate change-related extreme events is greater where large populations and high-value properties are at great risk (Brown et al., 2010), which are characteristic of urban areas. A variety of socioeconomic and development activities can be adversely affected by harsh climatic extremes. For instance, high-temperature extremes can cause the melting of tarred roads and affect the density of air, thereby causing aircrafts to lose lift as well as causing mechanical problems in machinery and human health issues (Abatan et al., 2016). Evidently, the effects of long-term historical urban growth patterns on the thermal environment help in understanding the cumulative effects of slow and unmitigated anthropogenic activities that are important for planning future development trajectories.

Urban growth causes LCZ transitions that alter the spatial distribution of the LST, which perpetually influences the air temperature above. Therefore, the analysis of LST patterns provides two-dimensional information on the extent to which land surfaces are heating the surrounding air and influencing extreme temperature events. Similarly, temporal changes in the LCZ and the LST provide an overview of the effect of changes in surface properties and in the amount of heat received and emitted by constant surfaces over time. On the other hand, a third dimension that expresses the consequence of anthropogenic and natural influences can be offered by extreme temperature indices. To date, studies have kept surface and air temperature analysis separate, thereby limiting understanding of the interaction between these interfacing components (e.g., Pielke et al., 2011; Wu et al., 2012; Ahmed et al., 2013). For instance, replacing a natural LCZ with an industrial area will not only change LST due to the construction of buildings and impervious surfaces but also change the air temperature and associated extremes due to increased pollution and the greenhouse effect. It is important to quantify changes in LST and extreme temperature indices and isolate the influence of LCZ changes from other causes of LST changes. Air and surface temperature complement each other as the former represents all-sky conditions while the other represents clear-sky conditions only. Air temperature measurements can add value by providing useful information for decision support, such as using indices to highlight trends in extreme temperatures. Evidently, combining LCZ and LST information with extreme temperature indices provides insights into the interface between development and long-term climate extremes in dynamic urban environments. In view of observed and projected changes in temperatures of cities and increased anthropogenic activities, it is important to assess the corresponding changes in indicators of extremes related to low and high temperatures. Therefore, understanding the patterns of low and high-temperature extremes is required for the formulation of adaptation and mitigation strategies as well as for the implementation of sustainable urban development strategies.

Similar to other cities in the developing world, Zimbabwean cities are experiencing exponential growth, thereby resulting in expansive LCZ transitions. A previous study that looked at climate extremes in Zimbabwe focused on a large area by including countries in western central Africa and Guinea Canakry (Aguilar et al., 2009). The study focused on general trends in extreme rainfall and temperature, not a localized link between growth patterns and extreme climate events, especially in the context of LCZ. It is necessary to monitor the long-term changes in the urban thermal environment and understand them in the context of both LCZ dynamics and background (global warming). Hence, this study seeks to quantify 1) the contribution of LCZ changes to long-term changes in LST and extreme temperature events in Bulawayo and 2) the long-term influence of background warming on LST in different LCZs. The study also assesses the combined effect of LCZ changes and background warming on extreme temperature events using extreme temperature indices.

DATASETS AND METHODS

The Study Area

Bulawayo is located in the southeast of Zimbabwe and is the country's second-largest city. The city is at an elevation of approximately 1358 m above sea level. Rainfall is prevalent between October and March, and the area is characterized as hot and wet, with an average temperature of 25°C. The rest of the months has an average temperature of 15°C under cool and dry conditions (Mutengu et al., 2007). The city is located in a semi-arid climate, where rainfall is erratic rainfall (annual average precipitation of 600 mm and rainfall ranging from 199.3 to 1258.8 mm). Proximity to the Kalahari makes the area vulnerable to droughts (Gumbo et al., 2003; Muchingami et al., 2012). While a network of weather stations is ideal for depicting spatial patterns in temperature extremes, only two weather stations, operated by the Meteorological Services Department, are operational in the city. One at Goertz Observatory is for public weather and climatological services and the other at Joshua Nqabukho Airport (Bulawayo Airport Meteorological Office - BAMO) is for aviation purposes, with its data inaccessible. Hence, due to the limited number of weather stations, combining space-borne LST with *in situ* air temperature observations enhances spatial and temporal analysis of the city's thermal environment. **Table 1** indicates the main sources of data in this study.

Retrieval of Responses of LCZ to Growth of Bulawayo

Multispectral optical data for 1990 (Landsat 5), 2005 (Landsat 7), and 2020 (Landsat 8) were resampled to ensure the same orientation of pixels for all periods (**Table 2**). The data were also corrected for atmospheric effects using the dark subtraction methods following solar zenith normalization. For each year, imageries were collected in the cool dry, hot dry, and wet (post-rain) seasons. The rainy season was not used due to difficulty in obtaining cloud-free imageries, thereby making it difficult to have data for the same seasons in all considered periods.

LCZs identified in the study area are described in **Table 3**. LCZ maps were produced for each year using the World Urban Database and Access Portal Tools (WUDAPT) Level 0

TABLE 1 | Sources of data used in this study.

Dataset	Source
In situ meteorological data	Meteorological Services Department of Zimbabwe
Worldclim data	Worldclim website (https://www.worldclim.org/data/monthlywth.html)
Landsat data	United States Geological Survey (USGS) earth explorer website (www.earthexplorer.usgs.gov)
Ground Truth Local Climate Zones	Field survey and Word Urban Database and Access Portal Tool level 0 procedure (www.wudapt.org)

TABLE 2 | Multitemporal and multispectral remote sensing imagery used in the study.

Imagery	Date	Season
Landsat 5	27 April 1990	Post rain
Landsat 7	12 April 2005	Post rain
Landsat 7	21 April 2020	Post rain
Landsat 5	14 June 1990	Cool
Landsat 5	7 June 2005	Cool
Landsat 7	24 June 2020	Cool
Landsat 5	20 October 1990	Hot
Landsat 7	21 October 2005	Hot
Landsat 8	15 October 2020	Hot

procedure (Bechtel et al., 2012; Mitraka et al., 2015; Cai et al., 2016). The technique involves digitizing training areas in Google Earth, mapping LCZ using the Random Forest classifier, and assessing accuracy in the SAGA GIS software. Sample locations (coordinates) of representative points were collected for each of the LCZ categories at evenly distributed places across the study area between 18 and 27 October. This experience also guided the selection of training areas for historical periods using Google Earth in the absence of field measurements. Field observations increased the validity of the analysis instead of exclusive reliance on Google Earth retrievals. Data were collected in a manner to capture not only interclass but also intraclass variabilities, especially those due to seasonality.

Approximation of Mean Spatial Distribution of Average Air Temperature Across LCZs

The city has only two weather stations (Goertz Observatory and Bulawayo Airport Meteorological Office). The two could not provide a spatial depiction of air temperature caused by LCZ variations in the city. As such, a 21 km^2 resolution bias corrected the Worldclim maximum and minimum temperature data (https://www.worldclim.org/data/monthlywth.html). The data for 1990–2018 were used to depict the spatial variations of average air temperature in the city. The 1 km^2 resolution data were not used because they did not cover periods after 2000. Although the study period continued to 2020, analysis of Worldclim data was only confined to up to 2018 due to the data available on the online platform. The gridded data were chosen due to the lack of weather stations to map the spatial structure of air temperature in the study area. The link between average air temperature and LST was qualitatively investigated. The Mann–Kendall test at a 95% confidence interval was performed to detect the effect of LCZ changes on annual average maximum and minimum air temperatures derived from the monthly Worldclim data.

Derivation of Extreme Temperature Indices and Their Trends

Brown et al. (2010) provided a definition of 27 extreme climate indices. In this study, we focused on 12 defined in **Table 4** which characterizes temperature extremes. In this study, we used indices that compute based on the percentage of days below or above the thresholds (cool nights, warm nights, cool days, and warm days) and the number of days below or above the thresholds (warm spell duration indicator, cool spell duration indicator, frost days, summer days, and tropical nights) as well as intensity-based thresholds (highest maximum temperature, lowest minimum temperature, highest minimum temperature, and daily temperature range). Due to years of improvements, the computation of

TABLE 3 | Description of LCZ categories identified in Bulawayo during field survey.

LCZ Type	Description
Compact low rise (LCZ3)	Dense mix of low-rise buildings (1–3 stories). Few or no trees. Land cover mostly paved. Stone, brick, tile, and concrete construction materials
Open low rise (LCZ6)	Open arrangement of low-rise buildings (1–3 stories). Abundance of pervious land covers (low plants, scattered trees). Wood, brick, stone, tile, and concrete construction materials
Light weight low rise (LCZ7)	Dense mix of single-story buildings. Few or no trees. Land cover mostly hard-packed. Lightweight construction materials (e.g., wood, thatch, corrugated metal)
Dense forest (LCZ A)	Heavily wooded landscape of deciduous and/or evergreen trees. Land covers mostly pervious (low plants). Zone function is natural forest, tree cultivation, or urban park
Low plants (LCZ D)	Featureless landscape of grass or herbaceous plants/crops. Few or no trees. Zone function is natural grassland, agriculture, or urban park
Water LCZ G)	Large, open water bodies such as seas and lakes, or small bodies such as rivers, reservoirs, and lagoons

TABLE 4 | Extreme temperature indices used to assess climate change impact in Bulawayo.

ID	Indicator Name	Definitions	Units
TN10p	Cool nights	Percentage of days when TN < 10th percentile	%
TN90p	Warm nights	Percentage of days when TN > 90th percentile	%
TNn	Min Tmin	Annual minimum value of daily minimum temperature	°C
TNx	Max Tmin	Annual maximum value of daily minimum temperature	°C
FD0	Frost days	Annual count when TN (daily minimum) < 0°C	Days
meanTmin	Average minimum temperature	Annual average value of minimum temperature	°C
TR20	Tropical nights	Annual count when TN (daily minimum) > 20°C	Days
CSDI	Cold spell duration indicator	Annual count of days with at least 6 consecutive days when TN < 10th percentile	Days
TX10p	Cool days	Percentage of days when TX < 10th percentile	%
TX90p	Warm days	Percentage of days when TX > 90th percentile	%
TXn	Min Tmax	Annual minimum value of daily maximum temperature	°C
TXx	Max Tmax	Annual maximum value of daily maximum temperature	°C
DTR	Diurnal temperature range	Annual mean difference between TX and TN	°C
meanTmax	Average maximum temperature	Annual average value of maximum temperature	°C
SU25	summer Days	Annual count when TX (daily maximum) > 25°C	Days
WSDI	Warm spell duration indicator	Annual count of days with at least 6 consecutive days when TX > 90th percentile	Days

indices and their temporal trends have been incorporated into the freely accessible RClimdex software used in this study. The computation of extreme temperature indices makes use of continuous records of daily minimum and maximum temperature data for a given area. As such, daily maximum (TX) and minimum (TN) temperature data for the period 1990 to 2020 were used. Although low-temperature extremes, such as ground frost, are experienced in the study area, the ice days (ID0) extreme temperature index was not investigated because there are no records of snow in this semi-arid location. The selection of area-relevant climate extreme indices was in line with Almazroui et al. (2014), as they excluded analysis of extreme precipitation indices between 1981 and 2010 in Saudi Arabia because the area is dry, thereby recording very few days of rainfall in any year. Sein et al. (2018) also selected 19 extreme climate indices in Myanmar based on their applicability in the study area. Although Bulawayo is semi-arid, it receives rainfall on a countable number of days in a year. In this study, rainfall extremes were not included because the focus was on responses of temperatures and related extremes to growth and anthropogenic activities in the area. The data were initially quality controlled and put through a homogeneity test using the RH test, which is also provided as a component for the retrieval of indices (Zhang et al., 2004; Almazroui et al., 2014). Since the procedure included analysis of trends in extreme temperatures, homogeneity test was performed to identify nonclimatic changes, such as changes in location of stations. Fortunately, in the period under study, there was assurance that the instruments and location of stations did not change, given that very recent and known 30 years were analyzed. Previous studies (Sensoy et al., 2013; Almazroui et al., 2014; Sein et al., 2018; Geleti et al., 2019) also used at least 30 years and 30-year intervals to investigate trends in climate extremes. Trends in the indices were computed in RClimdex using ordinary least squares fit, and the Mann–Kendal test was used to test the statistical significance (Abatan et al., 2016). RClimdex manual (Zhang et al., 2004) provides detailed steps on the derivation of extreme climate indices and analysis of trends.

Computation of Long-Term Changes in LST

Landsat 5, Landsat 7, and Landsat 8 thermal data were used to compute LST for 1990, 2005, and 2020. In each season, images were collected around the same dates [anniversary images–(Mouat et al., 1993)], with similar meteorological conditions (mainly on calm days with clear skies) on different days. Mouat et al. (1993) indicated that the influences in seasonal conditions are eliminated using anniversary images in change detection. Feng et al. (2014) used imageries of January to show the influences of land surface changes on LST from 1987 to 2007 in Xiamen City in China. Amorim (2018) showed that LSTs are influenced by rainfall activity prior to satellite overpass and data acquisition. This was achieved by ensuring rainfall activities 10 days prior to each scene were similar for imageries of the same season in different years. Since cloud cover also affects LST, cloud-free imageries were used. Therefore, LST changes in this study resemble changes for days with similar weather conditions preceding and during the satellite overpass. This eliminates randomness due to differences in weather conditions around the image acquisition time. Randomness was further reduced by computing an average LST layer for each year using retrievals from different seasons. Initially, the data were corrected for differences in solar zenith angles. While Landsat 8 has two thermal infrared bands, a single-channel technique was applied for all periods to minimize the effects of differences in computation algorithms on LST variations between times. Digital numbers of thermal data were converted to radiances using the reflectance toolbox in ArcGIS version 10.2, which were then used to determine the brightness and surface temperature using **Equation 1** (Stathopoulos et al., 2004; Chen et al., 2006; Srivanit et al., 2012).

$$T_b = \frac{K_2}{\ln\left(\frac{K_1}{L_\lambda} + 1\right)} \quad (1)$$

K_1 takes a value of 607.76, 666.09, and 774.89 W/(m^2 srμm), while K_2 has values of 1260.56, 1282.71, and 1321.08 W/(m^2 srμm) using Landsat 5, Landsat 7, and Landsat 8 data,

respectively. A method based on spectral and blackbody radiance of the thermal infrared band was used to obtain a pixel-based land surface emissivity map (ε) (Yang, 2004). Emissivity correction was applied to brightness temperature to obtain actual LST using **Equation 2** (Weng et al., 2007).

$$T_s = \frac{T_B}{1 + \left(\frac{\lambda T_B}{\rho}\right) \ln \varepsilon} \quad (2)$$

Where λ is the central wavelength of emitted thermal radiance (11.5 μm for Landsat 5 and Landsat 7 and 10.9 μm for band 10 of Landsat 8) and ρ is equal to 1.438×10^{-2} mK. The procedure above was used to retrieve LST on different dates; thus, an average LST was developed for each year. The spatial structure of LST intensities was used for visual and quantitative analysis of changes that occurred between 1990 and 2015.

Linking Long-Term Changes in LCZ to LST Dynamics

Using spatial overlays, the average LST per LCZ category was obtained for each period. LST variations in each LCZ were analyzed between 1990 and 2020. Furthermore, data for 1990 and 2020 were used to derive normalized temperatures as well as to determine the effect of LCZ transitions on LST intensities. The normalized temperature approach (Zhou and Wang, 2011) enables the separation of intraclass LST changes from those due to LCZ transitions between any two intervals. In this study, intra-LCZ LST changes were attributed to other external factors, such as background warming, which were removed from interclass LST changes to derive the effects of LCZ transitions. Changes in LST without transition in LCZ were computed using **Equation 3**.

$$\Delta T_i = T_{i_{2020}} - T_{i_{1990}} \quad (3)$$

Composite differences in LST between LCZ j and LCZ i was computed by **Equation 4**.

$$dT_{ij} = T_{j_{2020}} - T_{i_{1990}} \quad (4)$$

The normalized temperature was then used to represent the change in LST due to the transition from LCZ i to LCZ j using **Equation 5**.

$$dTn = dT_{ij} - \Delta T_i \quad (5)$$

Where dTn is the change in temperature caused by the replacement of LCZ i by LCZ j, ΔTi is the change due to other factors than LCZ change, and $dTij$ is the change in temperature before normalization.

RESULTS AND DISCUSSIONS

LCZ Mapping and Transitions

The LCZs were mapped with overall accuracies of 98, 98.2, and 95% for 1990, 2005, and 2020, respectively (**Figure 1**). Built-up LCZs, namely compact low rise, lightweight low rise, and open low rise, expanded between 1990 and 2020. Densely built-up LCZs expanded in the western direction, while open settlement arrangements expanded in the eastern direction. Visual inspection of **Figure 1A–C** suggests that the expansion of lightweight low rise mainly intruded the low plants LCZ. There is also evidence of change from dense vegetation to low plants, which indicates deforestation as the city grows. Throughout the study period, the Goertz Observatory weather station remained in the open low-rise LCZ category, although changes were experienced in other areas, including its surroundings. Compact low rise, which occupied 3% in 1990, increased coverage to 4.5% of the entire study area in 2020. Marked quantitative expansions were observed in lightweight low rise and open low rise, which increased from 9.1 to 17.3% and 10.4–20.4% of the study area between 1990 and 2020, respectively. Vegetation and water-based LCZ declined during the same period with a marked change in low plants LCZ, which reduced from 68.2 to 51.4% of the study area.

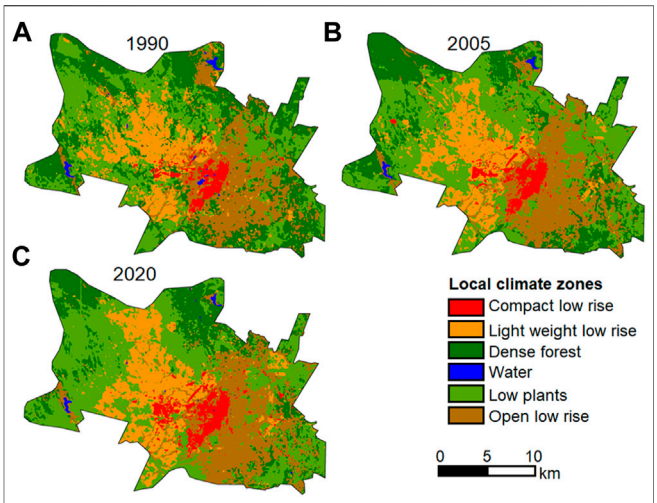

FIGURE 1 | Long-term changes in LCZs in Bulawayo. LCZ structure in 1990 **(A)**, 2005 **(B)** and 2020 **(C)**.

Spatial Distribution of Air Temperature and Link With LCZ

Average minimum and maximum temperatures decreased westwards in the city over the different study periods (**Figure 2A–H**). When comparing the built LCZs, high average minimum and maximum temperatures generally coincide with areas occupied by densely built LCZ, such as the compact low rise and lightweight low rise. High average temperatures also occurred in low plant areas, especially in the northern half of the city. Low plants LCZ included agricultural land, bare areas, and grasslands. The heat mitigation value of grasslands was overshadowed by the heat absorption effect of bare and dry vegetation of cropland areas in post-planting periods, thereby resulting in high temperatures in the low plants LCZ. On the contrary, low average air temperatures occurred in areas in the west occupied by open low rise, which are characterized by well-

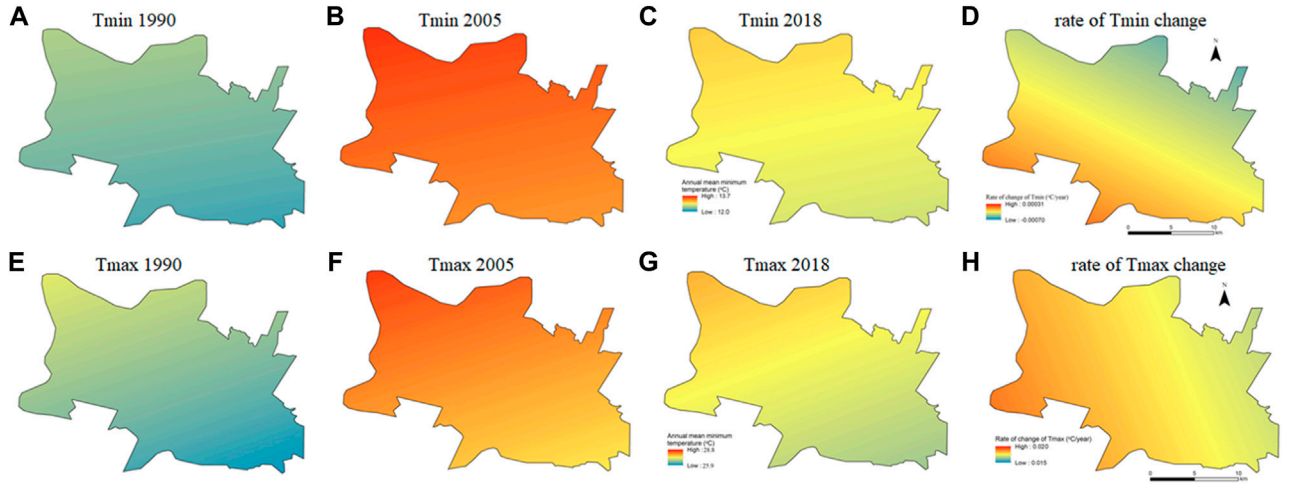

FIGURE 2 | Annual mean minimum temperatures **(A–C)** and their rate of change **(D)** as well as annual mean maximum temperatures **(E–G)** and their rate of change **(H)** from 1990 to 2018.

spaced buildings within a high fraction of healthy vegetation. **Figure 2D** shows that the northern half of the city experienced a drop in minimum air temperatures, while the southern half experienced increases. However, the rates of change in minimum air temperature over the 30-year period were almost insignificant (below 0.0001°C/year). On the other hand, **Figure 2G** shows a pronounced rate of change in maximum air temperature in all areas of the city. Larger rates of change in maximum air temperature were recorded mostly in the southern half of the city, which corresponded to areas where massive growth of built LCZ occurred between 1990 and 2018. A comparison of temperatures in 1990, 2005, and 2018 showed that the year 2005 was warmer than the others (**Figure 2B** and **Figure 2G**). Since the overall trends based on continuous data from 1990 to 2018 showed warming, larger temperatures in 2005 than the other years could be attributed to climate variability with the broad changes. Additionally, before the intensification of the economic crisis in 2008, Bulawayo was the industrial hub of Zimbabwe. The marked warming from 1990 to 2005 could be due to increased industrial pollutants, which slowed down post-2008, thereby causing a drop in temperatures from 2005 to 2018. The temperatures remained higher toward 2018 than around 1990 due to contributions from some of the industrial activities, which managed to continue and other effects, such as LULC changes due to city growth.

Responses of Air Temperature Extremes to Urban Growth and LCZ Changes

The changes in minimum temperature extremes were mostly characterized as insignificant trends ($p > 0.05$) and slope errors, which were greater than the slope at the Goertz Observatory station (**Figure 3**). As such, the average minimum temperature showed a decreasing trend with a slope of −0.008°C/year, a slope error of absolute value of 0.008°C/year, and an insignificant trend ($p = 0.323$)—(**Figure 3A–H**). Similarly, insignificant trends with slope error exceeding slope were observed on warm nights (**Figure 3D**), cold spell duration indicator (**Figure 3E**), and the highest minimum temperature (**Figure 3F**).

Maximum temperature–related extremes showed meaningfully (slope greater than slope error) and significant trends ($p < 0.05$) between 1990 and 2020 (**Figure 4**). From 1990 to 2020, the mean maximum temperature for Bulawayo increased significantly (slope of 0.06°C/year, slope error of 0.017°C/year, and p-value of 0.002) as observed at Goertz Observatory (**Figure 4A**). Significant trends were also observed in the increase in warm days (**Figure 4B**), rising in the daily temperature range (**Figure 4C**), and increase in the number of summer days (**Figure 4D**), as well as in decrease in cold days (**Figure 4E**). Significant rising trends were also recorded in lowest and highest maximum temperatures (**Figure 4G** and **Figure 4H**), all indicating shifts to tormentingly hot daytimes. Although the trend was insignificant, events of successive warm days are also increasing, as indicated by a rising trend in the warm spell duration indicator (**Figure 4F**).

Long-Term Changes in the Two-Dimensional LST in Response to LCZ Changes

Figure 5 shows the expansion of high-temperature surfaces between 1990 and 2015. In 1990, LSTs in the 37.8–43.8°C range (**Figure 5A**) dominated the city, while LSTs below 43.8°C became uncommon in 2005 (**Figure 5B**). Visual inspection shows that in 2020, LSTs became even higher, with most areas recording values above 46.8°C (**Figure 5C**). The water areas were the most stable, with LSTs in the 16.8 to 37.8°C range in 1990, 2005, and 2020.

Lower LSTs were observed in residential rather than commercial built LCZs, with a marked decline as vegetation abundance increased (**Figure 6**). In all LCZs, LST changes were larger in 1990 to 2005 than in the 2005 to 2020 interval. For instance, the average LST for compact low rise increased from

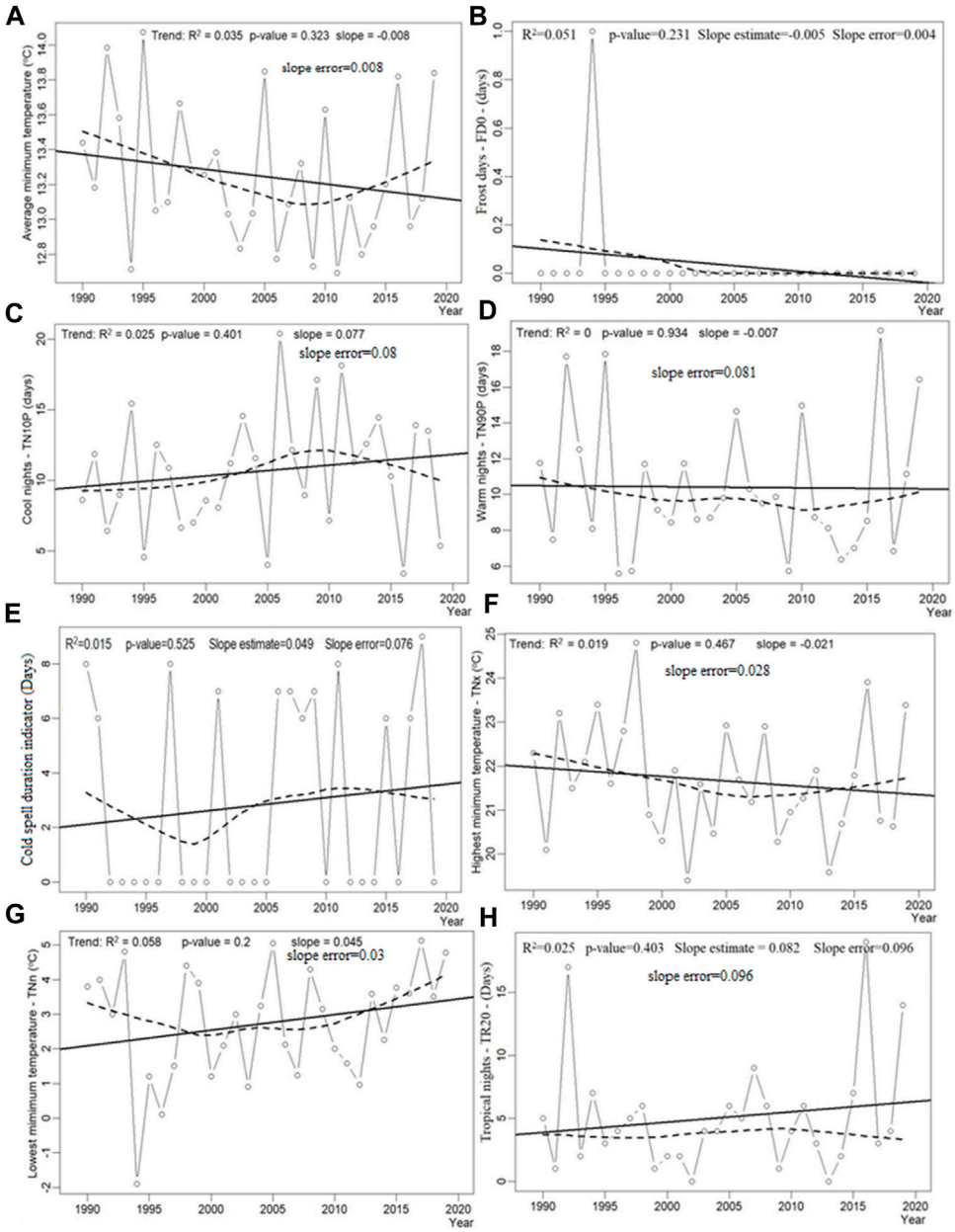

FIGURE 3 | Trends in **(A)** Average minimum, **(B)** Frost days, **(C)** Cool nights, **(D)** Warm nights, **(E)** Cold spell duration indicator, **(F)** Highest minimum, **(G)** Lowest minimum, and **(H)** Tropical nights at the Goertz Observatory in Bulawayo.

40.8 to 47.7°C between 1990 and 2005, while it increased from 47.7°C between 2005 and 2020. LST in dense forest areas was almost similar to those in open low-rise regions and cooler than those in other LCZs, except in water areas.

Background Warming Corrected Effects of LCZ Transitions on LST Dynamics

The change from other LCZ types to compact low rise resulted in warming except for such change from low plants' LCZ, which could lead to a 0.4°C drop in LST (**Table 5**). Replacing water with any other LCZ would cause warming by at least 9.6°C. Increased vegetation density in lightweight low-rise LCZ areas would cause an LST decrease of approximately 1.2°C.

Discussion of Findings

Although all built LCZs expanded between 1990 and 2020, the residential areas (open low rise and lightweight low rise) expanded more than the central business district (CBD) and industrial areas (compact low rise). The expansion of residential areas provides evidence that the population of urban dwellers is increasing with time in developing countries. People develop the

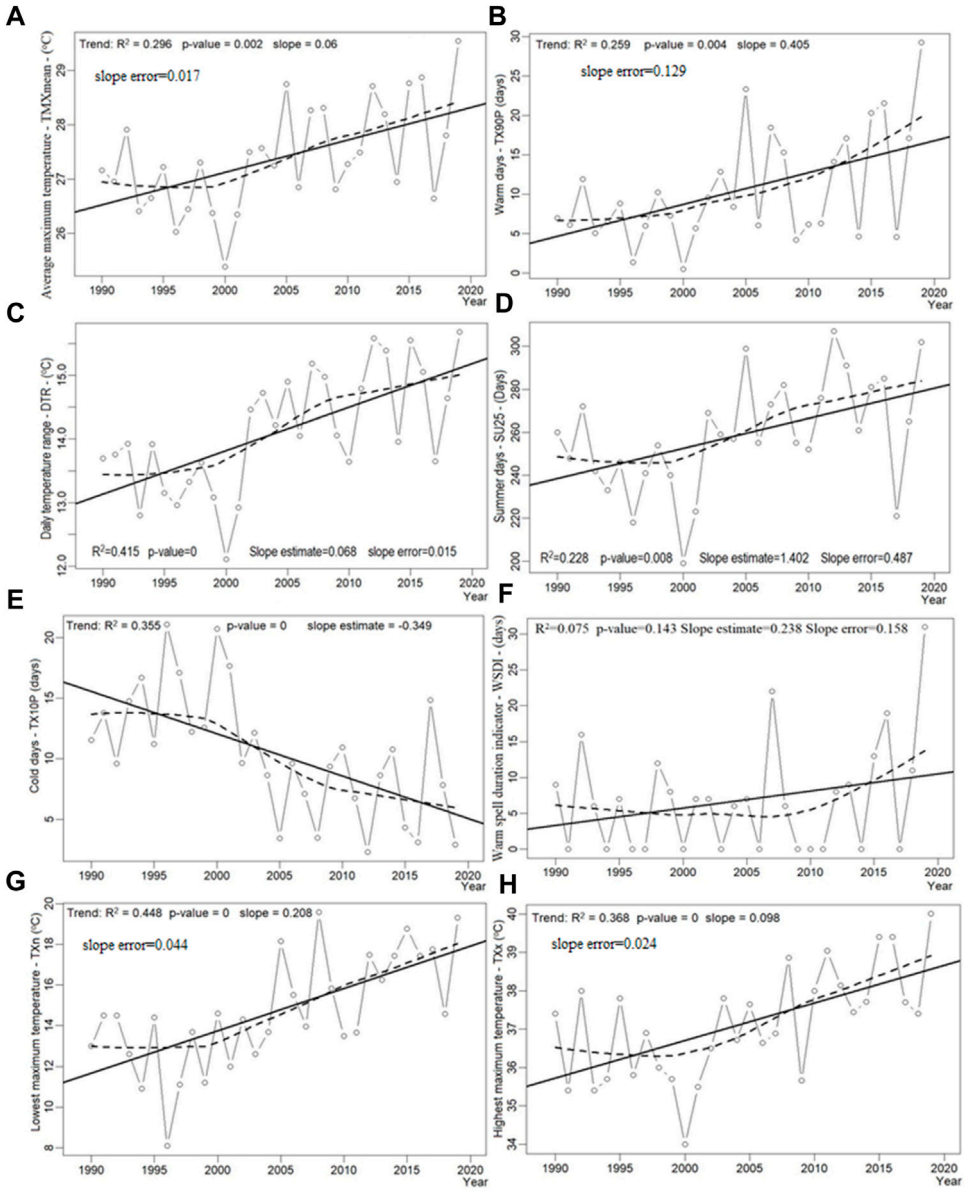

FIGURE 4 | Trends in **(A)** Mean maximum temperature, **(B)** Warm days, **(C)** Daily temperature range, **(D)** Summer days, **(E)** Cool days, **(F)** Warm spell duration indicator, **(G)** Lowest maximum temperature, and **(H)** Highest maximum temperature at the Goertz Observatory in Bulawayo.

tendency to prefer advanced areas of the country, where improved amenities are available and there is ease of access to basic needs. Generally, in Zimbabwe, ownership of a home in an urban area is a symbol of wealth, which drives citizens to work hard to purchase land and develop it. Furthermore, as incomes improve, people also purchase land in spacious areas, as evidenced by the expansion of open low-rise LCZ, which coincides with medium- to low-density residential areas, where medium- to high-income strata reside. While the built LCZ expanded, vegetation and water-based LCZs shrunk during the same time interval. This is because of spacious housing developments within vegetation LCZs (open low rise) and, in other areas, massive replacement of vegetation with densely built compact low rise and lightweight low rise LCZs. The slower expansion of compact low rise than other built LCZs could be due to the cost of land areas due to commercialization in the CBD and industrial areas.

Analysis of Worldclim air temperature data showed low-temperature values in vegetation than built LCZs. High vegetation fraction areas benefit from the cooling effect of vegetation due to latent heat of vaporization transfer (Ca et al., 1998; Thatcher and Hurley, 2012; Tao et al., 2013; Chun and Guldmann, 2014). Since air temperatures are measured at 1 m, trees provide a shading effect at that height, thereby resulting in low temperatures in occupied LCZ (Toudert, 2005; Hwang et al., 2011; Puliafito et al., 2013; Zhao et al., 2015). A

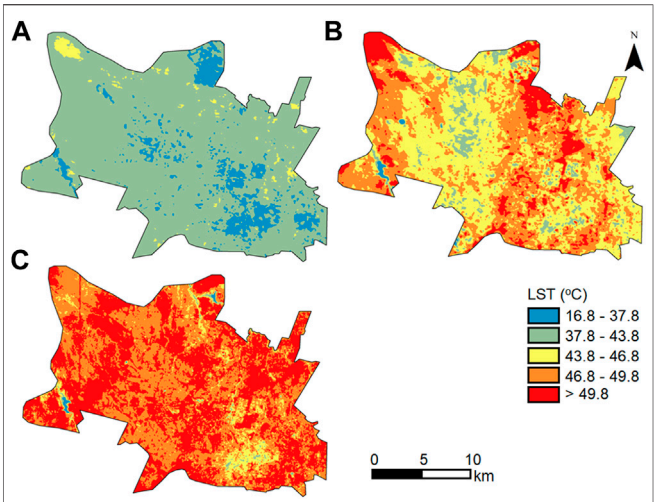

FIGURE 5 | Spatial structure of LSTs in Bulawayo in **(A)** 1990, **(B)** 2005, and **(C)** 2020.

generalization of air temperatures caused by the coarse spatial resolution of the Worldclim data was inadequate for depicting minute temperature structures caused by fragmentation and LCZ heterogeneity in the study area. The details were not as spatially explicit as LST counterparts mapped when using Landsat data resampled to 30 m resolution. However, although the resolution was coarse, the air temperature map successfully showed the general effect of the LCZ structure on the near-surface thermal environment of Bulawayo.

Meaningful, though statistically insignificant, trends were recorded in frost days, lowest minimum temperature, and tropical nights extreme climate indices, which were decreasing, increasing, and increasing, respectively. Based on these trends, we deduced that there is an insignificant increase in night temperature, thereby causing slight warming, which has reduced the occurrence of low-temperature extremes and increased warm/tropical nights in Bulawayo. The night warming could be insignificant, given that Bulawayo is semi-arid with high chances of cloud-free nights, which allow radiation to escape to outer space, thereby moderating nighttime warming extremes. The expansion of the urban fabric could also provide the capacity to lose heat at slow rates, thereby reducing the chances of low-temperature extremes. However, this study did not involve an in-depth analysis of the materials used in urban construction beyond partitioning the city based on the LCZ scheme.

Observed significant rise in daytime temperature concurs with general trends of rising air temperature recorded in other studies in Zimbabwe (Unganai, 1996; Zvigadza et al., 2010; Brazier, 2015). For instance, Zvigadza et al. (2010) observed that temperatures in the country rose by over 1°C over 40 years up

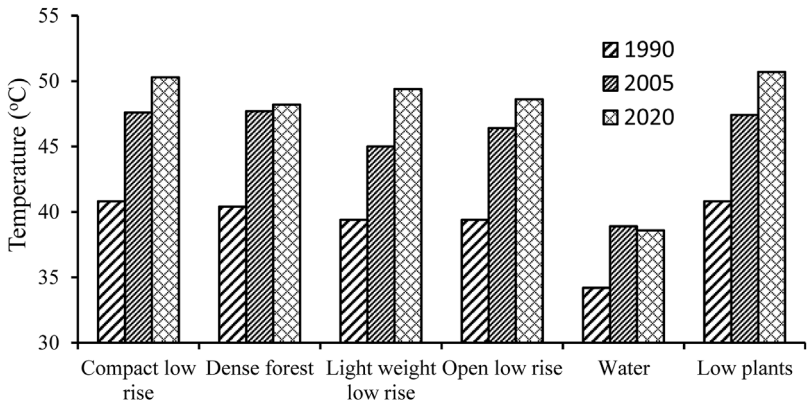

FIGURE 6 | Changes in mean LST across LCZs from 1990 to 2020 in Bulawayo.

TABLE 5 | Responses of LST to LCZ transitions corrected for background warming.

Initial LCZ Category						
Final LCZ Category	**Compact Low Rise**	**Dense Forest**	**Light Weight Low Rise**	**Open low Rise**	**Water**	**Low Plants**
Compact low rise	**0.0**	2.1	0.9	1.7	11.7	−0.4
Dense forest	−2.1	**0.0**	−1.2	−0.4	9.6	−2.5
Light weight low rise	−0.9	1.2	**0.0**	0.8	10.8	−1.3
Open low rise	−1.7	0.4	−0.8	**0.0**	10.0	−2.1
Water	−11.7	−9.6	−10.8	−10.0	**0.0**	−12.1
Low plants	0.4	2.5	1.3	2.1	12.1	**0.0**

The bold values showing diagonal axis.

to 1998. However, these previous studies used low temporal resolution analysis and focused on average temperatures rather than extreme events. The study also showed that the lowest maximum temperature, highest maximum temperature, and the number of successive hot days significantly increased between 1990 and 2020. In recent years, record-breaking high temperatures and heat waves have occurred in different parts of Zimbabwe, especially during the hot season. Although the LCZ did not change at the Goertz Observatory between 1990 and 2020, maximum temperature extremes significantly changed during the period. This is similar to the findings that the values of extreme climate indices in all LCZs in Brno, Czech Republic, increased from the sixth decade of the 20th century toward the first decade of the 21st century (Geleti et al., 2019). Although this study was on a much-localized scale, significant trends in warming-related climate extremes are also in tandem with observations from other parts of the world. For instance, Rahimi and Hejabi (2017) observed significant warming trends in extreme temperature indices between 1960 and 2014 in Iran. Similar to this study, Popov et al. (2018) observed decreasing/increasing trends in cold/warm extremes in Bosnia and Herzegovina. A decrease in cool days, an increase in warm days, and an increase in mean maximum temperature were also observed over Lagos, Nigeria (Ogunjo et al., 2021). The warming could be attributed to an increase in anthropogenic activities, such as changes in LCZ and industrial activities, which add pollutants to the lower atmosphere.

The city surface was warming as the spatial structure of LCZs changed between 1990 and 2005. According to Nayak and Mandal (2019), urbanization causes temperature changes due to both alterations of LULC and greenhouse gas concentrations. Similarly, in this study, we attributed surface warming to LCZ transitions and background caused by anthropogenic activities, such as industrial emissions. Blake et al. (2011) also reported that Harare was warming, despite cooling in the decade from 1900 to 2002. The heat mitigation value of vegetation was not evident in low plants LCZ during the study period. The low plants LCZ is composed of a mixture of bare, agricultural, and grassland areas, thereby resulting in varied effects on the thermal environment. For instance, dry, bare areas and dry vegetation eliminate the heat mitigation value of healthy low plants. Furthermore, the study was conducted during the hot, dry season when most of the trees had shed leaves during the cool season. Most low plant areas will be bare or covered with dry grass, while agriculture areas will mostly also be bare or covered with dry crop residues with no heat mitigation value due to the absence of moisture. The warming effects of LCZ transitions concur with the assertion by Feng et al. (2014) and Gallo et al. (1993) that urbanization-induced changes can impact temperature trends similar to those expected under an enhanced greenhouse warming scenario.

Vegetation moderated LSTs even in built-up LCZs, such as lightweight low rise. Field surveys and Google Earth images show that in Bulawayo, even in lightweight low rise areas, residents prefer trees and other vegetation covers in available spaces. Similar to patterns observed in Harare (Mushore et al., 2018), open low-rise areas, which correspond to spacious settlements of middle to high-income strata, have abundant and well-maintained vegetation cover. According to Sithole and Odindi (2015), green spaces act as heat sinks as they tend to be porous and assimilate local heat, which explains low temperatures in areas of abundant vegetation. In recent years, although not measured in this study, lifestyle changes noticed in Zimbabwe's cities, such as an increased volume of private vehicles, could explain larger increases in temperature after than before 2005. The smallest changes in LST were observed in the water LCZ, while similar surface warming patterns appeared in compact low rise and low plants LCZ areas. Even within an LCZ category, LST changes were recorded, thereby implying that the warming was not only due to LCZ transitions but also due to background warming. The warming effect of greenhouse gases within a city is not only confined to industrial areas as the pollutant spread around an open atmosphere. However, the impact is reduced by heat and carbon assimilation effects in areas where vegetation is abundant.

The study showed a three-dimensional warming pattern as the city of Bulawayo was growing. The LST was warming while air temperatures and associated extreme events rose between 1990 and 2020. The replacement of natural covers, especially vegetation and water with built LCZs, increases heat absorption capacity of the city, which warms the air as it moves over these areas, thereby resulting in increased air temperatures. The observed rates of change in LST were consistent with those observed in other studies and were larger than those in air temperatures. This could be due to differences in heat absorption rates and capacities between air and the LCZs. Additionally, air temperature measurements include variability due to clouds and are observed at higher temporal resolution (before averaging) than LST observations, which were only computed for cloud-free days and anniversary imagery. The findings concur with previous studies, which showed that urbanization causes warming in formerly natural environments (Weng et al., 2007; Grossman-Clarke et al., 2010; Jalan and Sharma, 2014). As such, Jalan and Sharma (2014) and Grossman-Clarke et al. (2010) indicated that replacing vegetation with urban fabric can increase LST by 2–4°C. Overall, the study showed that growth-induced LCZ transitions altered the spatial structure of LST while influencing air temperatures and temperature extremes.

CONCLUSION

This study investigated long-term changes in the thermal environment of Bulawayo metropolitan city by combining both surface and air temperature measurements. Air temperature measurements were used to derive indices for low- and high-temperature extremes. Both surface and air temperature measurements indicated that the city is warming. Although extreme low temperature–related indicators showed rising trends, the patterns were not statistically significant. On the other hand, warming is significantly increasing high temperature–related extremes. This concludes that comfortable hours are reducing during daytimes, while the nighttime relief has been maintained over the years. Besides warming due to LCZ transitions, the temperature rises were also observed within all LCZs. The study concluded that the background temperature rise

due to global warming and LCZ dynamics combined effects to cause temperature elevation in the city. Replacing the water with other LCZ categories has the strongest implications on the thermal environment, thereby causing warming by at least 9°C in the altered areas. Construction of buildings in formerly vegetation LCZ areas and densification of buildings also have significant temperature elevation effects. Conversely, the densification of forests, maintenance of vegetation covers, such as grasslands, and conservation of wetlands have strong heat mitigation effects. LCZs and extreme climate indices combine to adequately explain the responses of the climate system to anthropogenic activities.

DATA AVAILABILITY STATEMENT

Publicly available datasets were analyzed in this study. This data can be found here: https://earthexplorer.usgs.gov/.

AUTHOR CONTRIBUTIONS

TM was involved in all steps from conceptualization of the study to finalization of the manuscript. OM and JO played critical supervisory roles in all phases of the study. They were also involved in data collection and analysis and iterative preparation of the manuscript.

FUNDING

The research of this article was supported by DAAD within the framework of the climapAfrica program with funds from the Federal Ministry of Education and Research. The publisher is fully responsible for the content. This work was funded by the National Research Foundation of South Africa (NRF) Research Chair in Land Use Planning and Management (Grant Number: 84157).

REFERENCES

Abatan, A. A., Abiodun, B. J., Lawal, K. A., and Gutowski, W. J. (2016). Trends in Extreme Temperature over Nigeria from Percentile-Based Threshold Indices. *Int. J. Climatol.* 36 (6), 2527–2540. doi:10.1002/joc.4510

Aguilar, E., Aziz Barry, A., Brunet, M., Ekang, L., Fernandes, A., Massoukina, M., et al. (2009). Changes in Temperature and Precipitation Extremes in Western Central Africa, Guinea Conakry, and Zimbabwe, 1955-2006. *J. Geophys. Res.* 114, 1–11. doi:10.1029/2008JD011010

Ahmed, B., Kamruzzaman, M., Zhu, X., Rahman, M., and Choi, K. (2013). Simulating Land Cover Changes and Their Impacts on Land Surface Temperature in Dhaka, bangladesh. *Remote Sens.* 5 (11), 5969–5998. doi:10.3390/rs5115969

Almazroui, M., Islam, M. N., Dambul, R., and Jones, P. D. (2014). Trends of Temperature Extremes in Saudi Arabia. *Int. J. Climatol.* 34 (3), 808–826. doi:10.1002/joc.3722

Amiri, R., Weng, Q., Alimohammadi, A., and Alavipanah, S. K. (2009). Spatial-temporal Dynamics of Land Surface Temperature in Relation to Fractional Vegetation Cover and Land Use/cover in the Tabriz Urban Area, Iran. *Remote Sens. Environ.* 113 (12), 2606–2617. doi:10.1016/j.rse.2009.07.021

Amorim, M. C. d. C. T. (2018). Spatial Variability and Intensity Frequency of Surface Heat Island in a Brazilian City with Continental Tropical Climate through Remote Sensing. *Remote Sens. Appl. Soc. Environ.* 9, 10–16. doi:10.1016/j.rsase.2017.11.001

Athar, H. (2014). Trends in Observed Extreme Climate Indices in Saudi Arabia during 1979-2008. *Int. J. Climatol.* 34 (July 2013), 1561–1574. doi:10.1002/joc.3783

Bechtel, B., Langkamp, T., Böhner, J., Daneke, C., Oßenbrügge, J., and Schempp, S. (2012). Classification and Modelling of Urban Micro-climates Using Multisensoral and Multitemporal Remote Sensing Data. *Int. Arch. Photogramm. Remote Sens. Spat. Inf. Sci.* XXXIX-B8 (September), 463–468. doi:10.5194/isprsarchives-xxxix-b8-463-2012

Blake, R., Grimm, A., Ichinose, T., Horton, R., Gaffin, S., and Jiong, S. (2011). "Urban Climate: Processes, Trends and Projections," in *First Assessment Report of the Urban Climate Change Research Network*, 43–81.

Brazier, A. (2015). *CLimate Change in Zimbabwe. Facts for Planners and Decision Makers*. Alexandra Park, Harare: Konrad-Adenauer-Stiftung 26 Sandringham Drive.

Brown, P. J., Bradley, R. S., and Keimig, F. T. (20102006). Changes in Extreme Climate Indices for the Northeastern United States, 1870-2005. *J. Clim.* 23, 6555–6572. doi:10.1175/2010JCLI3363.1

Ca, V. T., Asaeda, T., and Abu, E. M. (1998). Reductions in Air Conditioning Energy Caused by a Nearby Park. *Energy Build.* 29 (1), 83–92. doi:10.1016/s0378-7788(98)00032-2

Cai, M., Ren, C., Xu, Y., Dai, W., and Wang, X. M. (2016). Local Climate Zone Study for Sustainable Megacities Development by Using Improved WUDAPT Methodology - A Case Study in Guangzhou. *Procedia Environ. Sci.* 36, 82–89. doi:10.1016/j.proenv.2016.09.017

Cai, M., Ren, C., and Xu, Y. (2017). "Investigating the Relationship between Local Climate Zone and Land Surface Temperature," in 2017 Joint Urban Remote Sensing Event (JURSE), Dubai, United Arab Emirates, 06-08 March 2017, 1–4. doi:10.1109/JURSE.2017.7924622

Chen, X.-L., Zhao, H.-M., Li, P.-X., and Yin, Z.-Y. (2006). Remote Sensing Image-Based Analysis of the Relationship between Urban Heat Island and Land Use/cover Changes. *Remote Sens. Environ.* 104 (2), 133–146. doi:10.1016/j.rse.2005.11.016

Chun, B., and Guldmann, J.-M. (2014). Spatial Statistical Analysis and Simulation of the Urban Heat Island in High-Density Central Cities. *Landsc. Urban Plan.* 125, 76–88. doi:10.1016/j.landurbplan.2014.01.016

D'ambrosio Alfano, F. R., Palella, B. I., and Riccio, G. (2013). On the Transition Thermal Discomfort to Heat Stress as a Function of the PMV Value. *Ind. Health* 51 (3), 285–296. doi:10.2486/indhealth.2012-0163

Dousset, B., and Gourmelon, F. (2003). Satellite Multi-Sensor Data Analysis of Urban Surface Temperatures and Landcover. *ISPRS J. Photogrammetry Remote Sens.* 58 (1–2), 43–54. doi:10.1016/S0924-2716(03)00016-9

Feng, H., Zhao, X., Chen, F., and Wu, L. (2014). Using Land Use Change Trajectories to Quantify the Effects of Urbanization on Urban Heat Island. *Adv. Space Res.* 53 (3), 463–473. doi:10.1016/j.asr.2013.11.028

Gallo, K. P., McNab, A. L., Karl, T. R., Brown, J. F., Hood, J. J., and Tarpley, J. D. (1993). The Use of NOAA AVHRR Data for Assessment of the Urban Heat Island Effect. *J. Appl. Meteor.* 32 (5), 899–908. doi:10.1175/1520-0450(1993)032<0899:TUONAD>2.0.CO;2

Geletič, J., Lehnert, M., Dobrovolný, P., and Žuvela-Aloise, M. (2019). Spatial Modelling of Summer Climate Indices Based on Local Climate Zones: Expected Changes in the Future Climate of Brno, Czech Republic. *Clim. Change* 152, 487–502. doi:10.1007/s10584-018-2353-5

Goddard, L., and Gershunov, A. (2020). Impact of El Niño on Weather and Climate Extremes. *Clim. Data Monit. WCDMP-No.* 72, 361–375. doi:10.1002/9781119548164.ch16

Grimmond, S. (2007). Urbanization and Global Environmental Change: Local Effects of Urban Warming. *Geogr. J.* 173 (1), 83–88. doi:10.1111/j.1475-4959.2007.232_3.x

Grossman-Clarke, S., Zehnder, J. A., Loridan, T., and Grimmond, C. S. B. (2010). Contribution of Land Use Changes to Near-Surface Air Temperatures during Recent Summer Extreme Heat Events in the Phoenix Metropolitan Area. *J. Appl. Meteorology Climatol.* 49 (8), 1649–1664. doi:10.1175/2010JAMC2362.1

Gumbo, B., Mlilo, S., Broome, J., and Lumbroso, D. (2003). Industrial Water Demand Management and Cleaner Production Potential: A Case of Three

Industries in Bulawayo, Zimbabwe. *Phys. Chem. Earth, Parts A/B/C* 28 (20–27), 797–804. doi:10.1016/j.pce.2003.08.026

Gusso, A., Bordin, F., Veronez, M., Cafruni, C., Lenz, L., and Crija, S. (2014). "Multitemporal Analysis of Thermal Distribution Characteristics for Urban Heat Islands Management," in The 4th World Sustainability Forum, f009. doi:10.3390/wsf-4-f009

Haghighat, F. (2002). Thermal Confort in Housing and Thermal Environments, *Sustainable Built Environment* 1

Hallegatte, S., and Corfee-Morlot, J. (2011). Understanding Climate Change Impacts, Vulnerability and Adaptation at City Scale: An Introduction. *Clim. Change* 104 (1), 1–12. doi:10.1007/s10584-010-9981-8

Harlan, S. L., and Ruddell, D. M. (2011). Climate Change and Health in Cities: Impacts of Heat and Air Pollution and Potential Co-benefits from Mitigation and Adaptation. *Curr. Opin. Environ. Sustain.* 3 (3), 126–134. doi:10.1016/j.cosust.2011.01.001

Hwang, R.-L., Lin, T.-P., and Matzarakis, A. (2011). Seasonal Effects of Urban Street Shading on Long-Term Outdoor Thermal Comfort. *Build. Environ.* 46 (4), 863–870. doi:10.1016/j.buildenv.2010.10.017

Imhoff, M. L., Zhang, P., Wolfe, R. E., and Bounoua, L. (2010). Remote Sensing of the Urban Heat Island Effect across Biomes in the Continental USA. *Remote Sens. Environ.* 114 (3), 504–513. doi:10.1016/j.rse.2009.10.008

Jalan, S., and Sharma, K. (2014). Spatio-temporal Assessment of Land Use/ Land Cover Dynamics and Urban Heat Island of Jaipur City Using Satellite Data. *Int. Arch. Photogramm. Remote Sens. Spat. Inf. Sci.* XL-8 (1), 767–772. ISPRS Archives. doi:10.5194/isprsarchives-XL-8-767-2014

Jawak, S. D., and Luis, A. J. (2013). Improved Land Cover Mapping Using High Resolution Multiangle 8-band WorldView-2 Satellite Remote Sensing Data. *J. Appl. Remote Sens.* 7 (1), 073573. doi:10.1117/1.jrs.7.073573

Kruger, A. C. (2006). Observed Trends in Daily Precipitation Indices in South Africa: 1910 – 2004. *Int. J. Climatol.* 2285 (June), 2275–2285. doi:10.1002/joc10.1002/joc.1368

Kruger, A. C., and Sekele, S. S. (2012). Trends in Extreme Temperature Indices in South Africa: 1962-2009. *Int. J. Climatol.* 33, 661–676. doi:10.1002/joc.3455

Mbithi, D. M., Demessie, E. T., and Kashiri, T. (2010). The Impact of Land Use Land Cover (LULC) Changes on Land Surface Temperature (LST); a Case Study of Addis Ababa City, *Ethiopia Kenya Metrological Services* 192, 10400.

McMichael, A. J., Woodruff, R. E., and Hales, S. (2006). Climate Change and Human Health: Present and Future Risks. *Lancet* 367 (9513), 859–869. doi:10.1016/S0140-6736(06)68079-3

Meng, X., Currit, N., Wang, L., and Yang, X. (2010). "Object-oriented Residential Building Land-Use Mapping Using Lidar and Aerial Photographs," in *American Society for Photogrammetry and Remote Sensing 2010 Annual Conference*, 2, 26–30. San Diego

Mitraka, Z., Del Frate, F., Chrysoulakis, N., and Gastellu-Etchegorry, J.-P. (2015). "Exploiting Earth Observation Data Products for Mapping Local Climate Zones," in 2015 Joint Urban Remote Sensing Event (JURSE), Lausanne, Switzerland, 30 March 2015 - 01 April 2015, 1–5. doi:10.1109/JURSE.2015.7120456June 2013

Mónica, S., and Santos, F. (2011). Trends in Extreme Daily Precipitation Indices in Northern of Portugal. *Geophys. Res. Abstr.* 13, 11285.

Mouat, D. A., Mahin, G. G., Lancaster, J., Mouat, D. A., Mahin, G. G., and Lancaster, J. (1993). Remote Sensing Techniques in the Analysis of Change Detection. *Geocarto Int.* 8 (2), 39–50. doi:10.1080/10106049309354407

Muchingami, I., Hlatywayo, D. J., Nel, J. M., and Chuma, C. (2012). Electrical Resistivity Survey for Groundwater Investigations and Shallow Subsurface Evaluation of the Basaltic-Greenstone Formation of the Urban Bulawayo Aquifer. *Phys. Chem. Earth, Parts A/B/C* 50-52, 44–51. doi:10.1016/j.pce.2012.08.014

Mushore, T. D., Mutanga, O., Odindi, J., and Dube, T. (2018). Determining Extreme Heat Vulnerability of Harare Metropolitan City Using Multispectral Remote Sensing and Socio-Economic Data. *J. Spatial Sci.* 63 (1), 173–191. doi:10.1080/14498596.2017.1290558

Mutengu, S., Hoko, Z., and Makoni, F. S. (2007). An Assessment of the Public Health Hazard Potential of Wastewater Reuse for Crop Production. A Case of Bulawayo City, Zimbabwe. *Phys. Chem. Earth, Parts A/B/C* 32 (15–18), 1195–1203. doi:10.1016/j.pce.2007.07.019

Nayak, S., and Mandal, M. (2019). Impact of Land Use and Land Cover Changes on Temperature Trends over India. *Land Use Policy* 89 (8), 104238. doi:10.1016/j.landusepol.2019.104238

Nurwanda, A., and Honjo, T. (2020). The Prediction of City Expansion and Land Surface Temperature in Bogor City, Indonesia. *Sustain. Cities Soc.* 52 (December 2018), 101772. doi:10.1016/j.scs.2019.101772

Nyamekye, C., Kwofie, S., Ghansah, B., Agyapong, E., and Boamah, L. A. (2020). Assessing Urban Growth in Ghana Using Machine Learning and Intensity Analysis: A Case Study of the New Juaben Municipality. *Land Use Policy* 99 (July), 105057. doi:10.1016/j.landusepol.2020.105057

Odindi, J., Mutanga, O., Abdel-Rahman, E. M., Adam, E., and Bangamwabo, V. (2017). Determination of Urban Land-Cover Types and Their Implication on Thermal Characteristics in Three South African Coastal Metropolitans Using Remotely Sensed Data. *South Afr. Geogr. J.* 99 (1), 52–67. doi:10.1080/03736245.2015.1117015

Ogunjo, S. T., Akinsusi, J. O., and Fuwape, I. A. (2021). "Trends in Extreme Temperature Indices over Lagos, Nigeria," in 4th International Conference on Science and Sustainable Development (ICSSD 2020), Ota, Nigeria, 3-5 August 2020, 012003. doi:10.1088/1755-1315/655/1/012003*IOP Conf. Ser. Earth Environ. Sci.*655

Parnell, S., and Walawege, R. (2011). Sub-Saharan African Urbanisation and Global Environmental Change. *Glob. Environ. Change* 21 (Suppl. 1), S12–S20. doi:10.1016/j.gloenvcha.2011.09.014

Pérez-Andreu, V., Aparicio-Fernández, C., Martínez-Ibernón, A., and Vivancos, J.-L. (2018). Impact of Climate Change on Heating and Cooling Energy Demand in a Residential Building in a Mediterranean Climate. *Energy* 165, 63–74. doi:10.1016/j.energy.2018.09.015

Pielke, R. A., Pitman, A., Niyogi, D., Mahmood, R., McAlpine, C., Hossain, F., et al. (2011). Land Use/land Cover Changes and Climate: Modeling Analysis and Observational Evidence. *WIREs Clim. Change* 2 (6), 828–850. doi:10.1002/wcc.144

Popov, T., Gnjato, S., Trbić, G., and Ivanišević, M. (2018). Recent Trends in Extreme Temperature Indices in Bosnia and Herzegovina. *Carpath. J. Earth Environ. Sci.* 13 (1), 211–224. doi:10.26471/cjees/2018/013/019

Puliafito, S. E., Bochaca, F. R., Allende, D. G., and Fernandez, R. (2013). Green Areas and Microscale Thermal Comfort in Arid Environments: A Case Study in Mendoza, Argentina. *Acs* 03 (03), 372–384. doi:10.4236/acs.2013.33039

Rahimi, M., and Hejabi, S. (2017). Spatial and Temporal Analysis of Trends in Extreme Temperature Indices in Iran over the Period 1960-2014. *Int. J. Climatol.* 38, 272–282. doi:10.1002/joc.5175

Sajjad, H., and Ghaffar, A. (2019). Observed, Simulated and Projected Extreme Climate Indices over Pakistan in Changing Climate. *Theor. Appl. Climatol.* 137, 255–281. doi:10.1007/s00704-018-2573-7

Satterthwaite, D. (2008). "Climate Change and Urbanization: Effects and Impliactions for Urban Governance," in United Nations Expert Group Meeting on Population Distribution, Urbanization, Internatl Migration and Development, New York, 21-23 January 2008. http://www.un.org/esa/population/meetings/EGM_PopDist/P16_Satterthwaite.pdf.

Sein, K. K., Chidthaisong, A., and Oo, a. K. L. (2018). Observed Trends and Changes in Temperature and Precipitation Extreme Indices over Myanmar. *Atmosphere* 9, 477. doi:10.3390/atmos9120477

Sensoy, S., Türkoğlu, N., Akçakaya, A., Ekici, M., and DemİrcanM. (2013). "Trends in Turkey Climate Indices from 1960 to 2010," in 6th Atmospheric Science Symposium, Istanbul, Turkey, April 24–26, 2013, 1–8. ATMOS 2013 3 - 5 Haziran 2013, İstanbul TRENDS.

Sithole, K., and Odindi, J. (2015). Determination of Urban Thermal Characteristics on an Urban/Rural Land Cover Gradient Using Remotely Sensed Data. *SA J Geomatics* 4 (4), 384. doi:10.4314/sajg.v4i4.3

Srivanit, M., Hokao, K., and Phonekeo, V. (2012). Assessing the Impact of Urbanization on Urban Thermal Environment: A Case Study of Bangkok Metropolitan. *Int. J. Appl. Sci. Technol.* 2 (7), 243–256. http://www.ijastnet.com/journals/Vol_2_No_7_August_2012/26.pdf.

Stathopoulos, T., Wu, H., and Zacharias, J. (2004). Outdoor Human Comfort in an Urban Climate. *Build. Environ.* 39 (3), 297–305. doi:10.1016/j.buildenv.2003.09.001

Stenseth, N. C., Ottersen, G., Hurrell, J. W., Mysterud, A., Lima, M., Chan, K. S., et al. (2003). Review Article. Studying Climate Effects on Ecology through the Use of Climate Indices: the North Atlantic Oscillation, El Niño Southern

Oscillation and beyond. *Proc. R. Soc. Lond. B* 270 (1529), 2087–2096. doi:10.1098/rspb.2003.2415

Stewart, I. D., Oke, T. R., and Krayenhoff, E. S. (2014). Evaluation of the 'local Climate Zone' Scheme Using Temperature Observations and Model Simulations. *Int. J. Climatol.* 34 (4), 1062–1080. doi:10.1002/joc.3746

Stewart, I. D., and Oke, T. R. (2012). Local Climate Zones for Urban Temperature Studies. *BAMS* 93 (12), 1879–1900. doi:10.1175/BAMS-D-11-00019.1

Tao, Z., Santanello, J. A., Chin, M., Zhou, S., Tan, Q., Kemp, E. M., et al. (2013). Effect of Land Cover on Atmospheric Processes and Air Quality over the Continental United States - a NASA Unified WRF (NU-WRF) Model Study. *Atmos. Chem. Phys.* 13 (13), 6207–6226. doi:10.5194/acp-13-6207-2013

Thatcher, M., and Hurley, P. (2012). Simulating Australian Urban Climate in a Mesoscale Atmospheric Numerical Model. *Boundary-Layer Meteorol.* 142 (1), 149–175. doi:10.1007/s10546-011-9663-8

Toudert, F. A. (2005). Dependence of Outdoor Thermal Comfort on Street Design in Hot and Dry Climate. Berichte des Meteorologischen Institutes der Universität Freiburg Fazia Ali Toudert. *Nr. 15*(15). Available at: http://www.freidok.uni-freiburg.de/volltexte/2005/2078/.

Touré, H. A., Kalifa, T., and Kyei-Baffour, N. (2017). Assessment of Changing Trends of Daily Precipitation and Temperature Extremes in Bamako and Ségou in Mali from 1961- 2014. *Weather Clim. Extrem.* 18, 8–16. doi:10.1016/j.wace.2017.09.002

Uddin, S., Al Ghadban, A. N., Al Dousari, A., Al Murad, M., and Al Shamroukh, D. (2010). A Remote Sensing Classification for Land-Cover Changes and Micro-climate in Kuwait. *Int. J. SDP* 5 (4), 367–377. doi:10.2495/SDP-V5-N4-367-377

Unganai, L. (1996). Historic and Future Climatic Change in Zimbabwe. *Clim. Res.* 6 (2), 137–145. doi:10.3354/cr006137

U.S. Geological Survey (2019). *Landsat 8 Data Users Handbook*, 8, 97. Nasa. https://landsat.usgs.gov/documents/Landsat8DataUsersHandbook.pdf.

Vincent, L. A., Aguilar, E., Saindou, M., Hassane, A. F., Jumaux, G., Roy, D., et al. (2011). Observed Trends in Indices of Daily and Extreme Temperature and Precipitation for the Countries of the Western Indian Ocean, 1961-2008. *J. Geophys. Res.* 116, 1–12. doi:10.1029/2010JD015303

Vlassova, L., Perez-Cabello, F., Nieto, H., Martín, P., Riaño, D., and de la Riva, J. (2014). Assessment of Methods for Land Surface Temperature Retrieval from Landsat-5 TM Images Applicable to Multiscale Tree-Grass Ecosystem Modeling. *Remote Sens.* 6 (5), 4345–4368. doi:10.3390/rs6054345

Weng, Q., Liu, H., and Lu, D. (2007). Assessing the Effects of Land Use and Land Cover Patterns on Thermal Conditions Using Landscape Metrics in City of Indianapolis, United States. *Urban Ecosyst.* 10 (2), 203–219. doi:10.1007/s11252-007-0020-0

Wu, S., Mickley, L. J., Kaplan, J. O., and Jacob, D. J. (2012). Impacts of Changes in Land Use and Land Cover on Atmospheric Chemistry and Air Quality over the 21st Century. *Atmos. Chem. Phys.* 12 (3), 1597–1609. doi:10.5194/acp-12-1597-2012

Yang, J. S. (2004). Estimation of Land Surface Temperature Using Spatial Interpolation and Satellite-Derived Surface Emissivity. *J. Env. Inf.* 4 (1), 40–47. doi:10.3808/jei.200400035

Zhang, X., and Yang, F. (2004). *RClimDex (1.0) User Manual*. Canada: Climate Research Branch Environment.

Zhao, Q., Myint, S., Wentz, E., and Fan, C. (2015). Rooftop Surface Temperature Analysis in an Urban Residential Environment. *Remote Sens.* 7 (9), 12135–12159. doi:10.3390/rs70912135

Zhou, X., and Wang, Y.-C. (2011). Dynamics of Land Surface Temperature in Response to Land-Use/Cover Change. *Geogr. Res.* 49 (1), 23–36. doi:10.1111/j.1745-5871.2010.00686.x

Zhou, Y., Weng, Q., Gurney, K. R., Shuai, Y., and Hu, X. (2012). Estimation of the Relationship between Remotely Sensed Anthropogenic Heat Discharge and Building Energy Use. *ISPRS J. Photogrammetry Remote Sens.* 67 (1), 65–72. doi:10.1016/j.isprsjprs.2011.10.007

Zubler, E. M., Scherrer, S. C., Croci-Maspoli, M., Liniger, M. A., and Appenzeller, C. (2014). Key Climate Indices in Switzerland; Expected Changes in a Future Climate. *Clim. Change* 123, 255–271. doi:10.1007/s10584-013-1041-8

Zvigadza, S., Mharadze, G., and Ngena, S. (2010). "Communitie and Climate Change: Building Local Capacity for Adaptation in Goromonzi District, Munyawiri Ward, Zimbabwe," in *African Centre for Technology Studies, June*, 1–16. Available at: https://www.africaportal.org/documents/13932/CBAA_Zimbabwe.pdf

Conflict of Interest: The authors declare that the research was conducted in the absence of any commercial or financial relationships that could be construed as a potential conflict of interest.

Publisher's Note: All claims expressed in this article are solely those of the authors and do not necessarily represent those of their affiliated organizations or those of the publisher, the editors, and the reviewers. Any product that may be evaluated in this article or claim that may be made by its manufacturer is not guaranteed or endorsed by the publisher.

frontiers | Frontiers in Environmental Science

ORIGINAL RESEARCH
published: 13 July 2022
doi: 10.3389/fenvs.2022.874614

Evaluating the Cooling Performance of Green Roofs Under Extreme Heat Conditions

Ye Feng[1,2,3], *Jia Wang*[4]*, *Weiqi Zhou*[4], *Xiaoma Li*[1,3] *and Xiaoying Yu*[2]*

[1]College of Landscape Architecture and Art Design, Hunan Agricultural University, Changsha, China, [2]College of Horticulture, Hunan Agricultural University, Changsha, China, [3]Hunan Provincial Key Laboratory of Landscape Ecology and Planning & Design in Regular Higher Educational Institutions, Changsha, China, [4]State Key Laboratory of Urban and Regional Ecology, Research Center for Eco-Environmental Sciences, Chinese Academy of Sciences, Beijing, China

The local rise in urban temperature is increasingly exacerbated due to the combined effect of urban heat islands and global climate change. Numerous studies have shown that green roofs (GRs) have great potential for facilitating urban heat mitigation. However, little is known about whether such cooling effects can be achieved under extreme heat conditions. With the expected occurrence of more extreme heat events under climate change, such understanding is crucially important for the effective design of heat mitigation. This study aims to fill this gap by investigating the pedestrian-level cooling effect of GR under two weather conditions (i.e., typical summer weather conditions and extreme heat conditions). This research employed a three-dimensional simulation model, ENVI-met, to simulate pedestrian-level air temperature for three typical residential areas with different roof heights in Beijing. We conducted the simulations in two different roof scenarios, conventional roofs versus green roofs. The results showed that green roofs could provide large cooling exceeding 0.2°C on downwind sides and in the daytime, although the average cooling intensity was small. The pedestrian-level cooling intensity of GR decreased significantly under extreme heat conditions compared to typical summer weather conditions. It varied diurnally following an inverted W-shape for both weather conditions. Results also showed that the pedestrian-level cooling intensity of GR decreased with the increase in roof height in a nonlinear way and became 0 when roof height reached ~50 m for both weather conditions. The results of our research can provide important insights for cooling-oriented urban design in the future, as we are expecting such extreme weather conditions nowadays may be the new normal in the future.

Keywords: urban heat island, green roofs, cooling effects, extreme heat, ENVI-met

OPEN ACCESS

Edited by:
Chenghao Wang,
Stanford University, United States

Reviewed by:
Jian Peng,
Peking University, China
Jike Chen,
the Nanjing University of Information Science and Technology, China
Meiling Gao,
Chang'an University, China

***Correspondence:**
Jia Wang
jiawang@rcees.ac.cn
Xiaoying Yu
yuxiaoying@hunau.edu.cn

Specialty section:
This article was submitted to Atmosphere and Climate, a section of the journal Frontiers in Environmental Science

Received: *12 February 2022*
Accepted: *09 June 2022*
Published: *13 July 2022*

Citation:
Feng Y, Wang J, Zhou W, Li X and Yu X (2022) Evaluating the Cooling Performance of Green Roofs Under Extreme Heat Conditions. Front. Environ. Sci. 10:874614. doi: 10.3389/fenvs.2022.874614

1 INTRODUCTION

The accelerating global warming significantly impacts cities where rapid urbanization is underway at the same time. For example, 68% of the population has been predicted to reside in urban areas by 2050 (UN, 2018). Among the many ecological challenges that cities face, urban heat island (UHI) is one of the most remarked (Francis and Jensen, 2017; Tian et al., 2021). UHI describes a well-known phenomenon that urban areas have higher temperature than the surrounding nonurban areas (Voogt and Oke, 2003; Shafique et al., 2018; Wang J. et al., 2019). Studies have shown that the higher urban temperature has adverse impacts, such as the alteration in species composition and

distribution (Niemela, 1999; White et al., 2002), the increase in energy consumption (Castleton et al., 2010; Susca, 2019), and the increased mortality and heat-stress illness (Sailor and Fan, 2002; Knowlton et al., 2004). Thus, effective urban heat mitigation and adaptation strategies are highly desirable for a more comfortable urban thermal environment (Zhou et al., 2021; Wang et al., 2022).

Urban greening has been recognized as an effective means to alleviate extreme urban temperature (Zhou et al., 2011; Kong et al., 2014). However, although many cities have ambitious intentions to increase their urban vegetation, there are limited space and resources for urban planting, especially in cities with high density (Wang et al., 2022). Roofs, commonly accounting for approximately 20–25% of the total urban areas (Izquierdo et al., 2008; Besir and Cuce, 2018), can provide extra and optional surfaces and space for urban greening (Berardi, 2016). Although roofs are typically not close to pedestrians, green roofs (GR) were found to provide significant cooling effects (Shafique et al., 2018; Gao et al., 2019; Gao et al., 2020; Cristiano et al., 2021; Jamei et al., 2021; Liu H. Q. et al., 2021). Previous studies have shown that green roofs, especially intensive green roofs (IGR), can reduce air temperature at the pedestrian levels by 0.05°C in Paris, 0.1°C in Tokyo (Morakinyo et al., 2017), and 0.04°C in Berlin (Knaus and Haase, 2020). In addition, the pedestrian-level cooling effect of GR decreased with the increase in roof height (Ng et al., 2012; Herath et al., 2018; Jin et al., 2018; Zhang et al., 2019; Knaus and Haase, 2020), and tended to be zero when roofs were higher than a certain height, for example, 60 m (Ng et al., 2012).

Against global warming and rapid urbanization, extreme heat conditions, such as heatwaves, have become more frequent (IPCC, 2014; Cao et al., 2021). Urban greening can reduce urban temperature, but its cooling effect has been affected by weather conditions, such as air temperature (Wang et al., 2022). For example, the extremely high air temperature may lead to a decrease in the cooling effect of urban vegetation (Wang C. et al., 2019; Wang et al., 2020). The cooling effect of green roofs has been molded and revealed in most previous studies under typical summer conditions (Morakinyo et al., 2017; Susca, 2019). However, little is known about whether such cooling effects of GR can be achieved under extreme heat conditions (Klein and Coffman, 2015; Sun et al., 2016). Can GR work effectively under extreme heat conditions and therefore still provide a significant cooling effect at the pedestrian level? Is the change in cooling effects at the pedestrian level with roof height under extreme heat conditions similar to that under typical summer weather conditions? Addressing such questions can promote the understanding of the cooling effect of GR, mainly because such extreme heat conditions nowadays may be a new normal in the future (Mauree et al., 2019; Qi et al., 2021).

Here, we address these questions by simulating the pedestrian-level cooling effect of green roofs for three typical residential areas in Beijing. These three residential areas have different roof heights, thus representing the typical residential areas in the city. We employed the ENVI-met model to simulate the pedestrian-level air temperature for the selected residential areas in two scenarios: conventional and green roofs. We conducted the simulations under two weather conditions, including typical summer and extreme heat conditions. The objectives of this study were to 1) investigate the pedestrian-level cooling effect of green roofs under extreme heat conditions and 2) explore the change of such cooling effect along with roof height.

2 MATERIALS AND METHODS

2.1 The Study Area

The three residential areas are located within the fifth ring road of Beijing, the capital of China (39°28′—41°25′N, 115°25′—117°30′E). Beijing has a monsoon-influenced humid continental climate characterized by hot, humid summers and cold, dry winters. The average annual temperature is 12.3°C, and the average annual precipitation, most of which occurs in summer, is 572 mm (Jiao et al., 2021). Beijing has a built-up area of 1,458 km^2 and a population of 21.54 million people in 2019.

Three residential areas, namely Guan Yin Jing Yuan (GYJY), Yu Ze Yuan (YZY), and Jin Chan Nan Li (JCNL), have been selected for this study. Their building heights were 18, 27, and 42 m, respectively, representing three typical residential areas in terms of building height in Beijing and most of the cities in China: multi-story, mid-rise, and high-rise(**Figure 1**). More than 80% of the total number of residential areas in Beijing belong to such types (Zheng et al., 2017). Except for building height, other characteristics of the three residential areas are similar, including the area of residential neighborhoods, the area of roofs, and the percentage of green space on the ground (**Supplementary Table A1**). They also have the same type of vegetation, including *Styphnolobium japonicum (L.) Schott* and *Platanus orientalis Linn.,* two typical trees in Beijing (Jiao et al., 2021). The landscape of these three residential areas is common in Beijing.

2.2 ENVI-met Model Validation

ENVI-met, which is a three-dimensional microclimate model (Huttner and Bruse, 2009; Tsoka et al., 2018), has been adopted in this study to simulate the cooling effect of green roofs. The model can simulate the complex interactions between buildings, vegetation, soil, and atmosphere in the urban environment based on fundamental laws of fluid mechanics, thermodynamics, and atmospheric physics (Crank et al., 2018). It is a grid-based model with a simulation resolution that can be down to 0.5 m in space and 1s in time (Tsoka et al., 2018).

We first evaluate the validation of the ENVI-met (version 4.4.6) model in Beijing. The evaluation has been applied to Research Center for Eco-Environmental Sciences (RCEES) campus (**Figure 1**). The domain size of the RCEES campus is 212.5 m × 262.5 m × 96 m. The spatial resolution of the ENVI-met model was 2.5 m × 2.5 m × 3.0 m (size of x, y, and z grids). Additional nesting grids were added to reduce the effects of model bounders. **Supplementary Table A2** shows the initial input conditions (e.g., wind speed, initial air temperature, etc.) of the ENVI-met model, which used hourly forcing (Salvati and Kolokotroni, 2019).

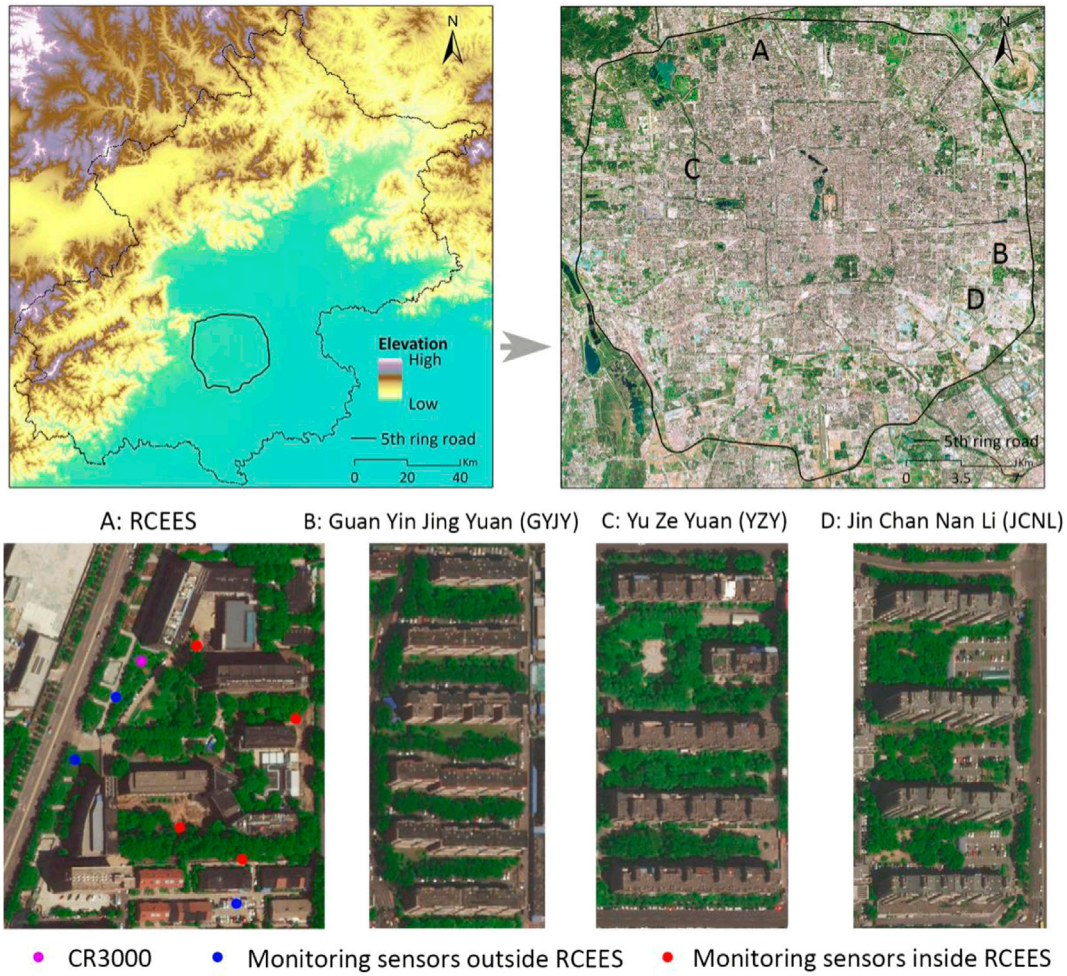

FIGURE 1 | Locations and the land cover base map in the true color of these three study residential areas and RCEES where the validation of the ENVI-met model was applied.

TABLE 1 | Evaluation results of the ENVI-met model performance in RCEES, Beijing.

Sensors	R^2	RMSE (°C)	MAE (°C)	MBE (°C)	d
Sensor 1	0.92	1.12	0.88	−0.69	0.94
Sensor 2	0.90	1.13	0.98	−0.85	0.92
Sensor 3	0.87	1.59	1.30	−1.20	0.88
Sensor 4	0.89	1.64	1.27	−1.13	0.88
Sensor 5	0.88	1.43	1.21	−1.09	0.89

Air temperature and relative humidity of the three sensors outside the RCEES campus, and wind speed of the auto meteorological station were input as initial conditions (**Figure 1**) (Salvati and Kolokotroni, 2019). Air temperature and relative humidity were obtained from monitoring sensors, HOBO MX2301, ONSET, with the measurement accuracy of ±0.2°C for air temperature and ±2.5% for relative humidity. The wind speed was collected by CR3000 auto meteorological station with a measurement accuracy of ±0.5 m/s. The measurements and ENVI-met evaluations were carried out starting at 6:00 a.m. on 31 July 2021 and till 11:00 p.m. on 1 August 2021.

The meteorological data (i.e., air temperature and relative humidity at 1.5 m) measured at five sites inside the RCEES campus was used to evaluate the ENVI-met model (**Figure 1**). The root-mean-square error (RMSE), mean absolute error (MAE), mean bias error (MBE), the index of agreement d, and the coefficient of determination R^2 were used to evaluate the accuracy of ENVI-met (Tsoka et al., 2018). The evaluation results were reported in **Table 1**, showing the high accuracy of the microclimate simulation of the ENVI-met model in Beijing. The simulated and measured results were highly correlated with R^2, and d were larger than 0.87 and 0.88 for all cases, respectively. Moreover, RMSE, MAE, and MBE were below 1.7°C for all sensors.

2.3 Scenario Design

We then ran ENVI-met models for the three study residential areas in two roof scenarios and under two kinds of weather conditions. This study designed models using two roof scenarios,

TABLE 2 | Simulation parameters of the three residential areas in ENVI-met models.

Input parameter	Extreme heat conditions	Typical summer conditions
Start date and time (Local)	At 6:00 a.m., on 03 August 2020	At 6:00 a.m., on 31 July 2021
Duration (h)	42	42
Wind speed at 10 m ($s \cdot m^{-1}$)	1.5	1.5
Wind direction (°)	220	220
Meteorological boundary conditions	Simple forcing	Simple forcing

including the Base Model (BM) and the Green Roof Model (GRM). BM was built using conventional roofs, and GRM was built based on BM, adding intensive green roofs (IGR). Two typical trees were selected as the three-dimensional (3D) trees, and other plants (e.g., shrubs) were simulated as the simple two-dimensional (2D) plants in ENVI-met models. The parameters of green roofs: the hedge of leaf area index (LAI), the soil substrate layer depth, and the plant height were 2, 70 cm, and 1 m, respectively (Morakinyo et al., 2017). Other parameters, such as materials of buildings and roads, used values presented in (Chen et al., 2020), which was conducted in Beijing.

These simulations were conducted under two weather conditions, including typical summer and extreme heat conditions. We considered the weather conditions on 4 August 2020 as extreme heat conditions, with the highest air temperature of 37.2 ˚C, ranking the highest of the historical records of the latest 5 years in Beijing. The weather conditions on 1 August 2021 (i.e., the day of the model validation) were identified as the typical summer conditions, with the highest and average air temperatures of 32.7 and 29.3˚C, respectively, very common in Beijing. The hourly wind speed, wind direction, air temperature, and relative humidity were input to create boundary conditions for the ENVI-met model, which used the simple forcing option (**Supplementary Figure A1**, **Table 2**). The model started at 6:00 a.m. on 3 August 2020 and at 6:00 a.m. on 31 July 2021. Although the models lasted 42 h, only the results of the last 24 h (i.e., 4 August 2020 and 1 August 2021) were used for the analysis because ENVI-met usually required a long initialization period (i.e., spin-up time) to obtain accurate simulation results (Sinsel et al., 2021).

2.4 Data Analysis

We then compared the two scenario models to derive the pedestrian-level air temperature difference between BM and GRM at each grid and every hour in three residential areas. Such temperature reduction due to green roofs was pedestrian-level cooling intensity. We used pedestrian-level cooling intensity to quantify the cooling effect of green roofs. We finally revealed the variations of the pedestrian-level cooling intensity with roof heights (i.e., building height). The polynomial function fitted the relationships between the pedestrian-level cooling intensity and roof height at multiple hours under two weather conditions.

3 RESULTS

3.1 The Cooling Effect of Green Roofs

The cooling intensity has significant spatiotemporal heterogeneity, especially showing large values on downwind sides and in the daytime (e.g., from 10:00 a.m. to 5:00 p.m.), although its average ones were small. Green roofs can provide large cooling on downwind sides, while the small ones were generally found on the upwind sides (**Figure 2**). For example, the cooling intensity at 4:00 p.m. on the downwind side can be larger than 0.1 ˚C but be zero on the upwind side (**Figure 2**). The cooling intensity of green roofs in three residential areas varied significantly diurnally in a similar inverted W-shaped way (**Figure 3**). The cooling intensity started to increase from 6: 00 a.m., when the Sun rose, till it peaked between 10:00 a.m. and 1:00 p.m. It decreased after the first peak to the valley around 2: 00 p.m. and then increased to the second peak values between 3: 00 p.m. and 5:00 p.m. It finally dropped till 8:00 p.m., the sunset time, and became relatively stable to a small value at night (**Figure 3**). For example, although the average cooling intensity was small (**Figure 3**), the largest cooling intensity can exceed 0.2˚C at 10:00 a.m. in GYJY (**Supplementary Table A3**).

Results showed that the cooling effect of green roofs has decreased due to extreme heat conditions. The average pedestrian-level cooling intensity in GYJY, YZY, and JCNL was 0.02 , 0.01, and 0.00˚C, respectively, under extreme heat conditions, much smaller than those which were 0.04 , 0.03, and 0.01˚C, respectively, under the typical summer conditions ($p < 0.01$). However, the spatial heterogeneity of the pedestrian-level cooling intensity of green roofs showed similarity under two weather conditions, and so did the diurnal variations of cooling intensity (**Figure 2**, **Figure 3**).

In addition, the different levels of pedestrian-level cooling intensity have the same inverted W-shaped diurnal variations. According to each pixel's averaged pedestrian-level cooling intensities, we divided the cooling effect of GR into different levels. Each level has an interval of 0.02 and 0.01˚C of averaged cooling intensities under typical and extreme heat conditions, respectively. The high levels of cooling intensity, for example, the averaged cooling intensity with an interval of 0.12–0.14˚C, suggested the large cooling that GR could provide. The diurnal variations of different levels were similar to an inverted W-shape (**Supplementary Figure A2**). The higher levels of the pedestrian-level cooling intensities reached the first peak earlier than the lower ones, but they reached the valleys and the second peaks almost simultaneously. Thus the higher levels not only reached the large values of cooling intensities earlier but lasted a longer time. This result indicated that their cooling lasted long in locations that achieved high cooling from green roofs. For example, the higher level of cooling intensity with an interval of >0.06 ˚C and the lower level of cooling intensity with an interval of 0.01–0.02 ˚C peaked at 10:00 a.m. and 1:00 p.m., respectively, in GYJY. Their second peak occurred at 5:00 p.m. It suggested that such large cooling can keep a long time in locations that achieve cooling greater than 0.06˚C under extreme heat

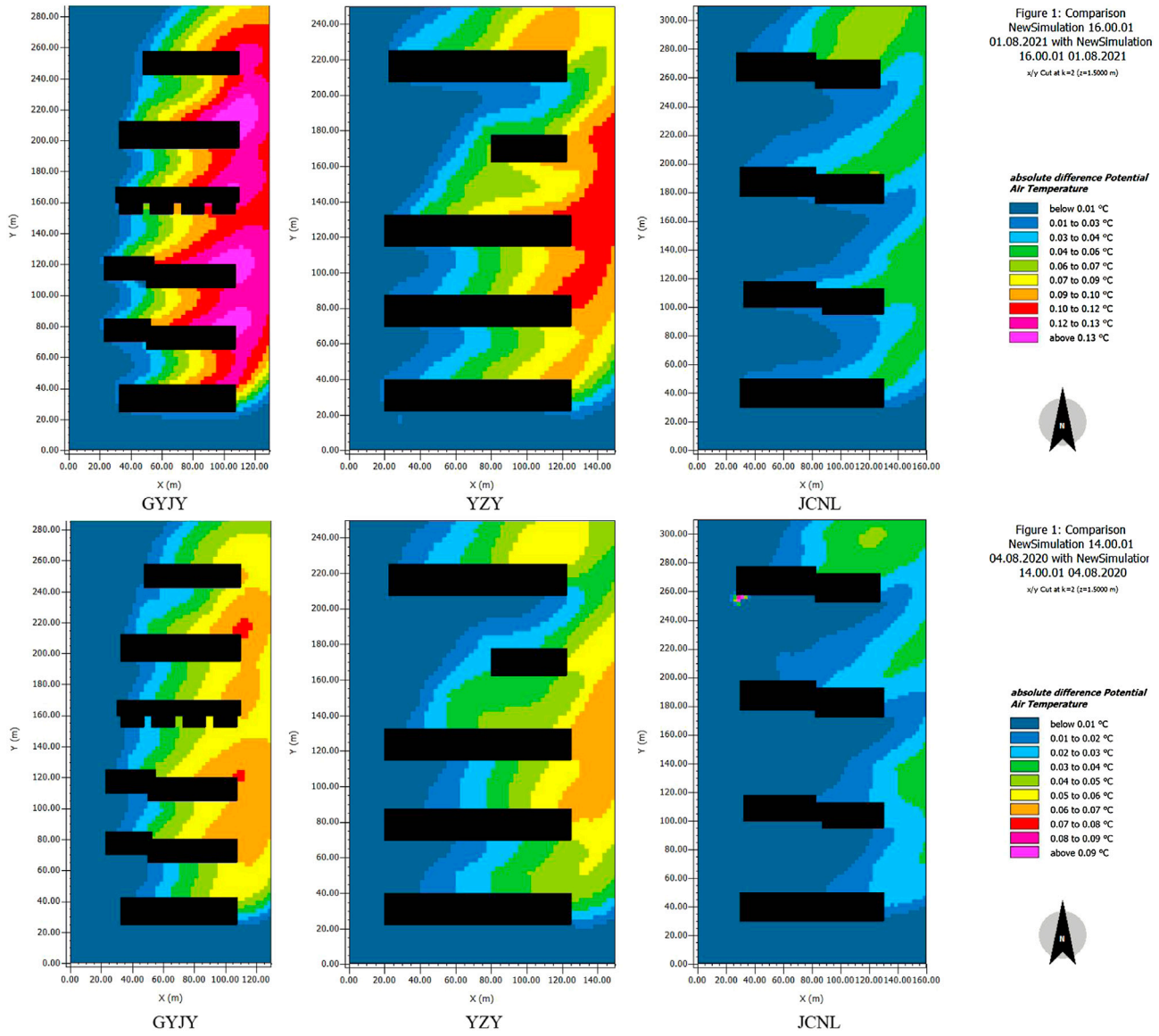

FIGURE 2 | The spatial distribution of pedestrian-level cooling intensity of green roofs at the time when the maximum air temperature of the day is reached. They were 4:00 p.m. on 1 August 2021 (Top) and 2:00 p.m. on 4 August 2020 (Bottom).

conditions (**Supplementary Figure A2**). Similar results were found in other residential areas and under two kinds of weather conditions.

3.2 Relationship Between Cooling Effect and Roof Height

The pedestrian-level cooling intensity of green roofs decreased with the roof height under two weather conditions, indicating that green roofs built on the high buildings would provide a low cooling effect at the pedestrian levels. For example, the average daytime pedestrian-level cooling intensities in GYJY, YZY, and JCNL with the building height of 18, 27, and 42 m were 0.05°C, 0.04°C, and 0.02°C, respectively, under typical summer conditions (**Figure 4**). Similarly, the average daytime cooling intensities under extreme heat conditions in these three residential areas were 0.03 , 0.03, and 0.01°C, showing a nonlinear decreasing trend.

There was an approximate threshold of roof height of 46–53 m, at which pedestrian-level cooling intensities of green roofs have been predicted to be zero (**Figure 4**), regardless of weather conditions. Although the cooling effect of green roofs significantly decreased under extreme conditions, its variations with roof height remain the same compared to results under typical summer conditions (**Figure 4**). For example, under typical summer conditions, GR built on the roofs of 18, 27, and 42 m can provide air temperature reduction of 0.05°C, 0.05°C, and 0.02°C at 4:00 p.m., but lost cooling effect when it was built on the roofs of

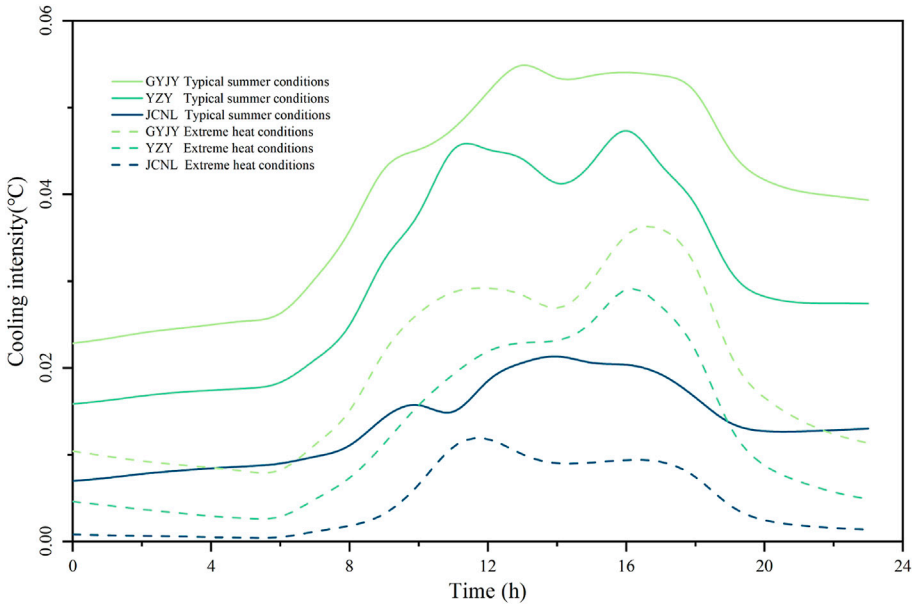

FIGURE 3 | Diurnal variation of pedestrian-level cooling intensity of green roofs for three study residential areas under two weather conditions.

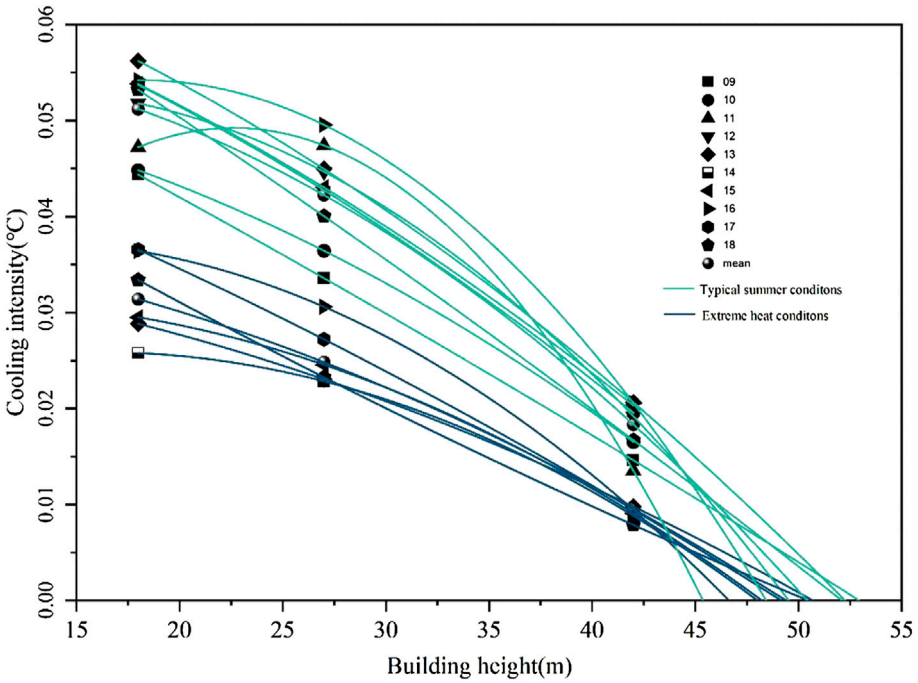

FIGURE 4 | Relationship between pedestrian-level cooling intensity and the roof height (or building height). A polynomial function fitted the relationships. Points with different shapes represent the pedestrian-level cooling intensity at different times, and the color of the lines represents two weather conditions.

49 m. Similar results were found under extreme heat conditions, and the maximum roof height was 47 m. Overall, the pedestrian-level cooling intensity of green roofs on buildings higher than ~50 m was predicted to be zero. It suggested that GR built on roofs higher than such threshold could not provide cooling at the pedestrian level under two weather conditions.

4 DISCUSSION

4.1 The Effects of Weather Conditions on the Cooling Effect of Green Roofs

Our results underscore the significant reduction of the cooling effect of green roofs under extreme heat conditions. Similar to the results from previous studies conducted in Beijing (~0.07°C) (Qiu et al., 2021), our results revealed the 0.02–0.05°C of the daytime pedestrian-level air temperature reduction under typical conditions. Although the average cooling intensity was small, we highlight the large air temperature reduction on the downwind sides and in the daytime (e.g., 10:00 a.m. to 5: 00 p.m.). However, such air temperature reduction under extreme heat conditions would be much smaller. This study is the first time to reveal that the cooling effect of green roofs at local scales would be reduced under extreme heat conditions, and similar results have been found in previous studies which focused on urban vegetation planted on the ground (Wang et al., 2020).

In addition, the cooling effects of GR varied significantly diurnally, showing an inverted W-shaped way, similar to previous results (Liu et al., 2018; Simon et al., 2018). Such variations were largely related to the response of evapotranspiration to air temperature (McAdam and Brodribb, 2015; Gillner et al., 2017). Increasing air temperature can induce the stomata to open and thus enhance evapotranspiration (Meili et al., 2021). However, the excessive air temperature would lead to the stomata being closed to protect trees from water loss and thus a dramatic reduction in evapotranspiration (Zhou et al., 2017). This water-saving strategy is reflected in the vegetation model in ENVI-met. Trees try to optimize their carbon gain-water loss relations, which are less beneficial under the high air temperature (Liu et al., 2018). Thus vegetation model assumes the high stomatal resistance to save water after midday (Bruse, 2004). Therefore a significant reduction in the cooling effect under extreme heat conditions or at the highest air temperature has been found.

Increasing urban vegetation, including vegetation planted on the ground and the roofs, is still an effective nature-based solution (NBS) to improve the urban thermal environment (Kumar et al., 2021). However, we must be aware that the cooling effect of the two types of aforementioned vegetation would be reduced under extreme heat conditions (Andric et al., 2020; Wang et al., 2020). Such reduction would be a challenge in the future when the extreme heat conditions would be the new normal because urban vegetation cannot provide significant cooling then (Ward et al., 2016; Pascal et al., 2021). Thus ecological management of urban vegetation (e.g., green roofs) is highly desired and warrants future research to achieve significant air temperature reduction under extreme heat conditions. The ecological management, such as the selection of species (Jim, 2015; MacIvor et al., 2016; Eksi et al., 2017), the optimization of the landscape of urban vegetation (Perini and Magliocco, 2014), and the maintenance (e.g., irrigation) of urban vegetation (Costanzo et al., 2016; Chagolla-Aranda et al., 2017), has been expected to help urban vegetation to generate the significant cooling, especially under extreme heat conditions.

4.2 The Effects of Roof Height on the Cooling Effect of Green Roofs

The cooling effect of green roofs at the pedestrian level depends on the evapotranspiration of green roofs and the roof height (Liu Z. et al., 2021). The evapotranspiration of green roofs suggests the cooling capacity of GR, and it is affected by the weather conditions (e.g., air temperature) (**Section 4.1**) (Rayner et al., 2016; Gilabert et al., 2021). The nonlinear response of evapotranspiration cooling of GR to air temperature leads to a nonlinear relationship between the cooling effect and roof height. Such findings are similar to the results of previous studies (Peng and Jim, 2013; Zhang et al., 2019; Sinsel et al., 2021).

Meanwhile, the roof height would determine how much of such cooling can travel vertically to the pedestrian level (Morakinyo et al., 2017). In this study, especially under typical summer conditions, 46–53 m of roof height was the farthest distance that evaporated cooling can travel vertically. In other words, when the roofs of the building are higher than such threshold, the evaporated cooling of the green roofs cannot travel to the pedestrian level. Similarly, under extreme heat conditions, the evaporated cooling of green roofs was decreased, and could not travel to the pedestrian level unless the roof of the building was low. Thus, a lower building height threshold was found under extreme heat conditions.

However, such a building height threshold, nearly 17-storey of residential buildings, is similar during urban planning and management. Our studies suggested that buildings lower than ~50 m (i.e., 17 stories) can be applied to plant on the roofs because evaporated cooling of green roofs can travel down to pedestrian levels to improve the urban thermal environment. This urban greening action can significantly promote the cooling effect in urban areas with limited urban green space on the ground (Lin et al., 2021). More than 97% (in number) and 95% (in the area) of the buildings in Beijing were included considering such a threshold (Zheng et al., 2017). Therefore, planting on most buildings in Beijing could reduce air temperature on the pedestrian levels and help improve the thermal environment in Beijing.

In addition, green roof planning requires the socio-ecological thinking of urban ecosystems, in which social and ecological benefits should be integrated (Zhou et al., 2021). Cooling-oriented urban green roof planning needs to consider both outdoor and indoor cooling. Outdoor cooling would improve the urban thermal comfort, especially at the pedestrian level and indoor cooling can reduce the energy resources (e.g., power consumption for air conditioners) used and further anthropogenic heat cities released from the buildings (Besir and Cuce, 2018). Meanwhile, urban planners should consider the cost of green roofs and the population achieving the benefits (Shafique et al., 2018). Although planting green roofs on the low buildings could deliver much cooling to the pedestrian level, they can provide indoor cooling for a small proportion of urban residents who live in low buildings. On the other hand, although green roofs on high buildings can benefit more people, they would cost more (Manso et al., 2021). The optimized roof height at which cooling and social benefits can

be balanced to create social and ecological win-wins warrants future research. In addition, the heights of buildings in the urban areas are staggered, showing spatial heterogeneity (Zheng et al., 2017). How to layout the green roof at more coarse scales is also worthy of further research.

This study has some limitations. First, we ran ENVI-met models without model evaluation in study areas (i.e. three residential areas) because there were not enough meteorological data. We evaluated ENVI-met models referencing the observed data on the RCEES campus. The validation suggested that the ENVI-met model had successful applications in Beijing, as much of previous research proved (Wang and Zacharias, 2015; Wu and Chen, 2017; Chen et al., 2020), but evaluating models in all study areas would be desirable. Second, we conducted the analysis only focusing on the air temperature reduction at the pedestrian level. Integrating green roofs' indoor and outdoor cooling effects would be interesting and warrant future research.

5 CONCLUSION

This study aimed to reveal whether green roofs can provide a significant cooling effect at pedestrian levels under extreme heat conditions and how such cooling effects varied along with roof height. Using ENVI-met model simulation, we found: 1) Green roofs can provide large cooling which can exceed 0.2°C on the downwind sides and at the daytimes, although the average cooling intensity was small. 2) The pedestrian-level cooling intensity of GR under extreme heat conditions was significantly lower than that under typical summer conditions. 3) These temperature reductions varied significantly diurnally in an inverted W-shaped way under both weather conditions. 4) Results also showed that the pedestrian-level cooling intensity of GR decreased with the increase in roof height in a nonlinear way and has been predicted to be 0 when roofs were higher than ~50 m (i.e. 17 stories) under both two weather conditions. This study enhances the understanding of the cooling effect of green roofs under extreme heat conditions. It can provide important insight for future cooling-oriented urban green roof planning.

DATA AVAILABILITY STATEMENT

The original contributions presented in the study are included in the article/**Supplementary Material**; further inquiries can be directed to the corresponding authors.

AUTHOR CONTRIBUTIONS

Conceptualization: YF, JW, and WZ; formal analysis: YF, JW, and XL; writing—original draft preparation: YF, JW, and WZ; and writing—review and editing: JW and XY.

FUNDING

This research was funded by the National Natural Science Foundation of China (Grant No. 32001160, No. 32001161), the Education Department of Hunan Province (Grant No. 20B297), and the Science and Technology Bureau, Changsha (kq2202227).

SUPPLEMENTARY MATERIAL

The Supplementary Material for this article can be found online at: https://www.frontiersin.org/articles/10.3389/fenvs.2022.874614/full#supplementary-material

REFERENCES

Andric, I., Kamal, A., and Al-Ghamdi, S. G. (2020). Efficiency of Green Roofs and Green Walls as Climate Change Mitigation Measures in Extremely Hot and Dry Climate: Case Study of Qatar. *Energy Rep.* 6, 2476–2489. doi:10.1016/j.egyr.2020.09.006

Berardi, U. (2016). The Outdoor Microclimate Benefits and Energy Saving Resulting from Green Roofs Retrofits. *Energy Build.* 121, 217–229. doi:10.1016/j.enbuild.2016.03.021

Besir, A. B., and Cuce, E. (2018). Green Roofs and Facades: A Comprehensive Review. *Renew. Sustain. Energy Rev.* 82, 915–939. doi:10.1016/j.rser.2017.09.106

Bruse, M. (2004). ENVI-met Implementation of the Jacobs A – Gs Model to Calculate the Stomata Conductance. [Online] Available at: http://www.envi-met.net/documents/new_a_gs.pdf (Accessed February 16th, 2004).

Cao, J., Zhou, W., Wang, J., Hu, X., Yu, W., Zheng, Z., et al. (2021). Significant Increase in Extreme Heat Events along an Urban-Rural Gradient. *Landsc. Urban Plan.* 215, 104210. doi:10.1016/j.landurbplan.2021.104210

Castleton, H. F., Stovin, V., Beck, S. B. M., and Davison, J. B. (2010). Green Roofs; Building Energy Savings and the Potential for Retrofit. *Energy Build.* 42 (10), 1582–1591. doi:10.1016/j.enbuild.2010.05.004

Chagolla-Aranda, M. A., Simá, E., Xamán, J., Álvarez, G., Hernández-Pérez, I., and Téllez-Velázquez, E. (2017). Effect of Irrigation on the Experimental Thermal Performance of a Green Roof in a Semi-warm Climate in Mexico. *Energy Build.* 154, 232–243. doi:10.1016/j.enbuild.2017.08.082

Chen, Y., Wu, J., Yu, K., and Wang, D. (2020). Evaluating the Impact of the Building Density and Height on the Block Surface Temperature. *Build. Environ.* 168, 106493. doi:10.1016/j.buildenv.2019.106493

Costanzo, V., Evola, G., and Marletta, L. (2016). Energy Savings in Buildings or UHI Mitigation? Comparison between Green Roofs and Cool Roofs. *Energy Build.* 114, 247–255. doi:10.1016/j.enbuild.2015.04.053

Crank, P. J., Sailor, D. J., Ban-Weiss, G., and Taleghani, M. (2018). Evaluating the ENVI-Met Microscale Model for Suitability in Analysis of Targeted Urban Heat Mitigation Strategies. *Urban Clim.* 26, 188–197. doi:10.1016/j.uclim.2018.09.002

Cristiano, E., Deidda, R., and Viola, F. (2021). The Role of Green Roofs in Urban Water-Energy-Food-Ecosystem Nexus: A Review. *Sci. Total Environ.* 756, 143876. doi:10.1016/j.scitotenv.2020.143876

Eksi, M., Rowe, D. B., Wichman, I. S., and Andresen, J. A. (2017). Effect of Substrate Depth, Vegetation Type, and Season on Green Roof Thermal Properties. *Energy Build.* 145, 174–187. doi:10.1016/j.enbuild.2017.04.017

Francis, L. F. M., and Jensen, M. B. (2017). Benefits of Green Roofs: A Systematic Review of the Evidence for Three Ecosystem Services. *Urban For. Urban Green.* 28, 167–176. doi:10.1016/j.ufug.2017.10.015

Gao, M., Chen, F., Shen, H., Barlage, M., Li, H., Tan, Z., et al. (2019). Efficacy of Possible Strategies to Mitigate the Urban Heat Island Based on Urbanized High-Resolution Land Data Assimilation System (U-HRLDAS). *J. Meteorol. Soc. Jpn.* 97, 1075–1097. doi:10.2151/jmsj.2019-060

Gao, M., Chen, F., Shen, H., and Li, H. (2020). A Tale of Two Cities: Different Urban Heat Mitigation Efficacy with the Same Strategies. *Theor. Appl. Climatol.* 142, 1625–1640. doi:10.1007/s00704-020-03390-2

Gilabert, J., Ventura, S., Segura, R., Martilli, A., Badia, A., Llasat, C., et al. (2021). Abating Heat Waves in a Coastal Mediterranean City: What Can Cool Roofs and Vegetation Contribute? *Urban Clim.* 37, 100863. doi:10.1016/j.uclim.2021.100863

Gillner, S., Korn, S., Hofmann, M., and Roloff, A. (2017). Contrasting Strategies for Tree Species to Cope with Heat and Dry Conditions at Urban Sites. *Urban Ecosyst.* 20 (4), 853–865. doi:10.1007/s11252-016-0636-z

Herath, H. M. P. I. K., Halwatura, R. U., and Jayasinghe, G. Y. (2018). Evaluation of Green Infrastructure Effects on Tropical Sri Lankan Urban Context as an Urban Heat Island Adaptation Strategy. *Urban For. Urban Green.* 29, 212–222. doi:10.1016/j.ufug.2017.11.013

Huttner, S., and Bruse, M. (2009). "Numerical Modeling of the Urban Climate- a Preview on ENVI-Met 4.0," in The seventh International Conference on Urban Climate ICUC-7, Yokohama, Japan, June 29–July 3, 2009.

IPCC (2014). Climate Change 2014: Synthesis Report. Contribution of Working Groups I, II and III to the Fifth Assessment Report of the Intergovernmental Panel on Climate Change. [Online] Available at: https://epic.awi.de/id/eprint/37530/ (Accessed November 1, 2014).

Izquierdo, S., Rodrigues, M., and Fueyo, N. (2008). A Method for Estimating the Geographical Distribution of the Available Roof Surface Area for Large-Scale Photovoltaic Energy-Potential Evaluations. *Sol. Energy* 82 (10), 929–939. doi:10.1016/j.solener.2008.03.007

Jamei, E., Chau, H. W., Seyedmahmoudian, M., and Stojcevski, A. (2021). Review on the Cooling Potential of Green Roofs in Different Climates. *Sci. Total Environ.* 791, 148407. doi:10.1016/j.scitotenv.2021.148407

Jiao, M., Xue, H. R., Yan, J. L., Zheng, Z., Wang, J., Zhao, C., et al. (2021). Tree Abundance, Diversity and Their Driving and Indicative Factors in Beijing's Residential Areas. *Ecol. Indic.* 125, 107462. doi:10.1016/j.ecolind.2021.107462

Jim, C. Y. (2015). Assessing Climate-Adaptation Effect of Extensive Tropical Green Roofs in Cities. *Landsc. Urban Plan.* 138, 54–70. doi:10.1016/j.landurbplan.2015.02.014

Jin, C., Bai, X., Luo, T., and Zou, M. (2018). Effects of Green Roofs' Variations on the Regional Thermal Environment Using Measurements and Simulations in Chongqing, China. *Urban For. Urban Green.* 29, 223–237. doi:10.1016/j.ufug.2017.12.002

Klein, P. M., and Coffman, R. (2015). Establishment and Performance of an Experimental Green Roof under Extreme Climatic Conditions. *Sci. Total Environ.* 512-513, 82–93. doi:10.1016/j.scitotenv.2015.01.020

Knaus, M., and Haase, D. (2020). Green Roof Effects on Daytime Heat in a Prefabricated Residential Neighbourhood in Berlin, Germany. *Urban For. Urban Green.* 53, 126738. doi:10.1016/j.ufug.2020.126738

Knowlton, K., Rosenthal, J. E., Hogrefe, C., Lynn, B., Gaffin, S., Goldberg, R., et al. (2004). Assessing Ozone-Related Health Impacts under a Changing Climate. *Environ. Health Perspect.* 112 (15), 1557–1563. doi:10.1289/ehp.7163

Kong, F., Yin, H., Wang, C., Cavan, G., and James, P. (2014). A Satellite Image-Based Analysis of Factors Contributing to the Green-Space Cool Island Intensity on a City Scale. *Urban For. Urban Green.* 13 (4), 846–853. doi:10.1016/j.ufug.2014.09.009

Kumar, P., Debele, S. E., Sahani, J., Rawat, N., Marti-Cardona, B., Alfieri, S. M., et al. (2021). Nature-based Solutions Efficiency Evaluation against Natural Hazards: Modelling Methods, Advantages and Limitations. *Sci. Total Environ.* 784, 147058. doi:10.1016/j.scitotenv.2021.147058

Lin, M., Dong, J., Jones, L., Liu, J., Lin, T., Zuo, J., et al. (2021). Modeling Green Roofs' Cooling Effect in High-Density Urban Areas Based on Law of Diminishing Marginal Utility of the Cooling Efficiency: A Case Study of Xiamen Island, China. *J. Clean. Prod.* 316, 128277. doi:10.1016/j.jclepro.2021.128277

Liu, H. Q., Kong, F. H., Yin, H. W., Middel, A., Zheng, X. D., Huang, J., et al. (2021a). Impacts of Green Roofs on Water, Temperature, and Air Quality: A Bibliometric Review. *Build. Environ.* 196, 107794. doi:10.1016/j.buildenv.2021.107794

Liu, Z., Cheng, W., Jim, C. Y., Morakinyo, T. E., Shi, Y., and Ng, E. (2021b). Heat Mitigation Benefits of Urban Green and Blue Infrastructures: A Systematic Review of Modeling Techniques, Validation and Scenario Simulation in ENVI-Met V4. *Build. Environ.* 200, 107939. doi:10.1016/j.buildenv.2021.107939

Liu, Z. X., Zheng, S. L., and Zhao, L. H. (2018). Evaluation of the ENVI-Met Vegetation Model of Four Common Tree Species in a Subtropical Hot-Humid Area. *Atmosphere* 9 (5), 198. doi:10.3390/atmos9050198

MacIvor, J. S., Margolis, L., Perotto, M., and Drake, J. A. P. (2016). Air Temperature Cooling by Extensive Green Roofs in Toronto Canada. *Ecol. Eng.* 95, 36–42. doi:10.1016/j.ecoleng.2016.06.050

Manso, M., Teotónio, I., Silva, C. M., and Cruz, C. O. (2021). Green Roof and Green Wall Benefits and Costs: A Review of the Quantitative Evidence. *Renew. Sustain. Energy Rev.* 135, 110111. doi:10.1016/j.rser.2020.110111

Mauree, D., Naboni, E., Coccolo, S., Perera, A. T. D., Nik, V. M., and Scartezzini, J.-L. (2019). A Review of Assessment Methods for the Urban Environment and its Energy Sustainability to Guarantee Climate Adaptation of Future Cities. *Renew. Sustain. Energy Rev.* 112, 733–746. doi:10.1016/j.rser.2019.06.005

McAdam, S. A. M., and Brodribb, T. J. (2015). The Evolution of Mechanisms Driving the Stomatal Response to Vapor Pressure Deficit. *Plant Physiol.* 167 (3), 833–843. doi:10.1104/pp.114.252940

Meili, N., Manoli, G., Burlando, P., Carmeliet, J., Chow, W. T. L., Coutts, A. M., et al. (2021). Tree Effects on Urban Microclimate: Diurnal, Seasonal, and Climatic Temperature Differences Explained by Separating Radiation, Evapotranspiration, and Roughness Effects. *Urban For. Urban Green.* 58, 126970. doi:10.1016/j.ufug.2020.126970

Morakinyo, T. E., Dahanayake, K. W. D. K. C., Ng, E., and Chow, C. L. (2017). Temperature and Cooling Demand Reduction by Green-Roof Types in Different Climates and Urban Densities: A Co-Simulation Parametric Study. *Energy Build.* 145, 226–237. doi:10.1016/j.enbuild.2017.03.066

Ng, E., Chen, L., Wang, Y., and Yuan, C. (2012). A Study on the Cooling Effects of Greening in a High-Density City: An Experience from Hong Kong. *Build. Environ.* 47, 256–271. doi:10.1016/j.buildenv.2011.07.014

Niemelä, J. (1999). Ecology and Urban Planning. *Biodivers. Conservation* 8 (1), 119–131. doi:10.1023/A:1008817325994

Pascal, M., Goria, S., Wagner, V., Sabastia, M., Guillet, A., Cordeau, E., et al. (2021). Greening is a Promising but Likely Insufficient Adaptation Strategy to Limit the Health Impacts of Extreme Heat. *Environ. Int.* 151, 106441. doi:10.1016/j.envint.2021.106441

Peng, L., and Jim, C. (2013). Green-Roof Effects on Neighborhood Microclimate and Human Thermal Sensation. *Energies* 6 (2), 598–618. doi:10.3390/en6020598

Perini, K., and Magliocco, A. (2014). Effects of Vegetation, Urban Density, Building Height, and Atmospheric Conditions on Local Temperatures and Thermal Comfort. *Urban For. Urban Green.* 13 (3), 495–506. doi:10.1016/j.ufug.2014.03.003

Qi, J., Ding, L., and Lim, S. (2021). Toward Cool Cities and Communities: A Sensitivity Analysis Method to Identify the Key Planning and Design Variables for Urban Heat Mitigation Techniques. *Sustain. Cities Soc.* 75, 103377. doi:10.1016/j.scs.2021.103377

Qiu, L., Zhang, H., Zhang, W., Lai, D., and Li, R. (2021). Effect of Existing Residential Renovation Strategies on Building Cooling Load: Cases in Three Chinese Cities. *Energy Build.* 253, 111548. doi:10.1016/j.enbuild.2021.111548

Rayner, J. P., Farrell, C., Raynor, K. J., Murphy, S. M., and Williams, N. S. G. (2016). Plant Establishment on a Green Roof under Extreme Hot and Dry Conditions: The Importance of Leaf Succulence in Plant Selection. *Urban For. Urban Green.* 15, 6–14. doi:10.1016/j.ufug.2015.11.004

Sailor, D. J., and Fan, H. (2002). Modeling the Diurnal Variability of Effective Albedo for Cities. *Atmos. Environ.* 36 (4), 713–725. doi:10.1016/S1352-2310(01)00452-6

Salvati, A., and Kolokotroni, M. (2019). "Microclimate Data for Building Energy Modelling: Study on ENVI-Met Forcing Data," in Proceedings of the 16th IBPSA Conference, Rome, Italy, September 2–4, 2019. doi:10.26868/25222708.2019.210544

Shafique, M., Kim, R., and Rafiq, M. (2018). Green Roof Benefits, Opportunities and Challenges - A Review. *Renew. Sustain. Energy Rev.* 90, 757–773. doi:10.1016/j.rser.2018.04.006

Simon, H., Lindén, J., Hoffmann, D., Braun, P., Bruse, M., and Esper, J. (2018). Modeling Transpiration and Leaf Temperature of Urban Trees - A Case Study Evaluating the Microclimate Model ENVI-Met against Measurement Data. *Landsc. Urban Plan.* 174, 33–40. doi:10.1016/j.landurbplan.2018.03.003

Sinsel, T., Simon, H., Broadbent, A. M., Bruse, M., and Heusinger, J. (2021). Modeling the Outdoor Cooling Impact of Highly Radiative "Super Cool" Materials Applied on Roofs. *Urban Clim.* 38, 100898. doi:10.1016/j.uclim.2021.100898

Sun, T., Grimmond, C. S. B., and Ni, G.-H. (2016). How Do Green Roofs Mitigate Urban Thermal Stress under Heat Waves? *J. Geophys. Res. Atmos.* 121, 5320–5335. doi:10.1002/2016JD024873

Susca, T. (2019). Green Roofs to Reduce Building Energy Use? A Review on Key Structural Factors of Green Roofs and Their Effects on Urban Climate. *Build. Environ.* 162, 106273. doi:10.1016/j.buildenv.2019.106273

Tian, P., Li, J., Cao, L., Pu, R., Wang, Z., Zhang, H., et al. (2021). Assessing Spatiotemporal Characteristics of Urban Heat Islands from the Perspective of an Urban Expansion and Green Infrastructure. *Sustain. Cities Soc.* 74, 103208. doi:10.1016/j.scs.2021.103208

Tsoka, S., Tsikaloudaki, A., and Theodosiou, T. (2018). Analyzing the ENVI-Met Microclimate Model's Performance and Assessing Cool Materials and Urban Vegetation Applications-A Review. *Sustain. Cities Soc.* 43, 55–76. doi:10.1016/j.scs.2018.08.009

UN (2018). 2018 Revision of World Urbanization Prospects. Available at: https://www.un.org/development/desa/en/news/population/2018-revision-of-world-urbanization-prospects.html (Accessed May 16, 2018).

Voogt, J. A., and Oke, T. R. (2003). Thermal Remote Sensing of Urban Climates. *Remote Sens. Environ.* 86 (3), 370–384. doi:10.1016/S0034-4257(03)00079-8

Wang, C., Wang, Z.-H., Wang, C., and Myint, S. W. (2019a). Environmental Cooling provided by Urban Trees under Extreme Heat and Cold Waves in U.S. Cities. *Remote Sens. Environ.* 227, 28–43. doi:10.1016/j.rse.2019.03.024

Wang, J., Zhou, W., and Jiao, M. (2022). Location Matters: Planting Urban Trees in the Right Places Improves Cooling. *Front. Ecol Environ* 20, 147–151. doi:10.1002/fee.2455

Wang, J., Zhou, W., Jiao, M., Zheng, Z., Ren, T., and Zhang, Q. (2020). Significant Effects of Ecological Context on Urban Trees' Cooling Efficiency. *ISPRS J. Photogramm. Remote Sens.* 159, 78–89. doi:10.1016/j.isprsjprs.2019.11.001

Wang, J., Zhou, W., and Wang, J. (2019b). Time-Series Analysis Reveals Intensified Urban Heat Island Effects but without Significant Urban Warming. *Remote Sens.* 11, 2229. doi:10.3390/rs11192229

Wang, Y., and Zacharias, J. (2015). Landscape Modification for Ambient Environmental Improvement in Central Business Districts – A Case From Beijing. *Urban For. Urban Green.* 14, 8–18.

Ward, K., Lauf, S., Kleinschmit, B., and Endlicher, W. (2016). Heat Waves and Urban Heat Islands in Europe: A Review of Relevant Drivers. *Sci. Total Environ.* 569-570, 527–539. doi:10.1016/j.scitotenv.2016.06.119

White, M. A., Nemani, R. R., Thornton, P. E., and Running, S. W. (2002). Satellite Evidence of Phenological Differences between Urbanized and Rural Areas of the Eastern United States Deciduous Broadleaf Forest. *Ecosystems* 5 (3), 260–273. doi:10.1007/s10021-001-0070-8

Wu, Z., and Chen, L. (2017). Optimizing the Spatial Arrangement of Trees in Residential Neighborhoods for Better Cooling Effects: Integrating Modeling With *in-situ* Measurements. *Landsc. Urban Plan.* 167, 463–472.

Zhang, G., He, B.-J., Zhu, Z., and Dewancker, B. J. (2019). Impact of Morphological Characteristics of Green Roofs on Pedestrian Cooling in Subtropical Climates. *Int. J. Environ. Res. Public Health* 16, 179. doi:10.3390/ijerph16020179

Zheng, Z., Zhou, W., Wang, J., Hu, X., and Qian, Y. (2017). Sixty-Year Changes in Residential Landscapes in Beijing: A Perspective from Both the Horizontal (2D) and Vertical (3D) Dimensions. *Remote Sens.* 9 (10), 992. doi:10.3390/rs9100992

Zhou, W., Huang, G., and Cadenasso, M. L. (2011). Does Spatial Configuration Matter? Understanding the Effects of Land Cover Pattern on Land Surface Temperature in Urban Landscapes. *Landsc. Urban Plan.* 102 (1), 54–63. doi:10.1016/j.landurbplan.2011.03.009

Zhou, W., Huang, G., Pickett, S. T. A., Wang, J., Cadenasso, M. L., McPhearson, T., et al. (2021). Urban Tree Canopy Has Greater Cooling Effects in Socially Vulnerable Communities in the US. *One Earth* 4 (12), 1764–1775. doi:10.1016/j.oneear.2021.11.010

Zhou, W., Wang, J., and Cadenasso, M. L. (2017). Effects of the Spatial Configuration of Trees on Urban Heat Mitigation: A Comparative Study. *Remote Sens. Environ.* 195, 1–12. doi:10.1016/j.rse.2017.03.043

Conflict of Interest: The authors declare that the research was conducted in the absence of any commercial or financial relationships that could be construed as a potential conflict of interest.

Publisher's Note: All claims expressed in this article are solely those of the authors and do not necessarily represent those of their affiliated organizations, or those of the publisher, the editors, and the reviewers. Any product that may be evaluated in this article, or claim that may be made by its manufacturer, is not guaranteed or endorsed by the publisher.

Frontiers in Environmental Science

Explores the anthropogenic impact on our natural world

An innovative journal that advances knowledge of the natural world and its intersections with human society. It supports the formulation of policies that lead to a more inhabitable and sustainable world.

Discover the latest Research Topics

See more →

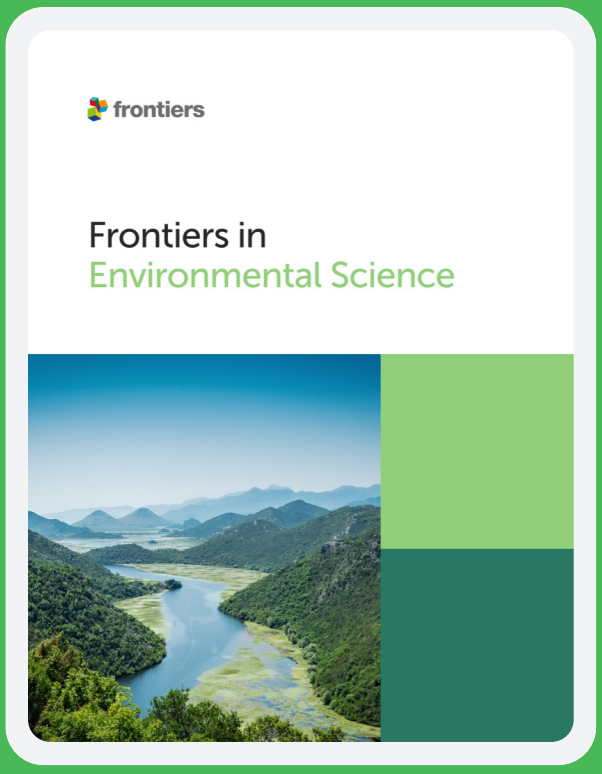

Frontiers

Avenue du Tribunal-Fédéral 34
1005 Lausanne, Switzerland
frontiersin.org

Contact us

+41 (0)21 510 17 00
frontiersin.org/about/contact